



universität
wien

DISSERTATION / DOCTORAL THESIS

Titel der Dissertation / Title of the Doctoral Thesis

„Silaffin-derived Peptides generate Silica Structures for
Delivery and Integral Membrane Protein Encapsulation“

verfasst von / submitted by
Friedrich Bialas, M.Sc.

angestrebter akademischer Grad / in partial fulfilment of the requirements for the degree of
Doktor der Naturwissenschaften (Dr. rer. nat.)

Wien, 2020 / Vienna 2020

Studienkennzahl lt. Studienblatt /
degree programme code as it appears on the student
record sheet:

A 796 605 419

Dissertationsgebiet lt. Studienblatt /
field of study as it appears on the student record sheet:

Doktoratsstudium Naturwissenschaften: Chemie

Betreut von / Supervisor:

Prof. Dr. Christian F. W. Becker

Acknowledgements

I thank Professor Christian Becker for the opportunity to be a part of his working group, for his continuous support, and the already legendary Christmas celebrations. The PhD was an unprecedented opportunity to pursue and test my own ideas, fail and succeed, and I am very grateful I had the chance to do so. It has been a pleasure to work at the Institute of Biological Chemistry and I would like to extend my gratitude to all its former and current members, including, but not limited to Claudia Bello, who was a very supportive first office neighbour, Michaela Cherrier, for not losing patience with me trying to fill out forms, Doris Ellmer, for her witty remarks, Manuel Hafner, for helping me get started, Meder Kamalov, for inspiring discussions not limited to serious science, Julia Kriegesmann, creator of the most amazing peptides and the most amazing Tiramisu, Gerhard Niederacher, for sharing his insider knowledge on microbiology and the best lunch options in Vienna, and Daniela Reichinger, for introducing me to the concept of Fika.

Furthermore, I would like to thank Laura Niederstätter and Alexander Preinfalk, also from the Faculty of Chemistry, for sticking to our business lunch tradition.

I also want to thank the staff of the mass and the NMR centres at the Faculty of Chemistry, as well as Stephan Puchegger for introducing me to scanning electron microscopy and Professor Christian Rentenberger for helping me with the transmission electron microscope.

I would like to especially thank the students Christoph Kornpointner, Johannes Strobl, Paul Primerano, Jiratchaya Arminsen and Sarah Isabella Stadlmayr who have worked with me on the projects. Without their interest and dedicated work this thesis would not have been possible.

I also want to thank Professor Tuomas Knowles and all members of the Centre for Misfolding Diseases in Cambridge, who have been most welcoming during a secondment there. It was a great time working there with Tuuli Hakala, Aviad Levin, Zenon Toprakcioglu, and all the others. Special thanks go to Heather Greer, who trusted me with the scanning electron microscope.

The PhD was an exceptional experience for me also because I had the chance to be part of a greater network of incredible people, together with Padma Akkapeddi, Charlotte Baker, Silvia Baldo, Xhenti Ferhati, Tuuli Hakala, Marco Lucchino, João Faria Nogueira, Roberto Russo, and Maksymilian Zegota. I want to thank all of them for being supportive and just great company during our many meetings. I am very grateful to Professors Christian Becker, Gonçalo Bernardes, Stephen Caddick, Vijay Chudasama, Pedro Gois, Francisco Corzana López, Johannes Ludger, Tanja Weil, Tuomas Knowles and the founding bodies for making the Protein Conjugates ITN possible.

Last, but far from least, my warmest thanks go to my parents, Anne and Frank Bialas, who have supported me during all the long years of studies and continue to believe in me.

Abstract

Silica nanoparticles are non-toxic and of tuneable biodegradability depending on their morphology and porosity. The biomimetic synthesis of silica nanoparticles is inspired by the shell-forming processes of organisms such as sponges and diatoms and proceeds under mild conditions and at neutral pH. Suitable catalysts are certain polyamines and peptides. In the first part of this work, the silica-precipitating R5 peptide from the diatom *C. fusiformis* was conjugated with two different polyphenols, galangin and quercetin, as model natural compounds. This required the introduction of a suitably functionalized linker, which was placed at the 7-O position of galangin and quercetin. Galangin was modified with a carboxylic acid linker in a one-step reaction; a four-step synthetic strategy was used to introduce a similar carboxylic acid linker on quercetin. Spherical silica particles were precipitated from both conjugates using a previously established protocol for unmodified R5 peptide. To observe the particles by (confocal) fluorescence microscopy, galangin-R5 silica particles were labelled with a fluorescein-derived silane compound, whereas quercetin-R5 particles were monitored based on the intrinsic quercetin fluorescence. Confocal fluorescence microscopy experiments with HT-29 human colorectal cancer cells showed that the quercetin-R5 silica particles, but not the galangin-R5 silica particles are efficiently taken up into the cells and localize in their nuclei within 3 hours of exposure. The uptake mechanism was shown to be an active, energy-dependent process different from micropinocytosis. At the investigated concentration of 70 μM conjugate, no toxic effects were observed. Non-toxic silica particles not only offer the possibility to encapsulate small molecules, but also entire proteins and membrane structures.

Integral membrane proteins are ubiquitous in nature and present an important class of drug targets. Their investigation is complicated by the difficulty to stabilize them in solution, requiring the use of detergents or solubility tags. Nanodiscs, membrane lipid bicelles surrounded by the membrane scaffold protein (MSP), were developed to enable such stabilization in a defined membrane environment. In the work presented here, new variants of MSP were designed by genetically fusing the silica-precipitating R5 peptide to its N- and/or C-terminus. In this way, plasmids for the expression of three new variants, R5-MSP, MSP-R5, and R5-MSP-R5 were obtained, including a removable His₆-tag for purification. The R5-MSP-R5 construct could be successfully expressed and purified. Analogous to the unmodified MSP, the R5-MSP-R5 protein could be used for the formation of nanodiscs with the membrane phospholipid DOPC, which were characterized by transmission electron microscopy (TEM) and dynamic light scattering (DLS). As expected, the R5-MSP-R5 nanodiscs, but not the MSP nanodiscs, induced silica particle formation in a solution of silicic acid. The particles were then characterized by TEM and atomic force microscopy (AFM). Both techniques revealed fibrous structures, corresponding to stacks of nanodiscs, which are covered by a layer of silica. This is a completely new material which might be equipped with various properties by embedding different molecules in the silica-covered nanodiscs. An attempt to embed the *E. coli* diacyl glycerol kinase (DGK) inside the nanodiscs did not succeed, therefore, a different strategy was devised to create silica-encapsulated DGK.

The amphiphilic BP-1 peptide was developed to stabilize membrane proteins in solution by direct interaction with the detergent-like amphiphilic peptide. In this work, four new peptide constructs, based on BP-1, were designed, synthesized and purified. As expected, the new variants, in contrast to the unmodified BP-1 peptide, induced the formation of silica particles of different morphologies from a solution of silicic acid. A stabilizing effect on the membrane protein diacylglycerol kinase (DGK) could not be observed when adding the peptides only. However, it was possible to encapsulate the DGK protein into spherical silica particles, when using the modified BP-1 constructs as catalysts. The BP-1-R5 peptide proved significantly more effective in this than the R5 peptide alone. The encapsulated DGK showed reduced kinase activity towards its hydrophobic substrate dioleoylglycerol, most likely due to the limited diffusion of dioleoylglycerol into the silica particles. However, DGK stability in BP-1-R5 silica particles was significantly increased as demonstrated in assays against Pronase E, simulated gastric fluid (SGF), and simulated intestinal fluid (SIF). Thus, BP-1-R5 proved to be a new tool to encapsulate functional membrane proteins in silica. These functionalised silica particles could be used to equip sensors or bioreactors.

Zusammenfassung

Silica-Nanopartikel sind ungiftig und ihre Bioabbaubarkeit kann, abhängig von Morphologie und Porosität, eingestellt werden. Die biomimetische Synthese von Silica-Nanopartikeln wurde von den skelettbildenden Vorgängen in Schwämmen und Kieselalgen inspiriert und verläuft bei milden Reaktionsbedingungen und neutralem pH. Dabei werden bestimmte Polyamine und Peptide als Katalysator genutzt. Im ersten Teil der vorliegenden Arbeit wurde das Silica-präzipitierende R5-Peptid aus der Kieselalge *C. fusiformis* mit verschiedenen Lebensmittelinhaltsstoffen aus der Substanzklasse der Polyphenole, Galangin und Quercetin, verknüpft. Um dies zu ermöglichen mussten die Polyphenole zunächst mit einem geeigneten Linker modifiziert werden, welcher an der 7-O-Position der Moleküle angebracht wurde. Die Modifikation konnte bei Galangin in einer einstufigen Reaktion durchgeführt werden; bei Quercetin kam eine vierstufige Synthesestrategie zum Einsatz. Mit einer bereits etablierten Methode, die auch bei unmodifiziertem R5-Peptid angewendet wird, wurden kugelförmige Silicapartikel mit beiden Konjugaten hergestellt. Für die (konfokale) Fluoreszenzmikroskopie wurden die mit Galangin-R5 hergestellten Partikel mit einem Silanderivat des Fluoreszeins gelabelt; die Quercetin-R5-Silicapartikel konnten durch die intrinsische Fluoreszenz des Quercetinchromophors beobachtet werden. Die so durchgeführten Fluoreszenzmikroskopieexperimente haben gezeigt, dass die Quercetin-R5-Silicapartikel, nicht aber die Galangin-R5-Silicapartikel innerhalb von drei Stunden mit hoher Effizienz in den Zellkern von humanen HT-29 Kolon-Tumorzellen aufgenommen werden. Die Aufnahme konnte als aktiver Endozytoseprozess, unabhängig von Mikropinozytose, identifiziert werden. Bei der angewendeten Konzentration von 70 μM wurden keine Toxizitäts-Effekte beobachtet. Ungiftige Silicapartikel dienen nicht nur zur Verkapselung von kleinen Molekülen, sondern können auch vollständige Proteine und Membranstrukturen enthalten.

Integrale Membranproteine sind in der Natur allgegenwärtig und bilden einen Großteil der Targetproteine für Arzneimittelwirkstoffe. Um sie zu erforschen, müssen sie in Lösung stabilisiert werden, was Detergenzien oder lösliche Fusionsproteine erfordert. Nanodiscs sind Membranlipidbizzellen, welche durch das Membrane Scaffold Protein (MSP) in Form gehalten werden und wurden entwickelt, um solch eine Stabilisierung in einem festgelegten Membranumfeld zu gewährleisten. Bei der hier vorgestellten Arbeit wurden neue Varianten des MSP entworfen, bei denen das R5-Peptid genetisch an den N- und/oder C-Terminus des Proteins geknüpft wurde. Dadurch konnten Plasmide für drei neue Konstrukte, R5-MSP, MSP-R5 und R5-MSP-R5, erhalten werden, inklusive eines entfernbaren His-Tags für die Proteinaufreinigung. Das R5-MSP-R5-Konstrukt konnte erfolgreich exprimiert und aufgereinigt werden. Ebenso wie beim ursprünglichen MSP konnten mit dem R5-MSP-R5-Protein Nanodiscs mit dem Phospholipid DOPC hergestellt werden, welche mittels Transmissionselektronenmikroskopie (TEM) und dynamischer Lichtstreuung (DLS) charakterisiert wurden. Wie erwartet, konnten die modifizierten R5-MSP-R5 Nanodiscs, nicht aber die MSP Nanodiscs die Bildung von Silicapartikeln induzieren, welche mittels TEM und Rasterkraftmikroskopie (AFM) untersucht wurden. Beide Untersuchungsmethoden zeigen fibrillenartige Strukturen, welche silicabeschichteten Stapeln von Nanodiscs entsprechen.

Diese stellen ein völlig neuartiges Material dar, welches sich je nach eingebetteten Molekülen mit Eigenschaften ausstatten lässt. Der Versuch, *E. coli* Diacylglycerolkinase (DGK) in die Nanodiscs einzubetten gelang nicht, weshalb eine andere Strategie entwickelt wurde um Silica-verkapselte DGK zu erzeugen.

Um Membranproteine direkt in Lösung zu stabilisieren, wurde das amphiphile BP-1-Peptid entwickelt. Im dritten Teil der vorliegenden Arbeit wurden vier verschiedene auf BP-1 basierende Peptide entworfen, synthetisiert und aufgereinigt. Wie erwartet zeigen nur die modifizierten Varianten Silicapartikel-bildende Aktivität, wodurch Partikel unterschiedlicher Morphologie erhalten wurden. Ein stabilisierender Effekt auf das Membranprotein Diacylglycerolkinase durch die Peptide selbst konnte nicht gezeigt werden. Dennoch war es möglich, mit dem BP-1-R5 Peptid DGK in kugelförmige Silicapartikel zu verpacken. Dabei war das BP-1-R5-Peptid effektiver als das R5-Peptid. Die verkapselte DGK zeigte eine beeinträchtigte Kinaseaktivität gegenüber dem Substrat Diolelylglycerin, was durch limitierte Diffusion in die Partikel erklärbar ist. Die verkapselte Kinase war jedoch stabiler gegenüber Pronase E, künstlichem Magensaft (SGF) und gegenüber künstlichem Darmmedium (SIF). Somit konnte das BP-1-R5-Peptid als neues Werkzeug zur Verkapselung von Membranproteinen in Silicapartikeln genutzt werden. Solche funktionalisierten Partikel könnten in Sensoren oder Bioreaktoren genutzt werden.

Table of Contents

Acknowledgements	2
Abstract	3
Zusammenfassung.....	5
Table of Contents	7
Part 1	11
Introduction.....	11
1.1 Silica nanoparticles.....	11
1.1.1 Conventional synthesis of mesoporous silica nanoparticles.....	13
1.1.2 Biomimetic synthesis of silica nanoparticles.....	16
1.1.3 Biomedical Aspects.....	22
1.2 Encapsulation of enzymes.....	27
1.2.1 Encapsulation in soft organic materials	28
1.2.2 Inorganic materials.....	44
1.2.3 Composite structures	51
1.3 Membrane protein stabilization.....	53
1.3.1 Lipid bilayer nanodiscs	53
1.3.2 Polymer-based nanodiscs.....	55
1.3.3 Beta-strand peptides.....	56
1.3.4 The membrane protein Diacylglycerol kinase	58
Part 2	60
Aims of this work.....	60
2.1 Polyphenol-conjugated R5 silica nanoparticles for targeted delivery	60
2.2 Silica-stabilized nanodiscs	61
2.3 Modified amphiphilic BP-1 peptides for the direct encapsulation of membrane proteins in silica	62
Part 3	63
Materials and Methods	63
3.1 Materials.....	63
3.1.1 Water.....	63
3.1.2 Chemicals.....	63
3.1.3 Cloning.....	63
3.1.4 Protein expression.....	63

3.1.5 Live cell imaging	63
3.1.6 Electron microscopy	63
3.2 Instrumentation	64
3.2.1 Peptide Synthesis	64
3.2.2 Protein Expression and purification	64
3.2.3 Centrifugation.....	64
3.2.4 Electrophoresis.....	64
3.2.5 Spectroscopy	64
3.2.6 Confocal fluorescence microscopy.....	65
3.2.7 Electron microscopy	65
3.2.8 Atomic force microscopy.....	65
3.2.9 Preparative and analytical High-performance liquid chromatography.....	65
3.3 Buffers and expression media	66
3.3.1 Protein expression.....	66
3.3.2 Gel electrophoresis and western blot	66
3.3.3 Protein Purification.....	67
3.3.4 Microscopy	68
3.3.5 Circular dichroism.....	68
3.4 Methods	69
3.4.1 Manual SPPS.....	69
3.4.2 Kaiser Test	69
3.4.3 Automated SPPS.....	69
3.4.4 Coupling of R5 peptide and modified polyphenols	70
3.4.5 Cleavage of peptides from resin.....	70
3.4.6 Preparative reversed-phase HPLC for peptide purification	70
3.4.7 Absorbance and emission spectra.....	71
3.4.8 Synthesis of silica nanoparticles.....	71
3.4.9 Release of quercetin.....	71
3.4.10 Live cell fluorescence imaging.....	72
3.4.11 Transformation of bacteria	72
3.4.12 Plasmid preparation	72
3.4.13 DNA digests	73
3.4.14 Agarose gel electrophoresis	73
3.4.15 DNA ligation.....	73
3.4.16 Expression and purification of MSP constructs.....	73

3.4.17 SDS-PAGE.....	74
3.4.18 Formation of nanodiscs	74
3.4.19 TEM sample preparation	75
3.4.20 Atomic force microscopy.....	75
3.4.21 CD measurements	75
3.4.22 Expression and purification of DGK.....	75
3.4.23 Kinase activity assay	76
3.4.24 Stability assays.....	77
3.5 Plasmids and expression strains.....	78
3.5.1 Plasmids.....	78
3.5.2 Bacterial strains	78
Part 4	79
Results and Discussion	79
4.1 Polyphenol-conjugated R5 silica nanoparticles for targeted delivery	79
4.1.1 Synthesis of modified polyphenols	79
4.1.2 Coupling of modified polyphenols with the R5 peptide.....	83
4.1.3 Absorbance and fluorescence spectra of quercetin-R5 conjugate	86
4.1.4 Silica particle formation with polyphenol-R5 conjugates	87
4.1.5 pH-dependent release of quercetin-R5 conjugate from particles	88
4.1.6 Cell uptake of silica particles into HT-29 cells	89
4.2 Silica-stabilized nanodiscs	93
4.2.1 Cloning of modified MSP constructs	93
4.2.2 Expression and purification of MSP constructs.....	96
4.2.3 Circular dichroism.....	101
4.2.4 Nanodisc formation.....	101
4.2.5 Silica precipitation	103
4.2.6 Nanodisc loading	105
4.3 Modified amphiphilic BP-1 peptides for the direct encapsulation of membrane proteins in silica	106
4.3.1 Synthesis and characterization of modified BP-1-peptides	106
4.3.2 Silica-precipitation activity of modified BP-1-peptides	111
4.3.3 Expression and purification of diacylglycerol kinase.....	112
4.3.4 DGK Encapsulation in silica.....	114
4.3.5 Stabilization of DGK using BP-1 peptides	116
4.3.6 Stabilization of silica encapsulated DGK.....	116

Part 5	118
Conclusions and Outlook.....	118
5.1 Polyphenol-conjugated R5 silica nanoparticles for targeted delivery	118
5.2 Silica-stabilized nanodiscs	119
5.3 Modified amphiphilic BP-1 peptides for the direct encapsulation of membrane proteins in silica	120
Appendix.....	121
NMR-Spectra	121
2-(3,4-diacetoxyphenyl)-4-oxo-4H-chromene-3,5,7-triyl triacetate	121
4-(3,5-diacetoxy-7-hydroxy-4-oxo-4H-chromen-2-yl)-1,2-phenylene diacetate	122
4-(3,5-diacetoxy-7-(2-ethoxy-2-oxoethoxy)-4-oxo-4H-chromen-2-yl)-1,2-phenylene diacetate	123
2-((2-(3,4-dihydroxyphenyl)-3,5-dihydroxy-4-oxo-4H-chromen-7-yl)oxy)acetic acid.....	124
3-((3,5-dihydroxy-4-oxo-2-phenyl-4H-chromen-7-yl)oxy)propanoic acid.....	125
EDX Spectra	126
Comet assay	127
List of Abbreviations.....	128
References.....	135

Part 1

Introduction

1.1 Silica nanoparticles

Nanomaterials have structures on the scale of nanometres. The exact definition varies; a recent paper identified 36 different definitions of the terms *nanomaterial* and *nanoparticle*. Some sources limit the greatest dimension of the nanostructures to 100 nm, others to 300 nm, or as much as 1000 nm; sometimes no definite limit is given. Nanoparticles are within these limits in all three size dimensions¹. For the sake of simplicity, I shall use the term nanoparticle to describe an object with all three dimensions between 1 nm and 1000 nm.

The bottom line, however, is that nanomaterials and nanoparticles have properties that are very different from those of the bulk material due to, among others, increased surface to volume ratio, anisotropy effects² or the interaction with light³. Therefore, they are relevant for diverse fields such as surface coatings⁴, catalysis⁵, and medicine⁶. The manufacture of nanoparticles and nanostructures has received increasing interest in recent years (see fig. 1.1.1).

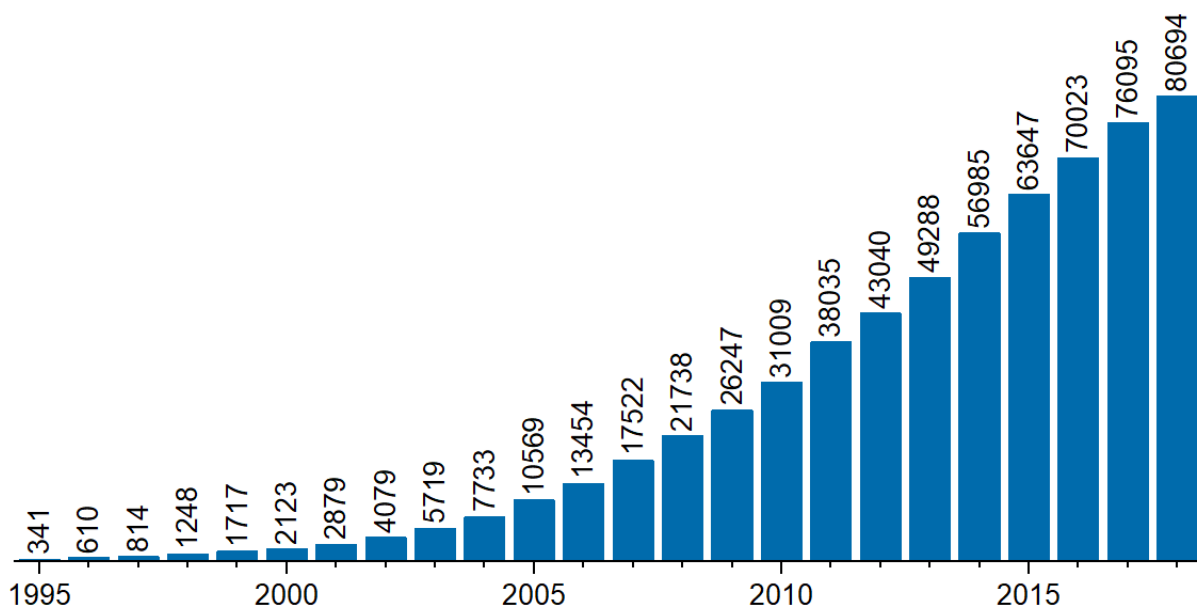


Fig. 1.1.1 | Number of publications connected to nanoparticles listed on web of science from the year 1995 to 2018 (source: web of science, wcs.webofknowledge.com, 08/14/2019).

It is based on two different general principles: the top-down and the bottom-up approach.

In the top-down approach, macroscopic structures are broken down to reduce their dimensions to the nanoscale. This attrition is achieved mechanically by using a ball-mill, for example. The disadvantage of this method is that the resulting particles have a broad size distribution and non-uniform shapes⁷.

In contrast, the bottom-up approach starts with a precursor substance from which the particles are assembled. This can be as simple as a solution of the desired material. In spray pyrolysis, this solution is sprayed before heating. The solvent is evaporated from the droplets and the remaining precipitate sintered to form the particles⁸. In the first part of the sol-gel process, a colloidal solution (a suspension of nanoparticles) is obtained through a condensation reaction of oxides, hydroxides or carbonates in solution⁹. In chemical vapour deposition (CVD), the precursor is instead a gas, which is decomposed on a surface to generate coatings on the nanoscale or nanostructures such as carbon nanotubes¹⁰. Variations of these processes make use of additives such as detergents or other self-assembling templates to achieve the desired porosity and morphology^{11,12}.

Using these and other methods, nanoparticles have been prepared from a variety of materials. Carbon nanostructures are very versatile in that they include graphene¹³, fullerenes (although only 0.7 nm in diameter)¹⁴, nano-onions¹⁵, carbon nanotubes (CNTs)¹⁶, and various carbon fibers¹⁷, as well as larger structures derived from them¹⁸. Porous nanoparticles with very large surfaces can also be created from silica¹⁹. Solid nanoparticles can be made from gold²⁰, aluminium⁷, silicon²¹, and other metals and their oxides²². There are also combinations of different materials, for example in the form of core-shell particles in which the core is coated with a very thin layer of shell material²³. Among nanoparticles, those made from silica are of continuous interest for medical purposes because of their excellent biocompatibility and adjustable porosity²⁴.

The reason for this interest is in the silica particles properties: they are considered non-toxic and their circulation time can be adjusted by changing the size and morphology²⁵. Two other important parameters are the porosity and the pore volume of the particles. This determines the kind and the amount of active compound, which can be adsorbed into the particles, resulting in a filling of the pores with the compound. The confinement within the pores limits the size of the compound molecule and usually prevents the formation of crystals inside, forcing it to be in its amorphous form. This is advantageous for poorly soluble compounds, the availability of which can be increased through this strategy²⁶. Particles with pore sizes of 2 – 50 nm, mesoporous silica nanoparticles (MSNs), have been particularly useful in this respect. Their synthesis is based on polymeric detergents, which are then removed by calcination in a separate step²⁴.

1.1.1 Conventional synthesis of mesoporous silica nanoparticles

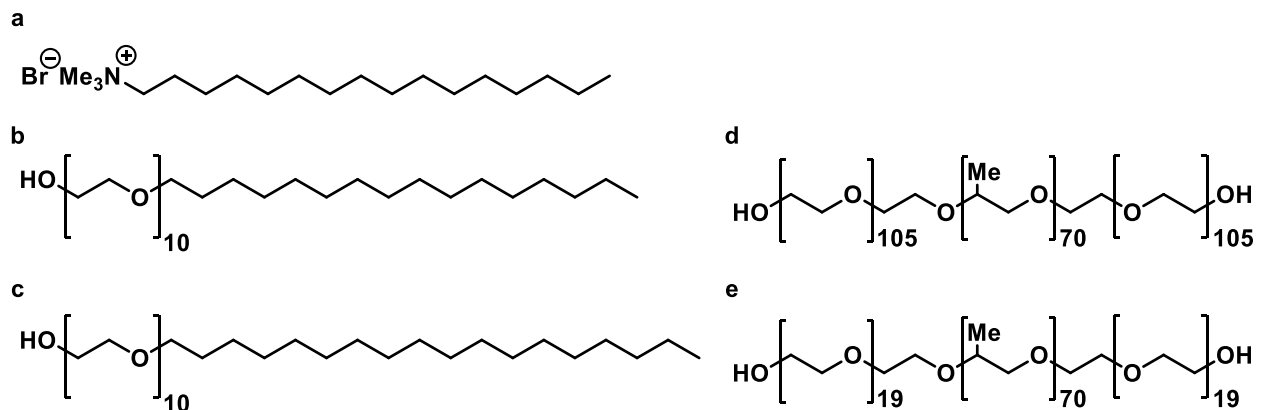


Fig 1.1.2 | Surfactant structures. a, ionic detergent cetrimonium bromide (CTAB). The polyglycol ethers Brij 56 (b), Brij 76 (c), pluronic F127 (d), and pluronic P123 (e).

Mesoporous silica nanoparticles (MSNs) feature pores of 2 – 50 nm (according to IUPAC definition)²⁴ and large surface areas between 700 – 1500 m²/g²⁷. Their synthesis is based on the Stöber method, which involves the hydrolysis of tetraalkyl orthosilicates, usually tetramethoxysilane (TMOS) or tetraethoxysilane (TEOS), in aqueous ammonia²⁸. In addition, different micelle-forming surfactants are required, which can be ionic, or non-ionic (see fig. 1.1.2)²⁴. Above the critical micelle concentration (CMC), ionic surfactants like cetrimonium bromide (CTAB) form spherical micelles with the hydrophobic tails pointing to the centre. Thus, the surface is positively charged due to the trimethyl ammonium headgroups. At higher concentrations, the spherical micelles become cylindrical and assemble into hexagonal stacks²⁹. These are referred to as a liquid crystalline mesophase²⁷. A silica precursor (sodium silicate or TEOS) is then added, along with a base. Under these harsh conditions, it is hydrolysed to silicic acid. The negatively charged silicic acid assembles on the positively charged micelle surfaces due to ion pairing. Polymerisation of the silicic acid yields the desired porous structure²⁹. The size of the micelles can be increased by using surfactants with a longer chain length, larger counter ions (e. g. tosylate instead of chloride)²⁴, or by addition of hydrophobic swelling agents such as mesitylene^{29,30}, which makes it possible to create pores from 2 – 30 nm in diameter²⁷. The size of the resulting particles ranges from below 10 nm to 1 μm²⁹. It can be decreased by using growth inhibitors, e. g. lysine²⁴ or formaldehyde³¹. To increase the particle size the temperature can be elevated³², or a tetraalkyl orthosilicate with longer alkyl residues, e.g. tetrabutoxysilane (TBOS) instead of TMOS, can be used³³. When using organo-substituted trialkoxysilanes as co-condensing reagents, alternative particle morphologies, like rods instead of spheres, can be achieved²⁷. Post-synthesis, the organic matter is removed to leave the pores hollow. There are several methods for this template removal. Either an ethanolic solution of ammonium nitrate is used at 60 °C³⁴, the surfactant is oxidised with H₂O₂³⁵, or the particles are calcinated at high temperature (275 °C) in organic solvent³⁶, or even higher temperature (500 °C) after lyophilisation³⁷.

The first such mesoporous material was developed in 1992 at Mobil, now ExxonMobil Corp. (Irving, Texas, USA), and is based on the ionic surfactant cetyltrimethylammonium bromide (CTAB). These Mobil Crystalline Materials (MCMs) have pore sizes between 2.5 – 6 nm and can be obtained with different structural arrangements depending on the conditions used. The pores in MCM-41 are arranged with hexagonal symmetry, whereas those in MCM-48 are cubic, and in MCM-50 lamella-like. Another class of mesoporous material comes from the University of California in Santa Barbara (SBA). For these MSNs, non-ionic ethoxylates are used as surfactants. These materials have larger pores (4.6 – 30 nm) and again can be obtained with different symmetries. SBA-11 is cubic, SBA-12 3D hexagonal, SBA-15 hexagonal, and SBA-16 cubic cage-structured²⁴. The most common mesoporous materials which the MSNs are based on are compared in table 1.1.1. An alternative synthesis strategy creates silica particles using the same compounds, peptides and polyamines, as marine organisms in their biomineralization process³⁸.

Table 1.1.1 | Comparison of different mesoporous materials.

MSN	reagents	silica source	pore symmetry	pore size (nm)	pore volume (cm ³ /g)	reference
MCM-41	CTAB, NH ₄ OH	TEOS	2D hexagonal P6mm	1.5 - 8	>1.0	Kumar et al., 2001
MCM-48	CTAB, NaOH	TEOS	3D cubic Ia3d	2.0 - 5.0	>1.0	Kumar et al., 2001
MCM-50	CTAB, NaOH	TEOS	lamellar p2	5.6	1.71	Wang et al., 2006 (Microp. and Mes. Materials)
SBA-11	Brij56, HCl	TEOS	3D cubic Pm3m	2.1 - 3.6	0.68	Kim et al., 2015 (J. Porous Mater.)
SBA-12	Brij76, HCl	sodium silicate	3D hexagonal P63/mmc	3.1	0.83	Ge et al., 2018 (Colloids and Sur.)
SBA-15	Pluronic P123, HCl	TEOS	2D hexagonal P6mm	6.0 - 10.0	1.17	Ge et al., 2018 (Colloids and Sur.)
SBA-16	Pluronic F-127, N-butanol, HCl	TEOS	cubic Im3m	5.0 - 15.0	0.91	Ferreira Soares et al., 2020
KIT-5	Pluronic F127, HCl	TEOS	cubic Fm3m	9.3	0.45	Kleitz et al., 2003
KIT-6	Pluronic P123, N-butanol, HCl	TEOS	cubic Ia3d	3.15	0.887	Chermahini et al., 2019
COK-12	Pluronic P123, citric acid	sodium silicate	hexagonal P6m	5.7 - 8.1	1.23	Henning et al., 2019

1.1.2 Biomimetic synthesis of silica nanoparticles

The biomimetic synthesis of silica nanoparticles is inspired by biomineralization processes in marine organisms. Biomineralization is the process by which living organisms create solid structures through the formation of one of more than 60 different minerals, including calcite (CaCO_3), hydroxyapatite ($\text{Ca}_{10}(\text{PO}_4)_6(\text{OH})_2$), and silica ($\text{SiO}_2 \cdot n\text{H}_2\text{O}$). In most species, their precipitation is confined to specialized organelles or vesicles, found in tissues like vertebrate bones, and in organisms like heterococcoliths or magnetotactic bacteria³⁹. The resulting biomaterials are composites of these inorganic salts and organic polymers such as polyamines and peptides. An outstanding example of a biomineral is diatomaceous silica³⁸.

Diatom silica

Diatoms (*Bacillariophyta*) are unicellular marine and freshwater algae. By an elaborate mechanism, they are able to take up silicic acid, $\text{Si}(\text{OH})_4$, from the ocean or from fresh water, in which it is present at a concentration of 10 – 70 μM , and convert it to silica ($\text{SiO}_2 \cdot n\text{H}_2\text{O}$)⁴⁰. This process is confined within their silica deposition vesicles (SDVs)³⁹. There the silica is precipitated in the form of tiny hydrated silica spheres, which are arranged in delicate patterns with a multitude of pores to form the diatom shell, the frustule. This allows the diatoms to exchange nutrients with their surroundings while protecting them mechanically^{38,41}. Besides silicon, a high concentration of titanium is found inside the diatom frustules along with long chain polyamines⁴², as well as four different peptides and proteins. The frustulins are cell wall-associated glycoproteins, pleuralins are found in the pleural bands, cingulins are found in microrings inside the frustule, and Silacidins and Silaffins are distributed throughout the frustule and are involved in the silica deposition process^{40,43}. Both contain many serine residues, but the silacidins are aspartate and glutamate-rich peptides, whereas the Silaffins are rich in lysines. They also share the RXL motif at the end of the repetition sequence, where X can be I, N, or R and were shown to have silica-precipitating activity under certain conditions^{40,44}. The long-chain polyamines are composed of up to 20 units of methylated or non-methylated ethyleneimine⁴².

The protein sil1 (see fig. 1.1.3a) from the diatom *Cylindrotheca fusiformis* is the precursor of the Silaffins in this species. The 265 amino acid protein (sequence shown in figure 1.1.3 A) starts with a translocation sequence for the endoplasmic reticulum at the N-terminus. The C-terminus is formed by seven repeat units which are between 19 and 33 amino acids long⁴⁰. The diatoms further process this precursor protein by post-translational modification and proteolysis to yield the Silaffins. The repeat unit R1 gives rise to the silaffin-1B, the repeat unit R2 to silaffin-1A₂ and the remaining units R3-R7 to silaffin-1A₁⁴⁵. The two isoforms of the Silaffin-1A peptide are shown in figure 1.1.3b. They contain 18 and 15 amino acids, respectively, which are obtained from the repetition sequences by removal of the RRIL motif. The peptides are further post-translationally modified with phosphate, methyl, and polyamine groups and precipitate silica nanospheres from a solution of orthosilicic acid⁴⁵.

The repeat units of the sil1 protein as well as the long-chain polyamines have received considerable interest for the creation of silica structures *in vitro*.

a **MKLTAIFPLL FTAVGYCAAQ** SIADLAAANL STEDSKSAQL ISADSSDDAS DSSVESVDAA SSDVSGSSVE
 SVDVSGSSLE SVDVSGSSLE SVDDSSSEDSE EEELRIL

R1 SSKKSGSYYS YGTTKSGSYS GYSTKKSASR RIL

R2 SSKKSGSYSG YSTKKSRR IL

R3 SSKKSGSYSG SKGSKRRIL

R4 SSKKSGSYSG SKGSKRRNL

R5 SSKKSGSYSG SKGSKRRIL

R6 SSKKSGSYSG SKGSKRRNL

R7 SSKKSGSYSG SKGSKRRILS GGLRGSM

b **R2** H-SSKKSGSYSGYSTKKS**RRIL**-OH

Silaffin-1A₂ H-SSKKSGSYSGYSTKKS**GS**-OH

R3 H-SSKKSGSYSGSKGSK**RRIL**-OH

Silaffin-1A₁ H-**SSKKSGSYSGSKGSK**-OH

Figure 1.1.3 | Silaffin amino acid sequences. **a**, The amino acid sequence of the sil1 protein. The translocation sequence is shown in yellow and the repetition sequences R1 – R7 are marked. Also note the KXXK and the RXL motifs. **b**, Amino acid sequences of the silaffins 1A1 and 1A2 from *C. fusiformis* compared to the repetition sequences R3 and R2. Amino acids marked in red are proteolytically removed from the repetition sequence. Other coloured amino acids are post-translationally modified in the silaffins. Blue – phosphorylation, brown – bound to polyamine, green – methylation, purple – phosphorylation and methylation.⁴⁶

The R5 peptide

It was shown that the R5 peptide (repeat unit 5 from sil1) also precipitates silica, even if it does not carry post-translational modifications⁴⁷. The RRIL motif, which is post-translationally cleaved from the Silaffins *in vivo*, is essential for the silica-precipitating activity of the unmodified R5 peptide *in vitro*. It is thought to be responsible for the self-assembly of the peptide which acts as a template to provide the structure of the resulting particles⁴⁸.

Studies on the structure of the R5 peptide within these silica particles, however, show different outcomes. A solid-state nuclear magnetic resonance (SSNMR) study from 2013 shows a pattern of shifts, which is in agreement with the N-terminus of the R5 peptide exposed to the surrounding silica, suggesting a micellar assembly of the peptide with the C-terminus buried in the centre⁴¹. However, a later study which used CD-spectroscopy, computer simulation, dynamic light scattering (DLS), as well as nuclear magnetic resonance (NMR) data found no evidence for the assembly of the R5 peptide into aggregates or micelles in solution and concludes that it is most likely present as a monomeric random coil⁴⁹. This is in agreement with another SSNMR study, in which the R5 peptide was coprecipitated in silica with a truncated version of matrix metalloprotease 12 (MMP12) from 2016, which found no defined peaks for the R5 sequence, suggesting a random distribution of the peptide with no preferred conformation⁵⁰. In contrast, a study using sum-frequency generation (SFG) spectroscopy from 2017 showed that the R5 peptide is in a defined conformation before and after precipitation. However, in this case, the R5 was assembled at the air-water interface and therefore the situation was a different one to the precipitation in bulk⁵¹. In conclusion, it is likely that the R5 peptide only forms assemblies in a limited population, for example that interacting with surfaces, whereas the majority of the peptide in solution is in random coil conformation, as illustrated by the data obtained from NMR and CD spectroscopy.

Nevertheless, the C-terminal RRIL-motif is assumed to be essential for the pre-assembly of the peptide. Indeed, peptides based on the RRIL-motif also act as a template for silica particles with different morphologies. Whether the resulting particles show a spherical, sheet-like, or rod-like morphology depends on the stereochemistry and linkage of the RRIL-motifs within the peptide^{47,52}.

The R5 peptide was also used to immobilize functional enzymes on a silica matrix. There are two possibilities for co-precipitating a protein of interest (POI) with the R5 peptide. First, by physically mixing the two as was done by Luckarift *et al.*⁵³. Second, by means of a fusion construct of the POI with the R5 peptide as was demonstrated by Nam *et al.*⁵⁴. The latter method allowed for a reduction of R5 peptide use from 9,000 molar equivalents to one molar equivalent compared to the POI⁵⁴. By immobilization, the stability of the proteins increases, which was shown for butyrylcholinesterase (BuChE). The free enzyme shows a 90% loss of activity after one week at room temperature, whereas once immobilized on silica it retains full activity even after three weeks⁵³. When heated to 65 °C for 1 h, the free enzyme loses 85% of its activity, whereas the immobilized enzyme retains full activity⁵³.

It was also possible to selectively release a cargo molecule from the silica particles. When the cargo is fused to the Cys-R5 peptide via a disulfide bridge, it can be released from the particles

using a reducing agent. With this strategy, up to 32% of an immobilised cargo peptide could be released with TCEP in 6 h⁵⁵.

Moreover, the R5 peptide can also be used to precipitate other minerals than silica. Titanium(II)-oxide spheres were obtained when incubating the R5 peptide with titanium(IV) bis-(ammonium lactato) dihydroxide and with or without poly(allylamine). Microspheres with an average diameter of $3.2 \pm 1.5 \mu\text{m}$ resulted^{56,57}.

Thus, the R5 peptide is a versatile example of a silica-precipitating peptide. The scope of these peptides can be further enhanced by making variants of R5. An example for the effect of such modification can be seen from the presence or absence of post-translational modifications (PTMs). The native Silaffins (see figure 1.1.3b) show silica-precipitating activity in a broad pH range (pH 5 to pH 8), whereas the R5 peptide, in the absence of PTMs, only precipitates silica above pH 6^{43,45}. In addition to R5 and its variants, other peptides derived from nature are used for silica-precipitation *in vitro*.

Other silica-precipitating peptides

Other silica-precipitating peptides from marine organisms include Volp1 (SGRRRGSRRRGSRRR) and Salp1 (CGRRRGGRGGRGGCRRR), from algae and siliceous choanoflagellate, which can be used to create silica nanospheres of $580 \pm 82 \text{ nm}$ diameter. Both peptides adopt random coil structures in solution and require phosphate ions for the precipitation, similar to R5⁵⁸. Another example, which was used for silica particle preparation, is *Salmo salar* protamine - a 32 amino acid peptide with 20 - 22 arginines (PRRRSSSRPVRRRRRPRVSRRRRRRGRRRR). This was used in a Tris buffer, in the absence of phosphate to obtain particles of only 25 nm in diameter⁵⁹.

Several more silica-precipitating peptides have been made to fabricate other particle morphologies. In one case, the goal was to perform silica precipitation on a membrane of dipalmitoyl-phosphatidylglycerol (DPPG). The R5 sequence was changed by introduction of two tyrosine residues, replacing the first four N-terminal amino acids and by an additional second KRRIL-motif at the C-terminus (compare figure 1.1.4a). The idea was to increase the hydrophobicity of the peptide to allow it to interact with a lipid membrane. This was the case, and with this peptide, it was possible to deposit a 4 nm layer of amorphous silica onto a monolayer of DPPG in 30 min⁶⁰.

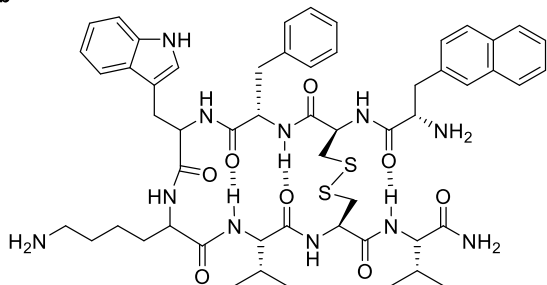
Double-walled silica nanotubes could be made from a cyclic peptide⁶¹. The octapeptide, Lanreotide (compare figure 1.1.4b), readily assembles into hollow nanotubes in water. It also has two free amine groups which might catalyse silica formation. Upon the addition of TEOS, hollow silica nanotubes of one to three nanometer length were found after a few days. They have a diameter of 25 nm and are coated in a 1.4 nm thick layer of silica⁶¹.

Silica nanorods of similar dimensions could be fabricated using the rriLK*RRIL peptide, which is a dimerized version of the C-terminal motif of the R5 peptide (figure 1.1.4c). While the morphology is spherical in the all-L-peptide, the epimer with D-amino acids in the first five positions changes the self-assembly, so that sticks are obtained. Sheets can be made when the fourth amino acid is mutated to an isoleucine and the two N-terminal amino acids are leucines (fig. 1.1.4d)⁵².

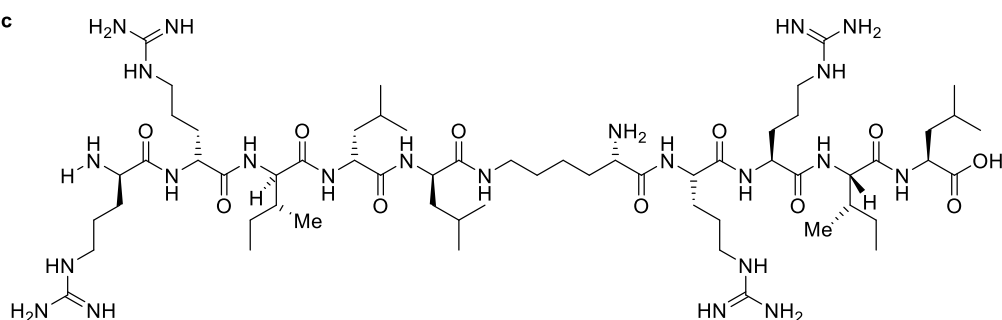
a

H-YYSGSYSGSKGSKRRILKRRIL-OH

b



c



d

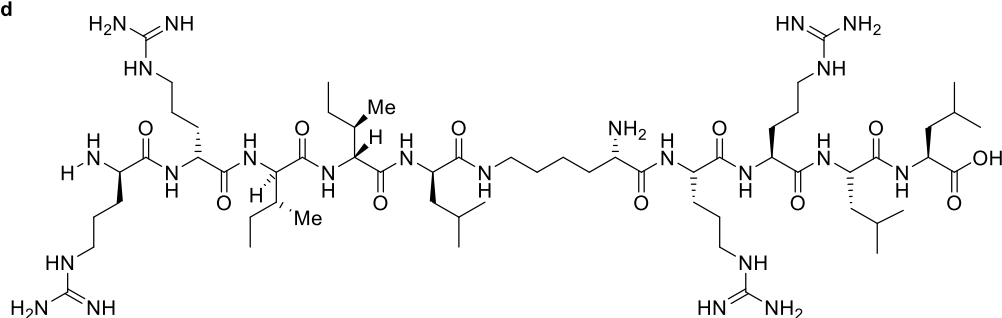


Figure 1.1.4 | Silica precipitating peptides. **a**, Sequence of the modified variant of R5 for lipid membrane adsorption. **b**, Lanreotide. **c**, the rod-forming rriLK*RRIL peptide (K* denotes an isopeptide bond on lysine). **d**, the sheet-forming rriLK*RRLL peptide.

Amine-based initiators

In addition to peptides, various amines, shown in figure 1.1.5, are used to precipitate silica particles. The simplest is cysteamine, which is a mimic of the active site of the silica-precipitating enzyme silicatein. In one study, it was used to induce the formation of amorphous silica particles, which were 40 – 100 nm in diameter⁶². Ethyleneimines of different molecular weights were also used. In one study, diethylenetriamine (DETA), triethylenetetramine (TETA), tetraethylenepentaamine (TEPA), and pentaethylenhexamine (PEHA) were compared. All produced silica particles within five minutes in pH neutral phosphate buffer, but their morphologies were not characterized in detail⁶³. Another small

molecule amine for silica precipitation is spermine, which could be used to precipitate spherical silica particles with 300 – 400 nm diameter⁶⁴.

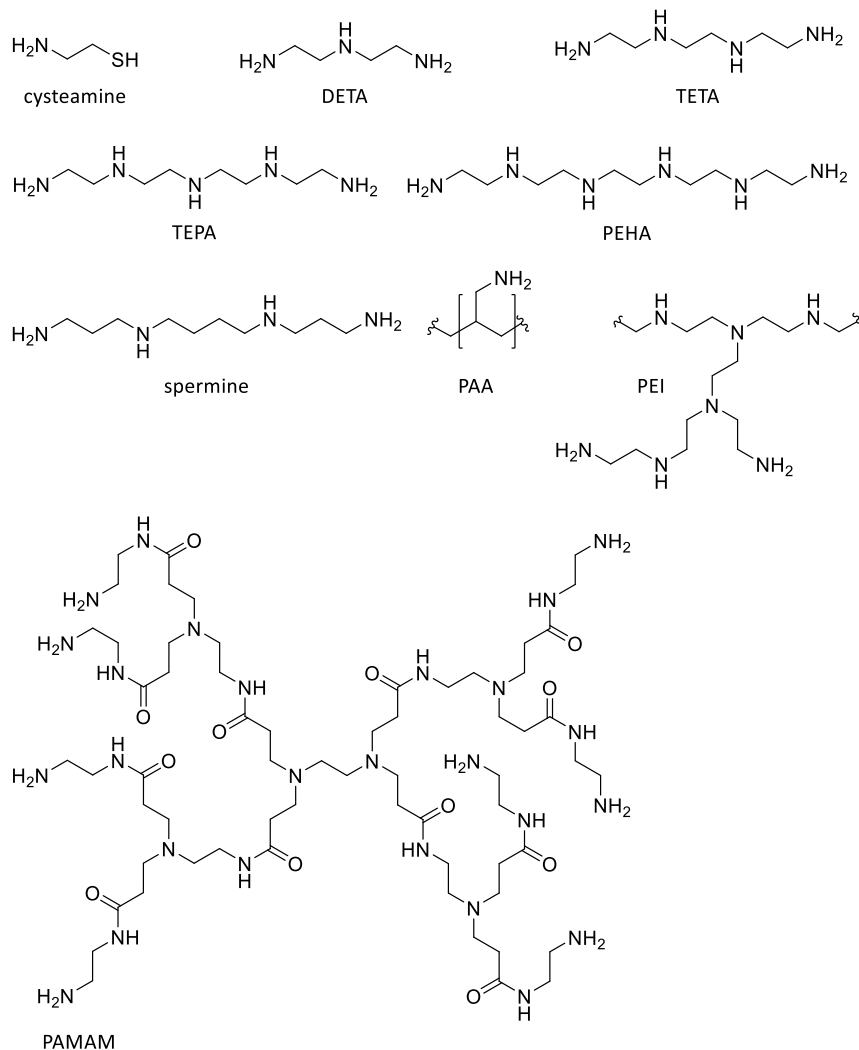


Figure 1.1.5 | Amine-based initiators used for biomimetic silica precipitation.

High molecular weight polyamines which are used for silica precipitation are polyallylamine (PAA) and polyethyleneimine (PEI). Polyallylamine was shown to aggregate in phosphate buffer and form spherical silica particles upon the addition of silicic acid already after 12 min. The size distribution is broad, with a maximum diameter of 3 μm ⁶⁵. Polyethyleneimines (PEI) were used in the same way. The size of the resulting particles was linearly correlated with the PEI molecular weight⁶⁶. Dendrimers are a more well-defined kind of polymer which is grown in a step-by-step reaction. A generation four polyamido(amine) (PAMAM) dendrimer was used to precipitate spherical silica particles with a bimodal size distribution with 244 ± 106 nm and 745 ± 102 nm averages⁶⁷.

1.1.3 Biomedical Aspects

Cells operate at the nanoscale. Their outer barrier, the cell membrane, is between 3.5 and 4.6 nm thick⁶⁸. The ribosome (eukaryotic) has a diameter of up to 30 nm⁶⁹. Cell organelles such as lysosomes are between 300 and 1000 nm in diameter⁷⁰. Super molecular complexes are at the small end of the scale. Therefore, nanomaterials are expected to interact with such structures and allow for new therapeutic approaches. They also offer the possibility to protect sensitive cargo such as proteins or nucleic acids and deliver it into tissues and cells⁷¹.

Degradability

Silica particles were shown to degrade in biological media by a simple hydrolysis mechanism²⁵. The degradability depends on the size of the particles and on their porosity. Mesoporous silica nanoparticles (MSNs) degrade faster than non-porous, dense silica particles and the degradability increases with pore size⁷². This means that their stability can be tuned from 24 h⁷³ to several weeks in biological fluids²⁵. Recently, the degradation of MSNs in phosphate buffer has been employed to increase surface roughness and loading capacity⁷⁴.

Fine-tuning the particle degradability is not only important to release the particle's cargo, but also to improve particle clearance from the body and thus lower their toxicity⁷².

Toxicity

We are consuming approximately 20 – 200 mg of silica on a daily basis as part of fresh water, vegetables, grains, and seafood⁷⁵. Silica nanoparticles, however, come in different morphologies than those present in nature and therefore need to be considered separately. The toxicity of amorphous silica nanoparticles presented through different routes of exposure was tested both by *in vitro* and *in vivo* studies.

The inhalation of amorphous silica nanoparticles triggers an inflammatory response and induces apoptosis. *In vitro*, A549 cells, derived from human bronchoalveolar carcinoma, show an increase in reactive oxygen species (ROS) and lowered glutathione when exposed to amorphous silica nanoparticles, which indicates oxidative damage⁷⁶. Accordingly, lungs of rats inhaling silica particles displayed inflammatory and apoptotic effects, but normalized 8 months after exposure⁷⁷. Thus, there seems to be a severe but reversible response to inhalation exposure to silica NPs.

Intravenous exposure has not been linked to such dramatic effects. MSNs injected in mice showed decreasing blood circulation time with increasing particle size. They were almost completely cleared within a month, although particles initially accumulated in liver, spleen and lungs⁷⁸. A study using fluorescently labelled silica particles showed the route of clearance in mice. After intravenous injection, fluorescence was first observed in the liver, then in the gall bladder, and then in the intestinal tract which suggests excretion via the bile⁷⁹.

Many studies have been carried out on oral toxicity to assess the risk of silica nanoparticles as food ingredients⁸⁰. It was found that in simulated digestion of amorphous silica, smaller primary particles can be released from aggregates in a simulated small intestine environment⁸¹. Further studies indicate that the percentage of these particles, which are taken up from the gut, is very low, 0.01 – 0.06 %, depending on the dose^{80,82}. There were no

acute toxic effects, but an increased incidence of liver fibrosis⁸². In a mouse study using nanostructured silica, no pathological changes were observed even at 10 g/kg of oral administration⁸³. However, an *in vitro* study on HT29 human colon cancer cells showed cell toxicity and uptake for 12 nm silica nanoparticles, depending on the concentration of serum⁸⁴. Thus, oral consumption of silica nanoparticles is generally considered safe, even though there can be a toxic effect on colon cells.

Topological uptake is also significant. Skin cancer cells can internalize silica nanoparticles *in vitro* and a concentration dependent apoptotic effect was observed⁸⁵. Another *in vitro* assay with HaCaT human keratinocytes showed that they can take up amorphous silica particles and their location within the cell as well as toxicity is size-dependent. Particles larger than 300 nm were taken up into endosomes, whereas smaller particles could penetrate the cytoplasm and nuclei of cells and also induce DNA damage. Accordingly, toxicity decreased with particle size⁷⁹. In a dermal exposure study, the same authors then topologically applied 70 nm amorphous silica nanoparticles to mice over 28 days. Transmission electron microscopy (TEM) analysis showed particles not only in the skin, but also in lymph nodes, liver, and cerebral cortex⁷⁹. Clearly, more studies are needed to determine the fraction of particles which are absorbed through the skin.

These results indicate that amorphous silica nanoparticles can be cleared from the body and have reversible effects on it. However, the acute toxicity seems to be strongly dependent on the exposure route and particle size. Thus, drugs based on silica NPs need to be evaluated case-by-case, especially if they feature additional coatings or functionalizations, which were not considered in the studies presented here.

Cell uptake

The cellular uptake of nanoparticles depends on their dimensions and usually decreases with increasing particle size. Ion channel pores inside the cell membrane vary in size between 0.3 Å and 12 Å; they are too small to accommodate nanoparticles. Therefore, cell penetration by nanoparticles can either occur passively through the lipid bilayer membrane or by an active endocytosis mechanism⁸⁶.

Endocytosis is divided into phagocytosis, by which large objects such as entire bacteria can be taken up, and pinocytosis, by which objects of up to 2 µm can be internalized⁸⁷. The pinocytosis can occur through several mechanisms, requiring different proteins. Clathrin-mediated endocytosis (CME) is the most common mechanism and responsible for about half of the pinocytosis events⁸⁸. Three-legged clathrin trimers and the adaptor protein 2 (AP-2) on the inner membrane leaflet assemble into a cage around the cargo, which buds off, forming a clathrin-coated vesicle^{86,89}. Clathrin-independent carrier (CLIC) mechanisms require either caveolin, RhoA, CDC42, ARF6, flotillin or actin to form the endosomes⁸⁷. In practice, all mechanisms, as well as passive transport, were observed for nanoparticles⁸⁶. Once the particle is taken up, the challenge remains to target it to a specific cell organelle⁷¹. There are, however, targeting sequences to achieve this effect, for example for the peroxisome⁹⁰.

If nanoparticles are taken up by endocytosis, they are still separated from the cytoplasm by the membrane of the endosome; the nanoparticles (or the drug bound to them) can only enter the cytoplasm via endosomal escape. Several mechanisms of endosomal escape have been identified: the proton sponge effect, membrane fusion and pore formation⁷¹.

The proton sponge effect is brought about by polycationic materials. Upon acidification of the late endosome, two effects take place. First, the incoming protons are buffered by the polymer, leading to an increased ion influx which results in osmotic swelling. Secondly, the polymer swells due to charge repulsion, causing endosome rupture and release of its contents⁹¹.

Membrane fusion can be found in nature in the form of viruses, the envelope of which fuses to the endosomal membrane. Liposomes can also fuse with the endosome and release their cargo into the cytosol⁷¹.

An example for pore formation from nature are bacterial exotoxins of the AB class. These include anthrax toxin-like and diphtheria toxin-like platforms, forming translocation pores in the shape of a β-barrel or α-helices, respectively⁹². In this case, the size of the cargo is limited by the dimensions of the pore.

Targeted Drug Delivery

Nanoparticles, especially MSNs, have been investigated for targeted drug delivery for about 20 years⁹³. The use of targeted drug delivery has two advantages. First, compounds that are far too toxic for systemic application can be used, because their effect is localized to the affected tissue. Secondly, side-effects in healthy tissue are reduced, for the same reason. Furthermore, due to their sensitivity, several types of cargo are especially suited to a

nanoparticulate delivery system. These include antisense and short interfering RNA (siRNA), DNA, vaccine antigens, and proteins or enzymes^{71,94}.

The drug delivery nanoparticles themselves need to be created from non-toxic precursors. This poses a difficulty since even polymers that are approved for implants might not be suitable for nanoparticles, which can be internalized by macrophages and converted to toxic monomers⁹⁵. Silica nanoparticles, which have tuneable biodegradability are thus particularly suited to this purpose²⁵. In addition to macrophage uptake, the adsorption of serum proteins onto the nanoparticle surface is a challenge to targeted drug delivery. This formation of a protein corona potentially obstructs the targeting moieties and interferes with drug release. The modification of the particles with charged silanes to produce a zwitterionic surface as well as their PEGylation have been shown to significantly reduce both macrophage uptake and serum protein absorption⁹⁶.

There are two general approaches to achieve targeting; passive targeting and active targeting⁹⁶. Passive targeting makes use of the enhanced permeation and retention (EPR) effect of tumours. This ten- to fiftyfold accumulation of large polymers and nanoparticles inside tumour tissue as compared to healthy tissue was first reported in 1986⁹⁷. The effect is caused by vascular irregularities, which come about due to the increased metabolism and need for angiogenesis inside solid tumours. There, blood vessels are often defective and leak plasma components. The vascular wall may lack a basement membrane and the smooth muscle layer. It also features pores as large as 400 nm. This means that large particles can extravasate into the surrounding tissue. In addition, lymphatic drainage is poor, impeding the clearance of such particles⁹⁸. Different factors are associated with this phenomenon and enhance it: vascular endothelial growth factor (VEGF), Bradykinin, Prostaglandins and matrix metalloproteases as well as nitric oxide and peroxynitrite. Consequently, these factors can also be applied for increasing this effect further without overly affecting the blood flow to healthy organs⁹⁸. However, the causes of the EPR effect such as vascular pore size, are different for primary tumours and metastases.⁹⁹ Therefore, passive targeting is of limited use to treat all of them.

Active targeting is based on biological recognition, meaning the interaction of membrane receptors with ligands on the nanoparticle. Several classes of binders can be used to decorate the nanoparticles. Antibodies are large but very specific binders which can be attached to the nanoparticles via PEG linkers⁹⁶. An example for such a therapeutic antibody is trastuzumab, which has antigen binding sites for the human epidermal growth factor receptor HER2, which is overexpressed on many human breast cancer cells¹⁰⁰. Another possibility is to use the protein substrate of the receptor directly. Cancer cells have an elevated metabolism which relies on import of epidermal growth factor (EGF) or transferrin (Tf), for example. Even short peptides can target receptors on the cell surface. The RGD motif is recognized by the $\alpha_v\beta_3$ integrins and the NGR motif by the CD13 receptor, for example⁹⁶. An alternative to these protein and peptide targeting ligands are aptamers which are synthetic DNA single-strands with a specific three-dimensional structure that can be made to target almost any molecule¹⁰¹. Even polysaccharides are used as targeting ligands, such as hyaluronic acid, which is

recognized by the CD44 and CD168 receptors. Useful small molecules are vitamins such as folic acid, which is recognized by the folate receptor overexpressed on many cancer cells⁹⁶.

Silica nanoparticles can be tuned in size and shape for passive targeting and decorated for active targeting. They are a promising vehicle to deliver toxic or sensitive cargo such as cancer drugs, peptides, or even proteins and enzymes²⁹.

1.2 Encapsulation of enzymes

Encapsulation is a means to enable enzyme recycling and prevent enzyme degradation in adverse conditions, by embedding it in a particulate nano- or microstructure. This confined reaction space modifies the size- and chemoselectivity of the catalysed reaction. The reaction rate can be enhanced due to surface effects⁵⁹ and the efficiency of a multi-component-reaction can be improved, by elevating the local concentration of intermediates¹⁰². As opposed to a purified enzyme in solution, the conditions for an encapsulated enzyme are often much closer to those present within cells, where the protein concentration is between 200 - 300 g/L. Thus, an encapsulated enzyme is often a better mimic of nature than one in solution¹⁰³. Enzyme encapsulation offers several practical advantages for applications in catalysis as well as medicine¹⁰⁴.

Enzymatic reactions are very specific so that protecting groups can be avoided in synthesis, thus increasing the atom economy¹⁰⁵. The consumption of harmful solvents can also be lowered since they proceed in aqueous buffers¹⁰⁶. Thus, the use of enzymes in catalysis can help to achieve the goals of green chemistry¹⁰⁷. For an efficient synthesis, however, the catalyst needs to be easily removed from the reaction mixture. Encapsulated enzymes can be immobilised on a surface¹⁰⁸, magnetically separated¹⁰⁹, or recovered by filtration¹¹⁰, for example. This avoids product contamination with trace metal ions, potential immunogenicity, and increases enzyme recovery for reuse^{104,105,111}.

In medicine, enzymes are used both for therapy and for diagnosis. In enzyme replacement therapy, enzymes not sufficiently produced in the body, such as lactase in patients with lactose intolerance, are provided from the outside¹¹². In enzyme prodrug therapy (EPT), enzymes are used to convert a prodrug to the active compound at the desired site¹¹³. Furthermore, they can degrade endogenous (in metabolic disorders such as hyperuricemia) as well as exogenous toxins¹¹⁴. The encapsulation of such therapeutic enzymes can increase their oral bioavailability¹¹⁵ and target the enzyme to specific areas using antibodies¹¹³. For diagnostic purposes, encapsulated enzymes can be used in the fabrication of miniaturised devices such as microfluidic flow-reactors or biosensor microarrays¹⁰⁴. In proteomics, encapsulated trypsin can reduce sample preparation time and improve reproducibility of the analyte digest¹¹⁶.

The enzyme encapsulation can be achieved using different matrix materials¹¹⁷ as well as different techniques including physical entrapment, adsorption through non-covalent interactions, and covalent bonding to the matrix^{104,118}. In the following overview, enzyme capsules are classified by matrix material. First, soft organic materials will be discussed. Biopolymer capsules such as protein capsids, DNA structures, and carbohydrate hydrogels as well as liposomes and other lipid-based particles belong in this category. Second, solid capsules from silica and other minerals will be discussed. Finally, composite materials such as core-shell particles containing hydrogels and mineral shells will be compared. Cross-linked enzyme aggregates (CLEAs) are purposely excluded from the following review, because they do not possess a defined particulate structure¹¹⁹. Also excluded are systems which

encapsulate organometallic, non-enzymatic catalysts or non-enzyme proteins and systems which do not form particles.

1.2.1 Encapsulation in soft organic materials

Protein-based encapsulation

Protein-based enzyme encapsulation makes use of naturally occurring shell-forming proteins. There are viral and non-viral capsids, which have been exploited for this purpose. The viral capsids, or virus-like particles (VLPs) are multimeric protein assemblies with a high number of copies, which form hollow shells with a high degree of symmetry¹²⁰.

Bacteriophage MS2 is a small RNA virus that infects *Enterobacteriaceae* such as *Escherichia coli*¹²¹. Its capsid is assembled from 180 protein molecules (triangulation number $T = 3$), 27 nm in diameter, and features 3 nm pores. The capsid can be disassembled by treating it with glacial acetic acid at a concentration of 66 % and then desalting it. For encapsulation, the target enzyme is equipped with a negatively charged tag. This can be DNA, which is ligated to it, or a genetically encoded tag consisting of glutamic and aspartic acid residues. In the presence of this modified target enzyme and trimethylamine-N-oxide, the capsules can be re-assembled^{122,123}. The enzyme alkaline phosphatase (PhoA) from *E. coli* was encapsulated using this strategy. The negatively charged peptide EEEEDDDEDDDEEDD was genetically fused to the C-terminus of PhoA. This construct (PhoA-neg) was able to induce the formation of the capsids and an average of 3.2 molecules PhoA-neg could be encapsulated per capsid¹²². An inhibitory effect on the k_{cat} was found for the encapsulated enzyme. Genetically modified variants of the capsid protein, in which the charge around the pores was increased lowered the reaction rate of the encapsulated protein¹⁰².

Another suitable viral capsid comes from the cowpea chlorotic mottle virus (CCMV). The icosahedral capsid ($T = 3$) has an outer diameter of 28 nm, an inner diameter of 18 nm and is self-assembled from 180 protein molecules. The assembly of the capsid is reversible and occurs when lowering the pH from 7.5, at which it is present in dimerised form, to pH 5. This phenomenon can be exploited to physically encapsulate single horseradish peroxidase (HRP) enzymes when lowering the pH of a mixture of the two proteins by dialysis. The downside to this approach is that at physiological pH, which is usually the optimum for enzyme activity, the complex is again disassembled¹²⁴. In order to increase the loading capacity and stability of the capsid at physiological conditions, the assembly was also performed with a covalently linked enzyme. The *Candida Antarctica* lipase B (CalB) was fused to the N-terminus of the capsid protein using Sortase A (SrtA). An elastin-like polypeptide (ELP) linker was put in between the two proteins. The linker consists of the VPGXG motif and facilitates the formation of $T = 1$ capsids even at pH 7.5. In this way, an incorporation of 8 % of CalB-ELP-CCMV, corresponding to two copies of the enzyme per capsid, could be achieved¹²⁵.

Bacteriophage P22, which infects *Salmonella typhimurium*, has an icosahedral capsid ($T = 7$) made from two different proteins. There are 100 – 330 scaffold proteins (SPs) of 33.6 kDa and 420 coat proteins (CPs) of 46.6 kDa; the capsid is 58 nm in diameter^{126,127}. Its structure changes at elevated temperatures. At 65 °C the capsid loses its scaffold proteins and forms a 64 nm diameter expanded form (EX). At 75 °C windows form in its shell; the resulting structure is

referred to as a wiffle ball (WB). These transformations are irreversible¹²³. Enzymes have been loaded into the capsids *in vivo* by creating fusion constructs with the scaffold protein. One example is the *Pyrococcus furiosus* alcohol dehydrogenase D (AdhD). It was genetically fused to the N-terminus of a truncated SP. Capsids could be assembled with this technique and were found to contain 249 ± 13 copies of AdhD. The enzyme is active within the capsules, however, activity (k_{cat}) decreases by about 7-fold¹²⁸. The same approach was used to encapsulate an entire enzyme cascade with two or three enzymes, mimicking a multi-enzyme-complex (metabolon). The metabolon was that of the β -glucosidase (CelB), galactokinase (GALK) and glucokinase (GLUK) from the thermophile *Pyrococcus furiosus*. A 160 kDa construct was made in which all of the target enzymes are fused to the scaffold protein of the viral capsid. The fusion construct has the advantage that the enzymes are present in the correct stoichiometry and they are evenly distributed in between the capsules¹²⁹. Another use of the P22 capsid was the encapsulation of the *Escherichia coli* [NiFe] hydrogenase 1 for hydrogen production. This enzyme is composed of two subunits, *hyaA*, the small subunit, with a [FeS] active site, which protects the larger subunit from oxidation, and *hyaB*, the large subunit, with a [NiFe] active site, which is responsible for the hydrogen production itself. *HyaA* additionally contains a membrane-binding C-terminal domain, which was removed for this study. Both subunits were fused to the P22 SP individually. When expression in *E. coli* was sequentially started, first for the SP fusion constructs, then 4 h later for the P22 CP, functional capsids with hydrogenase activity could be obtained. They encapsulated 88 heterodimers on average and the turnover rate was 41 s^{-1} per enzyme. Also, compared to the free enzyme, the capsid had higher resistance to trypsin, elevated temperatures and oxygen¹³⁰.

A non-viral capsid-forming protein is ferritin (Ftn) which can take up and transport up to 4500 iron atoms *in vivo*. The ferritin capsid consists of 24 subunits with outer and inner diameters of 12 nm and 8 nm and is very stable even at 80 °C and pH 2 – 11¹²³. *Archaeoglobus fulgidus* Ferritin has successfully been used for protein encapsulation. Electrostatic interactions were employed to load five molecules of supercharged GFP(+36) per capsule. It was also possible to load different enzymes (human carbonic anhydrase 2, retroaldolase RA95.5-8F, and Kemp Eliminase HG3.17) when they were tagged with GFP(+36). This encapsulation lead to an increased stability towards protease treatment and high temperature¹³¹.

Chaperonins have also been used as capsules. The *Thermoplasma acidophilum* thermosome (THS) is a protein cage assembled from eight α - and eight β -subunits with an outer diameter of 16 nm and two 5.4 nm cavities. A mutant version of the β -subunit (K316C) was used to covalently attach and encapsulate HRP. The heterobifunctional linker maleimido trioxa-6-formyl benzamide (MTFB) was used for the ligation. As an attachment point, the lysines on HRP were modified with succinimidyl-hydrazino-nicotinamide (HyNic) before treating the thermosomes with 25 equivalents of them. However, the thermosomes could only be filled with 0.4 ± 0.1 copies of HRP on average, which means that the encapsulation efficiency was only 1.6 % and only 5 % of the available ligation sites could be made use of. The resulting encapsulated HRP was then used for the atom-transfer radical polymerization (ATRP) of poly (ethylene glycol) methylether acrylate (PEGA) in activators regenerated under electron transfer (ARGET) conditions using the initiator 2-Hydroxyethyl-2-bromoisobutyrate (HEBIB)

and sodium ascorbate as reducing agent. The reaction yielded a polymer with a very low dispersity of only 1.08, but the yield was only 6 % after 20 h reaction time¹¹¹.

Lumazine synthase from *Aquifex aeolicus* is another non-viral capsid. Through self-assembly of 60 subunits (T = 1 state) or 180 subunits (T = 3 state) it forms icosahedral capsids. A modified version of the lumazine synthase (AaLS-neg) with four additional glutamates (R83E, T86E, T120E, and Q123E) can encapsulate positively charged proteins through electrostatic interactions in a capsid of 29 ± 3 nm outer diameter. This variant of the capsid protein has been further modified through screening of a library of mutants to yield AaLS-13 with seven additional point mutations (D28G, R52C, T112S, V115D, A118D, R127C, and K131E). AaLS-13 has a much higher loading capacity and forms larger capsules (35 ± 3 nm outer diameter)¹³². Proteins with a polyarginine or supercharged GFP(+36) tag to introduce positive charge can be encapsulated inside this mutant. The enzyme retro-aldolase (RA) was successfully encapsulated with high efficiency (45 enzymes per capsule) using this strategy¹³³. The fusion construct of GFP(+36) and RA shows a tenfold reduction in activity, however. Also, the k_{cat} value drops with packing density. In addition, seven other enzymes were successfully encapsulated using the same method: Kemp eliminase (KE), β -lactamase (β Lac), cyclohexylamine oxidase (CHAO), catalase-peroxidase (KatG), NADH oxidase (NOX), aldehyde dehydrogenase (AldH), and monoamine oxidase (MAO). The encapsulation efficiency, however, depends on the net charge of the protein. Whereas proteins with neutral charge can be encapsulated just like RA, those with negative charge tend to assemble on the outside of the capsid, whereas those with positive charge precipitate from solution¹³³.

The encapsulation of enzymes with other proteins has thus shown promising results; table 1.2.1 gives an overview of the examples mentioned here. The resulting encapsulated enzymes are sometimes referred to as nanoreactors. These reactors are not a closed system and allow the diffusion of small substrate molecules in and out of the capsule, while granting some protection from proteases, depending on the pore size of the capsule. In some cases this strategy can be applied simply by co-expression of enzyme and structure-giving protein. Other strategies include covalent ligation of capsule protein and enzyme as well as capsule disassembly and re-assembly in the presence of the target enzyme. In conclusion, protein capsules offer a variety of conditions, sizes (compare fig. 1.2.1) and are specifically modifiable through mutation, which allows for the encapsulation of single enzyme molecules or many copies of huge protein constructs with up to 160 kDa mass¹²⁹. However, for biomedical applications viral capsids might cause undesirable immunogenicity and should therefore be selected with great care¹²⁰.

Table 1.2.1 | Comparison of viral capsids used for enzyme encapsulation.

organism	capsule	outer diam.	inner diam.	enzyme(s)	method	efficiency	enz. per caps.	intended use	reference
CCMV	viral capsid	28 nm	18 nm	HRP	rev. capsid disassembly	n.a.	1	single enzyme monitoring	Comellas-Aragones, M. <i>et al.</i> , 2007
CCMV	viral capsid	28 nm	18 nm	CalB	SrtA ligation	8%	n.a.	n.a.	Schoonen, L. <i>et al.</i> , 2016
bacteriophage MS2	phage capsid	27 nm	n.a.	<i>E. coli</i> PhoA	pH-induced disassembly	n.a.	3.2	n.a.	Glasgow, J. E. <i>et al.</i> , 2012
<i>Sal. typhimurium</i> bacteriophage P22	phage capsid	58 nm	n.a.	AdhD	scaffold pr. gen. fusion	n.a.	249 ± 13	n.a.	Patterson, D. P. <i>et al.</i> , 2012 (ACS Nano)
<i>Sal. typhimurium</i> bacteriophage P22	phage capsid	58 nm	n.a.	CelB	scaffold pr. gen. fusion	n.a.	87 ± 3.5	n.a.	Patterson, D. P. <i>et al.</i> , 2012 (Soft Matter)
<i>Sal. typhimurium</i> bacteriophage P22	phage capsid	58 nm	n.a.	<i>E. coli</i> [NiFe] hydrogenase	scaffold pr. gen. fusion	n.a.	88	hydrogen production	Jordan, P. C. <i>et al.</i> , 2015
<i>Therm. acidophilum</i>	THS	16 nm	5.4 nm	HRP	β -subunit ligation	2%	0.4 ± 0.1	ATRP	Renggli, K. <i>et al.</i> , 2017
<i>Aquifex aeolicus</i>	AaLS-13	35 ± 3 nm	n.a.	RA	GFP(+36) fusion	100%	45	n.a.	Azuma, Y. <i>et al.</i> , 2016
<i>Aquifex aeolicus</i>	AaLS-13	35 ± 3 nm	n.a.	KE	GFP(+36) fusion	100%	n.a.	n.a.	Azuma, Y. <i>et al.</i> , 2016
<i>Aquifex aeolicus</i>	AaLS-13	35 ± 3 nm	n.a.	β Lac	GFP(+36) fusion	100%	n.a.	n.a.	Azuma, Y. <i>et al.</i> , 2016
<i>Aquifex aeolicus</i>	AaLS-13	35 ± 3 nm	n.a.	CHAO	GFP(+36) fusion	100%	n.a.	n.a.	Azuma, Y. <i>et al.</i> , 2016
<i>Aquifex aeolicus</i>	AaLS-13	35 ± 3 nm	n.a.	KatG	GFP(+36) fusion	100%	n.a.	n.a.	Azuma, Y. <i>et al.</i> , 2016
<i>Aquifex aeolicus</i>	AaLS-13	35 ± 3 nm	n.a.	NOX	GFP(+36) fusion	~80%	n.a.	n.a.	Azuma, Y. <i>et al.</i> , 2016
<i>Ar. fulgidus</i>	ferritin	12 nm	8 nm	CA	GFP(+36) fusion	100%	3.0 ± 0.1	n.a.	Tetter, S. <i>et al.</i> , 2017
<i>Ar. fulgidus</i>	ferritin	12 nm	8 nm	RA	GFP(+36) fusion	73%	2.2 ± 0.1	n.a.	Tetter, S. <i>et al.</i> , 2017
<i>Ar. fulgidus</i>	ferritin	12 nm	8 nm	KE	GFP(+36) fusion	87%	2.6 ± 0.1	n.a.	Tetter, S. <i>et al.</i> , 2017

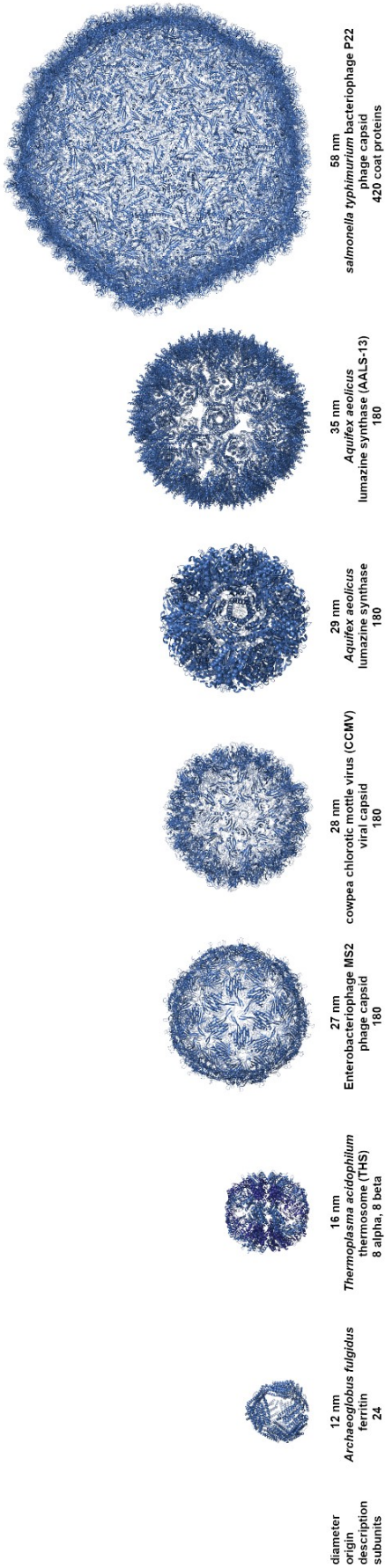


Fig 1.2.1 | Size comparison of the different viral and non-viral protein capsids used for enzyme encapsulation.
 Source: PDB-IDs 1SQ3, 1A6D, 2B2G, 1CWP, 1HQQ, 5MQ7, 5uu5.

DNA-based cages

Thanks to hybridization, DNA can form a variety of structures. This has been exploited in the *de novo* design of various DNA scaffolds. DNA origami yields various 2D designs as well as 3D DNA shapes such as cubes, octahedrons, and tetrahedrons¹³⁴.

A 12 nm DNA tetrahedron has successfully been used as a cage surrounding the enzyme RNase A. The enzyme was covalently attached to the inside of the cage using a heteroreactive linker with dibenzylcyclooctyne and N-Hydroxysuccinimide as reactive groups. An encapsulation efficiency of 86% could be achieved. The DNA tetrahedron was equipped with a pH sensitive i-motif which uses the non-canonical base-pairing C-C+. At pH 8, the enzyme was protected from protease K degradation inside the cage. At pH 6.4, however, it was made accessible due to a conformational change in the i-motif and the protective effect lost. In this way, the accessibility and the activity of the enzyme could be regulated¹³⁵.

Another nanocage was built by combining two honeycomb shaped half-cages made from DNA with pores of 2.5 nm diameter. The half-cages feature 24 short-bridge ssDNA sequences which hybridize with each other. The complete cage is then 54 nm x 27 nm x 26 nm in size. The half-cages could be covalently attached to enzymes using a succinimidyl 3-(2-pyridyldithio) propionate linker. In this way the enzymes horseradish peroxidase (HRP), glucose oxidase (GOx), Glucose-6-phosphate dehydrogenase (G6pDH), lactate dehydrogenase (LDH), malic dehydrogenase (MDH), and β -galactosidase (β -gal) could be encapsulated within the cages with more than 60% encapsulation efficiency¹³⁶. Also, use was made of the modular assembly of these nanocages by adding one of two enzymes, GOx and HRP, to each half of the nanocage. Thus, a two-enzyme cascade could be enabled inside the capsules in a very defined manner. Compared to the free enzymes in solution, the relative activity of the caged enzymes is increased six-fold. Even when the enzymes are encapsulated individually, their resulting activity is increased (four-fold). Therefore, there must also be an influence of the local environment, which features a high charge density within the cages¹³⁶.

In another approach, DNA was used to form hydrogel microparticles. DNA forming long hybrid strands was biotinylated at one end and the formation of the hydrogels induced by addition of streptavidin. The resulting particles were approximately 7 μm in size. These could be loaded with the enzyme alcohol dehydrogenase (AOx), whereupon the size slightly increased to 10 μm . The encapsulation efficiency was 42 % and the hydrogels could be loaded with 18 mg AOx/g hydrogel. This resulted in increased stability in serum and increased resistance to heating (78% of activity lost in free enzyme after 30 min in 55 °C, 60% retained in capsules)¹³⁷.

DNA flowers, also in the micrometer range, were also used to encapsulate HRP. In a one-pot reaction, DNA flowers are fabricated in a rolling circle amplification (RCA) in the presence of HRP. Via unspecific interaction, 3.82 ± 0.25 million copies of HRP were embedded in a single DNA flower particle with approximately 2.9 μm diameter¹³⁸. The DNA sequence contained a thrombin aptamer and the particles could thus be used for ultrasensitive thrombin detection.

DNA as a material for enzyme encapsulation offers the advantage of very precise control over the shape of the resulting structures, including their porosity, the location of the enzymes

within, and their accessibility. The resulting capsules are on the small nanoscale, but also hydrogels in the micrometer range can be made from DNA (compare table 1.2.2). It can successfully be applied to protect enzymes from degradation by proteases and elevated temperatures although it is also prone to melting itself.

Table 1.2.2 | Comparison of different DNA capsules used for enzyme encapsulation.

DNA structure	outer diameter	inner/pore diameter	enzyme(s)	method	efficiency	enzymes per capsule	intended use	reference
tetrahedron	12 nm	n.a.	RNAse A	covalent linkage	86 %	1	rev. enzyme regulation	Kim, S. H., <i>et al.</i> , 2017
honeycomb cage	54 nm x 27 nm x 26 nm	20 nm x 20 nm x 17 nm	HRP	covalent linkage	94 %	1.0	single enz. monitoring	Zhao, Z. <i>et al.</i> , 2016
honeycomb cage	54 nm x 27 nm x 26 nm	20 nm x 20 nm x 17 nm	MIDH	covalent linkage	96 %	1	single enz. monitoring	Zhao, Z. <i>et al.</i> , 2016
honeycomb cage	54 nm x 27 nm x 26 nm	20 nm x 20 nm x 17 nm	G6PDH	covalent linkage	98 %	1.1	single enz. monitoring	Zhao, Z. <i>et al.</i> , 2016
honeycomb cage	54 nm x 27 nm x 26 nm	20 nm x 20 nm x 17 nm	LDH	covalent linkage	82 %	1	single enz. monitoring	Zhao, Z. <i>et al.</i> , 2016
honeycomb cage	54 nm x 27 nm x 26 nm	20 nm x 20 nm x 17 nm	GOx	covalent linkage	98 %	1	single enz. monitoring	Zhao, Z. <i>et al.</i> , 2016
honeycomb cage	54 nm x 27 nm x 26 nm	20 nm x 20 nm x 17 nm	β -Gal	covalent linkage	64 %	0.9	single enz. monitoring	Zhao, Z. <i>et al.</i> , 2016
honeycomb cage	54 nm x 27 nm x 26 nm	20 nm x 20 nm x 17 nm	HRP, Gox	covalent linkage	n.a.	2	single enz. monitoring	Zhao, Z. <i>et al.</i> , 2016
hydrogel particle	10 μ m	n.a.	AOx	Biotin-Streptavidin	42 %	18 mg/g	alcohol antidote	Wan, L. <i>et al.</i> , 2016
DNA flower	2.9 μ m	n.a.	HRP	spontaneous encapsulat.	n.a.	$3.82 \pm 0.25 \cdot 10^6$	amplified labels for thrombin	Yan, Y. <i>et al.</i> , 2018

Carbohydrates

Carbohydrates from plants and fungi are another class of biopolymers which are used for enzyme encapsulation. Examples include alginate, chitosan, and carrageenan, usually in the form of hydrogel beads.

Alginate comes from brown algae and is composed of blocks of β -(1 \rightarrow 4) D-mannuronic acid and α -(1 \rightarrow 4) L-guluronic acid (see fig. 1.2.2). There are two methods to form alginate gels: through the addition of cations (ionic) and by protonating the carboxylic acid groups (acidic)¹³⁹. For enzyme encapsulation, the ionic gelation using calcium chloride as cation source is preferred. To encapsulate α -amylase from *Aspergillus oryzae*, it was mixed with alginate and incubated for 30 min before dripping the mixture into a CaCl₂ solution, forming the beads. 76% of the enzyme could thus be entrapped. The activity of the encapsulated enzyme was reduced by a factor of twelve, but the midpoint of thermal inactivation was increased from 57 °C to 63 °C and its reusability shown over six cycles. However, 30% of the initial activity was lost by the sixth cycle¹⁴⁰. Due to the large pore size (200 nm) of the alginate hydrogel, enzymes leach from the beads when mere physical entrapment is used. To prevent this leaching, the enzymes can be cross-linked with glutaraldehyde, as was done with *Trichoderma reesei* cellulase, forming aggregates of approximately 300 nm size, which were then entrapped in the alginate hydrogels. Leaching of the enzyme over 3 h was completely prevented, whereas 38.7% of non-cross-linked enzyme leached from the beads during the same time. When performing a cellulose hydrolysis reaction, 96.4% of the cross-linked enzyme remained inside the beads after 10 cycles, whereas for the non-cross-linked enzyme only 17% remained. The hydrolysis rate was not significantly affected by the cross-linking, but decreased by about 15% when the enzyme was entrapped in the beads¹⁴¹. A similar method was successfully used for the crosslinking and entrapment of *Aspergillus oryzae* β -galactosidase (lactase). In this case, a mixture of the polymers gelatin (hydrolysed collagen) and alginate with the enzyme was used and dropped into a CaCl₂-solution, containing the cross-linker glutaraldehyde. The resulting beads could be reused for 25 rounds of lactose hydrolysis, losing only 20% activity¹⁴².

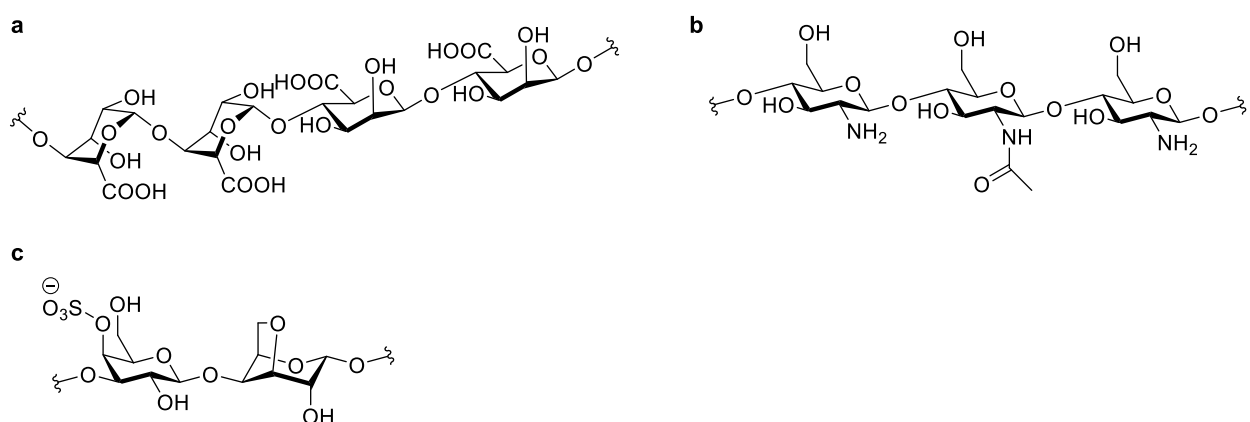


Fig 1.2.2 | Structures of the polysaccharides alginate (a), chitosan (b), and κ -carrageenan (c).

The alginate is also used in combination with other carbohydrates. In one study, *Aspergillus oryzae* lactase was encapsulated in alginate mixed with guar gum or Arabic gum. Additionally, trehalose was used to prevent crystallization while freezing. Particles of approximately 1.5 mm diameter were obtained with loading efficiencies close to 90%. When subjected to freezing/thawing cycles, particles without trehalose lost all activity, whereas those containing 20% trehalose still had more than 60% of the initial lactase activity¹⁴³. In another study, alginate was combined with chitosan to encapsulate *Bos taurus* trypsin and *Aspergillus oryzae* protease, with the goal of releasing the two enzymes under specific conditions. A ratio of 2:1 of alginate to chitosan was found to be optimal, with encapsulation efficiencies of $65 \pm 2\%$ and $54 \pm 2\%$ for protease and trypsin, respectively. However, more than 15% of the encapsulated enzymes leached out of the beads during 2 h incubation already. The release was slightly pH-dependent, with higher release at elevated pH¹⁴⁴.

Chitosan is another linear polysaccharide with β -(1 \rightarrow 4) glucosamine as monomeric unit. Some of the glucosamines are N-acetylated. It is derived from chitin, from shrimp or fungi, by alkaline deacetylation^{144,145}. Since chitosan is a cationic polymer, the gelation can be induced by increasing the pH above 6.4¹⁴⁶. In one example, horseradish peroxidase (HRP) was encapsulated by mixing it with 2.5% chitosan dissolved in 1% acetic acid solution, then extruding it into a 1 M KOH solution. The encapsulation efficiency was very high ($92.5 \pm 2.5\%$). Upon encapsulation, the temperature optimum shifted from 30 °C to 70 °C. Encapsulated HRP also showed enhanced stability against high temperatures (more than 90% activity remained after 120 h incubation at 50 °C, whereas the free enzyme lost 60%) and enhanced pH tolerance (whereas for the free enzyme, the relative activity decreases to 36.6% at pH 3 and 27.3% at pH 9, for the encapsulated enzyme it remains at 48.9% and 57.8%, respectively)¹⁴⁷. Another option for chitosan particle synthesis is the use of polyanions such as sodium tripolyphosphate. This ionotropic gelation method was used to encapsulate porcine catalase (CAT) and bovine diamine oxidase (DAO). The resulting particles were on average 366 nm and 261 nm in diameter, but the polydispersity was relatively high (0.42 and 0.47, respectively). The encapsulation efficiency was very good, 99.7% for CAT and 97.3% for DAO. The particles showed a burst release of the encapsulated protein during the first 2 h (60% for DAO, 20% for CAT) and subsequently a slower steady leaking which is proposed to be beneficial for topic enzyme delivery¹⁴⁵.

Carrageenans are linear polygalactosides obtained from red seaweed (*Rhodophyta*). The *Kappaphycus alvarezii* κ -carrageenan contains the monomers β -(1 \rightarrow 3) D-galactopyranose-4 sulfate and α -(1 \rightarrow 4) 3,6-anhydro-D-galactopyranose^{148,149}. To encapsulate lactase (β -glucosidase) for use in supplements for lactose intolerance Zhang *et al.* used a 1 wt% solution of κ -carrageenan dropped into a 5% KCl solution to create the hydrogel drops. They took 30 min to form and 63% of the enzyme in the solution could be successfully encapsulated. The encapsulated lactase had an increased resistance to temperature degradation, but the desired resistance to acidic conditions (pH 2 - 4) to overcome denaturation in the stomach could not be achieved. Another problem is that the κ -carrageenan is prone to hydrolysis at the 1,3-glycosidic bonds, so that the capsules are potentially degraded in the stomach. Again, the hydrogels leach 45% of the trapped enzyme at 37 °C after 8 h.¹¹⁸

An overview of the carbohydrate capsules is given in table 1.2.3. They offer the possibility to form capsules in the macroscopic and microscopic ranges from the nm to the mm scale. Carbohydrates are well tolerated, which is why many capsules are designed for cosmetic, food, and oral drug administration purposes. However, a disadvantage is swelling of the capsules which leads to leaching of the encapsulated enzymes. On the other hand, this behaviour can be desired as a release mechanism.

Table 1.2.3 | Comparison of different carbohydrate capsules for enzyme encapsulation.

polymer(s)	bead diameter	enzyme(s)	organism(s)	method	enc. efficiency	intended use	reference
alginate	n. a.	α -amylase	<i>Asp. oryzae</i>	ionic gelation	76%	fructose corn syrup prod.	Kumar <i>et al.</i> , 2006
alginate	~ 2 mm	cellulase	<i>Trichoderma reesei</i>	cross-linking, ionic gelation	~100 %	palm oil fiber hydrolysis	Nguyen <i>et al.</i> , 2016
alginate, gelatin	n. a.	lactase	<i>Asp. oryzae</i>	cross-linking, ionic gelation	(30 % activity)	lactose-free dairy prod.	Freitas <i>et al.</i> , 2012
alginate	1.51 \pm 0.15 mm	lactase	<i>Asp. oryzae</i>	ionic gelation	n. a.	long-term storage	Traffano-Schiffo <i>et al.</i> , 2017
alginate	1.48 \pm 0.08 mm	lactase	<i>Asp. oryzae</i>	ionic gelation w. trehalose	92 \pm 4 %	long-term storage	Traffano-Schiffo <i>et al.</i> , 2017
alginate, arabic gum	1.57 \pm 0.11 mm	lactase	<i>Asp. oryzae</i>	entrapment w. trehalose	88 \pm 8 %	long-term storage	Traffano-Schiffo <i>et al.</i> , 2017
alginate, guar gum	1.63 \pm 0.07 mm	lactase	<i>Asp. oryzae</i>	entrapment w. trehalose	88 \pm 8 %	long-term storage	Traffano-Schiffo <i>et al.</i> , 2017
alginate, chitosan (2:1)	1 - 8 μ m	protease	<i>Asp. oryzae</i>	ionic gelation	65 \pm 2 %	cosmetics	Ozaltin <i>et al.</i> , 2019
alginate, chitosan (2:1)	1 - 8 μ m	trypsin	<i>Bos taurus</i>	ionic gelation	54 \pm 2 %	cosmetics	Ozaltin <i>et al.</i> , 2019
chitosan	2 \pm 0.4 mm	HRP	<i>A. rusticana</i>	alkaline gelation	92.5 \pm 2.5 %	Ind. wastew. treatm.	Bilal <i>et al.</i> , 2016
fungal chitosan	365.8 nm	CAT	<i>Bos taurus</i>	ionotropic gelation	99.70%	skin allergy treatm.	Leonida <i>et al.</i> , 2019
fungal chitosan	260.7 nm	DAO	<i>Sus scrofa</i>	ionotropic gelation	97.27%	skin allergy treatm.	Leonida <i>et al.</i> , 2019
k-carrageenan	2 - 3 mm	lactase	<i>Kluyv. lactis</i>	ionic gelation	63%	lactase repl. therapy	Zhang <i>et al.</i> , 2016

Liposomes, polymersomes, and other lipid and polymer-based particles

Liposomes are hollow spherical particles consisting of phospholipids and cholesterol (or a similar sterol such as stigmasterol) between 20 nm and several μm in diameter. The phospholipid composition influences their stability and permeability. Phospholipids with unsaturated and short fatty acids increase the flexibility and permeability, whereas long and saturated fatty acids lead to more rigid, non-permeable liposomes. There are three classes; small unilamellar vesicles (SUVs) and large unilamellar vesicles (LUVs) are made from a single lipid bilayer, whereas large multilamellar vesicles (LMVs) are formed from two or more lipid bilayers^{150,151}. Liposomes are used for the single or co-encapsulation of various enzymes.

Lactoferrin is an Fe^{3+} -binding glycoprotein of 80 kDa which can be found in mammalian glandular secretions such as milk, sweat, and saliva¹⁵². Among others it has protease, DNase and RNase activity¹⁵³. The enzyme was encapsulated in rapeseed phospholipid liposomes passively, by forming the liposomes in a LF solution, with a high encapsulation efficiency of $91.9 \pm 0.6\%$. The liposomes were 149 ± 3 nm in diameter. The activity of the Lactoferrin was not tested¹⁵⁰.

This strategy is also used for the encapsulation of multiple enzymes into liposomes to create an enzymatic cascade. In one study, catalase (CAT) and uricase (URE) were co-encapsulated in soybean phospholipids. While catalase catalyses the reaction of hydrogen peroxide to water and oxygen, uricase catalyses the reaction of uric acid and oxygen to allantoin and hydrogen peroxide, so that a circular reaction is created¹⁵⁴. The aim is to treat hyperuricemia, which is a pathologic increase in uric acid levels that leads to hypertension, gout, and even kidney failure¹⁵⁵. The liposomes could lower uric acid levels without increasing reactive oxygen species (ROS) concentration. The bienzymatic liposomes are 760 - 850 nm in diameter with an encapsulation efficiency between 53% and 57%. Liposomes with CAT only are slightly smaller (410 - 590 nm diameter). The activity in the bienzymatic liposomes could be increased 1.4 times and the half-life extends 6 times. In rats, the bienzymatic liposomes significantly lowered uric acid levels, when injected intravenously¹⁵⁴.

Another approach is to generate polymersomes, which are analogous to liposomes, just consisting of synthetic polymer. In one study, the block copolymer poly(2-methyloxazoline)-block-poly(dimethylsiloxane)-block-poly(2-methyloxazoline) (PMOXA-b-PDMS-b-PMOXA) was used to create polymersomes encapsulating the enzyme ribitol dehydrogenase (RDH) to detect sugar alcohols. The reaction produced NADH which can be observed spectroscopically. In order for the substrate to effectively diffuse into the capsules, the channel glycerol facilitator (GlpF) was embedded in the polymer layer¹⁰⁸.

The activity of the enzymes in the liposomes or polymersomes depends on their permeability. Since this is temperature dependent, the maximum activity corresponds to the lipid melting temperature. This was shown in a study by Kaszuba *et al.*, in which glucose oxidase (GOx) and horseradish peroxidase (HRP) were either co-encapsulated or encapsulated individually to be used as an anti-biofilm system. Two kinds of liposomes were used. Anionic liposomes were prepared using dimyristoylphosphatidylcholine (DMPC) and phosphatidylinositol (PI), whereas cationic liposomes were made from DMPC, dimethyldioctadecylammonium bromide

(DDAB) and cholesterol. The anionic and cationic liposomes were 125.75 nm and 136.97 nm in diameter, respectively. The encapsulation efficiency was not measured. The hydrogen peroxide concentration was measured using a Rank oxygen electrode and it was found that for the anionic liposomes, the hydrogen peroxide formation is dependent on temperature and maximum activity is found near the DMPC melting temperature of 23 °C¹⁵⁶.

There are several strategies to overcome this permeability limitation. One example is detergent-induced loading of liposomes (DILL). In one study, phosphorylase a and glycogen were loaded into 1-palmitoyl-2-oleoyl-sn-glycero-3-phosphocholine (POPC) liposomes in order to perform glycogen elongation. When adding 13.3 mM of sodium cholate to these liposomes, it was possible for glucose phosphate to diffuse from the outside, and the elongation reaction occurred¹⁵⁷.

Another strategy is to employ membrane protein channels to serve as pores inside the liposomes, allowing for substrate transport across the membrane. For example, the *E. coli* outer membrane protein F (OmpF) was used. It forms a trimeric channel, which allows molecules of up to 600 Da to pass through¹⁵⁸. The enzyme β -lactamase, which catalyzes the hydrolysis of the antibiotic ampicillin was encapsulated inside 1-palmitoyl-2-oleoyl-sn-glycero-3-phosphocholine (POPC) liposomes. It could then be shown that there is no activity in the absence of the OmpF, whereas when OmpF is present (at an estimated 2 trimeric channels per liposome) the activity is restored. At low concentrations of Ampicillin, below 0.5 μ M, the hydrolysis activity of the liposomes is reduced compared to that of the free enzyme, because it is limited by the diffusion of Ampicillin across the membrane. The liposomes were also stabilized by a UV-induced free radical polymerization inside the membrane using n-butyl methacrylate (BMA) and the cross-linker ethylene glycole dimethacrylate (EGDMA) which only reduced the activity at low substrate concentrations, but did not change the activity at higher ampicillin concentration¹⁵⁹. In another study, the enzymes glucose oxidase (GOx) and catalase (CAT) from *aspergillus niger* were co-encapsulated in liposomes made from egg phosphatidylcholine (PC), 1,2-dimyristoyl-sn-glycero-3-phosphoethanolamine (DMPE), and cholesterol. The addition of OmpF to the liposomes could increase the catalytic efficiency of the GOx from 2.9% to 51% of that of the free enzyme at an optimum average of 5 monomers per capsule. A further increase in OmpF content led to a reduction in activity. As expected, the OmpF embedding did not have any influence on the CAT activity, which was 73% of the free enzyme activity, because the substrate, hydrogen peroxide, can diffuse through the membrane more freely. The two-enzyme liposomes with OmpF could be used to convert glucose with more than 80% efficiency during at least five consecutive runs at 40 °C. It was shown that the encapsulated enzymes have improved resistance against guanidinium hydrochloride (5 M) and temperature¹⁶⁰.

Stomatocytes are a type of anisotropic liposome or polymersome. The term stomatocyte originally describes a red blood cell, which is folded in on itself. Conditions were found to form these stomatocytes out of poly(ethylene glycol) polystyrene (PEG-PS) block copolymer by the addition of a small amount of organic solvent. Using this morphology change, the enzyme catalase (CAT) could be encapsulated with or without GOx to create an enzyme cascade. The

reaction products, water and oxygen can escape from the stomatocytes opening in a stream, turning the capsules into nanomotors, moving at up to 176 body lengths/s. In addition, the capsule offers some protection against the protease trypsin. However, small molecule inhibitors, such as sodium azide, can enter the cavity and inhibit the enzymes¹⁶¹.

An alternative to liposomes is to use congealed lipid particles, which are not made up of individual bilayers, but a continuous lipid phase¹¹⁵. In one study, these were prepared by spraying the target enzyme, lactase, with glycerol trimyristate. The spray nozzle was heated 5 °C above the melting temperature of the lipid and the spray was chilled in a cooling chamber, where the particles were collected and sorted by size. With the optimum sized particles (150 - 250 µm) it was possible to avoid complete degradation of lactase in Fasted State Simulated Gastric Fluid (FaSSGF). Even after 30 min incubation in FaSSGF containing Trypsin, 62.8% of the initial activity was retained, whereas for the free enzyme, only 0.8% activity remained. The particles were designed to withstand the stomach, but dissolve in the intestine in order to release the lactase. Indeed, in Fed State Simulated Intestinal Fluid (FeSSIF) 71% of the enzyme was released already after 15 min incubation¹¹⁵.

Polymer particles were made using the emulsification/cross-linking method in which an aqueous polymer solution is forced through a porous membrane into an organic phase. This has been used to entrap *Candida rugosa* lipase in polyvinyl alcohol (PVA) microspheres cross-linked with glutaraldehyde (GA). Spheres with a diameter of 28 µm were obtained from a membrane with 10 µm holes. The microspheres shrink to 16 µm when dried. When adding the enzyme to the PVA dispersion, it could be entrapped with 54% to 100% efficiency, depending on the concentration. The lipase retained $78 \pm 4\%$ activity within the droplets which were used to hydrolyse olive oil¹⁶².

The enzyme itself could also be used for initiation of the capsule formation. Glucose oxidase (GOx) was used to produce hydroxyl radicals in the presence of glucose and ferrous ions (Fe^{2+}) at 45 °C. N-vinylcaprolactam (VCL) and N,N'-methylenebisacrylamide (BIS) as cross-linker were added to form PVCL microgels with a hydrodynamic diameter of 200 nm. These self-encapsulated enzymes were still active within the particles. The encapsulation efficiency was not determined¹⁶³.

The solvent evaporation method can be used to create capsules from a W/O/W emulsion by evaporating the organic solvent, leaving capsules from the polymer dissolved in it. This technique was used to encapsulate HRP in Eudragit RS 100 for enteric delivery. The capsules were on average 178 µm in diameter and the encapsulated enzyme showed increased resistance towards simulated gastric fluid (SGF) and simulated intestinal fluid (SIF). The enzyme activity was retained¹⁶⁴.

Another process to form the capsules is by initiating the polymerization of monomers inside the aqueous phase of a W/O emulsion by irradiation. This has been performed to encapsulate GOx inside PDEGMA-b-PMMA nanocapsules. The substrate could diffuse inside the capsules and the encapsulated enzyme showed high residual activity (71 - 100%)¹⁶⁵.

Table 1.2.4 | Comparison of different lipid and polymer-based particles for enzyme encapsulation.

lipids or polymers	enzyme	size	type	enc. eff.	loading	intended use	reference
rapeseed phospholipids	lactoferrin	149 ± 3 nm	liposomes	91.9 ± 0.6 %	n.a.	incr. oral avail.	D. Vergara <i>et al.</i> , 2019
soybean phospholipids	CAT	410 - 590 nm	liposomes	53 - 57 %	n.a.	hyperur. treatm.	Y. Li <i>et al.</i> , 2017 (I. J. Pharm.)
soybean phospholipids	CAT + URE	760 - 850 nm	liposomes	53 - 57 %	n.a.	hyperur. treatm.	Y. Li <i>et al.</i> , 2017 (I. J. Pharm.)
PMOXA-b-PDMS-b-PMOXA	RDH	100 nm	polymersomes	n. a.	n. a.	sugar alc. detec.	X. Zhang <i>et al.</i> , 2016
DMPC, PI	GOx	122.99 nm	liposomes	n.a.	6.55 *10 ⁻² μM	anti-biofilm act.	Kaszuba <i>et al.</i> , 1999
DMPC, PI	HRP	132.93 nm	liposomes	n.a.	6.80 * 10 ⁻¹ μM	anti-biofilm act.	Kaszuba <i>et al.</i> , 1999
DMPC, PI	GOx + HRP	116.00 nm	liposomes	n.a.	8.70 *10 ⁻² μM (GO), 3.33 *10 ⁻¹ μM (HRP)	anti-biofilm act.	Kaszuba <i>et al.</i> , 1999
DMPC, DDAB, cholesterol	GOx	129.03 nm	liposomes	n.a.	1.40 * 10 ⁻¹ μM	anti-biofilm act.	Kaszuba <i>et al.</i> , 1999
DMPC, DDAB, cholesterol	HRP	132.95 nm	liposomes	n.a.	2.50 * 10 ⁻¹ μM	anti-biofilm act.	Kaszuba <i>et al.</i> , 1999
DMPC, DDAB, cholesterol	GOx + HRP	125.11 nm	liposomes	n.a.	4.06 *10 ⁻² μM (GO), 1.56 *10 ⁻¹ μM (HRP)	anti-biofilm act.	Kaszuba <i>et al.</i> , 1999
POPC + sodium cholate	phosphorylase a	150 nm	liposomes	n.a.	n. a.	polym. micror.	Oberholzer <i>et al.</i> , 1999

lipids or polymers	enzyme	size	type	enc. eff.	loading	intended use	reference
POPC	β -lactamase	150 nm	liposomes	n. a.	n. a.	size-sel. nanor.	Graff <i>et al.</i> , 2001
POPC	β -lactamase	168 nm	pol.-stabil. lipos	n. a.	n. a.	size-sel. nanor.	Graff <i>et al.</i> , 2001
PC + DMPE + cholesterol	GOx	100 nm	liposomes	n. a.	1.3 enz. per lipos.	airlift bior. cat.	M. Yoshimoto <i>et al.</i> , 2005
PC + DMPE + cholesterol	CAT	100 nm	liposomes	n. a.	0.53 enz. per lipos.	airlift bior. cat.	M. Yoshimoto <i>et al.</i> , 2005
PC + DMPE + cholesterol	GOx + CAT	100 nm	liposomes	n. a.	1.6 + 0.66 enz. p. lip.	airlift bior. cat.	M. Yoshimoto <i>et al.</i> , 2005
PEG-PS	CAT	500 nm	stomatocytes	n. a.	n. a.	nanomotor	Abdelmohsen <i>et al.</i> , 2016
PEG-PS	CAT, GOx	500 nm	stomatocytes	n. a.	n. a.	nanomotor	Abdelmohsen <i>et al.</i> , 2016
glyceryl trimyristate	β -gal	50 – 150 μ m	solid lipid microp.	95.6 \pm 5.5%	4.78 \pm 0.28%	small int. delivery	Bertoni <i>et al.</i> , 2018
PVA + GA (1:0.2)	lipase	28 μ m	microspheres	54 - 100 %	n. a.	or. imm. of biom.	Piacentini <i>et al.</i> , 2017
PVCL + BIS	GOx	200 nm	microgels	n. a.	n. a.	self-encapsulation	Gau <i>et al.</i> , 2018
EUDRAGIT RS 100	HRP	178 \pm 67 μ m	microcapsules	95.8 \pm 2.3 %	n. a.	enteric delivery	Gracia <i>et al.</i> , 2018
PDEGMA-b-PMMA	GOx	120-170 nm	nanocapsules	n. a.	n. a.	org. solv. res. enz.	Ishizuka <i>et al.</i> , 2018

Liposomes and other lipid particles offer the possibility to encapsulate enzymes in particles from 100 nm to hundreds of μ m (see table 1.2.4). Substrate accessibility depends on the fluidity of the lipids but can be tuned using detergents and pore-forming channels inside the membrane.

1.2.2 Inorganic materials

Biomimetic Silica

The biomimetic synthesis of silica particles using peptides and amines was discussed in chapter 1.1.2. The following examples show how it was used to encapsulate functional enzymes.

Luciferase was encapsulated in silica particles precipitated with cysteamine. The encapsulation efficiency was not determined, but the enzyme retained 87% activity inside the particle⁶².

Spermine was used to encapsulate *Hahella chejuensis* carbonic anhydrase (HCA) within 10 min and with more than 80% encapsulation efficiency. The resulting particles were 300 - 400 nm in diameter and retained 60% of the enzyme activity. The encapsulated enzyme showed superior heat tolerance, with $97 \pm 5\%$ activity retained after incubation at 60 °C for 30 min, while the free enzyme retained only $51 \pm 8\%$ activity under the same conditions⁶⁴.

Diethylenetriamine (DETA), triethylenetetramine (TETA), tetraethylenepentamine (TEPA), and pentaethylenehexamine (PEHA) were compared in one study to encapsulate the enzyme nitrilase A (NitA) from *Acidovorax facilis*. In this way, aggregates of particles in the μm range were obtained. The highest encapsulation efficiency ($94.4 \pm 2.5\%$) was found for TETA. The enzyme retained $92.6 \pm 3.8\%$ of its activity after encapsulation and showed increased thermostability at 60 °C. The particles could be used for the production of 1-cyanocyclohexaneacetic acid, which is an intermediate used in the pharmaceutical industry, in a bioreactor⁶³. Polyethyleneimines (PEIs) of larger molecular weights were used for encapsulation of the enzymes acetylcholinesterase (AChE)⁶⁶, nitroreductase (NbzA)¹⁶⁶, as well as co-encapsulation of nitroreductase (NbzA) and glucose-6-phosphate dehydrogenase (G6pDH)¹⁶⁷. The measured encapsulation efficiencies were very high (80 - 100%) and spherical particles with sizes between 0.2 μm and 1 μm were obtained. There are several variations of this approach. One is the addition of Fmoc-FF as a structure-giving component, which was used for encapsulation of the *Sphingomonas* epoxide hydrolase (SpEH). 1.2 μm sized particles with a multi-layered structure like an onion could be created when injecting a mixture of Fmoc-FF, silicic acid, and the enzyme into a buffered PEI solution. The encapsulated enzyme retained its high enantioselectivity (88% enantiomeric excess) and leaching was very little (2.3% over 48 h)¹¹⁰. Another approach was to first cross-link *Rhodotorula glutinis* Phenylalanine Ammonia Lyase (PAL) enzymes using porous CaCO_3 nanoparticles as templates. Cross-linking was performed with glutaraldehyde and afterwards, the calcium carbonate was dissolved at pH 5.2. Thus, cross-linked protein nano-spheres were obtained, which were then coated with silica at pH 6.8 using PEI as a catalyst. In this way, 2 μm particles were made with pores of 2 - 40 nm. The encapsulated PAL had only about 20% of the activity of the free enzyme, but was highly resistant to heat (80% activity remaining after incubation at 60 °C for 1 h, 19% for free enzyme) and trypsin degradation ($90 \pm 5\%$ remaining activity after 30 min exposure, no activity for free enzyme)¹⁶⁸.

A PAMAM dendrimer was used to encapsulate horseradish peroxidase (HRP) with 30% and glucose oxidase (GOx) with quantitative encapsulation efficiency. The particles were 162 ± 92

nm and 113 ± 60 nm in diameter; they retained $27.2 \pm 13.9\%$ and $53.9 \pm 5.3\%$ activity, respectively⁶⁷.

Detergents have been used as well. Hong *et al.* encapsulated single bovine α -Chymotrypsin molecules by first extracting them into hexane using Dioctyl sulfosuccinate sodium salt (DOSS) as detergent. TMOS was added to the hexane as a silica source. When back extracting the enzyme into phosphate buffer, single enzyme caged nanoparticles (SECN) were formed. The particles were 6.9 ± 0.5 nm in diameter with a silica layer of 1.5 ± 0.5 nm. The activity was lower than that of the free enzyme by about 20% ($k_{\text{cat}} = 25.4 \pm 0.1 \text{ s}^{-1}$ (encapsulated), $k_{\text{cat}} = 31.8 \pm 0.8 \text{ s}^{-1}$ (free)), but the SECNs were more stable than the free enzyme (90% activity after 3 d storage, no activity for free enzyme)¹⁶⁹.

Another possibility is to use a molecule which is both precursor and template. One example is PEG-PEOS, an amphiphilic molecule, containing two polyethylene glycol moieties, and a polar head consisting of partially polymerized TEOS. It was used to form micelles in an aqueous solution of the target enzyme, a *Bacillus* protease. Silica formation was induced by the addition of ammonia. The resulting particles were 180 nm in diameter, with a 30 nm thick silica shell, containing 3.8 nm pores. 48% of the protease, 900 molecules per capsule on average, could be encapsulated using this method, and the enzyme activity was reduced to 38.7%. The capsule offered good protection from elevated temperatures. Whereas 90% of the free enzyme were deactivated after 1 h incubation at 80 °C, only 20% of the encapsulated enzyme were deactivated¹⁷⁰.

The enzymes horseradish peroxidase (HRP) and catalase (CAT) were encapsulated using the R5 peptide, forming aggregated particles in the μm range. Encapsulation efficiency was not measured, but it was found that the particles have roughly the same activity as the free enzyme and retain the activity when the particles are dried¹⁷¹. *Equus caballus* butyrylcholinesterase (BuChE) was encapsulated in the same manner. Particles of 500 nm diameter were obtained and retained $90 \pm 7.2\%$ of the initial enzyme activity. The encapsulated enzyme showed improved stability at elevated temperature (65 °C for 1h)⁵³. The method was also used for soybean peroxidase (SBP). The particles were not characterized, but retained 65 - 85% of their activity when used in a microfluidic device for 2-aminophenoxazin-3-one (APO) synthesis¹⁷². A more controlled approach to encapsulation with R5 is to create a fusion construct of the target enzyme with the peptide. This was done with the catalytic domain of the human matrix metalloprotease 12 (catMMP12). R5 was fused to its C-terminus with an 8 amino acid linker (GSASGGGG) in between. From this construct, silica could be precipitated with a loading of 2.56 mmol of protein per mol SiO_2 . The catalytic activity was slightly reduced by R5 fusion and further reduced by encapsulation⁵⁰.

Even entire proteins, such as lysozyme, can be used for silica precipitation. It was shown that not only lysozyme itself can be encapsulated in silica, but it can also co-encapsulate another enzyme, butyrylcholinesterase (BuChE). The resulting particles were 300 - 650 nm in diameter and spherical. Lysozyme retained $85 \pm 7\%$ enzyme activity when encapsulated, BuChE was still fully active. The resulting encapsulated enzymes had improved thermostability. When

incubated at 75 °C for 1 h, the free lysozyme lost 90% activity, whereas the encapsulated enzyme lost 25% only¹⁷³.

As exemplified here, the biomimetic enzyme encapsulation in silica yields stable particles and can be set up in a number of ways using readily available reagents or peptides. Encapsulation efficiencies are usually high, and the size and morphology of the particles can be tuned by varying the initiator molecular weight and the precipitation conditions. The results of the studies mentioned here are summarized in table 1.2.5.

Table 1.2.5| Biomimetic silica for enzyme encapsulation.

silica catalyst	silicic acid precursor	particle diameter	particle shape	enzyme(s)	organism(s)	MW	Enc. efficiency	rel. activity	intended use	reference
cysteamine	TMOS	40 - 100 nm	amorphous	luciferase	<i>Ph. pyralis</i>	60.75 kDa	n. a.	87%	funct. arrays	Roth et al., 2004
DETA	Na ₂ SiO ₃	µm range	aggregates	NitA	<i>A. facilis</i>	41.27 kDa	88.2 ± 2.2%	86.6 ± 3.2%	1-CHAA prod.	Xu et al., 2019
TETA	Na ₂ SiO ₃	µm range	aggregates	NitA	<i>A. facilis</i>	41.27 kDa	94.4 ± 2.5%	92.6 ± 3.8%	1-CHAA prod.	Xu et al., 2019
TEPA	Na ₂ SiO ₃	µm range	aggregates	NitA	<i>A. facilis</i>	41.27 kDa	89.8 ± 3.1%	86.3 ± 2.3%	1-CHAA prod.	Xu et al., 2019
PEHA	Na ₂ SiO ₃	µm range	aggregates	NitA	<i>A. facilis</i>	41.27 kDa	81.9 ± 2.2%	76.8 ± 2.1%	1-CHAA prod.	Xu et al., 2019
PEI (25 kDa)	TMOS	260 nm	spherical	AChE	n. a.	n. a.	n. a.	39.10%	Biosensors	Neville et al., 2011
PEI	TMOS	0.5 - 1.0 µm	spherical	NbZA	<i>Ps. Pseudobalc.</i>	33 kDa	80%	60 ± 5%	drug screen.	Berne et al., 2006
PEI	TMOS	n. a.	n. a.	NbZA, G6PDH	<i>P. pseudoalcal.</i> , n. a.	33 kDa, n. a.	quantitative, 98.4 ± 0.6%	52.5 ± 0.2%, 33.0 ± 0.3%	nitroar. comp. red.	Betancor et al., 2006
PEI (+ Fmoc-FF)	Na ₂ O(SiO ₂) _k · xH ₂ O	1.2 mm	spherical	SpEH	<i>Sphingomonas</i> s sp. HXN-200	42.94 kDa	94%	60%	diol synthesis	Huang et al., 2015
PEI (1.8 kDa)	TMOS	2 µm	spherical	cross-linked PAL	<i>Rhodotorula glutinis</i>	76.05 kDa	n.a.	20%	industrial applications	Cui et al., 2017
spermine	TMOS	300 nm - 400 nm	spherical	HCA	<i>Hah. chejuensis</i>	26.5 kDa	80%	60%	CO ₂ seques.	Min et al., 2016

silica catalyst	silicic acid precursor	particle diameter	particle shape	enzyme(s)	organism(s)	MW	Enc. efficiency	rel. activity	intended use	reference
PAMAM	TMOS	162 nm ± 92 nm	spherical	HRP	<i>A. rusticana</i>	38.83 kDa	30%	27.2 ± 13.9%	hybrid mater.	Miller et al., 2006
PAMAM	TMOS	113 nm ± 60 nm	spherical	GO	n.a.	n. a.	quantitative	53.9 ± 5.3%	hybrid mater.	Miller et al., 2006
PEG-PEOS	TEOS	180 nm	Sphere. shell	protease	<i>Bacillus</i>	27.30 kDa	48%	38.7 ± 6.6%	biosens. dev.	Zhang et al., 2015
DOSS	TMOS	6.9 nm ± 0.5 nm	spherical	α-Chymo-trypsin	<i>Bos taurus</i>	13.92 kDa	n. a.	79.9 ± 0.02%	recycl. bioc.	Hong et al., 2017
R5 peptide	TMOS	500 nm	spherical	BuChE	<i>Equus caballus</i>	68.84 kDa	n. a.	90 ± 7.2%	decontamin.	Luckariff et al., 2004
R5 peptide	TMOS	µm range	aggregates	HRP	<i>A. rusticana</i>	38.83 kDa	n. a.	full activity	biosensing	Naik et al., 2004
R5 peptide	TMOS	µm range	aggregates	CAT	n.a.	60 kDa	n. a.	full activity	Biosensing	Naik et al., 2004
R5 peptide	n. a.	n. a.	n. a.	SBP	<i>Glycine max</i>	42.32 kDa	n.a.	65 - 85%	Microfl. APO synthesis	Luckariff et al., 2007
R5 peptide fusion tag	TMOS	µm range	aggregates	catMMP12	<i>Homo sapiens</i>	20.15 kDa	n. a.	ca. 58%	SSNMR	Martelli et al., 2016
Lysozyme	TMOS	300 nm - 650 nm	nanospheres	Lysozyme	<i>Gallus gallus</i>	14.3 kDa	n. a.	85 ± 7%	Antib. bio-nanocomp.	Luckariff et al., 2006 (small)
Lysozyme	TMOS	300 nm - 650 nm	nanospheres	BuChE	n. a.	n. a.	n. a.	full activity	Antib. bio-nanocomp.	Luckariff et al., 2006 (small)

Mesoporous silica

Mesoporous silica nanoparticles are made using a cationic or non-ionic surfactant. The synthesis process and the different available materials are described in chapter 1.1.1.

One example are hollow mesoporous particles into which the enzyme can diffuse. After calcination they are incubated with the enzyme solution. After this process, the pores are sealed by a second silica deposition process using TMOS, allowing small molecules to diffuse into the hollow interior, but retaining the enzymes. This process was successfully demonstrated for the model enzyme penicillinase from *B. cereus* of which 67 enzymes could be encapsulated per particle. It was then shown that after treatment of the particles with proteinase-K, the encapsulated enzymes were not detectable by antibody, but still active toward a CCF2 substrate. The substrate consists of a coumarin and a fluorescein moiety. During the reaction, the linker is cleaved, which lowers fluorescence resonance energy transfer (FRET). Activity of the particles was also demonstrated in vivo in mice using the enzymes *Gaussia princeps* luciferase and *E. coli* L-asparaginase¹⁷⁴.

In another study, the enzymes *B. taurus* catalase and *G. gallus* lysozyme were encapsulated in small mesoporous silica nanoparticles. The particles were first synthesized using the surfactants Pluronic P123 and FC-4 (to inhibit particle growth). Also, 1,3,5-trimethylbenzene (TMB) was added as swelling agent. The resulting particles were 90 ± 20 nm in the longest dimension and 43 ± 7 nm in the shortest dimension and featured 10 ± 1 nm channels as observed by TEM. After calcination, they could be functionalized with 3-[2-(2-aminoethylamino)ethylamino]propyltrimethoxysilane (AEPTMS) to obtain a positively rather than negatively charged surface. The enzymes were then retained in the particles due to ion pairing. Lysozyme, which is positively charged (pI 10) at neutral pH could be encapsulated quantitatively in the non-modified silica particles. Catalase, which has a pI of 5.8, could be encapsulated with 96% efficiency inside the AEPTMS modified particles. Enzymatic activity was not monitored¹⁷⁵.

The encapsulation in MSNs can have varying influence on the enzyme activity as has been demonstrated for *B. taurus* trypsin and *M. miehei* lipase. They were encapsulated in 2 μ m particles made of SBA-15 material. For trypsin, the optimised encapsulation was performed at pH 7.6 using particles with 6 nm pores. 73% of the enzymes were encapsulated but retained only 6.2% activity. In contrast, lipase was encapsulated at pH 6.0 using the 8.9 nm pore particles with 42% encapsulation efficiency. The activity compared to the free enzyme was increased to 215%, supposedly thanks to a surface effect, which favours the active conformation of the lipase¹⁷⁶.

Thus, depending on the pore size of the MSNs, they can be used to efficiently encapsulate enzymes of small (23 kDa) to very large (250 kDa) size (compare table 1.2.6).

Table 1.2.6 | MSNs for enzyme encapsulation.

material	particle diameter	particle shape	enzyme(s)	organism(s)	MW	encapsulation efficiency	rel. activity	intended use	reference
SHELS	425 nm	hollow sphere	β Lac	<i>B. cereus</i>	28 kDa	n. a.	99%	therapeutic platform	Ortac et al., 2014
AEP-MSN	90 \pm 20 nm	cuboidal	CAT	<i>B. taurus</i>	250 kDa	96%	n. a.	protein therapy	Tu et al., 2016
MSN	90 \pm 20 nm	cuboidal	LYS	<i>G. gallus</i>	14.3 kDa	quantitative	n. a.	protein therapy	Tu et al., 2016
SBA-15	2 μ m	rod	trypsin	<i>B. taurus</i>	23 kDa	73%	6.20%	autolysis prevention	Gustafsson et al., 2011
SBA-15	2 μ m	rod	lipase	<i>M. miehei</i>	323 kDa	42%	215%	activation	Gustafsson et al., 2011

1.2.3 Composite structures

Various core-shell structures exist, combining several materials, for enzyme encapsulation. Usually a soft, polymeric matrix is surrounded by a solid oxide material such as silica.

In one example, the enzyme β -glucuronidase (GUS) was encapsulated in alginate and carboxymethylcellulose hydrogels which were then coated in a layer of silica precipitated from a solution of sodium silicate within 30 min. The precipitation reaction was facilitated by the protamine peptide from *Salmo salar* (compare section 1.1.1). The capsules were 3 mm in diameter and the encapsulation efficiency was 77%. The relative activity measured was 125% of that of the free enzyme, which the authors explain with the adsorption properties of the silica shell⁵⁹. The same approach was used in a microfluidic device to encapsulate laccase in microcapsules with only 157 μm in diameter. The ultrathin (420 nm) silica shell permitted the encapsulated enzyme to reach 94% activity¹⁷⁷. A similar approach was used to encapsulate thermoalkalophilic esterase in silica-coated alginate particles with 68% encapsulation efficiency. In this case, no catalyst was used for the silica precipitation, which necessitated an incubation with TEOS over 24 h. The enzyme activity was reduced to 45.8% but the encapsulated enzyme showed increased temperature stability¹⁷⁸. Another inducer of silica formation is (3-Aminopropyl)triethoxysilane (APTES). Phosphoenolpyruvate carboxylase (PEPCase) was encapsulated in alginate capsules which were covered in silica on which carbonic anhydrase was immobilised to facilitate CO_2 conversion to oxaloacetate. The particles were 500 - 800 μm in diameter and contained dynabeads to allow for magnetic separation and recovery of the enzyme^{179,180}.

Another strategy to obtain magnetic capsules was to use Fe_3O_4 particles directly. They were covered with silica using TMOS and APTES, then catalase (CAT) was immobilized and finally covered with a second layer of mesoporous silica using CTAB and TMOS. This layer was 20 - 30 nm thick with 3.2 nm pores. The encapsulated enzyme showed reduced activity (57%) but increased stability against heat, trypsin, urea, SDS, and ethanol¹⁸¹.

Another inorganic shell material is calcium phosphate. Particles made from chitosan and yeast alcohol dehydrogenase (YADH) could be covered with a calcium phosphate shell, which was 45 – 55 μm thick, *in situ*. The encapsulation efficiency was 96%. The shell prevents the enzyme from leaking from the 3 mm large particles and thus improves their recyclability¹⁸².

Composite structures for enzyme encapsulation combine the advantages of the materials used which has a significant impact on the stability of the resulting capsules. The most precise method for their manufacture is using a microfluidic device. A comparison of the obtained capsules and their various applications is shown in table 1.2.7.

Table 1.2.7] Composite particles for enzyme encapsulation.

core material	precipitation method	shell material	particle diamete	shell thickness	enzyme(s)	organism(s)	encaps. efficiency	relative activity	intended use	reference
alginate, carboxymethyl cellulose	protamine-induced	silica	3 mm	15 µm	GUS	<i>E. coli</i>	77%	125%	recyclable catalyst	Zhang et al., 2008 (Chem. Mater.)
alginate	hexane + TEOS	silica	0.5 mm	n. a.	thermoalkalophilic esterase	<i>Geobacillus</i>	69%	45.80%	improved storage	Gülçay et al., 2011
alginate	protamine-induced	silica	157.4 µm	421 ± 40 nm	laccase	<i>T. versicolor</i>	n. a.	94%	waste detoxification	Wu et al., 2015 (J. Mater. Chem. B)
alginate, PEG amine, Dynabeads	APTES-induced	silica	500 - 800 µm	n. a.	CA + PEPCase	<i>Bos taurus</i> + n. a.	20%	32 % + 35 % (combin)	CO ₂ -conversion	Hwang et al., 2016 (Catal. Sci. Technol.)
Fe ₃ O ₄	CTAB-induced	silica	n. a.	20 - 30 nm	CAT	<i>Bos taurus</i>	n. a.	59%	recyclable biocatalyst	Cui et al., 2018 (Int. J. Biol. Macromol.)
chitosan	in situ precipitation	Ca ₃ (PO ₄) ₂	3 mm	45-55 µm	YADH	<i>S. cerevisiae</i>	96%	n. a.	biosensor	Han et al., 2015 (Ind. Eng. Chem.)

1.3 Membrane protein stabilization

Membrane proteins are ubiquitous in nature. Approximately 23% of all proteins in the human proteome are membrane proteins¹⁸³. A study from 2017 found that 32.3% of approved drug compounds target a member of the seven transmembrane (7TM) protein family alone¹⁸⁴. The total fraction of membrane proteins among the drug targets is estimated to exceed 60%; their role in the discovery of new therapies is therefore crucial¹⁸⁵.

Yet, as of the start of 2020, only 4.1% of the protein structures in the Protein Data Bank (PDB) are membrane protein structures (rcsb.org, 16.01.2020). The reason for this discrepancy is most likely that membrane proteins are notoriously hard to purify and crystallise, which sparked the development of several new methods for protein stabilization¹⁸⁶. Conventional methods to increase the expression yield of the proteins and to improve their solubility are based on genetic modification of the protein itself. Either a soluble protein is fused to the protein of interest, or mutations are introduced on its surface to increase solubility. However, these can impede its native function¹⁸⁷. Consequently, methods for membrane protein stabilization without genetic modification have been developed¹⁸⁶.

1.3.1 Lipid bilayer nanodiscs

Lipid molecules with polar head groups tend to form aggregates which minimize their surface area in aqueous solvent. These aggregates form different shapes such as liposomes, vesicles and bicelles. Lipid bicelles can be stabilized in solution by an amphipathic protein¹⁸⁸.

In nature, such particles occur in the form of high-density lipoprotein (HDL), which is involved in reverse cholesterol transport (RCT), delivering cholesterol to the liver¹⁸⁹. Although more than 80 different proteins as well as several microRNAs are associated with HDL, the most abundant is apolipoprotein A-I (apo A-I)¹⁹⁰. The HDL particles containing apo A-I can take up cholesterol and free phospholipids and have been shown to ameliorate atherosclerosis by reducing plaque formation¹⁸⁹. At least eight different models of the structure of full length apo A-I have been published, all of which consist of α -helical domains interspersed with random coil sections. A consensus model of these has been proposed in which there are six helical domains in the monomeric protein: H1 (residues 8 - 35), H2 (residues 37 - 45), H3 (residues 54 - 64), H4 (residues 68 - 78), H5 (residues 81 - 115), and H6 (residues 148 - 179). The three main helices H1, H5, and H6 form a helical bundle and the rest of the protein forms random coil loops. It is suggested that this bundle can unpack to allow for the interaction with lipid molecules and dimerization¹⁹¹. This is in agreement with previous studies suggesting that several possible structures lead to a 'molten globule' behavior in solution¹⁸⁹.

A truncated version of apo A-I, called membrane scaffold protein 1 (MSP1), was created in order to enable the formation of lipoprotein particles *in vitro*. In this construct, the first 67 amino acids of apo A-I are removed¹⁹². This N-terminal region is assumed to stabilize the proteins lipid-free conformation¹⁸⁹. The remaining 200 amino acids, fused to a polyhistidine tag and factor X cleavage site, form the MSP1 construct (as shown in figure 1.3.1)¹⁹².

Apo A-I

MKAAVLT**LAV** LFLTGSQARH FWQQDEPPQS PWRVKDLAT VYVDVLKDSG RDYVSQFEGS ALGKQLN**LKL**
 LDNWD**SVTST** FSKLREQLGP VTQEFWDNLE KETEGLRQEM SKDLEEVKAK VQPYLDDFQK KWQEEMELYR
 QKVEPLRAEL QEGARQKLHE LQEKLSPLGE EMRDRARAHV DALRTHLAPY SDELQRQLAA RLEALKENGG
 ARLAEYHAKA TEHLSTLSEK AKPALEDLRQ GLLPVLESFK VSFLSALEEY TKKLNTQ

MSP1

MGHHHHHH**IE** GRLKLLDNWD SVTSTFSKLR EQLGPVTQEF WDNLEKETEG LRQEMSKDLE EVKAKVQPYL
 DDFQKKWQEE MELYRQKVEP LRAELQEGAR QKLHELQEKL SPLGEEMRDR ARAHVDALRT HLAPYSDEL
 QRLAARLEAL KENGGARLAE YHAKATEHLS TLSEKAKPAL EDLRQGLLPV LESFKVSFLS ALEEYTKKLN TQ

MSP1D1

MGHHHHHHHD YDIPTT**ENLY** FQGSTFSKLR EQLGPVTQEF WDNLEKETEG LRQEMSKDLE EVKAKVQPYL
 DDFQKKWQEE MELYRQKVEP LRAELQEGAR QKLHELQEKL SPLGEEMRDR ARAHVDALRT HLAPYSDEL
 QRLAARLEAL KENGGARLAE YHAKATEHLS TLSEKAKPAL EDLRQGLLPV LESFKVSFLS ALEEYTKKLN TQ

MSP1E3D1

MGHHHHHHHD YDIPTT**ENLY** FQGSTFSKLR EQLGPVTQEF WDNLEKETEG LRQEMSKDLE EVKAKVQPYL
 DDFQKKWQEE MELYRQKVEP LRAELQEGAR QKLHELQEKL SPLGEEMRDR ARAHVDALRT HLAPY**LDDFQ**
KKWQEEMELY RQKVEPLRAE LQEGARQKLH ELQEKLSPLG EEMRDRARAH VDALRTHLAP YSDELQRQLA
 ARLEALKENG GARLAEYHAK ATEHLSTLSE KAKPALEDLR QGLLPVLESF KVSFLSALEE YTKKLNTQ

Figure 1.3.1 | Amino acid sequences of the human Apo A-I (<http://www.uniprot.org/uniprot/P02647>, 29.12.2017) and the synthetic MSP1 proteins¹⁹². Purple - amino acids truncated in the MSP1, blue - added purification tag, red – factor Xa cleavage site, yellow - insert. Alpha-helices according to the consensus model¹⁹¹ are highlighted in grey.

Incubation of the MSP1 with phospholipids in the presence of a detergent at the right temperature leads to formation of lipid bilayer nanodiscs 10 nm in diameter. The structure of these nanodiscs corresponds to a ‘molecular belt model’, wherein two copies of MSP1 wrap around the rim of the discoidal lipid bilayer¹⁹³. A monodisperse nanodisc sample can be obtained when using the optimum ratio of MSP1 to phospholipid¹⁹².

Several versions of the MSP1 construct have been created (compare figure 1.3.1). In the MSP1D1, the His tag has been extended to 7 Histidines, the factor Xa cleavage site (IEGR) has been replaced with a TEV protease cleavage site (ENLYFQG) and the following 11 amino acids have been removed. A linker (DYDIPTT) has been inserted between the His-tag and the cleavage site¹⁹⁴. In addition, the MSP1D1E3 is elongated by 66 amino acids. The fragment 70 – 135 has been copied and inserted into the sequence after the template. In other variants this doubled fragment is 44 (MSPD1E2) or 22 (MSPD1E1) amino acids long¹⁹⁴.

Lipid bilayer nanodiscs are applied to reconstitute and analyse membrane proteins¹⁹³. These are difficult to solubilize due to the hydrophobic effect. Hydrophobic patches tend to come into contact, minimizing solvent exposure. This results in oligomerization and agglomeration, so that precipitates form. In order to avoid precipitation, these protein-protein interactions need to be disrupted using detergent. The use of detergent, however, usually also inhibits protein function¹⁸⁸. Therefore, in order to measure enzymatic activity of membrane proteins,

it is necessary to reconstitute them in a native-like environment. This can be provided by a lipid bicelle¹⁹⁵. The lipid bilayer nanodisc provides such a bicelle. The nanodiscs with embedded membrane protein are used for analysis techniques such as solution NMR, enzyme activity assays, isotope labeling, MALDI or fluorescence microscopy^{193,196}.

When observed by transmission electron microscopy, lipid bilayer nanodiscs appear as 'rouleaux'¹⁹⁷, fibers that are striped perpendicular to their longest dimension. The repeat distance of the stripes (5.9 nm) is equivalent to the diameter of a phospholipid bilayer and therefore leads to the conclusion that the rouleaux are stacks of nanodiscs on top of each other¹⁹⁷.

They can also be used to purify membrane proteins directly from homogenized cell membranes¹⁹⁸ and create membrane protein libraries¹⁹⁶. The cell membranes are treated with His-tagged MSP, so that the resulting nanodiscs can be purified by Ni-affinity chromatography¹⁹⁸. Further separation by SEC allows the isolation of individual proteins. These can then be identified by proteomic analysis after protease digest¹⁹⁶.

Nanodiscs have also been stabilized by polymers or created from them¹⁹⁹.

1.3.2 Polymer-based nanodiscs

The formation of nanodiscs from liposomes can also be induced by the addition of polymer, such as styrene maleic acid (SMA) copolymer. This led to the formation of Nanodiscs of 10 - 11 nm in diameter and could be used to stabilize the proteins *E. coli* Lipid A palmitoyltransferase PagP and *Halobacterium salinarum* bacteriorhodopsin (bR)²⁰⁰. These Styrene maleic acid lipid particles (SMALPs) can then be used for structure determination by Cryo-EM, as has been demonstrated with the *E. coli* secondary transporter AcrB¹⁸⁶. The hypercoiling amphiphilic styrene/maleic anhydride copolymer shields the hydrophobic domain of the protein along with surrounding lipid molecules from the aqueous solution, enabling the isolation of single, non-aggregated proteins.²⁰⁰

The drawback of SMALPs is the strong UV-absorbance of the Styrene moiety of the polymer. To avoid this, other polymers have been found which work in the same way. One of them is poly(diisobutylene-*alt*-maleic acid) (DIBMA) which forms Nanodiscs of 29 nm diameter with DMPC. They were shown to solubilize outer membrane phospholipase A (OmplA)²⁰¹. Another example are amphiphilic methacrylate random copolymers which have been found to form nanodiscs 17 nm in diameter and 5.5 nm thick when mixed with DMPC liposomes. However, they have not been used to embed a membrane protein²⁰².

It was also possible to create polymeric nanodiscs from monomers templated with lipid bicelles. Styrene-divinylbenzene copolymer was created by UV-induced free radical polymerization inside bicelles from DMPC and DHPC. The polymer nanodiscs were 20 nm in diameter at 4 nm height. However, no membrane protein was embedded inside them¹⁹⁹.

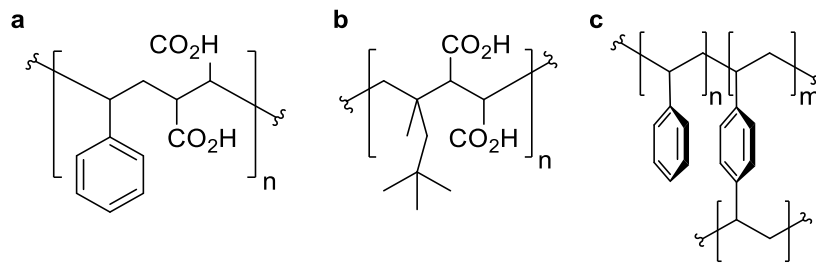


Fig 1.3.2 | Structure of the copolymers poly(styrene-*alt*-maleic acid) (SMALP) (a), poly(diisobutylene-*alt*-maleic acid) (DIBMA) (b), poly(styrene-1,4-divinylbenzene) (c).

1.3.3 Beta-strand peptides

The β -strand is the most basic structural motif formed by peptides. The main chain is nearly in a single plane; the residues are oriented perpendicular to the plane and point into alternating directions. Thus, two edges for hydrogen bonding and two faces shaped by the alternating residues are formed (compare fig 1.3.3)²⁰³.

In proteins, the β -strands often align with other β -strands running in the same or opposite direction, resulting in parallel, or anti-parallel β -sheets, respectively (see fig. 1.3.3)²⁰³. They are characterized by dihedral angles of $\phi = -119^\circ$ and $\psi = 113^\circ$ for the parallel β -sheet and $\phi = -139^\circ$ and $\psi = 135^\circ$ for the antiparallel β -sheet²⁰⁴.

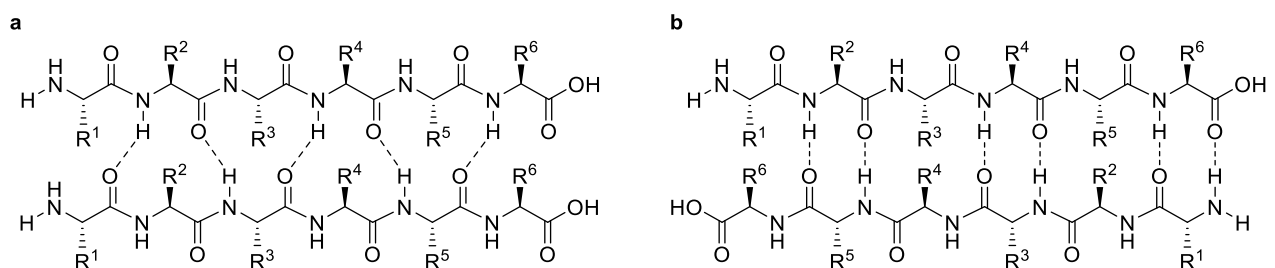


Fig. 1.3.3 | Parallel (a) and anti-parallel (b) β -sheets formed by two hexapeptides. The hydrogen bonding pattern results in 12-membered cycles in a parallel β -sheet and alternating 10- and 14-membered cycles in an anti-parallel β -sheet.

Beta-sheets assemble into crucial structural motifs like the β -barrel²⁰⁵, the β -propeller²⁰⁶, and the immunoglobulin fold²⁰⁷, which are found in many functional proteins.

However, also the highly ordered structures in misfolded proteins contain β -sheet motifs. β -strands assemble into so-called amyloid fibrils which run perpendicular to the strands²⁰⁸. In vivo, the amyloid fibrils form extracellular proteinaceous deposits (plaques) or intracellular inclusions, some, but not all of which are associated with diseases. Different proteins can aggregate to form these fibrils; the most studied examples being Amyloid β (Alzheimer's disease), the Prion protein (Spongiform encephalopathy), α -Synuclein (Parkinson's disease) and Tau (dementia)²⁰⁹.

In the development of new proteins and peptides, β -sheets play an essential role. β -strand structures can be used as scaffolds to design *de novo* proteins²¹⁰. It is desirable to develop these new protein structures to achieve selective binding of small molecules or to expand the chemical space of reactions that can be catalysed by enzymes²¹¹. Various peptides also make

use of the β -strand motif. Antimicrobial peptides are one example. They often adopt a cyclic β -hairpin conformation which enhances their stability²¹². Antimicrobial peptides are highly sought after due to the increasing incidence of antibiotic resistance in pathogenic bacteria²¹³. Another application are peptide hydrogels, which due to their biodegradability are especially suitable for biomedical applications²¹⁴, and amphiphilic peptides which serve as detergents²¹⁵.

Tao *et al.* designed a series of octapeptides (BP-1 through BP-3) with alternating hydrophobic and hydrophilic residues, resulting in amphiphilic molecules. The sequences also include a C-terminal amide, acetylation on the N-terminus, two octylglycine residues and one to three N-methylated amino acids (see fig. 1.3.4a-c)²¹⁶. N-methylation is known to limit the formation of insoluble aggregates and increase solubility of β -strand peptides by preventing the formation of some of the intermolecular hydrogen bonds²¹⁷. This strategy could even be used to create peptides which are able to disassemble amyloid fibrils. These highly soluble analogues of the Amyloid β protein core domain feature alternating N-methylated amino acids preventing their aggregation²¹⁸.

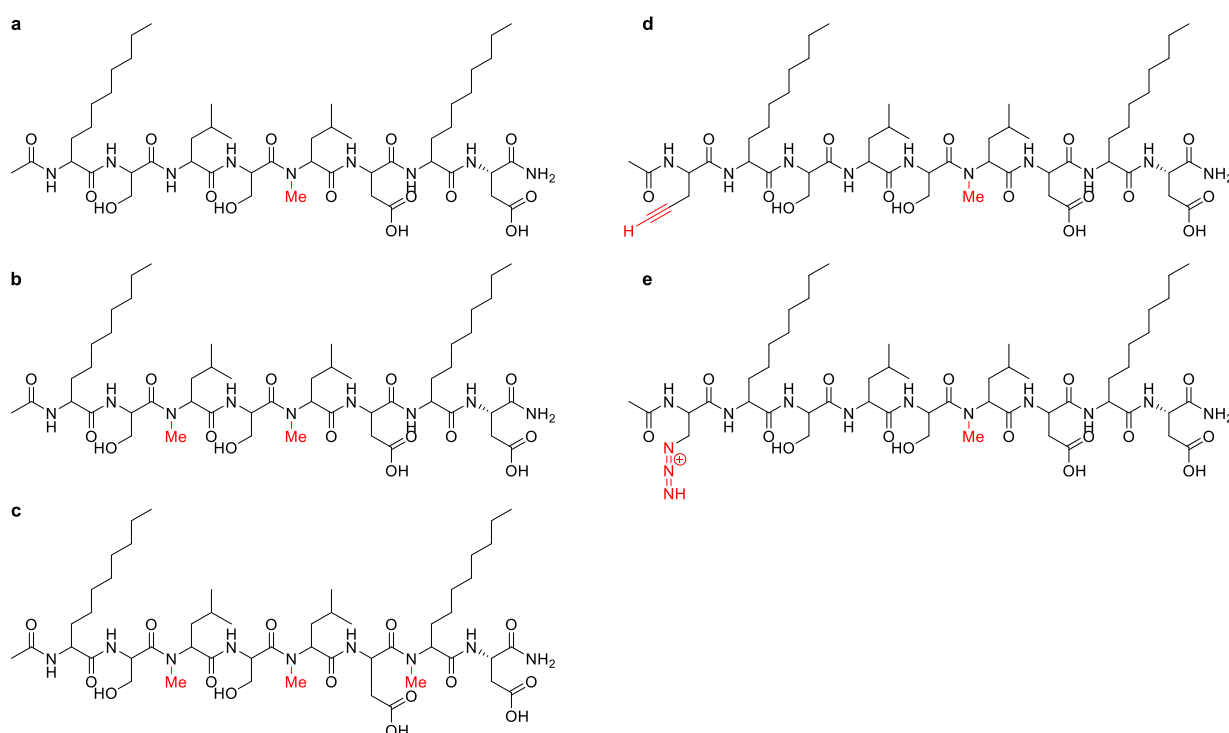


Fig. 1.3.4 | Structures of the β -strand peptides BP-1 (a), BP-2 (b) and BP-3 (c) and the modified peptides propargyl-BP-1 (d) and azido-BP-1 (e).

The peptides BP-1 to BP-3 stabilize membrane proteins in solution and thus serve the same function as the lipid-bilayer nanodiscs, with the mono-methylated variant BP-1 being the most effective²¹⁶. A molecular dynamics study suggested that the BP-1 peptide forms an anti-parallel β -sheet structure²¹⁹. The β -sheet is supposed to span the hydrophobic, transmembrane region of the IMP, thus stabilizing it in solution and preventing its aggregation²¹⁶. In 2018, Hoi *et al.* published modified versions of the BP-1 peptide, carrying additional non-natural amino acids at the N-terminus (propargyl-glycine or azido-alanine, fig. 1.3.4d-e). These were used as an immobilization tag for membrane proteins. The proteins stabilized with propargyl-BP-1 could be covalently bound on an azido-functionalized polysulfone surface, and the azido-BP-1 stabilized proteins could be covalently linked to an alkyne-functionalized glass surface using the well-established Cu-catalyzed click-reaction²¹⁹.

Thus, it is expected that other modifications of the BP-1 N-terminus or even C-terminus are possible, without impairing its membrane protein-stabilizing function.

1.3.4 The membrane protein Diacylglycerol kinase

Diacylglycerol kinase (DGK) from *E. coli* is a 121 amino acid integral membrane protein forming a homotrimer. Accordingly, it can be expressed and purified from *E. coli*, but a functional synthetic DGK has also been prepared by ligating three segments prepared by SPPS²²⁰. The enzyme transfers the γ -phosphate of adenosine triphosphate (ATP) to diacylglycerols and is therefore a promiscuous enzyme, accepting various hydroxyl lipids as substrate. The products are the corresponding phosphatidic acid and adenosine diphosphate (ADP)²²¹. The active site is also unusual as it is a composite or shared active site which consists of residues contributed by different monomers. This suggests that the enzyme is only active when the trimer is fully assembled²²².

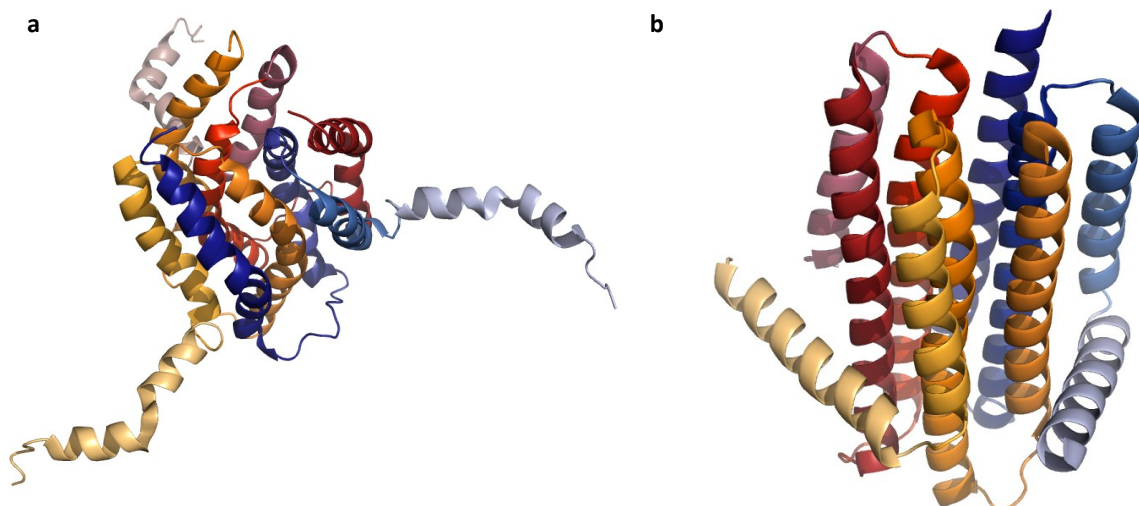


Fig. 1.3.5 | Structures of diacylglycerol kinase from NMR spectroscopy, PDB ID 3ZE4, (a) and X-ray crystallography data, PDB ID 2KDC, (b). The three monomers are coloured in blue, orange, and red. Different helices are different shades of the respective colour. In the NMR structure, the helices from different monomers are interspersed with one another, which is not the case in the X-ray structure.

Each monomer of the enzyme features three transmembrane helices²²¹. The crystal structure shows an additional N-terminal helical domain (residues 7-27). It places the transmembrane helices at the positions 29 – 47 (H1), 52 - 82 (H2) and 88 – 119 (H3)²²². The core of the structure is formed by a three-helix bundle formed by the H2 helices of all three copies of the protein. The active site of the enzyme is located between the transmembrane helices at the interface of the membrane with the cytoplasm²²². This is expected because the hydrophilic substrate ATP needs to contact the hydrophilic substrate diacylglycerol. In the crystal structure, the active site is formed by residues from the helices 1-3 of the same monomer (compare fig. 1.3.5b) and the N-terminal helix of another²²². There is a discrepancy between the structures that result from solution NMR and from X-ray-crystallography. The order of helices forming the core structure is different in the NMR structure (domain swapping), resulting in an altered quaternary structure (see fig. 1.3.5a), even though the secondary structure is almost identical for both. A possible explanation is that there are several conformations in which the enzyme is active^{222,223}. In both structures, however, the active site is a composite formed by two monomers²²².

The enzyme has therefore been used as a model protein for the folding of membrane proteins. It was shown that it can insert into preformed lipid vesicles²²⁴, and that it is active when reconstituted in lipid bilayer bicelles but not in micelles²²⁵.

Aims of this work

2.1 Polyphenol-conjugated R5 silica nanoparticles for targeted delivery

Biomimetic silica particles are biocompatible vehicles²⁹ and can be reversibly loaded with sensitive cargo molecules, for example via adsorption. A covalent conjugate of the cargo and a silica-precipitating moiety, such as the R5 peptide, increases the efficiency of this loading process. Particle preparation is thus possible using just one equivalent of the silica-precipitating peptide. Triggered release can be achieved by using disulfide bonds in the construct. A reducing environment or pH shifts can be the trigger⁵⁵. This constitutes a facile method for cargo immobilization and delivery.

Polyphenols are an important class of plant secondary metabolites present in a variety of foods. From this group, especially the flavonoids feature diverse pharmacological activities, among them antioxidant, antibacterial, anti-inflammatory²²⁶, and glycaemia-lowering²²⁷.

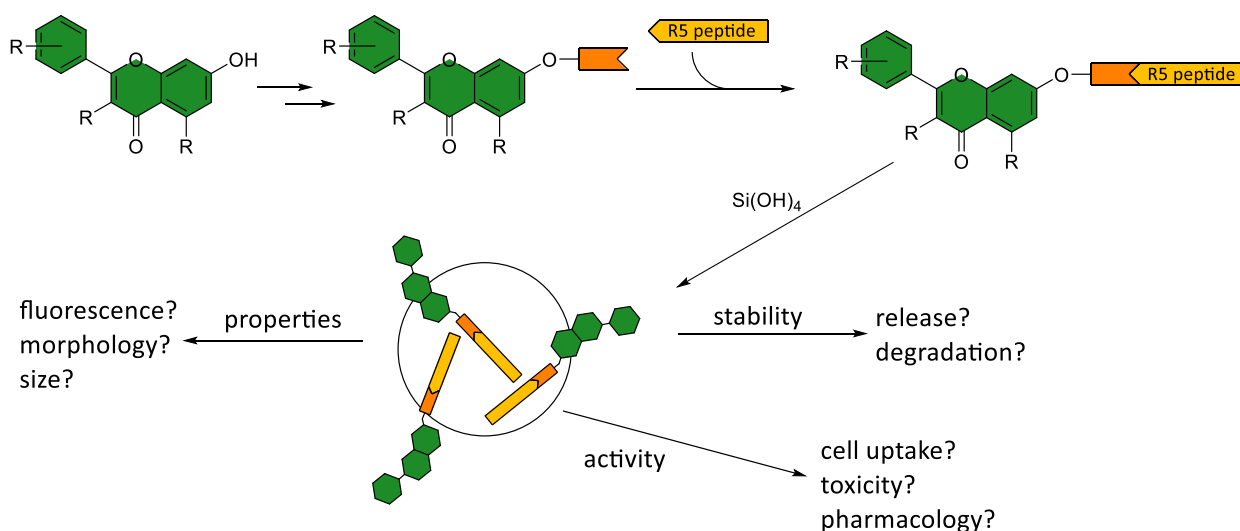


Fig. 2.1 | Schematic representation of the polyphenol-conjugated R5 silica nanoparticles. The polyphenol molecule is shown in green. Via a linker (orange) it will be attached to the silica-precipitating R5 peptide. The conjugate will be tested for silica particle generation and the particles for their properties, stability, and pharmacological activity.

Accordingly, the aim of this part of the work was to deliver these food ingredients into the cell using the biomimetic silica particles. Conjugates of the flavonoids and the R5 peptide will be created (compare fig. 2.1). The constructs will be tested for their silica-precipitating activity and the morphologies of the resulting particles characterized. Cell assays will then be performed to elucidate the pharmacological activities of the flavonoids when immobilized on a silica particle and the cell uptake of these particles. Questions to answer are if and how the

conjugation affects the silica-particle formation, how the biodistribution of the resulting particles is different from that of the regular R5 silica particles and from the polyphenol used, and if and how the cells are affected by the modified particles.

2.2 Silica-stabilized nanodiscs

Membrane proteins are ubiquitous in nature and present a major fraction of drug targets¹⁸⁵. They have various functions which are not limited to transport, but also include receptors such as G-protein coupled receptors (GPCRs)²²⁸ and other enzymes with various activities²²⁹. Enzymes are very efficient catalysts but tend to denature and lose activity under harsh conditions which are needed for large scale syntheses of compounds for example for the pharmaceutical industry. Encapsulation of the enzymes in a solid matrix can help to increase their stability and recyclability¹⁰⁵. Thus, a system for facile encapsulation of membrane proteins in silica is desirable.

Previous work on biomimetic silica particles prepared via precipitation with the R5 peptide showed that not only small cargo, but entire proteins can be encapsulated in the particles. The most efficient way to employ the R5 peptide is to use it as a fusion tag on the protein of interest (POI), so that only one equivalent per POI molecule is needed²³⁰. To enable the immobilisation without genetic modification silica-precipitating peptides which bind POI molecules are needed, especially to immobilise integral membrane proteins (IMPs).

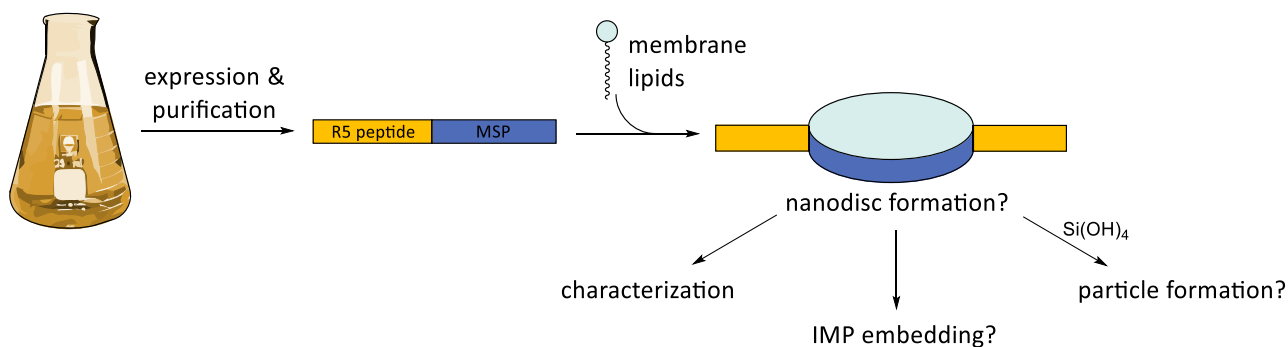


Fig. 2.2 | Schematic representation of silica-stabilized nanodiscs. New variants of the membrane scaffold protein (MSP), shown in blue, will be used to create nanodiscs, which will need to be characterized, tested for particle formation, and embedding of membrane proteins.

Nanodiscs are protein-stabilized lipid bicelles, which are used in the purification¹⁹⁸, stabilization and structure determination of membrane proteins²³¹ and mimic their natural environment. They are created from the amphiphilic membrane scaffold protein (MSP) and phospholipids¹⁹². The aim of the second part of the work was to create new variants of the MSP fused with a silica-precipitating tag for the creation of silica-stabilized nanodiscs (see fig. 2.2). How the modifications affect the formation of nanodiscs will need to be evaluated. Also, if the resulting constructs retain the potential to form silica particles and what structures result from this.

2.3 Modified amphiphilic BP-1 peptides for the direct encapsulation of membrane proteins in silica

To enable the reconstitution of IMPs in the absence of lipids, an amphiphilic peptide was developed which directly interacts with the protein. This BP-1 peptide has been used to stabilise the *E. coli* ABC exporter MsbA in solution²¹⁶. Hoi and colleagues have used an N-terminally modified version of BP-1 to immobilize reconstituted *E. coli* aquaporin Z (AqpZ) on a functionalized surface by means of a simple click-reaction²¹⁹. Further variants of this peptide could enable the facile immobilization of membrane proteins in silica particles.

Accordingly, the third aim of this work is to develop a modified BP-1 peptide to allow reconstitution of membrane proteins and subsequent encapsulation in silica particles (see fig. 2.3). Two different silica-precipitating tags are used for this purpose: the full-length R5 peptide from the diatom *Cylindrotheca fusiformis*, and its five N-terminal amino acids KRRIL. The model membrane enzyme diacylglycerol kinase (DGK) will then be tested with the new peptide variants with the aim to create active silica particles. It will be investigated how the modifications affect the peptide structure, if they are able to form silica particles, and what morphologies they feature. Finally, the potential to stabilize and encapsulate membrane proteins will be tested and what the influence is on the activity and stability of the encapsulated protein.

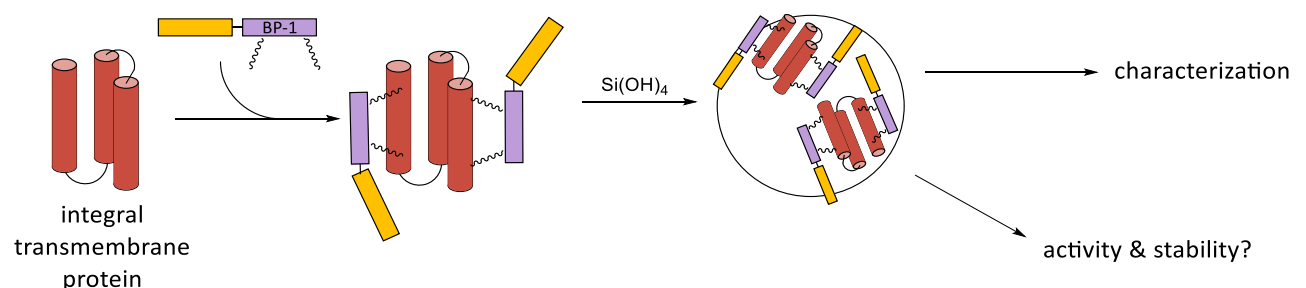


Fig. 2.3 | Schematic representation of modified BP-1 peptides, which can be directly used for the encapsulation of membrane proteins. It will need to be investigated if this encapsulation is possible and what the influence is on the activity and stability of the protein.

Part 3

Materials and Methods

3.1 Materials

3.1.1 Water

A Milli-Q Reference A+ water purification system by Merck GmbH (Vienna, Austria) was used to further purify water deionised with a Professional G7895 Aqua Purificator by Miele GmbH (Salzburg, Austria).

3.1.2 Chemicals

Solvents were obtained from VWR International LLC (Vienna, Austria) in HPLC grade or peptide synthesis grade. Resins were obtained from Iris Biotech (Marktredwitz, Germany) and Novabiochem by Merck GmbH (Vienna, Austria). Fmoc-protected amino acids were obtained from Alfa Aesar by Thermo Fisher Scientific GmbH (Vienna, Austria). Lipids were obtained from Avanti Polar Lipids, Inc. (Alabaster, USA). *Streptomyces griseus* Pronase E was obtained from F. Hoffmann-La Roche AG (Vienna, Austria). All other chemicals were obtained from Sigma-Aldrich by Merck GmbH (Vienna, Austria) unless otherwise specified.

3.1.3 Cloning

Restriction enzymes, buffers and markers were obtained from New England Biolabs GmbH (Frankfurt am Main, Germany). Gel extraction kits were obtained from Invitrogen by Thermo Fisher Scientific GmbH (Vienna, Austria). Plasmid extraction was performed using the GeneJET Plasmid Miniprep Kit also from Thermo Fisher Scientific GmbH (Vienna, Austria).

3.1.4 Protein expression

n-Octyl- β -D-glucoside (OG) and n-dodecyl- β -D-maltoside (DDM) were obtained from Gerbu Biotechnik GmbH (Heidelberg, Germany). Ingredients for media were obtained from AppliChem (Darmstadt, Germany) in microbiology grade. Spectrapor dialysis membranes were obtained from Spectrum Chemical Mfg. Corp. (New Brunswick, USA). Spin filters were Amicon Ultra Centrifugal Filters by Merck GmbH (Vienna, Austria). Zeba Spin Desalting Columns were obtained from Thermo Fisher Scientific GmbH (Vienna, Austria). The LMW-SDS marker kit was from GE Healthcare (Vienna, Austria).

3.1.5 Live cell imaging

HT-29 human colorectal adenocarcinoma cells were obtained from ATCC (Manassas, USA). The culture medium and supplements used were obtained from GIBCO Invitrogen (Karlsruhe, Germany) and Sigma-Aldrich by Merck GmbH (Vienna, Austria).

3.1.6 Electron microscopy

Carbon film coated copper grids (200 mesh) were obtained from Plano GmbH (Marburg, Germany). SEM samples were spotted onto 13 mm Nunc Thermanox cell culture cover slips from Thermo Fisher Scientific GmbH (Vienna, Austria).

3.2 Instrumentation

3.2.1 Peptide Synthesis

Automated Fmoc-SPPS was performed on a Liberty Blue Microwave Peptide Synthesizer equipped with a HT12 Resin Loader Upgrade, both by CEM GmbH (Kamp-Lintfort, Germany) or on a Tribute Peptide Synthesizer by Protein Technologies, Inc. (Manchester, U. K.). A Sonorex RK 100 ultrasonic bath by Bandelin electronic GmbH & Co. KG (Berlin, Germany) was used for dissolving precipitated peptides.

3.2.2 Protein Expression and purification

Media were autoclaved in a Varioklav by HP Labortechnik GmbH (Oberschleißheim, Germany) or a La-MCS by SANOclav (Bad Überkingen, Germany). Cultures were incubated in a Multitron Standard System by Infors HT (Einsbach, Germany). For small-scale incubations either a TS-100 Thermo-Shaker by BioSan (Riga, Latvia) or a Thermomixer comfort by Eppendorf AG (Vienna, Austria) was used. Lysis was performed on a CF1 cell disrupter by Constant Systems Ltd. (Daventry, U. K.) equipped with an RC-10 Digital Chiller by VWR International LLC (Vienna, Austria). Affinity chromatography was performed on a ÄKTAprime plus LC system by GE Healthcare (Vienna, Austria). Ni-affinity columns were HisTrap High Performance also by GE Healthcare (Vienna, Austria).

3.2.3 Centrifugation

Table-top centrifuges were the models 5418 by Eppendorf Austria GmbH (Vienna, Austria), Microfuge 22R and Allegra X-30R by Beckman Coulter GmbH (Vienna, Austria), and 3-16PK by Sigma Laborzentrifugen GmbH (Osterode, Germany). Large-scale centrifugations were performed on an Avanti J-26 XP by Beckman-Coulter GmbH (Vienna, Austria).

3.2.4 Electrophoresis

SDS-PAGE and western blots were performed on a Mini-PROTEAN Tetra cell system by Bio-Rad GmbH (Vienna, Austria) and a Semi dry blotter Mini by Carl Roth GmbH & Co. KG (Karlsruhe, Germany). Pictures of protein gels, agarose gels and blots were taken on a ChemiDoc MP Imaging System also by Bio-Rad GmbH (Vienna, Austria). For Agarose Gel Electrophoresis the model 40-0708 by Peqlab Biotechnologie GmbH (Erlangen, Germany) was used.

3.2.5 Spectroscopy

UV-vis spectra were collected on a NanoDrop 2000c spectrophotometer by Thermo Fisher Scientific GmbH (Vienna, Austria). Micro UV-cuvettes were obtained from Brand GmbH & Co. KG (Wertheim, Germany). Fluorescence spectra were collected on a FluoroMax-4 Spectrofluorometer by Horiba GmbH (Tulln, Austria). Circular Dichroism (CD) spectra were collected on a Chirascan plus instrument by Applied Photophysics Ltd. (Leatherhead, U. K.), equipped with a TC 125 Temperature control unit by Quantum Northwest, Inc. (Liberty Lake, USA).

3.2.6 Confocal fluorescence microscopy

Live cell imaging was performed using a LSM 710 ELYRA PS.1 microscope by Carl Zeiss AG (Oberkochen, Germany). Objectives were Plan Apochromat 63X/1.4 and Plan-Apochromat 63x/1.0.

3.2.7 Electron microscopy

Scanning electron microscopy was performed at 5 kV acceleration voltage on a Supra 55 VP by Carl Zeiss AG (Oberkochen, Germany) equipped with an EDX detector after sputter coating the samples with 5 nm gold using an EM QSG 100 by Leica Camera AG (Wetzlar, Germany). Transmission electron microscopy was performed at 20 kV acceleration voltage on a CM200 system by Philips GmbH (Vienna, Austria) equipped with an Orius SC600 CCD camera by Gatan GmbH (Munich, Germany).

3.2.8 Atomic force microscopy

Atomic force micrographs were recorded on a Park NX10 by Park Systems Corp. (Suwon, South Korea) using a silicon tip with a nominal radius below 10 nm operating in tapping mode.

3.2.9 Preparative and analytical High-performance liquid chromatography

Preparative RP-HPLC was carried out either on a ProStar system by Varian, Inc., now Agilent Technologies (Santa Clara, USA) or an Open Architecture HPLC System with a 2767 Sample Manager, a 2545 Binary-Gradient Module with a 515 HPLC Pump, a SFO System Fluid Organizer, a 2489 UV/Visible Detector, and a 3100 Mass Detector by Waters S. A. S. (Saint-Quentin, France).

For analytical HPLC-MS, either the Open Architecture HPLC System by Waters S. A. S. (Saint-Quentin, France), or an UltiMate 3000 HPLC system equipped with a MSQ Plus mass spectrometer by Thermo Fisher Scientific GmbH (Vienna, Austria) was used.

The columns were of the Kromasil brand by Nouryon (Amsterdam, the Netherlands), formerly AkzoNobel N. V. The column dimensions were 250 x 21.2 mm for prep columns, 250 x 10 mm for semiprep columns, and 150 x 4.6 mm for analytical columns. The material had pores of 300 Å and the particles size was 10 µm for the prep columns and 5 µm for semiprep and analytical size.

3.3 Buffers and expression media

3.3.1 Protein expression

Agar plates

- 10 g/l tryptone
- 5 g/l yeast extract
- 10 g/l NaCl
- 15 g/l agar
- antibiotic (100 µg/ml ampicillin, 100 µg/ml chloramphenicol, 30 µg/ml kanamycin)

LB medium

- 10g/l sodium chloride, pH 7
- 10 g/l tryptone
- 5 g/l yeast extract
- antibiotic (100 µg/ml ampicillin, 100 µg/ml chloramphenicol, 30 µg/ml kanamycin)

3.3.2 Gel electrophoresis and western blot

1 x Lämmli buffer (SDS-PAGE running buffer)

- 25 mM Tris
- 0.2 M glycine
- 0.1% (w/v) SDS

2 x SDS sample loading buffer

- 500 mM Tris-HCl, pH 6.8
- 6% (w/v) SDS
- 35% (v/v) glycerin
- 3.55% (v/v) β-mercaptoethanol
- 0.05% (w/v) bromophenol blue

Coomassie-Staining Solution

- 0.1% (w/v) Coomassie R250
- 10% (v/v) Acetic acid
- 45% (v/v) methanol

Destaining solution

- 10% (v/v) Acetic acid
- 40% (v/v) methanol in water

TAE buffer

- 50 mM Tris-acetic acid, pH 8.0
- 1 mM EDTA

3.3.3 Protein Purification

MSP Lysis buffer

- 20 mM NaH₂PO₄-NaOH, pH 7.4
- 1 mM PMSF
- 1% Triton-X100

MSP Equilibration buffer

- 20 mM NaH₂PO₄-NaOH, pH 7.4
- 1% Triton-X100

MSP Washing buffer 1

- 40 mM Tris-HCl, pH 8.0
- 0.3 M NaCl
- 1% Triton

MSP Washing buffer 2

- 40 mM Tris-HCl, pH 8.0
- 0.3 M NaCl
- 50 mM sodium cholate

MSP Washing buffer 3

- 40 mM Tris-HCl, pH 8.0
- 0.3 M NaCl

MSP Elution buffer

- 40 mM Tris-HCl, pH 8.0
- 0.3 M NaCl
- 0.3 M imidazole

DGK Solubilization buffer

- 50 mM sodium phosphate-HCl, pH 7.5
- 300 mM NaCl
- 1 mM phenylmethylsulfonyl fluoride (PMSF)
- 3% n-octyl- β -d-glucoside (OG)

DGK Equilibration buffer

- 50 mM sodium phosphate-HCl, pH 7.5
- 300 mM NaCl

DGK Washing buffer

- 50 mM sodium phosphate-HCl, pH 8
- 300 mM NaCl
- 250 mM imidazole

DGK elution buffer

- 50 mM sodium phosphate-HCl, pH 8
- 300 mM NaCl
- 250 mM imidazole
- 0.5% n-dodecyl β -D-maltoside (DDM)

DGK dialysis buffer

- 50 mM sodium phosphate-HCl pH 8
- 300 mM NaCl

3.3.4 Microscopy

TEM negative staining solution

- 1% phosphotungstic acid-NaOH, pH 7.2

3.3.5 Circular dichroism

CD buffer

- 100 mM Tris-HCl, pH 7.35
- 40 mM NaCl

3.4 Methods

3.4.1 Manual SPPS

Peptides were synthesized using Fmoc protected amino acids with the side-chain protecting groups Arg(Pbf), Lys(Boc), Ser(tBu), and Tyr(tBu) on a polystyrene resin with the Wang (p-alkoxybenzyl alcohol)²³² linker or a Rink amide AM resin (100 - 200 mesh) at a scale between 0.05 mmol to 0.2 mmol. In addition, the non-canonical amino acids Fmoc-(N-met)Leu-OH and Fmoc-(Octyl)Gly-OH were used.

The resin was swollen in DMF for at least 60 min, then the following steps were performed to extend the peptide by one amino acid. During each deprotection, coupling, and cleaving step, the resin was agitated by turning the syringe on a wheel.

For deprotection, DMF was drained and the resin was suspended in a solution of 20% piperidine in DMF. The solution was replaced after 5 min and the resin rotated for another 25 min before washing it five times with DMF.

Before coupling, the Fmoc-protected amino acid was first activated by dissolving 2.5 equivalents in a 0.5 M solution of HBTU (2.38 eq.) and 2.5 equivalents of DIPEA were added. After 3 min incubation, it was added to the resin and rotated for 15 min. Afterwards the solution was removed, and the resin washed 5 times with DMF.

N-terminal acetylation was performed by incubating the resin-bound peptide with a 3:2:1 mixture of DMF, pyridine, and acetic anhydride. 12 ml of this acetylation mixture were used per 100 μ mol of peptide. The reaction was carried out for 60 min, exchanging the solution after 30 min.

A test cleavage and LC-MS analysis was performed to confirm the peptide's molecular weight before continuing with cleavage or conjugation of the modified polyphenols.

3.4.2 Kaiser Test

Successful deprotection and coupling was confirmed using the method described by Kaiser *et al.*²³³. Two glass tubes were prepared. One empty (blank) and one with a few grains of resin. To both tubes were added 30 μ l of phenol solution (80% phenol in ethanol), 50 μ l of KCN solution (0.2 mM KCN in pyridine) and 30 μ l of ninhydrin solution (6% ninhydrin in ethanol). The tubes were incubated at 100 °C for 5 min. In the absence of free amines both solutions show a yellowish colour, resin beads remain colourless. In contrast, blue beads and a purple or green solution in the test tube with the resin indicate successful deprotection and the presence of free primary amino groups. If the N-terminal amino acid is proline, the result is an orange colour, which can be distinguished by comparison with the blank.

3.4.3 Automated SPPS

Alternatively, synthesis of the R5 peptide was performed using the Liberty Blue Microwave Peptide Synthesizer by CEM GmbH (Kamp-Lintfort, Germany) on a scale from 0.05 mmol to 0.15 mmol. In addition to the aforementioned Fmoc-protected amino acids, the pseudo-proline dipeptide Fmoc-Gly-Ser(Ψ Me,Mepro)-OH was used at suitable positions in the

sequence, as described previously^{234,235}. The peptide was deprotected with 20% piperidine in DMF and the Fmoc-amino acids (5 eq.) were activated with 5 equivalents of ethyl cyanohydroxyiminoacetate (oxyma) and five equivalents DIC.

3.4.4 Coupling of R5 peptide and modified polyphenols

Quercetin-R5

611 mg (95.8 μmol) of resin-bound deprotected R5 peptide were swollen in DMF for 60 min. 29 mg (189 μmol , 1.97 eq.) HOBt hydrate were dissolved in 2 ml DMF. 72.5 mg (201 μmol , 2.10 eq.) 2-((2-(3,4-dihydroxyphenyl)-3,5-dihydroxy-4-oxo-4H-chromen-7-yl)oxy)acetic acid were dissolved in 2 ml DMF and added to this solution. 30.7 μl (24.7 mg, 196 μmol , 2.04 eq.) DIC were added, the mixture was vortexed and incubated for 30 s before adding it to the resin, which was then rotated in the dark for 16 h. The coupling solution was drained, and the resin washed 5 times with DMF and 5 times with DCM before drying it overnight in the desiccator.

Galangin-R5

37.4 mg (5 μmol , 1 eq.) of resin-bound deprotected R5 peptide were swollen in DMF for 60 min. 4.1 mg (12.5 μmol , 2.5 eq.) of the modified galangin in DMSO (500 μl) were activated by adding 1.6 μl of DIC and 1.3 mg (10 μmol , 2 eq.) HOBt in 500 μl DMF. This reaction mixture was added to the resin, which was rotated in the dark for 16 h. The reaction solution was then removed from the resin and it was washed 3 times with DMF, then 5 times with DCM before drying it in the desiccator.

3.4.5 Cleavage of peptides from resin

After the final deprotection or coupling the modified polyphenol, the peptide-loaded resin was washed five times with DMF, then five times with DCM, then dried in the desiccator overnight. To cleave the peptide from the resin, it was rotated in 40 ml/mmol cleaving solution (92.5% TFA, 5% TIS, 2.5% water) for 3 h at room temperature. The cleavage solution was filtered into five times its volume of cold diethyl ether and vortexed. For complete precipitation, the mixture was incubated at $-20\text{ }^{\circ}\text{C}$ for 60 min, then the mixture was centrifuged at 5,500 rpm for 5 min. The recovered pellet was washed 3 times with diethyl ether and then dried in an argon stream. Before purification, the pellets were then redissolved in a mixture of water and ACN using the sonicator, flash frozen in liquid nitrogen, and lyophilized.

3.4.6 Preparative reversed-phase HPLC for peptide purification

Peptides and peptide conjugates were purified using reversed-phase HPLC. After lyophilizing, the crude peptide (up to 100 mg per batch) was dissolved in 10 ml guanidinium chloride buffer (6 M GuHCl, 50 mM Tris-HCl pH 7.5). The solution was filtered through a 20 μm syringe filter, then loaded onto a Kromasil C4 prep column at 95% eluent A (0.01% TFA in water) and 5% eluent B (0.08% TFA in acetonitrile). Products were eluted using a suitable gradient of eluent B in eluent A. The obtained fractions were analysed by MS and those containing the desired product were pooled and lyophilized.

3.4.7 Absorbance and emission spectra

Spectra were recorded in 50 mM potassium phosphate buffer (pH 7). Absorbance was measured using a Thermo Scientific NanoDrop 2000c spectrophotometer. Excitation and emission spectra were measured using a Horiba Scientific FluoroMax-4 spectrofluorometer with 5 nm slit width.

3.4.8 Synthesis of silica nanoparticles

Silica particles were precipitated from a 1 mg/ml solution of the silica-precipitating peptide in 50 mM potassium phosphate buffer at pH 7. Concentration was determined either by weighing the lyophilized peptide or, in case of the Quercetin-R5, using the absorption coefficient of quercetin ($\epsilon_{375} = 11806 \text{ M}^{-1} \text{ cm}^{-1}$)²³⁶. This solution was then incubated overnight at room temperature in the absence of light. A silicic acid solution was created by adding 40 μl of TMOS to 960 μl of 1 mM HCl, vortexing, then incubating the mixture for 4 min. Of this silicic acid solution, 10 μl were added to a 90 μl aliquot of the peptide solution. The mixture was vortexed and incubated for 30 min at room temperature in the absence of light. It was then centrifuged at 14,000 rpm for 5 min. After removing the supernatant, the particles were washed with water and the particles dried at reduced pressure.

In order to obtain fluorescent galangin-R5 silica particles, a fluorescein-derived molecule, ce386, was used, which contains a siloxane moiety that is incorporated into the silica structure after hydrolysis. 10 μl of a solution of 0.1 mg ce386 in 250 μl of 100 mM pH 9 phosphate buffer (pre-incubated for 3 h) was added to the precipitation mixture in addition to the silicic acid according to the method published by Ciccione *et al.*²³⁷.

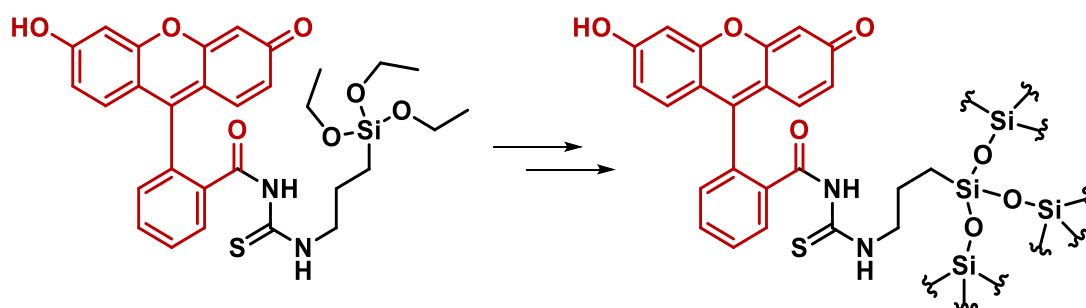


Fig. 3.4.1 | Structure of ce386 with the fluorescein moiety marked in red. After hydrolysis, it is incorporated into the silica structure.

3.4.9 Release of quercetin

Particles were created from 250 μl of a quercetin-R5 conjugate solution as described above. After removing the supernatant, 250 μl potassium phosphate buffer of either pH 4 or pH 7 was added. The particles were carefully resuspended by pipetting up and down and vortexed carefully. They were then incubated at room temperature in the absence of light. Every 60 min, spectra were taken of the supernatant as follows:

- The sample was centrifuged at 14,000 g for 5 min.
- 100 μl of the supernatant were taken out, a UV-vis spectrum was measured and the solution put back onto the particles
- The sample was resuspended using a pipette, then vortexed shortly to ensure even distribution of the particles

This was repeated until 10 h incubation. Concentration of the conjugate was calculated from the extinction coefficient of quercetin at 375 nm $\epsilon_{375} = 11,806 \text{ M}^{-1} \text{ cm}^{-1}$ ²³⁶.

3.4.10 Live cell fluorescence imaging

Silica particle uptake of HT-29 human colorectal adenocarcinoma cells was monitored by incubating them in a suspension of particles. Particles were precipitated as described above from 500 μl of a 1 mg/ml solution of the peptide or peptide conjugate. When the R5 peptide or the galangin-R5 conjugate were used, particles were additionally stained with ce386 as described above. After washing and drying, they were resuspended in 1 ml live cell imaging solution. From this suspension a volume corresponding to half the volume of the cell culture medium was added to the cells in a well plate, which were stained with CellMask Deep Red Plasma Membrane Stain (white) and LysoTracker Red DND-99 (red). They were incubated in humidified incubators with 5% CO_2 at 37 °C for 3 h and imaged every 60 min.

3.4.11 Transformation of bacteria

To transform *E. coli* strains with the different plasmids, a fresh aliquot of 100 μl chemically competent bacteria (10 mM HEPES-HCl, pH 7.0, 10 mM RbCl, 75 mM CaCl_2 , 15% (v/v) glycerol), stored at -80 °C, was thawed on ice. 1 μl of aqueous solution of the plasmid (>100 ng/ μl concentration) was added and carefully mixed in by pipetting up and down. The mixture was then incubated on ice for 15 min, before heating it to 42 °C for 90 s. 1 ml of LB medium (10 g/l tryptone, 10 g/l NaCl, 5 g/l yeast extract), pre-heated to 37 °C, was then immediately added and the mixture transferred to a thermo shaker for 1 h at 37 °C and 600 rpm. Of this culture, 200 μl were plated onto a LB-Agar plate with antibiotic, pre-heated to 37 °C. The rest of the suspension was centrifuged at 8,000 rpm for 2 min using a table-top centrifuge. 600 μl were discarded and the pellet resuspended in the remaining supernatant. Of this suspension, 200 μl were plated onto a second LB-agar plate. The plates were incubated at 37 °C for approximately 16 h. Glycerol stocks for further usage of the bacteria were made in the following way: 4 ml of LB medium with antibiotic in a 20 ml test tube were inoculated with a colony picked from the respective plate and incubated at 37 °C and 210 rpm for approximately 16 h. 500 μl of this culture were mixed with 500 μl of a 40 % solution of glycerol and frozen at -80 °C in a sterile glass vial.

3.4.12 Plasmid preparation

4 ml of LB medium with the suitable antibiotics in a 20 ml test tube were inoculated with a colony picked from the respective plate and incubated at 37 °C and 210 rpm for approximately 16 h. The bacteria were then pelleted by centrifugation at 8,000 rpm for 5 min. The pellet was resuspended, and the plasmid isolated using a Plasmid Miniprep Kit according to the specifications of the manufacturer.

3.4.13 DNA digests

Test digests were performed on a 20 μ l scale, using:

- 12 μ l H₂O
- 4 μ l purified plasmid (> 100 ng/ μ l)
- 2 μ l 10x buffer (CutSmart)
- 1 μ l restriction endonuclease 1
- 1 μ l restriction endonuclease 2.

The reactants were mixed carefully with a pipette, then incubated for 1 h at 37 °C.

Preparative digests were performed on a 50 μ l scale, using:

- 21 μ l H₂O
- 20 μ l purified plasmid (> 100 ng/ μ l)
- 5 μ l 10x buffer
- 2 μ l restriction endonuclease 1
- 2 μ l restriction endonuclease 2.

The reaction was performed for 2 h at 37 °C. The backbone into which the insert was ligated was then also dephosphorylated by adding 1 μ l of rSAP and allowing the reaction to proceed at 37 °C for a further 15 min. The phosphatase was then inactivated for 5 min at 65 °C.

3.4.14 Agarose gel electrophoresis

DNA gel electrophoresis was performed using 1.2% agarose gels. At analytical scale, 4 μ l of 6x purple loading dye were added to the 20 μ l digestion product before loading it onto the gel next to 2 μ l of a GeneRuler 1kbp plus DNA ladder. The gel was run for 70 min at 80 V in TAE running buffer, then stained with a 0.5 μ g/ml ethidium bromide solution for 15 min.

Preparative DNA electrophoresis was performed by adding 10 μ l 6x purple loading dye to 50 μ l digestion mixture before loading it next to 2 μ l of a GeneRuler 1kbp plus DNA ladder. The gel was run at 80 V for 70 min in TAE running buffer. The gel was then stained in 50 ml of a 0.1% methylene blue solution for 5 min before destaining it in water for 1 h. Bands were cut out with a scalpel and cut into small cubes before extracting the DNA with a gel extraction kit according to protocol.

3.4.15 DNA ligation

Ligations were performed in 20 μ l volume using 50 ng of the backbone plasmid and 150 ng of the insert. 1 μ l of T4 Ligase and 2 μ l of 10 x T4 Ligase buffer were added and the remaining volume filled up with water. Ligation was allowed to proceed for 2 h at 37 °C.

3.4.16 Expression and purification of MSP constructs

Protein expression and purification was performed as described by Sligar *et al.*¹⁹². The MSP constructs were expressed in *E. coli* BL21 (DE3) Rosetta 2 transformed with the expression plasmid pET 28a containing the desired insert. A 200 ml LB culture inoculated with the bacteria was grown overnight at 37 °C and 200 rpm and the resulting OD₆₀₀ was measured. To a 2 l culture of LB medium was then added a volume of the pre-culture to reach a starting OD₆₀₀ of 0.1. The expression culture was then grown at 37 °C and 180 rpm to OD₆₀₀ = 0.6 - 0.9 before induction with IPTG to a final concentration of 1 mM. After induction, the culture was incubated at 37 °C for another 3 h. It was then centrifuged at 6000 rpm (11978 g) for 25 min

to harvest the bacteria. The pellet was resuspended in 40 ml of MSP lysis buffer and the bacteria lysed using a cell disrupter at a pressure of 2.4 kbar. The lysed bacteria were centrifuged at 20,000 rpm (60480 g) for 25 min to separate non-dissolved fragments. The supernatant was then loaded onto a 5 ml Ni-NTA column, which was previously equilibrated with MSP equilibration buffer at 1 ml/min flow rate. After loading, the column was washed with MSP equilibration buffer until the UV-trace at 280 nm was constant. It was then washed with the MSP washing buffers 1, 2, and 3, each time until the UV-trace was constant. For the washing, a flow rate of 2 ml/min was used. Subsequently, a linear gradient from 0% to 100% MSP elution buffer in MSP washing buffer 3 was applied to elute the His-tagged protein. The gradient was applied over 60 min at a flow rate of 1 ml/min. Fractions containing the desired protein were unified and the identity of the protein confirmed by SDS-PAGE. The imidazole was removed by buffer exchange against MSP washing buffer 3 and the His-tag removed by incubation with 30 µg TEV-protease per mg of MSP overnight at 4 °C. The TEV protease and the cut fragment containing the His-tag were then removed using a second Ni-NTA affinity chromatography. The column was equilibrated with MSP washing buffer 3, before loading the protein. The cut R5-MSP-R5 was then eluted using a gradient from 0 - 20% MSP elution buffer in MSP washing buffer 3 over 10 ml. The buffer was exchanged against MSP washing buffer 3 (to remove imidazole) using a 6-8 kDa MWCO dialysis tubing and the protein concentrated using a spin filter with 10 kDa MWCO according to the instructions of the manufacturer.

3.4.17 SDS-PAGE

Protein expression was followed by gel electrophoresis (SDS-PAGE). When bacteria were used, a sample of the size $V = \frac{1}{OD_{600}} \cdot 200 \mu l$ was taken. The sample was centrifuged at 8000 rpm (9642 g) using a table-top centrifuge, the supernatant removed, and the pellet resuspended in 20 µl of water. Of this resuspension, 10 µl were added to 10 µl of 2x loading buffer and heated to 90 °C for 5 min before loading onto a Lämmli SDS-gel with 15% polyacrylamide. Samples of the proteins were directly diluted with the loading buffer.

The SDS-Gels were run at 250 V and 121 mA for 40 min. The gels were stained by microwaving them in Coomassie-staining solution for 30 s and incubating them for a further 30 min at room temperature. Destaining was performed with destaining solution in the same way. Before imaging, gels were incubated in water for another 30 min.

3.4.18 Formation of nanodiscs

The method used to induce the formation of lipid-bilayer nanodiscs was based on the protocol by Luthra *et al.*²³⁸. 1,2-Dioleoyl-sn-glycero-3-phosphocholine (DOPC) was solubilized at 50 mM concentration in the following way. 25.6 mg (32.6 µmol) of the lipid were dissolved in 2.5 ml chloroform in a glass tube. The solvent was evaporated in an argon stream while turning the tube at an angle. The lipid-coated glass tube was dried overnight in the desiccator. The lipid was again dissolved in 650 µl of a solution of 100 mM sodium cholate and 100 mM NaCl by repeated cycles of heating to 60 °C and sonicating for 3 min. The process was repeated until the solution was completely clear.

A 500 μ l nanodisc formation solution was prepared from 70 μ l of solubilized DOPC (7 mM final concentration) by adding MSP washing buffer 3 and purified protein to a final protein concentration of 50 μ M (1:140 ratio of protein to lipid). This was incubated for 30 min on ice. After incubation, the mixture was transferred to a pre-hydrated dialysis cassette (10 kDa MWCO) and dialysed against 200 ml MSP washing buffer 3. The buffer was changed 2 times and the final dialysis step run overnight.

3.4.19 TEM sample preparation

Samples for transmission electron microscopy (TEM) on 200 mesh copper grids were prepared using the following steps. In between each step, the liquid was carefully removed with a precision wipe.

- 3 μ l of the sample were spotted onto the grid and allowed to adsorb for 5 min
- 3 μ l of milli-Q water was spotted onto the grid and left for 2 min (3x)
- 3 μ L of TEM negative staining solution were spotted and left for 15 min
- the grid was dried for at least 10 min

3.4.20 Atomic force microscopy

Samples were prepared by dipping freshly cleaved mica substrates into the nanodisc solution, then air drying them before recording.

3.4.21 CD measurements

To measure CD spectra, the peptides were dissolved in degassed CD buffer at the desired concentration, then filled into a quartz cuvette with 1 mm light path. The cuvette holder was constantly kept at 20 °C. A background measurement was performed for the buffer and subtracted from the subsequent measurements. The spectra were obtained by averaging three single measurements with 2 data points per s.

3.4.22 Expression and purification of DGK

The method used for expression and purification of DGK was modified from the one described by Lau *et al.*²²¹ The protein was expressed in BL21 (DE3) *E. coli* transformed with the expression plasmid pSD004. A 200 ml culture of the bacteria was grown overnight at 37 °C and 200 rpm in LB medium with 100 mg/l Ampicillin and the resulting OD₆₀₀ was measured. To a 2 l culture of LB medium with 100 mg/l Ampicillin was then added a volume of the pre-culture to reach a starting OD₆₀₀ of 0.1.

The bacteria were then grown at 37 °C and 180 rpm to OD₆₀₀ = 0.6 - 0.9 before induction with IPTG to a final concentration of 1 mM. After induction, the culture was incubated at 37 °C and 180 rpm overnight. To harvest bacteria, the culture was centrifuged at 6000 rpm for 25 min. The supernatant was discarded and the pellet containing the bacteria stored at -80 °C until further use.

To purify, the protein was first solubilized directly from the whole bacteria by resuspending the pellet in 40 ml DGK solubilization buffer at 4 °C for three days during which the mixture was constantly stirred. Afterwards, it was cleared by centrifugation at 20,000 rpm for 30 min.

The supernatant was loaded onto a 5 ml His-Trap Ni-NTA column at 1 ml/min which was pre-equilibrated with DGK equilibration buffer. The column was then washed with DGK equilibration buffer at 2 ml/min until the UV absorbance remained constant. It was further washed with DGK washing buffer to constant absorbance. The protein was eluted using the DGK elution buffer and fractions were collected during elution.

The fractions were tested by SDS-PAGE and fractions containing the protein were pooled and dialysed against 2l DGK dialysis buffer. The buffer was changed two times. The protein was concentrated using a spin-filter with a MWCO of 3 kDa. The concentrated protein solution was flash-frozen in liquid nitrogen and stored at -80 °C until further use.

3.4.23 Kinase activity assay

To measure the kinase activity of the DGK samples, the assay published by Lau *et al.* was used²²¹. Accordingly, the following mixture was prepared in a micro cuvette.

- 372 µl DGK dialysis buffer
- 10 µl NADH (10 mM, fresh)
- 10 µl dioleoylglycerol (7 mM, in DMSO)
- 4 µl LDH (2,750 U/ml)
- 1,25 µl pyruvate kinase (5,530 U/ml)
- 1 µl phosphoenol pyruvate (100 mM)
- 1 µl ATP (0.5 M)
- 1 µl MgCl₂ (1.5 M)

The spectrometer was blanked against the DGK dialysis buffer. 10 µl of the sample were then added, mixed in, and the absorbance at 340 nm monitored over 30 min every 2 s.

For the nanoparticle samples, 20 µl of resuspended nanoparticles were pre-incubated with 10 µl dioleoylglycerol (7mM, in DMSO) for 20 min before adding the mixture to the cuvette. Accordingly, the volume of buffer was reduced to 362 µl.

3.4.24 Stability assays

The encapsulated and free DGK enzymes were subjected to three different conditions to evaluate the stabilization due to silica encapsulation.

Pronase E

To a 100 µl sample (1 mg/ml DGK or particles created with the same amount) were added 1 µl of a Pronase E stock solution (20 mg/ml) and 1 µl CaCl₂ solution (1 M). The mixture was incubated at 40 °C for 16 h. Afterwards, 20 µl aliquots were made, flash frozen in liquid nitrogen and stored on ice. A negative control was prepared from 100 µl of buffer without DGK or particles and treated in the same way. Activity tests were then performed as described above.

Simulated gastric fluid assay

Simulated gastric fluid (SGF) was prepared according to the specifications provided by the United States Pharmacopeia (USP) and the National Formulary (NF)²³⁹. 100 µl samples were first lyophilized, then resuspended in 100 µl of SGF (0.8 g/l porcine pepsin, 34 mM NaCl, pH 1.2) and incubated for 16 h at 37 °C. Afterwards, 20 µl aliquots were made, flash frozen in liquid nitrogen and stored on ice. A negative control was prepared by incubating 100 µl of SGF without particles or DGK and treating it in exactly the same way. Activity test were then performed as described above.

Simulated intestinal fluid assay

Simulated intestinal fluid (SIF) was prepared according to the specifications provided by the United States Pharmacopeia (USP) and the National Formulary (NF)²³⁹ by mixing 100 mg of pancreatin with 10 ml of 50 mM potassium phosphate buffer pH 6.8. The mixture was vortexed, sonicated for 15 min at 25 °C, then centrifuged and filtered through a 20 µm syringe filter. Samples were first lyophilized, then resuspended in 100 µl of SIF and incubated for 16 h at 37 °C. Again, 20 µl aliquots were made, flash frozen in liquid nitrogen and stored on ice. A negative control was prepared by incubating 100 µl of SIF without particles or DGK and treating it in exactly the same way. Activity test were then performed as described above.

3.5 Plasmids and expression strains

3.5.1 Plasmids

The expression vectors pET-28a and pTrcHisB shown in figure 3.5.1 were used in this work. The pET-28a plasmid, featuring a Kanamycin resistance gene, was used to express the MSP constructs, which were inserted between the NcoI and NotI cutting sites. Diacylglycerol kinase (DGK) was expressed from the psD004 plasmid, which was created by Lau *et al.*, who inserted the DGK gene in between the SacI and HindIII cutting sites of the pTrcHisB expression vector, which features an Ampicillin resistance gene²²¹.

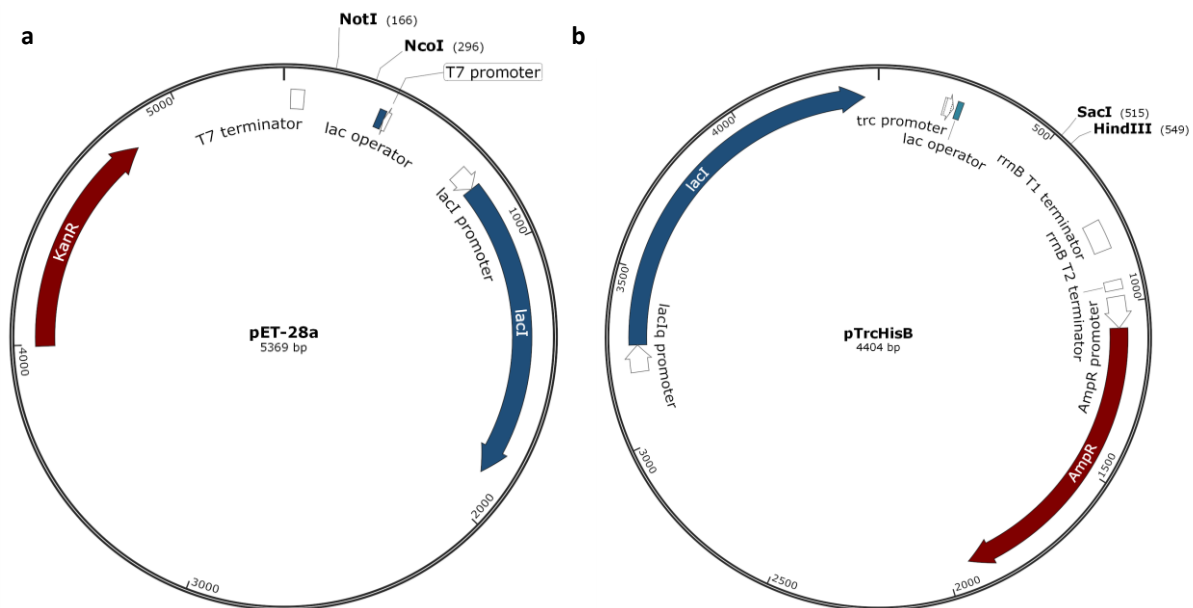


Fig. 3.5.1 | Plasmid maps of the expression plasmids pET-28a (a) and pTrcHisB (b).

3.5.2 Bacterial strains

The *E. coli* XL-1 strain was used for plasmid amplification. The *E. coli* strains BL21 (DE3), BL21 (DE3) plysS, BL21 (DE3) Gold, and BL21 (DE3) Rosetta 2 were used for protein expression. The BL21 (DE3) strains lack the Lon and ompT proteases, resulting in lower protein degradation and the prophage DE3 with the T7 RNA polymerase gene²⁴⁰. The pLysS strains also contain the pLysS plasmid, which encodes the T7 lysozyme, lowering the background expression level of target genes which are controlled by the T7 promoter²⁴¹. The Rosetta 2 strains contain a chloramphenicol-resistant plasmid coding for tRNAs for codons, which are rare in *E. coli* (AGA, AGG, AUA, CUA, GGA, CCC, and CGG)²⁴² which enables the expression of non-optimized sequences.

Results and Discussion

4.1 Polyphenol-conjugated R5 silica nanoparticles for targeted delivery

Parts of the following results were published as ‘Silica particles with a quercetin-R5 peptide conjugate are taken up into HT-29 cells and translocate into the nucleus’ together with Dr. Giorgia del Favero, who performed the live cell imaging and cell viability assays, and Prof. Dr. Doris Marko from the Department of Food Chemistry and Toxicology at the University of Vienna²⁴³. The synthesis of the polyphenol conjugates and silica particles and their analyses were performed by me.

4.1.1 Synthesis of modified polyphenols

2-(3,4-diacetoxyphenyl)-4-oxo-4H-chromene-3,5,7-triyl triacetate (2)

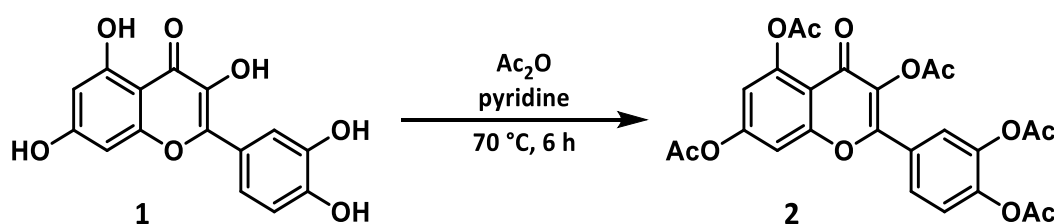


Figure 4.1.1 | Synthesis scheme for the acetylation of quercetin (1).

Quercetin (1) was fully acetylated according to the method described by Li *et al.*²⁴⁴. 20 mg (66.2 μmol , 1 eq.) of quercetin were dissolved in 1 ml of anhydrous pyridine at room temperature. 62.2 μl (67.6 mg, 662 μmol , 10 eq.) of acetic anhydride were added to the yellowish solution. It was then heated to 70 $^{\circ}\text{C}$ and stirred for 6 h before cooling it to room temperature. To remove the solvent, 5 ml of toluene were added and the solution dried at reduced pressure. This drying process was repeated twice to obtain a slightly brownish, crystalline solid, which was then recrystallized overnight from a minimal amount of acetone. The product 2 was obtained in 80% yield. The reaction should be quantitative in theory and the loss of one fifth is due to the inefficiency of the recrystallization. Thus, the yield could likely be improved when upscaling the reaction and allowing the recrystallization to proceed for longer. The following analytical data was generated for the product 2.

HR-MS (pos.):

$[\text{M}+\text{H}]^+$ m/z calc. 513.1028 obs. 513.1034

$[\text{M}+\text{Na}]^+$ m/z calc. 535.0847 obs. 535.0853

$^1\text{H-NMR}$ (600.25 MHz, CDCl_3): δ = 2.32 (s, 6H), 2.33 (s, 3H), 2.34 (s, 3H), 2.43 (s, 3H), 6.87 (d, J = 2.2 Hz, 1H), 7.33 (d, J = 2.2 Hz, 1H), 7.34 (d, J = 8.5 Hz, 1H), 7.69 (d, J = 2.1 Hz, 1H), 7.71 (dd, J = 8.5, 2.1 Hz) ppm.

¹³C-NMR (150.95 MHz, CDCl₃): δ = 20.63, 20.78, 21.15, 21.29, 109.11, 114.01, 114.87, 123.95, 124.05, 126.54, 127.86, 134.16, 142.31, 144.50, 150.50, 153.88, 154.38, 156.96, 167.87, 167.93, 167.95, 167.98, 169.36, 170.14 ppm.

4-(3,5-diacetoxy-7-hydroxy-4-oxo-4H-chromen-2-yl)-1,2-phenylene diacetate (3)

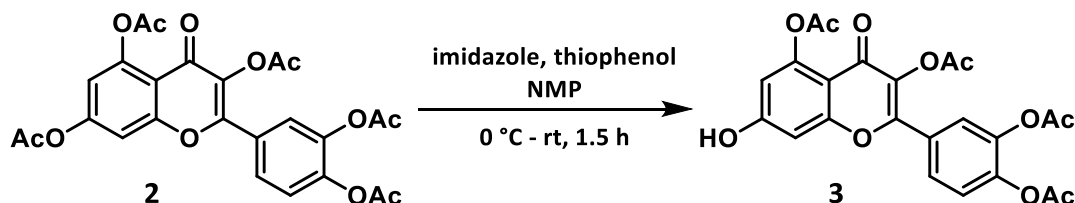


Figure 4.1.2 | Synthesis scheme for the selective deacetylation of quercetin pentaacetate (2).

Selective deprotection of the acetylated product 2 was performed according Kim *et al.*²⁴⁵. 2.87 g (5.60 mmol, 1.00 eq.) of 2-(3,4-diacetoxyphenyl)-4-oxo-4H-chromene-3,5,7-triyl triacetate (2) were dissolved in a solution of 351 mg (5.15 mmol, 0.92 eq.) imidazole in 50 ml of 1-Methyl-2-pyrrolidinone (NMP) using the sonicator. The solution was cooled to 0 °C before adding 540 μ l (5.32 mmol, 0.95 eq.) of thiophenol. The mixture was stirred for 1.5 h while warming to room temperature. Afterwards, it was acidified with 50 ml 2 M HCl and extracted three times with 100 ml of ethyl acetate. The unified extracts were dried at reduced pressure to obtain the crude product, which was a mixture of tri- and tetraacetylated quercetin. To purify the crude product, it was dissolved in a minimal amount of DMSO. The solution was loaded onto a wet-loaded silica column and purified by flash column chromatography with petroleum ether and ethyl acetate (1:2) as mobile phase. The product 3 was obtained in 21% yield after drying with magnesium sulfate and removing the solvent at reduced pressure. The low yield was due to the extensive separation required to isolate the desired product from the reactant and the triacetylated quercetin. However, it would be possible to recycle the side products by again acetylating them fully. The purified product 3 was characterized as follows.

HR-MS (pos.):

[M+H]⁺ m/z calc. 471.0922, obs. 471.0917

[M+Na]⁺ m/z calc. 493.0741, obs. 493.0735

[2M+Na]⁺ m/z calc. 963.1590, obs. 963.1581

¹H-NMR (600.25 MHz, DMSO-d₆): δ = 2.29 (s, 3H), 2.30 (s, 3H), 2.33 (s, 3H), 2.33 (s, 3H), 6.64 (d, J = 2.3 Hz, 1H), 6.93 (d, J = 2.3 Hz, 1H), 7.51 (d, 1H, J = 8.5 Hz), 7,80 - 7.82 (m, 2H), 11.33 (s, 1H) ppm.

¹³C-NMR (600.25 MHz, DMSO-d₆): δ = 20.69, 20.84, 20.91, 21.34, 101.45, 109.50, 109.78, 124.01, 124.91, 126.97, 127.90, 133.22, 142.60, 144.66, 150.66, 152.86, 158.02, 163.29, 168.37, 168.50, 168.67, 169.21, 169.41 ppm.

4-(3,5-diacetoxy-7-(2-ethoxy-2-oxoethoxy)-4-oxo-4H-chromen-2-yl)-1,2-phenylene diacetate (4)

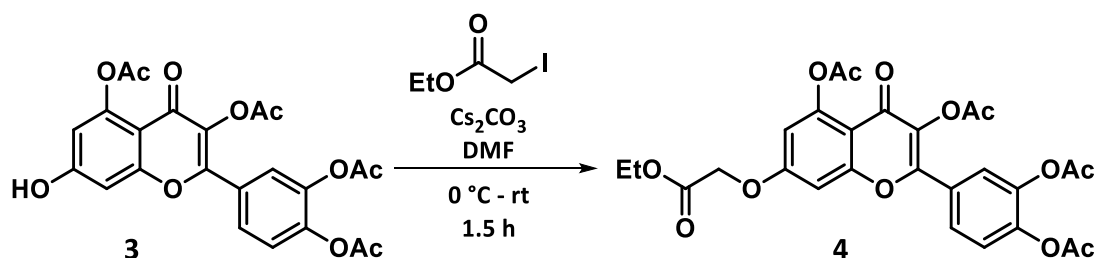


Figure 4.1.3 | Synthesis scheme for the reaction with ethyl iodoacetate.

The linker was introduced on the selectively deprotected quercetin using the method described by Wang *et al.*²⁴⁶. 327.4 mg (696 μmol , 1 eq.) of 4-(3,5-diacetoxy-7-hydroxy-4-oxo-4H-chromen-2-yl)-1,2-phenylene diacetate (3) were dissolved in 20 ml of dry DMF with 4 Å molecular sieves added under argon atmosphere. 108 μl (195 mg, 912 μmol , 1.31 eq.) of ethyl iodoacetate were added and the mixture was cooled to 0 °C. While stirring, 270 mg (828 μmol , 1.19 eq.) of Cs_2CO_3 were added to the solution. The mixture was allowed to warm to room temperature and stirred for 1.5 h in the dark. Afterwards it was titrated to pH 6 using HCl. The solution was concentrated at reduced pressure and the residue purified by silica flash column chromatography using a 1:1.5 mixture of petroleum ether and ethyl acetate as mobile phase. The product was dried using magnesium sulfate and the solvent removed at reduced pressure. To remove residual DMF, approximately 5 ml of heptane were added, and the solvent removed under vacuum. This was repeated five times to obtain a slightly beige solid product in 75% yield, which is only slightly lower than that reported previously²⁴⁶. Analysis of the product 4 gave the following results.

HR-MS (pos.):

$[\text{M}+\text{Na}]^+$ m/z calc. 579.1109 obs. 579.1115

$[2\text{M}+\text{Na}]^+$ m/z calc. 1135.2326 obs. 1135.2323

$^1\text{H-NMR}$ (400.27 MHz, CDCl_3): δ = 1.31 (t, J = 7.1 Hz, 3H), 2.33 (s, 3H), 2.33 (s, 6H), 2.43 (s, 3H), 4.30 (q, J = 7.1 Hz, 2H), 4.71 (s, 2H, H-C), 6.68 (d, J = 2.5 Hz, 1H), 6.81 (d, J = 2.5 Hz, 1H), 7.34 (d, J = 8.5 Hz, 1H), 7.67 (d, J = 2.1 Hz, 1H), 7.70 (dd, J = 8.5, 2.1 Hz, 1H) ppm.

$^{13}\text{C-NMR}$ (151 MHz, DMSO-d_6): δ = 14.03, 20.24, 20.39, 20.42, 20.84, 60.99, 65.28, 100.46, 109.20, 110.61, 123.53, 124.51, 126.58, 127.32, 133.03, 142.18, 144.33, 149.97, 152.71, 157.38, 162.06, 167.81, 167.84, 168.03, 168.21, 168.72, 169.05 ppm.

2-((2-(3,4-dihydroxyphenyl)-3,5-dihydroxy-4-oxo-4H-chromen-7-yl)oxy)acetic acid (5)

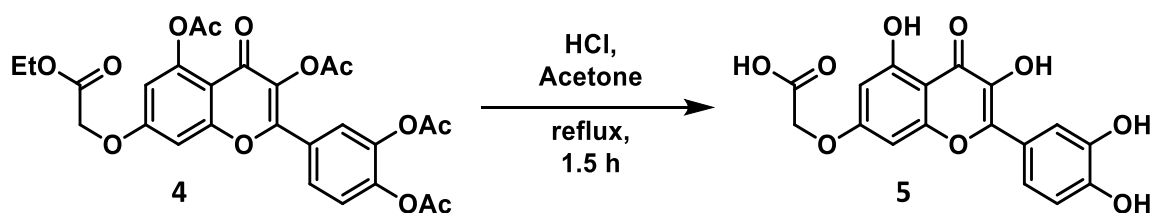


Figure 4.1.4 | Synthesis scheme for the deprotection step.

Deprotection of the acetylated product 4 was performed according to Mattarei *et al.*²⁴⁷. 300 mg (539 μmol) of 4-(3,5-diacetoxy-7-(2-ethoxy-2-oxoethoxy)-4-oxo-4H-chromen-2-yl)-1,2-phenylene diacetate were dissolved in 20 ml of acetone. 10 ml of a 6 M hydrochloric acid were added. The colourless mixture was refluxed for 1.5 h. During the reaction, it turned yellow. After cooling to room temperature, 100 ml of water and 100 ml of ethyl acetate were added. Approximately 1 ml of brine was added, and the phases were separated. The aqueous phase was extracted two more times with 100 ml of ethyl acetate. The unified organic extracts were washed three times with 100 ml of 3 M HCl. The solvent was removed at reduced pressure and the product recovered in 90% yield. Analysis of product 5 generated the following data.

MS (pos.):

[M+H]⁺ m/z calc. 361.06, obs. 360.57

MS (neg.):

[M-H]⁻ m/z calc. 359.04, obs. 359.02

¹H-NMR (600.25 MHz, DMSO-d₆): δ = 4.84 (s, 2H), 6.36 (dd, J = 7.8 Hz, 2.2 Hz, 1H), 6.70 (dd, J = 11.4 Hz, 2.2 Hz, 1H), 6.89 (d, J = 8.5 Hz, 1H), 7.58 (dd, J = 8.5 Hz, 2.2 Hz, 1H), 7.73 (dd, J = 10.1 Hz, 2.2 Hz, 1H), 9.31 (s, 1H), 9.51 (s, 1H), 9.63 (s, 1H), 12.43 (s, 1H), 12.49 (s, 1H), 13.02 (s, 1H) ppm.

¹³C-NMR (150.95 MHz, DMSO-d₆): δ = 64.86, 92.55, 97.82, 104.27, 115.20, 115.58, 120.06, 121.82, 136.07, 145.09, 147.38, 147.88, 155.85, 160.36, 163.29, 169.56, 175.94 ppm.

3-((3,5-dihydroxy-4-oxo-2-phenyl-4H-chromen-7-yl)oxy)propanoic acid (7)

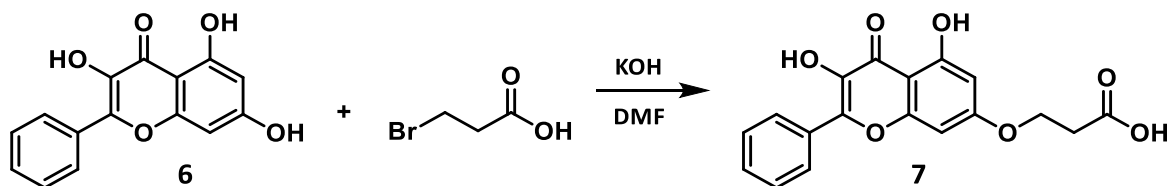


Figure 4.1.5 | Synthesis scheme for the modification of galangin (6).

The introduction of the carboxylic acid linker on galangin was based on a reaction published by Verghese *et al.*²⁴⁸. 20 mg (74 μmol , 1 eq.) of galangin were dissolved in 250 μl of DMF. A 5 ml round flask was filled with 51.2 mg (370 μmol , 5 eq.) of powdered KOH. The galangin solution was added onto the KOH and stirred for 15 min in an ice bath. 17 mg (111 μmol , 1.5 eq.) of 3-bromopropanoic acid in 170 μl DMF were added and the reaction stirred overnight. It was quenched by adding 2 ml of DCM and 2 ml of 1 M HCl. The phases were separated, and the aqueous phase was extracted with another 2 ml of DCM. The organic phases were unified, and the solvent removed at reduced pressure. The product was purified by flash column chromatography, using 10% methanol in DCM (+ 0.1% acetic acid) as mobile phase. The product 7 could be isolated in 23% yield, as opposed to 50% conversion reported in the literature²⁴⁸. A possible explanation would be inefficient extraction from the aqueous phase; additional extraction steps could improve the yield. Analysis of product 7 gave the following results.

HR-MS (neg.):

$[\text{M}-\text{H}]^-$ m/z calc. 341.0667, obs. 341.0667

$^1\text{H-NMR}$ (600.25 MHz, DMSO- d_6): δ = 2.59 (t, J = 6.3 Hz, 2H), 4.24 (t, J = 6.3 Hz, 2H), 6.23 (d, J = 2.1 Hz, 1H), 6.47 (d, J = 2.1 Hz, 1H), 7.55 - 7.56 (m, 3H), 8.03 (dd, J = 7.7, 2.0 Hz, 2H), 10.54 (s, 1H), 12.56 (s, 1H) ppm.

$^{13}\text{C-NMR}$ (150.95 MHz, d_6 -DMSO- d_6): δ = 34.89, 68.20, 93.82, 98.73, 104.41, 128.34, 128.60, 130.02, 131.10, 137.63, 155.26, 156.58, 161.29, 164.45, 172.10, 178.10 ppm.

4.1.2 Coupling of modified polyphenols with the R5 peptide

Conjugation of the modified polyphenols with the R5 peptide was performed on resin after manual or automated solid-phase peptide synthesis (SPPS), as described in sections 3.4.1 to 3.4.4. An overview of the syntheses resulting in the conjugates quercetin-R5 and galangin-R5 is given in figure 4.1.6.

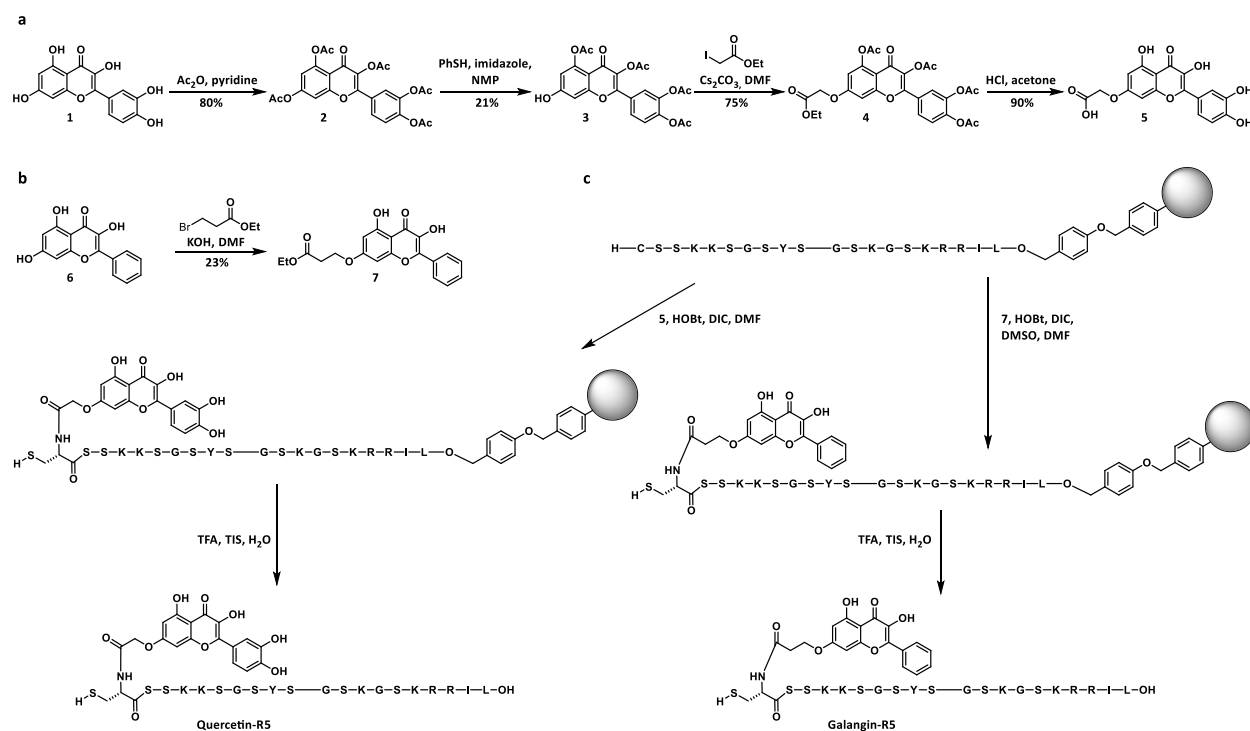


Figure 4.1.6 | Synthesis overview of the modification of quercetin (**a**) and galangin (**b**) with a carboxylic acid linker, and the coupling of the modified polyphenols to the R5 peptide on resin (**c**).

Quercetin-R5

The quercetin-R5 conjugate was obtained after coupling of the modified quercetin overnight as described in the methods section 3.4.4. It was then cleaved and purified by preparative RP-HPLC, using a gradient of 5% - 65% eluent B in eluent A. The yield of the purified conjugate was 4% of the maximum expected yield according to resin loading. For example, 5.1 mg (2.09 μmol) of purified quercetin-R5 could be obtained from 51.8 μmol resin-bound peptide. Analysis by HPLC shows a single peak and a mass spectrum shows the expected multiply charged ion series (see figure 4.1.7, compare table 4.1.1). These results indicate that the desired conjugate was obtained in high purity.

Table 4.1.1 | Molecular weight and m/z values of quercetin-R5.

MW	m/z (1+)	m/z (2+)	m/z (3+)	m/z (4+)	m/z (5+)
2458.69 g/mol	2459.17	1230.09	820.40	615.55	492.64

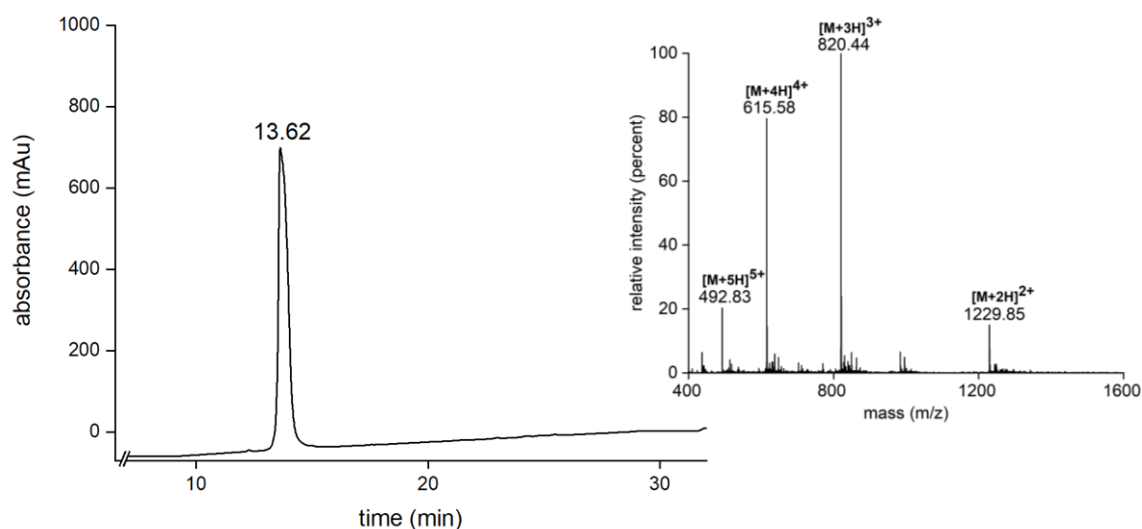


Fig. 4.1.7 | Final analysis of the quercetin-R5 conjugate. HPLC chromatogram (left) and mass spectrum (insert). The injection peak was cut off from the chromatogram.

Galangin-R5

The galangin-R5 conjugate was successfully obtained after coupling overnight as described in the methods section 3.4.4. It was then cleaved and purified by preparative RP-HPLC, using a gradient of 20% - 40% eluent B in eluent A. The yield of the purified conjugate was 25%. For example, 3.0 mg (1.23 μmol) of purified galangin-R5 could be obtained from 5.0 μmol resin-bound peptide. Analysis by HPLC shows a sharp peak, however, some small additional peaks are visible (see figure 4.1.8). Integration of the peaks still indicates a purity exceeding 90%. The mass spectrum the expected multiply charged species (compare table 4.1.2), indicating that the galangin-R5 conjugate was obtained in good purity and high yield.

Table 4.1.2 | Molecular weight and m/z values of galangin-R5.

MW	m/z (1+)	m/z (2+)	m/z (3+)	m/z (4+)	m/z (5+)
2440.72 g/mol	2441.20	1221.10	814.40	611.05	489.05

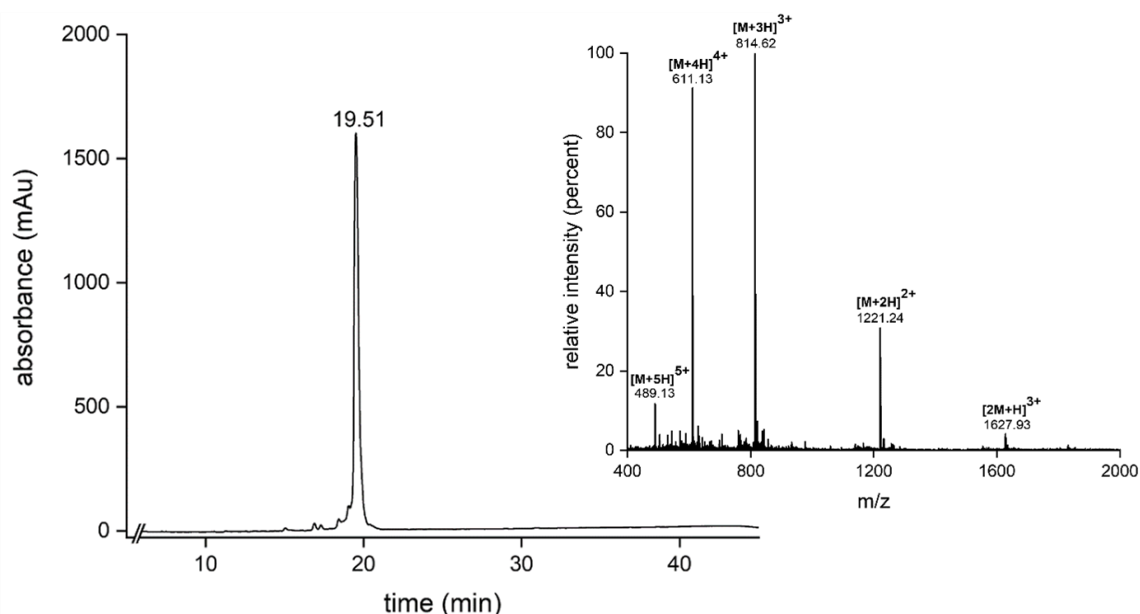


Fig. 4.1.8 | Final analysis of the galangin-R5 conjugate. HPLC chromatogram (left) and mass spectrum (insert). The injection peak was cut off from the chromatogram.

4.1.3 Absorbance and fluorescence spectra of quercetin-R5 conjugate

To determine whether the conjugates can be observed under the fluorescence microscope, absorbance and emission spectra were measured as described in the methods section 3.4.7. The absorbance spectrum of quercetin-R5 (see fig. 4.1.9b) shows the expected peak for the quercetin chromophore at 380 nm. Fluorescence emission is observed with a maximum at 540 nm, excitation is most efficient at 440 nm (see fig. 4.1.9c-e). A previous study with quercetin in PBS buffer found similar values. An excitation maximum was found at 430 nm and the emission maximum at 500 nm²⁴⁹. Studies have also shown that quercetin is a suitable chromophore for confocal fluorescence microscopy of cells^{249,250}. Thus, it was concluded, that the cell uptake of the quercetin-R5 conjugate and the silica particles precipitated with it can be observed using confocal fluorescence microscopy.

The galangin-R5 conjugate shows a similar absorption spectrum with a maximum absorbance at 350 nm (see figure 4.1.9a), but no fluorescence was observed. Thus, galangin-R5 silica particles were stained with a fluorescein-derived compound, as described in the methods section 3.4.8.

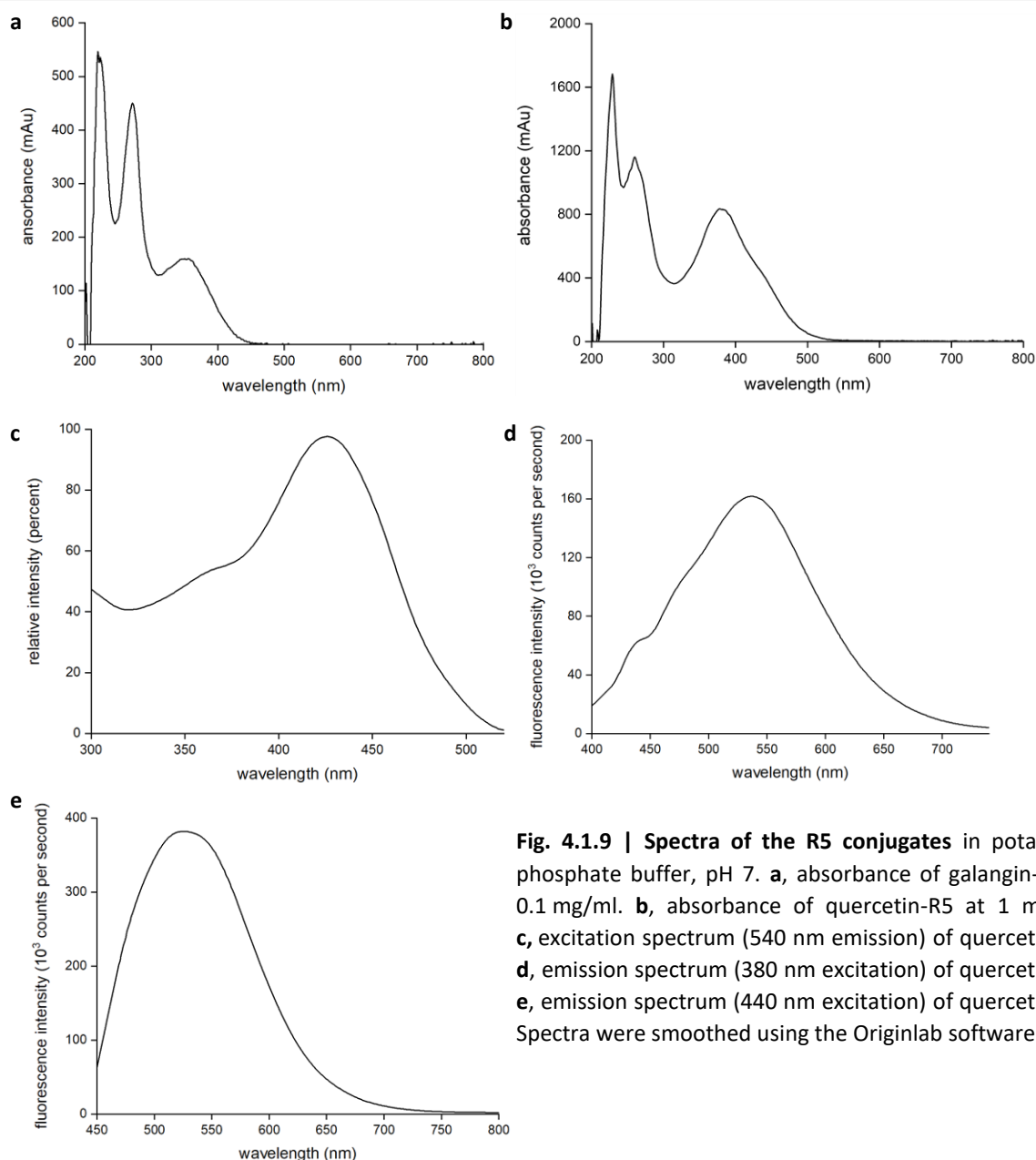


Fig. 4.1.9 | Spectra of the R5 conjugates in potassium phosphate buffer, pH 7. **a**, absorbance of galangin-R5 at 0.1 mg/ml. **b**, absorbance of quercetin-R5 at 1 mg/ml. **c**, excitation spectrum (540 nm emission) of quercetin-R5. **d**, emission spectrum (380 nm excitation) of quercetin-R5. **e**, emission spectrum (440 nm excitation) of quercetin-R5. Spectra were smoothed using the Originlab software.

4.1.4 Silica particle formation with polyphenol-R5 conjugates

Silica particles were generated under standard precipitation conditions as described in the methods section (3.4.8). These are the same conditions that were used for the unmodified R5 peptide previously²³⁴. Scanning electron microscopy (SEM) of the particles reveals their spherical morphology and size distribution (see fig. 4.1.10). As expected, the particles are spherical and approximately half a micrometre in size, very similar to the silica particles formed with the unmodified R5 peptide²³⁴, indicating that the N-terminal polyphenol does not hinder peptide assembly and particle formation. However, the quercetin-R5 silica particles are slightly smaller than the galangin-R5 particles. Measurements of 100 individual quercetin-R5 silica particles reveal an average size of 436 ± 4 nm, whereas the galangin-R5 silica particles are on average 588 ± 6 nm in diameter (62 particles were measured). Possibly the smaller and less polar galangin is better suited to stacking interactions²⁵¹, supporting the formation of larger assemblies. Further studies using conjugates with various aromatic systems are needed to evaluate such a trend.

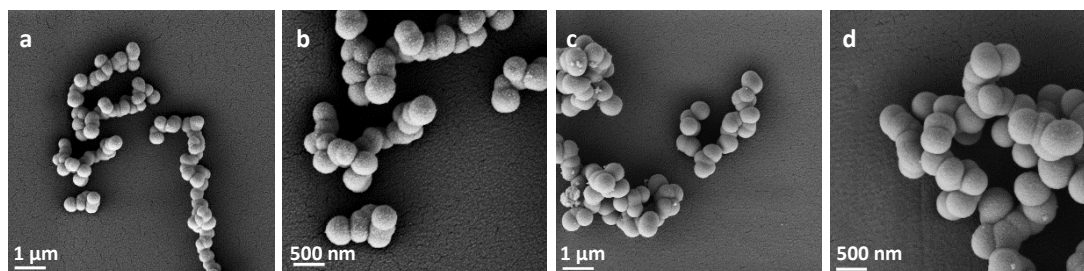
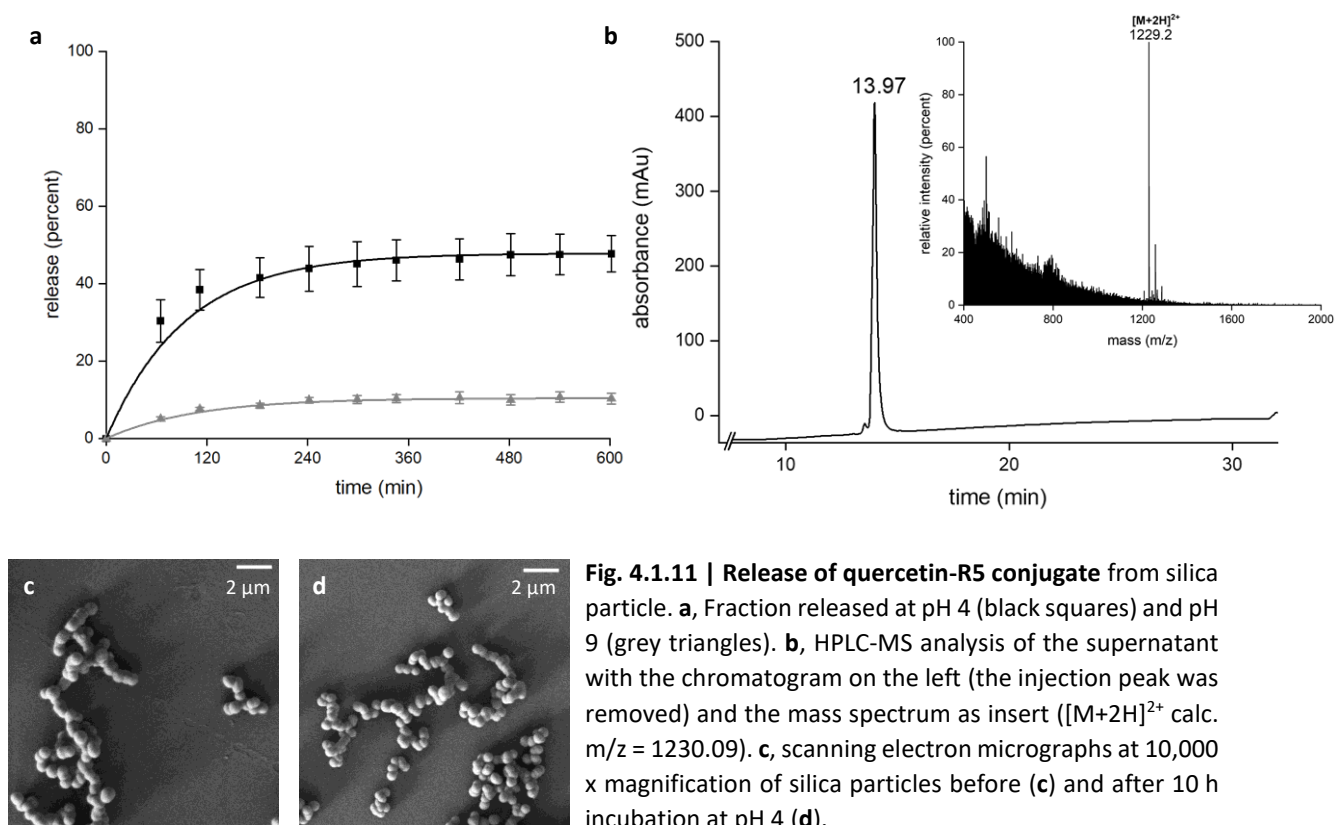


Fig. 4.1.10 | Scanning electron micrographs of silica particles precipitated with quercetin-R5 at 10,000 x (a) and 20,000 x magnification (b), and of galangin-R5 silica particles at 10,000 x (c) and 20,000 x magnification (d).

4.1.5 pH-dependent release of quercetin-R5 conjugate from particles

The silica particles precipitated using the fluorescent quercetin-R5 conjugate were incubated in 50 mM potassium phosphate buffer at pH 4 and pH 9 for 10 h to monitor release of the conjugate from the particles by measuring absorbance of the supernatant. It was found that at pH 4 approximately 40% of the conjugate are released, whereas at pH 9, only about 10% are released from the particles (see fig. 4.1.11a). LC-MS analysis of the supernatant showed that the conjugate released at pH 4 was fully intact (see fig. 4.1.11b). The particles show no morphological changes due to the incubation (see fig. 4.1.11c), which indicates that the release is not due to degradation of the silica matrix. This suggests that there is a certain fraction of the conjugate, which is bound to the particles by ionic interactions, which can be disturbed by a change in pH. At low pH, the anionic surface of the silica (pKa can be as low as 5.6²⁵²) would be neutralized and interaction with the cationic R5 peptide (pI 11.22) weakened, causing the release of the peptide conjugate.



4.1.6 Cell uptake of silica particles into HT-29 cells

The cell experiments were performed in collaboration with the Department of Food Chemistry and Toxicology at the University of Vienna and handled by collaboration partner Dr. Giorgia del Favero. HT-29 human colorectal adenocarcinoma cells, which mimic the intestinal epithelium²⁵³, were treated with quercetin at different concentrations and after 3 h incubation observed under the confocal fluorescence microscope. The membranes were stained with a Deep Red Plasma membrane stain, which is shown here in white, fluorescence from quercetin is shown in bright green. In accordance with previous studies, where cell uptake and an even distribution of quercetin in HepG2 human liver carcinoma cells is shown²⁴⁹, we could observe a similar distribution of fluorescence throughout the cells (compare figure 4.1.12a-d), albeit more grainy. Further experiments are needed to find out if quercetin is distributed throughout all fractions of the cells or whether it is accumulated in certain cell organelles, which could explain the grainy fluorescence distribution. The same experiment was repeated with the quercetin-R5 silica particles (figure 4.1.12e-h). A very different distribution is observed; the particles clearly accumulate within the cells' nuclei at all concentrations.

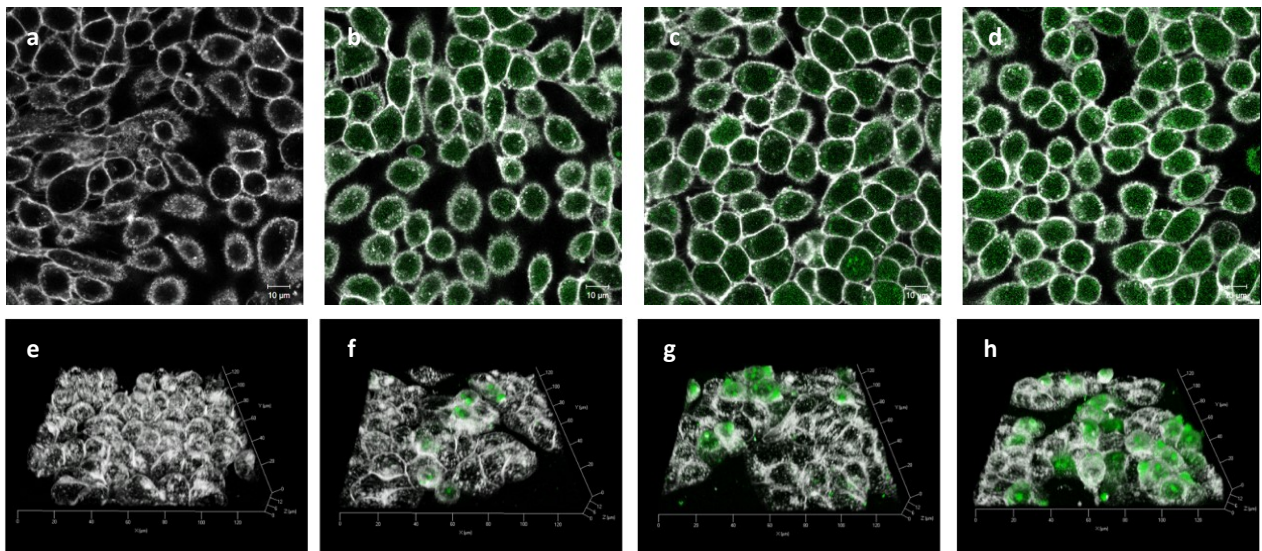


Fig. 4.1.12 | HT-29 cells after 3 h incubation. **a**, control. **b**, with 20 μM quercetin. **c**, with 70 μM quercetin. **d**, with 100 μM quercetin. **e**, control. **f**, with 20 μM quercetin-R5 silica particles. **g**, with 70 μM quercetin-R5 silica particles. **h**, with 100 μM quercetin-R5 silica particles.

Further experiments were then conducted, comparing the different silica particle variants. Suspensions of silica particles precipitated either with the R5 peptide, the galangin-R5 conjugate, or the quercetin-R5 conjugate were used and uptake tracked by live cell fluorescence imaging as described in the methods section (3.4.10). The particles are fluorescent due to the quercetin conjugate's inherent fluorescence (compare section 4.1.3) or were stained with the ce386 fluorescein derivative and are shown here in bright green. After 3 h incubation with particles corresponding to 0.25 mg/ml, the cells are still intact; there are no significant morphological differences to the control cells (compare fig. 4.1.13a).

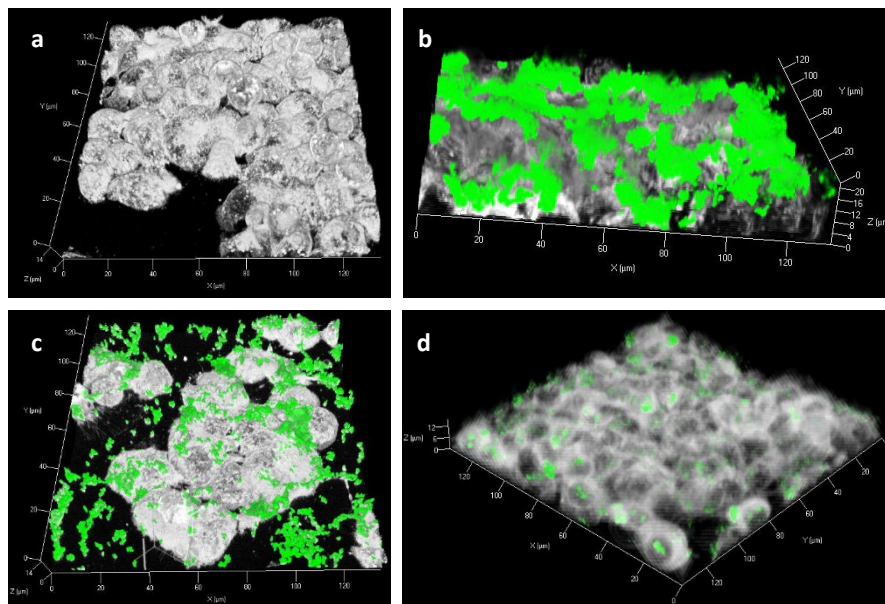


Fig. 4.1.13 | HT-29 cells after 3 h incubation. a, control. **b,** with R5 silica particles. **c,** with galangin-R5 silica particles. **d,** with quercetin-R5 silica particles.

Fluorescence signal from the R5 silica particles and galangin-R5 silica particles is located in between clumps of cells and on top of the cells (compare fig. 4.1.13b-c). It is thus assumed that within this timeframe the particles remained outside of the cell membrane and there is no uptake. Fluorescence in the cells treated with quercetin-R5 silica particles is located inside the cells' nuclei as observed before (see fig. 4.1.13d). The time-dependent uptake of the quercetin-R5 silica particles was monitored. Initially, the fluorescent spots are located on top of the cells only (see fig. 4.1.14a). The uptake can then clearly be followed over time (see fig. 4.1.14b-e). After 2 h, a fraction of the particles has entered cell nuclei. After 3 h, all particles are inside the cells' nuclei. The fraction of cells which take up particles is hard to estimate from these images, however, only a minority of cells does not contain particles.

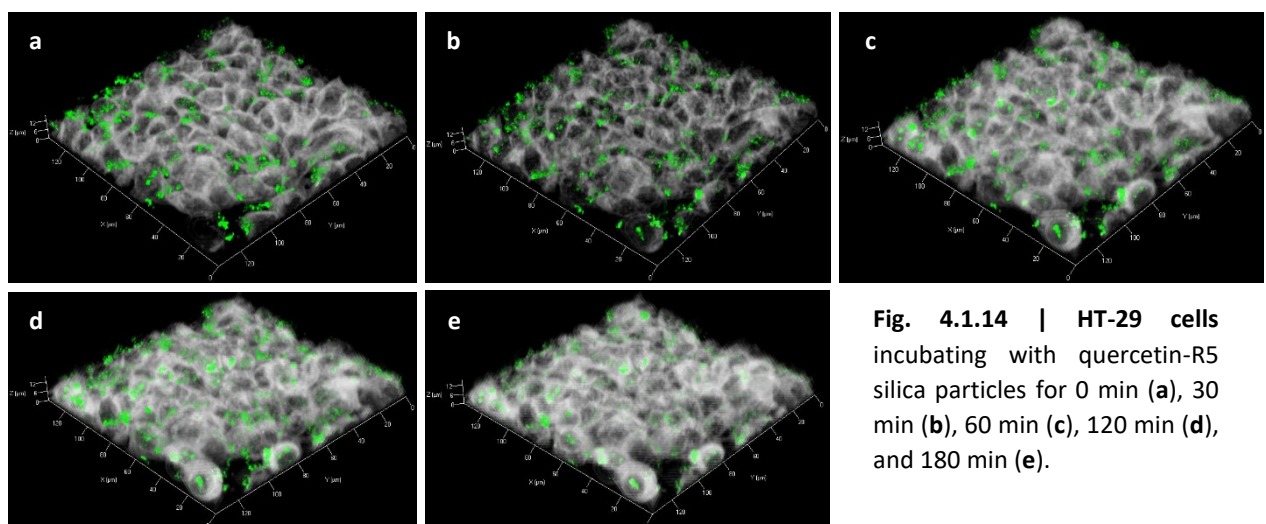


Fig. 4.1.14 | HT-29 cells incubating with quercetin-R5 silica particles for 0 min (a), 30 min (b), 60 min (c), 120 min (d), and 180 min (e).

In order to elucidate the uptake mechanism of the cells, a series of further experiments were conducted. Uptake of quercetin-R5 silica particles was first compared at 4 °C and 37 °C (see fig. 4.1.15). The resulting images show a significantly lower uptake at 4 °C, indicating that the uptake mechanism is active, i.e. energy-dependent. This conclusion is further supported by the observation that particles are engulfed by the cell membrane. To further differentiate between uptake pathways, the effect of two different inhibitors was investigated. Wortmannin is an inhibitor of phosphatidylinositol-3-kinase and micropinocytosis²⁵⁴, whereas the cholesterol-removing agent methyl- β -cyclodextrin is a mechanosensitivity inhibitor²⁵⁵. Both inhibitors do not cause a significant change in the uptake behaviour (see fig. 4.1.16). This further indicates that the uptake mechanism is neither micropinocytosis nor caveolin-mediated endocytosis. Further experiments are needed to elucidate the exact pathway leading to the active uptake of the quercetin-R5 silica particles. A first step could be to compare the uptake by different cell lines in which proteins mediating cell uptake, for example clathrin, have been knocked out²⁵⁶.

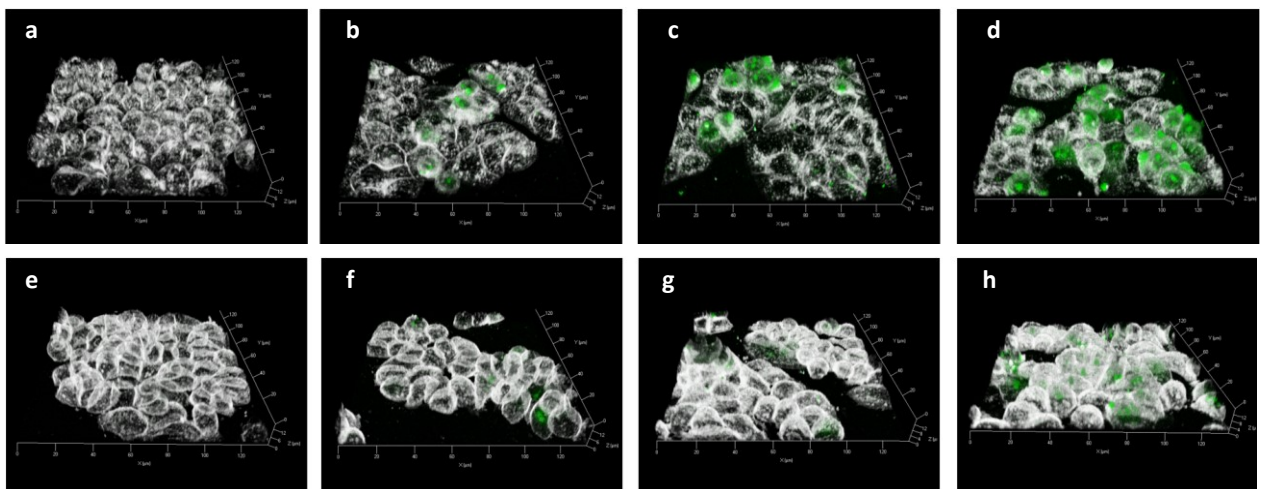


Fig. 4.1.15 | HT-29 cells after 3 h incubation with quercetin-R5 silica particles at 37 °C: **a**, control. **b**, 20 μ M. **c**, 70 μ M. **d**, 100 μ M. At 4 °C: **e**, control. **f**, 20 μ M. **g**, 70 μ M. **h**, 100 μ M.

The quercetin-R5 silica particles enable efficient transport into eukaryotic cells which mimic the intestinal epithelium. Their toxicity was evaluated using a comet assay (data shown in appendix, fig. A14), which showed that the DNA damage caused was much lower than that caused by free quercetin at the same concentration²⁴³. This is in sharp contrast with other oxide nanoparticles, for example from alumina, which were shown to induce significant, dose-dependent DNA damage in Chinese hamster lung cells²⁵⁷.

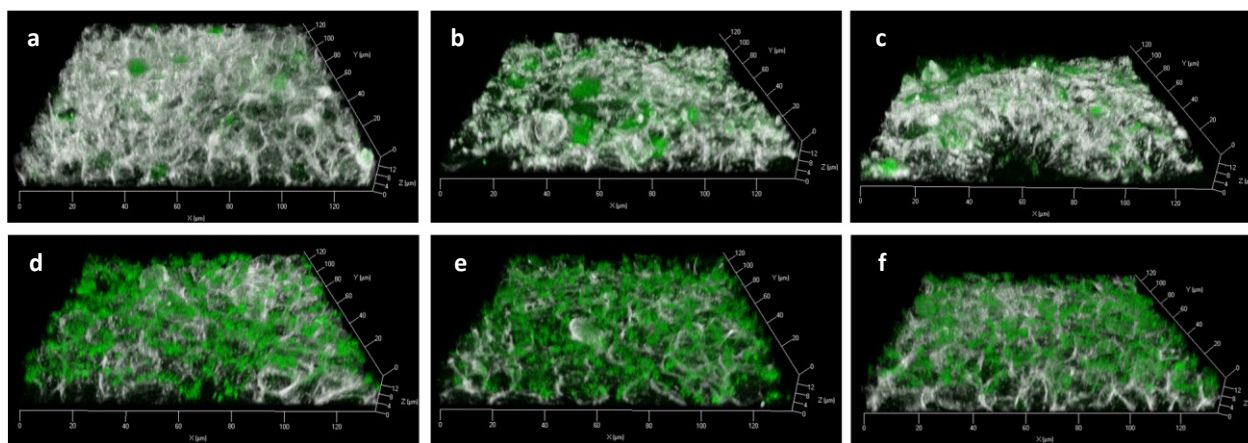


Fig. 4.1.16 | HT-29 cells after 3 h incubation with quercetin-R5 silica particles without inhibitor at 37 °C (a) and 4 °C (d). In the presence of 10 μM wortmannin (micropinocytosis inhibitor) at 37 °C (b) and 4 °C (e). In the presence of 50 μM methyl-β-cyclodextrin (cholesterol-removing agent) at 37 °C (c) and 4 °C (f).

Thus, the quercetin-R5 silica particles present a suitable vehicle to transport cargo to cell nuclei. If the issue of peptide loss at low pH could be solved to increase stability in the stomach, using a coating for example, they might be useful for oral delivery of cargo compounds to intestinal cells. Cargo molecules can be attached to the quercetin-R5 conjugates via formation of a disulfide bridge to the cysteine (see fig. 4.1.17), as has been demonstrated previously⁵⁵.

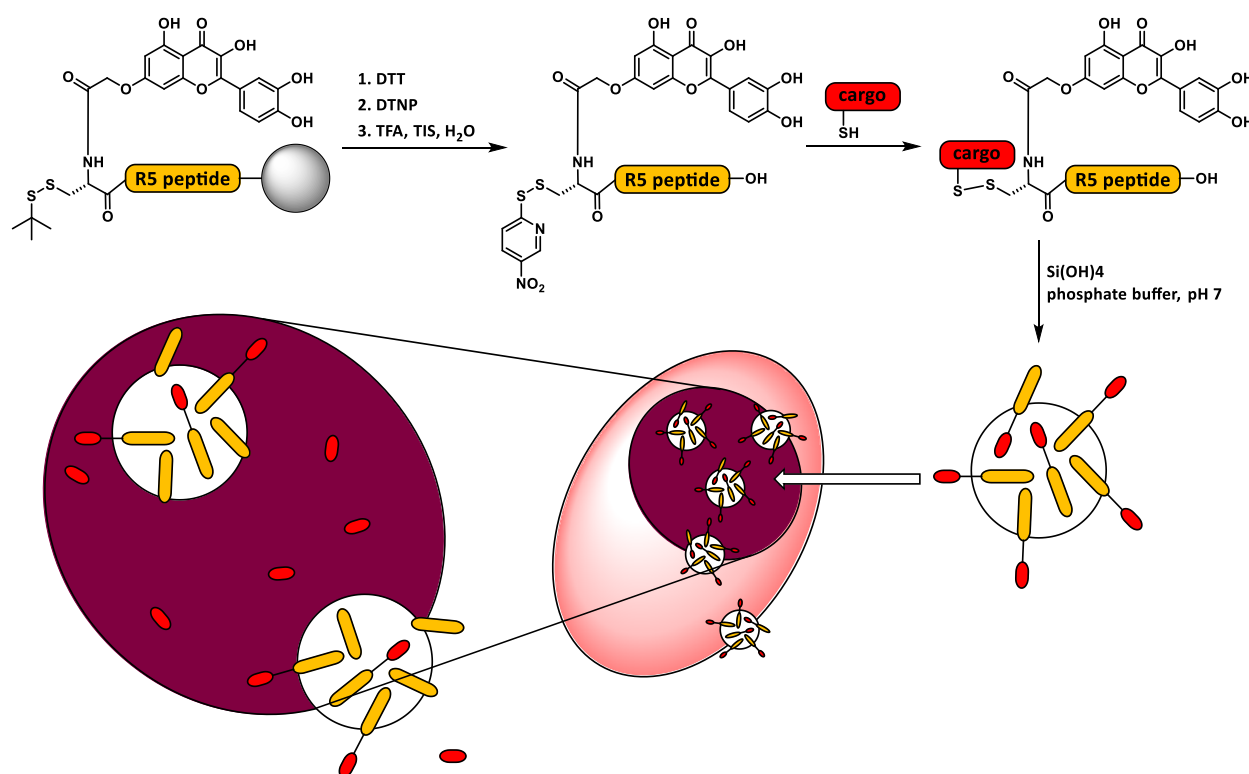


Fig. 4.1.17 | Schematic representation of cargo immobilised on quercetin-R5 silica particles via disulfide bonds. Bond formation is induced using 2,2'-dithiobis(5-nitropyridine) (DTNP), as described by Galande et al.²⁵⁸. The tert-butylsulfenyl protecting group on cysteine is first removed on resin using DTT, before activation with DTNP. After cleavage with TFA, the peptide conjugate is coupled to the cargo. The resulting disulfide is then used for silica particle formation. The particles can be taken up into a cell's nucleus. Inside the cell, the cargo is released due to the reduction of the disulfide bond by glutathione.

4.2 Silica-stabilized nanodiscs

4.2.1 Cloning of modified MSP constructs

As outlined in the aims section, the first step to obtain silica-precipitating nanodiscs was to make constructs, in which the silica-precipitating R5 tag is genetically fused to the membrane scaffold protein, which stabilizes the lipid bilayer nanodiscs in solution. Three new variants were designed, in which the R5 peptide is fused to the N-terminus of the protein, to the C-terminus, or both (compare fig. 4.2.1).

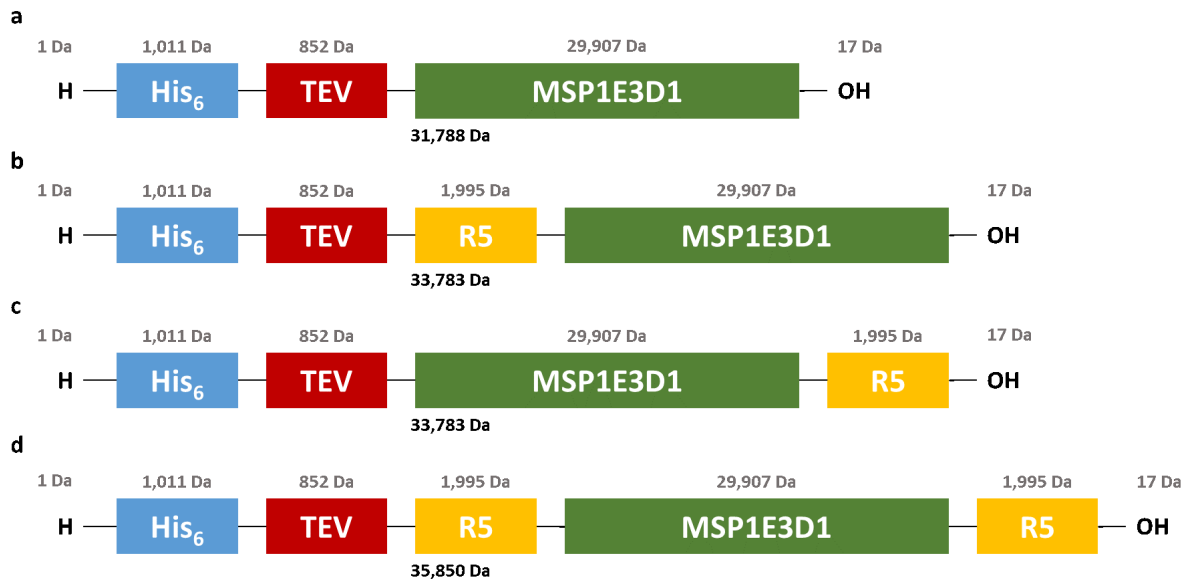


Fig. 4.2.1 | Schematic representation of the modified membrane scaffold protein sequences. a, MSP. b, R5-MSP. c, MSP-R5. d, R5-MSP-R5.

To obtain these constructs the MSP1E3D1-containing pET28a plasmid was sequenced with the T7 terminator and T7 promoter primers and the sequence searched for unique restriction sites. Four sites (NcoI, BmgBI, EcoRI and NotI) were identified in the insert (see fig. 4.2.2a). The translated insert sequence is shown in figure 4.2.2b with the protein of interest marked in black. A test digest was then performed on the plasmid (as described in section 3.4.13) with these enzymes to confirm the location of the recognition sites. The resulting gel is shown in figure 4.2.2c. As expected, the plasmid is linearized when digested with any of the restriction endonucleases, leading to the appearance of a single band around 5,000 bp. When performing the dual digest with NcoI and EcoRI, a 116 bp fragment is cut out; the dual digest with BmgBI and NotI leads to the appearance of a fragment with 212 bp slightly higher on the gel. Accordingly, these restriction sites were used to introduce inserts with the desired N- and C-terminal modifications contained in the sequence.



Fig. 4.2.2 | MSP1E3D1 sequence. **a**, sequencing results with recognition sites for NcoI (blue), EcoRI (red), BmgBI (yellow), and NotI (green). **b**, derived amino acid sequence with the translated protein marked in black. **c**, test digest of the MSP1E3D1-pET28a plasmid. Lanes: NcoI (1), EcoRI (2), NcoI + EcoRI (3), BmgBI (4), NotI (5), BmgBI + NotI (6). The cut-out fragments are marked with boxes.

The inserts were designed to introduce a TEV-protease cleavage site (ENLYFQG) in between the N-terminal His-tag and the protein sequence and to introduce N- and C-terminal R5-tags (see fig. 4.2.3). The desired amino acid sequences were reverse translated into nucleotide sequences and the restriction sites added.

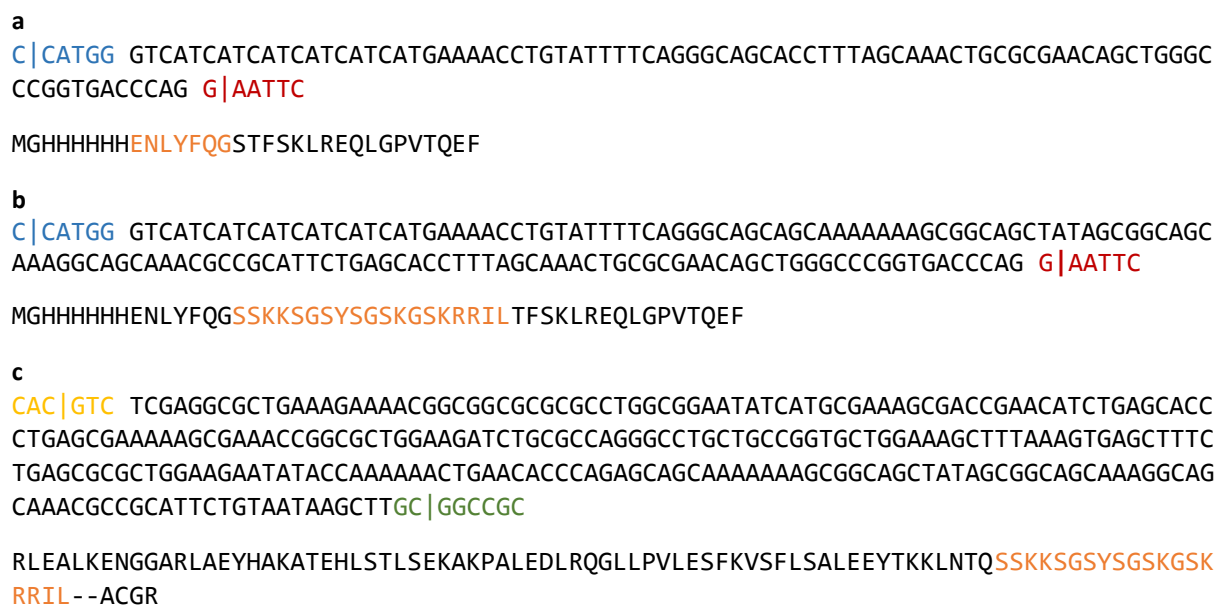


Fig. 4.2.3 | Insert design. **a**, nucleotide sequence of the N-terminal TEV-site insert with the recognition sites for NcoI (blue) and EcoRI (red) and translated amino acid sequence with the TEV protease cleavage site marked in orange. **b**, nucleotide sequence of the N-terminal R5 insert with the recognition sites for NcoI (blue) and EcoRI (red) and translated amino acid sequence with the R5 peptide sequence marked in orange. **c**, nucleotide sequence of the C-terminal insert with the recognition sites for BmgBI (yellow) and NotI (green) and translated amino acid sequence with the R5 peptide sequence marked in orange.

Ligation of the inserts into the MSP1E3D1-pET28a plasmid was performed as described in the methods section and identity of the resulting plasmids confirmed by sequencing. The properties of the resulting proteins of interest are summarized in table 4.2.1. The obtained plasmids were then transformed into several *E. coli* expression strains in order to find a suitable strain for overexpression.

Table 4.2.1 | Properties of the MSP variants constructed in this work before and after the cleavage of the His-tag at the TEV protease recognition site.

protein	number of aa	MW	pI	ϵ_{280nm}
His ₆ -TEV-MSP	269	31,657 Da	6.00	28,420 M ⁻¹ cm ⁻¹
MSP	256	29,982 Da	5.76	26,930 M ⁻¹ cm ⁻¹
His ₆ -TEV-R5-MSP	288	33,652 Da	6.77	29,910 M ⁻¹ cm ⁻¹
R5-MSP	275	31,977 Da	6.82	28,420 M ⁻¹ cm ⁻¹
His ₆ -TEV-MSP-R5	288	33,652 Da	6.77	29,910 M ⁻¹ cm ⁻¹
MSP-R5	275	31,977 Da	6.82	28,420 M ⁻¹ cm ⁻¹
His ₆ -TEV-R5-MSP-R5	307	35,647 Da	8.91	31,400 M ⁻¹ cm ⁻¹
R5-MSP-R5	294	33,972 Da	9.06	29,910 M ⁻¹ cm ⁻¹

4.2.2 Expression and purification of MSP constructs

R5-MSP-R5

Expression tests were performed in different *E. coli* strains. Figure 4.2.4 shows the results of test expressions of R5-MSP-R5 in BL21 (DE3) Rosetta 2, BL21 (DE3) pLysS, BL21 (DE3) Gold, and BL21 (DE3) for 1 h to 18 h at 37 °C. As expected, a band is observed at approximately 36 kDa, corresponding to the molecular weight of the protein of interest (compare table 4.2.1). In the strains BL21 (DE3) Gold and BL21 (DE3) it is visible already in the first samples, taken before induction of the expression with 1 mM IPTG. In contrast, the strains BL21 (DE3) Rosetta 2 and BL21 (DE3) pLysS expressed the protein of interest only after the addition of IPTG. However, in the Rosetta 2 strain, the band is much more intense, indicating higher overexpression. After expression overnight, however, an additional band is observed at approximately 22 kDa, and the R5-MSP-R5 band is weaker than in the sample taken after 3 h expression. This indicates that a fraction of the protein is already degraded. Thus, it was decided to express the R5-MSP-R5 protein in the BL21 (DE3) Rosetta 2 strain for 3 h.

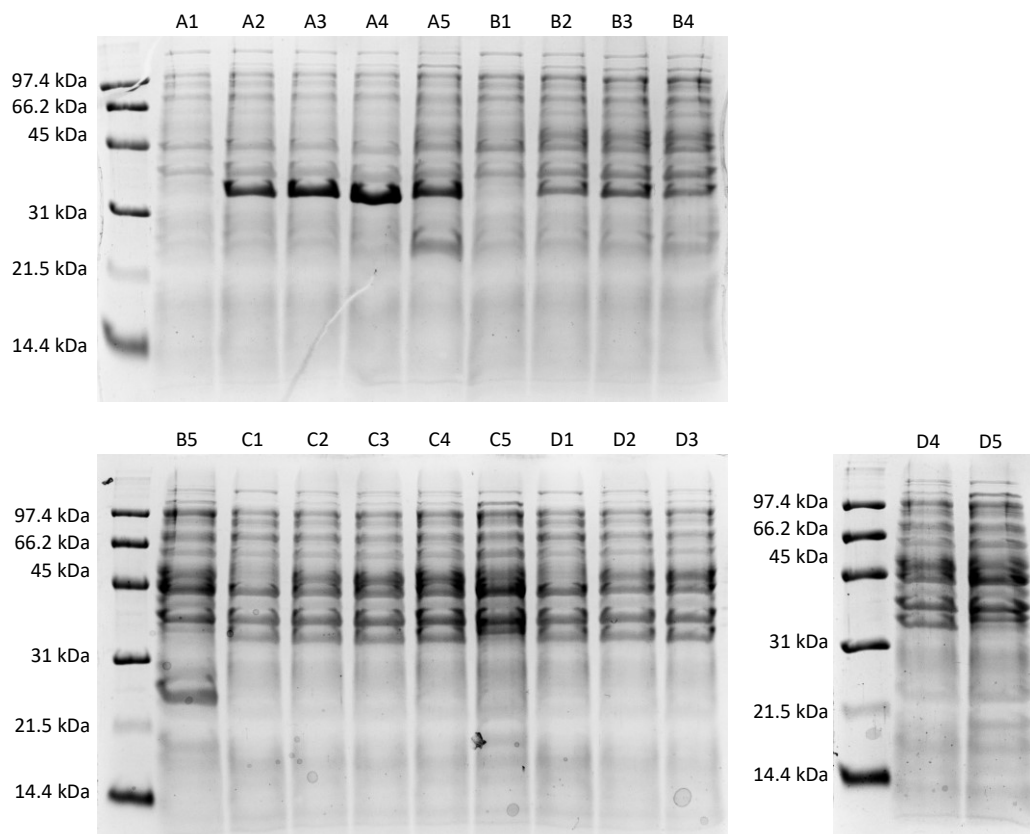


Fig. 4.2.4 | SDS-PAGE of R5-MSP-R5 test expressions. Four different strains were used: BL21 (DE3) Rosetta 2 (A), BL21 (DE3) pLysS (B), BL21 (DE3) Gold (C), and BL21 (DE3) (D). Samples were taken before induction (1) and 1 h (2), 2 h (3), 3 h (4), and 18 h (5) after induction with 1 mM IPTG.

Based on these findings, the R5-MSP-R5 construct was successfully expressed from the *E. coli* BL21 (DE3) Rosetta 2 strain, as described in the methods section. After expression for 3 h at 37 °C, the bacteria were lysed using the cell disrupter and the cleared lysate purified by Ni-NTA affinity chromatography, then treated with TEV protease and re-purified as described in the methods section (compare fig. 4.2.5a). Protease cleavage was confirmed by SDS-PAGE (see fig. 4.2.5b). The final analysis was performed by LC-MS and the deconvoluted mass spectrum shows the expected mass of 33,972 Da (see fig. 4.2.5c). In a typical expression, 8.45 mg/l of protein were obtained, of which 6.10 mg/l (76%) were recovered after TEV protease cleavage.

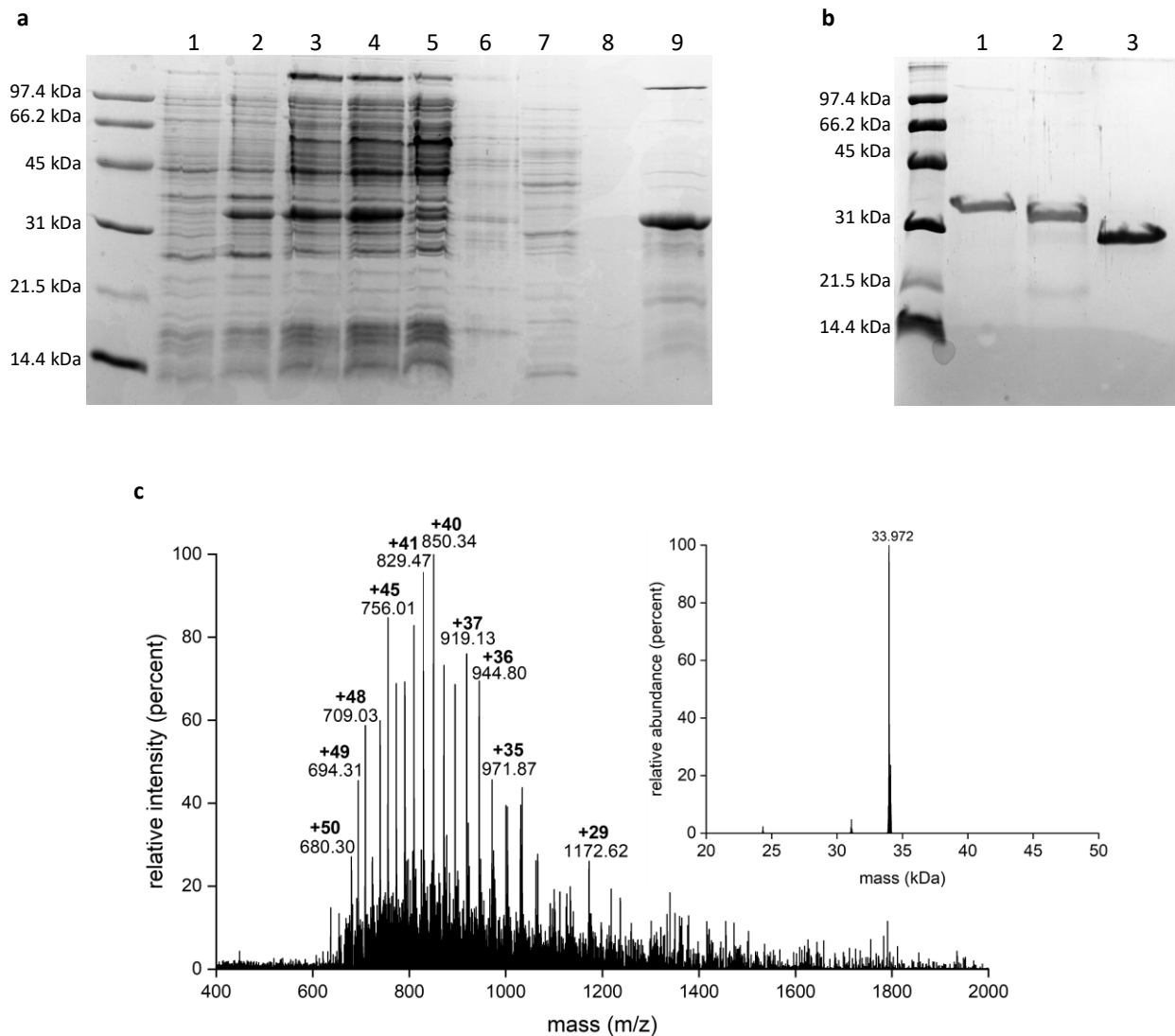


Fig. 4.2.5 | Expression and purification of R5-MSP-R5 in Rosetta (DE3). **a**, Samples taken: before induction (1), after 3 h expression (2), lysate (3), supernatant (4), flow-through (5), wash 1-3 (6-8), eluent (9). **b**, Samples taken before (1) and after (2) TEV digest, TEV protease (3). **c**, Mass spectrum and deconvoluted mass spectrum (insert) of the cleaved R5-MSP-R5 protein (calc. mass 33,972 Da), from LC-MS.

R5-MSP

The expression of the R5-MSP construct was tested in the *E. coli* strains BL21 (DE3) and BL21 (DE3) Rosetta 2 at 37 °C. After induction with 1 mM IPTG, no additional band is visible on the resulting gel and after 6 h of expression, still no band is visible at 34 kDa (see figure 4.2.6). No purification was therefore possible. It is not clear why the overexpression of R5-MSP should not be possible. Since the bacteria are kanamycin resistant, the plasmid has to be present. It has also been used in the construction of R5-MSP-R5, which was successfully expressed, so the lac-operon could not have been damaged. It is therefore unclear why the induction of expression failed.

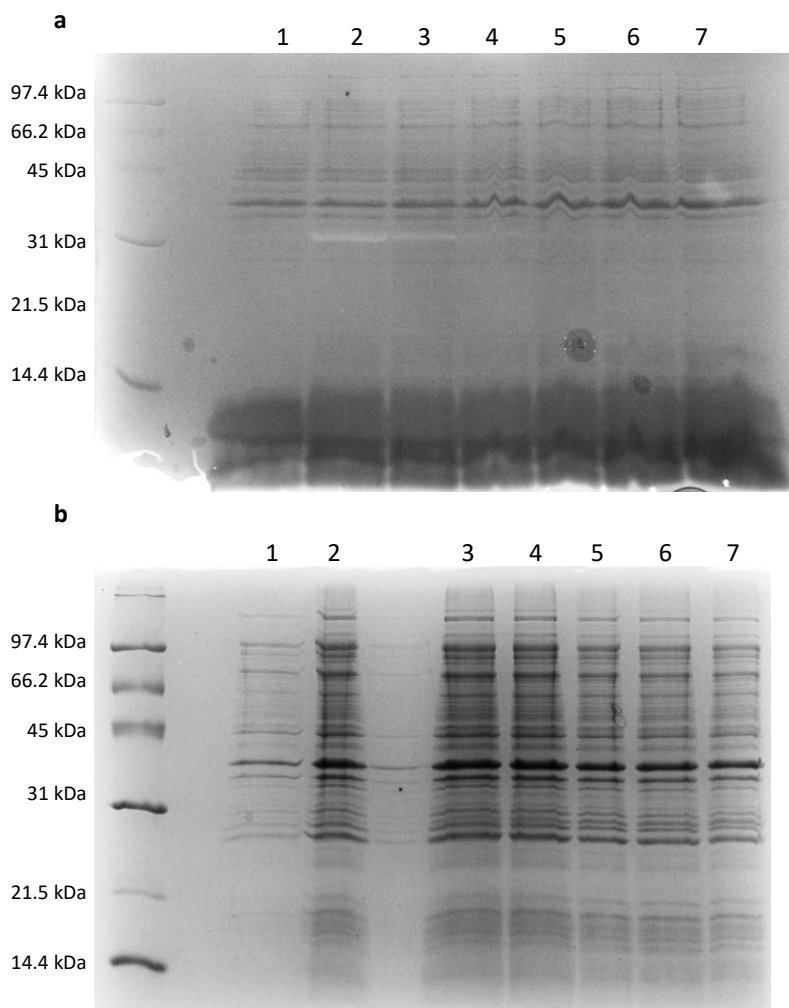


Fig. 4.2.6 | Expression test with the R5-MSP plasmid in BL21 (DE3) (a) and BL21 (DE3) Rosetta 2 (b). Samples were taken before induction (1) and 1 h (2), 2 h (3), 3 h (4), 4 h (5), and 6 h (7) after induction with 1 mM IPTG.

MSP-R5

The expression of MSP-R5 was initially successful, as shown in figure 4.2.7a. The SDS-PAGE shows clear induction of a band appearing at 34 kDa. However, during purification, two bands were co-purified and could not be separated from each other (fig.4.2.7b). Of this mixture, 10.14 mg/l culture were obtained. This was then cleaved using TEV protease, which yielded 9.10 mg/l of cut protein mixture. The LC-MS analysis (fig. 4.2.5c) reveals the presence of a second protein with 24 kDa in addition to the POI. This is most likely a fragment caused by degradation of the construct, but it is unclear why this occurs only in this variant.

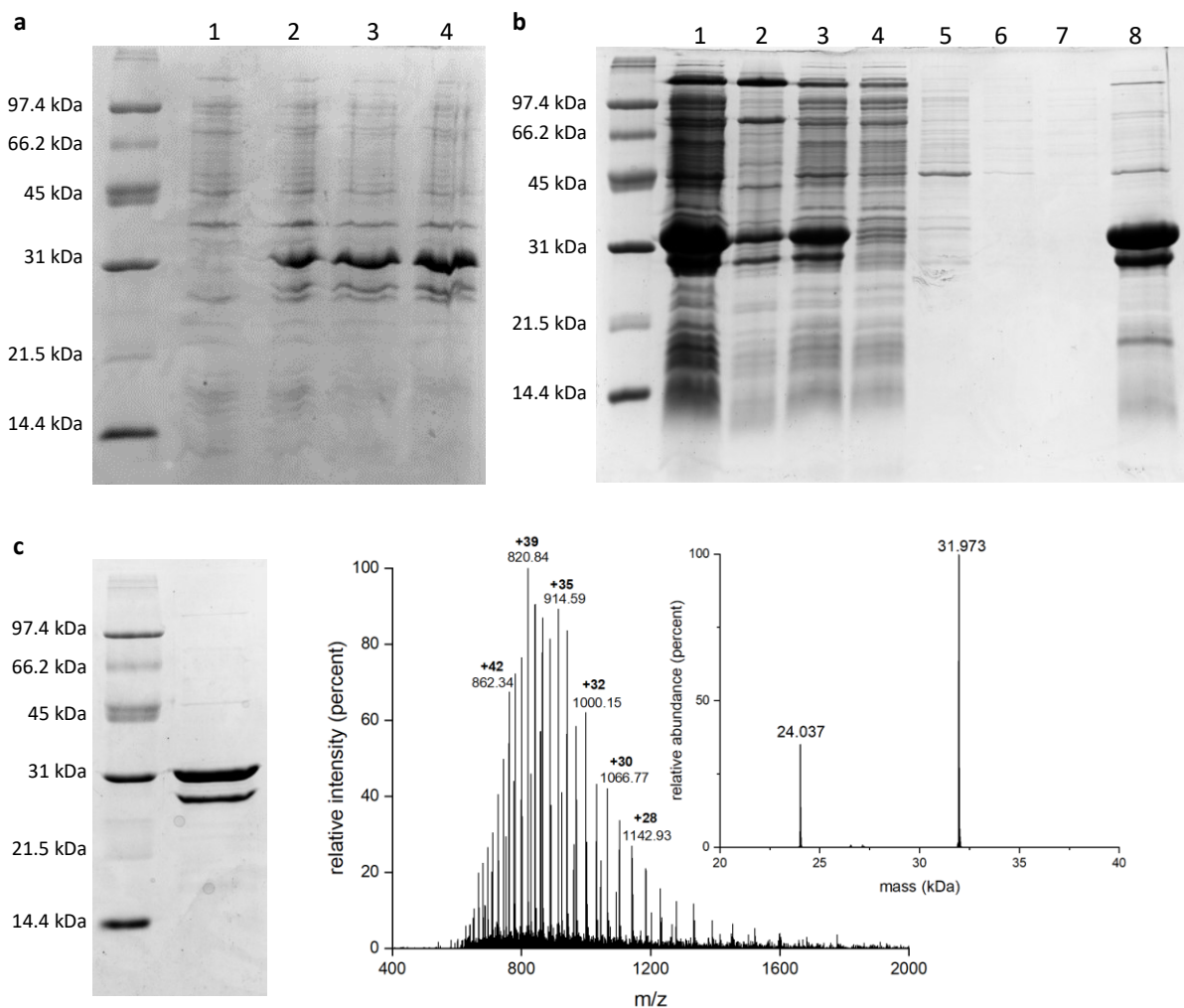


Fig. 4.2.7 | Expression and purification of the MSP-R5 plasmid in BL21 (DE3) Rosetta 2. **a**, overexpression, samples taken before induction (1) and 1 h (2), 2 h (3), 3 h (4) after induction with 1 mM IPTG. **b**, purification, samples: lysate (1), pellet (2), supernatant (3), flow-through (4), wash 1-3 (5-7), and eluent (8). **c**, purified product. SDS-PAGE and mass spectrum from LC-MS with deconvolution (insert).

MSP

Since the R5-MSP and MSP-R5 variants could not be obtained, the new R5-MSP-R5 construct could only be compared to the unmodified MSP, which was expressed and purified according to the literature¹⁹² and yielded the analysis results shown in figure 4.2.8. The deconvoluted mass spectrum shows that the desired product could be obtained (calc. mass 29,982 Da), however, there are some minor impurities as seen in the SDS-PAGE of the purified product (see fig. 4.2.8a). The circular dichroism of the proteins R5-MSP-R5 and MSP was then analysed to find out if the new variant adopts the same conformation.

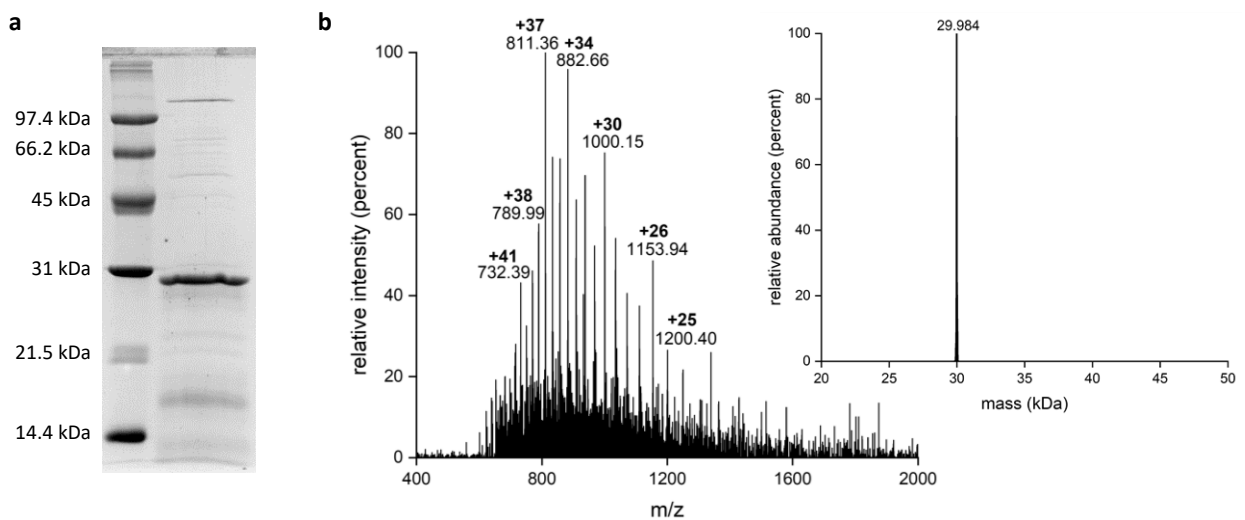


Fig. 4.2.8 | Analysis of MSP. Mass spectrum and deconvoluted mass spectrum (insert) of the MSP protein (calc. mass 29,982 Da), from LC-MS.

4.2.3 Circular dichroism

The two variants were diluted to 10 μM concentration and the CD-spectra measured. Both show minima at 210 nm and 222 nm, indicating an alpha helical conformation (see fig. 4.2.9). The curve shape of both variants is nearly identical. Thus, the presence of the R5 tags does not seem to obstruct the native conformation of the MSP protein. Based on this analysis, it was assumed that both constructs form nanodiscs in the presence of phospholipids, which was then tested.

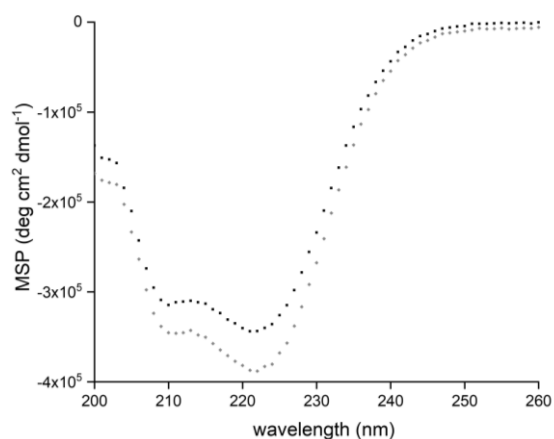


Fig. 4.2.9 | CD spectra of the MSP (black squares) and R5MSPR5 (grey diamonds) proteins at 10 μM concentration.

4.2.4 Nanodisc formation

Nanodiscs were prepared as described in the methods section, using DOPC as membrane lipid and sodium cholate as detergent. Transmission electron microscopy revealed the presence of nanodiscs in the samples with MSP (fig. 4.2.10a) as well as R5-MSP-R5 (fig. 4.2.10b), which appear either as circles, when the nanodiscs are lying flat on the carbon film surface, or as alternating dark and light stripes, indicating toppled stacks of nanodiscs, as was described previously as 'rouleaux'¹⁹⁷. The nanodiscs made with the MSP protein have an average diameter of 14.1 ± 0.2 nm (average of 70 individual discs), whereas those made from the modified R5-MSP-R5 are slightly larger with 14.8 ± 0.3 nm (average of 92 individual discs).

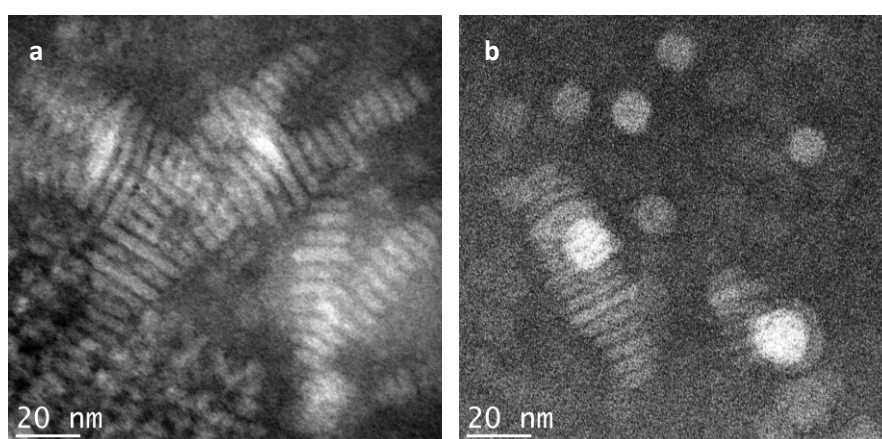


Fig. 4.2.10 | Transmission electron micrographs of nanodiscs created with the two MSP variants. **a**, MSP nanodiscs, which are visible mainly as toppled stacks. **b**, R5-MSP-R5 nanodiscs, which are a mixture of nanodisc stacks and individual nanodiscs lying flat.

A second analysis was performed by imaging the R5-MSP-R5 nanodiscs on a mica surface using atomic force microscopy (AFM). Nanodiscs appear as dots in the resulting picture (see fig. 4.2.11a). A line plot (fig. 4.2.11b) shows areas covered by discs at approximately 8 nm height and free areas at approximately 2 nm height, revealing the thickness of the discs, which is approximately 6 nm and thus in good agreement with the values published for the MSP nanodiscs, 5.6 – 5.9 nm¹⁹². This further indicates that a single layer of individual nanodiscs is present on the surface. Further analysis was performed to measure individual nanodiscs in solution.

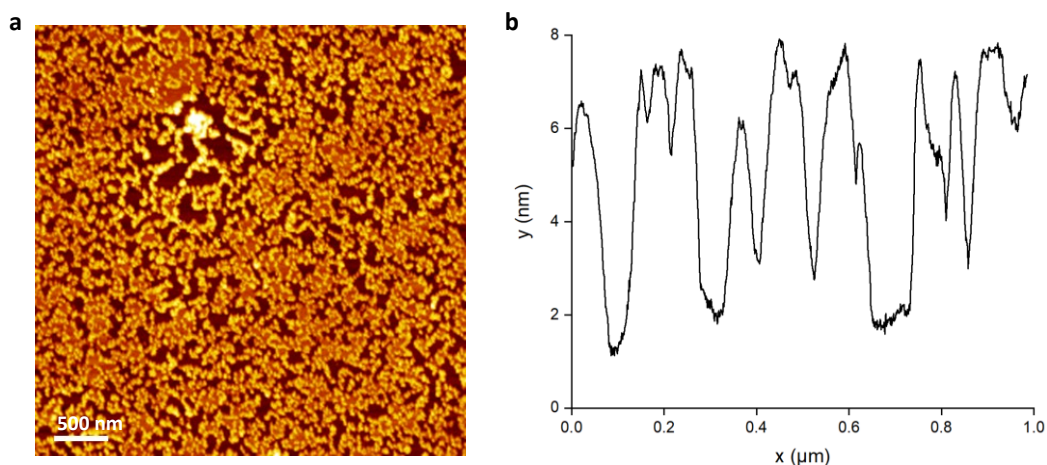


Fig. 4.2.11 | AFM analysis of R5-MSP-R5 nanodiscs. **a**, Individual nanodiscs are visible as dots on a mica surface. **b**, A line plot reveals areas covered by nanodiscs are approximately 6 nm higher than free areas. The plot was generated using the Gwyddion software.

To measure nanodisc dimensions in bulk and to validate these observations by a third method, solutions with the nanodisc variants were subjected to dynamic light scattering (DLS). This technique measures the hydrodynamic diameter of particles or polymers suspended or dissolved in a liquid. It is expected that the hydrodynamic diameter is higher than the size observed in TEM because it increases when the particle is surrounded by a dipole layer in the solvent. For the MSP nanodiscs, a maximum at 15.9 nm was measured (fig. 4.2.12a), confirming this expectation. However, the maximum for the R5-MSP-R5 nanodiscs is at only 11.4 nm (fig. 4.2.12b), even though under the electron microscope, they appear smaller. A possible explanation might be that due to the increased polarity of the R5-MSP-R5 the solvent layer is thinner, and they are able to move faster in solution. Still, both measurements are in the expected range between 10 nm and 20 nm, which indicates that individual nanodiscs are present in solution as well.

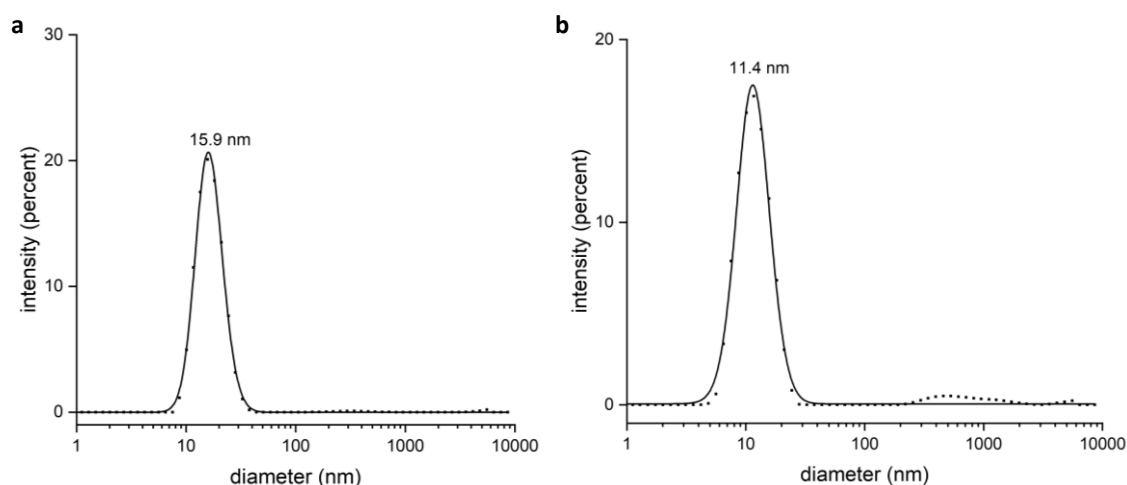


Fig. 4.2.12 | Size distributions of MSP nanodiscs (a) and R5-MSP-R5 nanodiscs (b) prepared with DOPC.

4.2.5 Silica precipitation

With the nanodisc variants in hand it was then investigated if they lead to silica particle formation. The R5-MSP-R5 protein or the nanodiscs were transferred to 50 mM potassium phosphate buffer pH 7 using a Zeba spin desalting column (0.5 mL, 7 kDa MWCO), according to protocol. The protein concentration was measured and adjusted to 1 mg/mL by diluting with 50 mM potassium phosphate buffer pH 7. To 90 μ L of the resulting precipitation solution, 10 μ L of freshly prepared silicic acid (960 μ L 1 mM HCl, 40 μ L TMOS, hydrolysed for 4 min) were added. The mixture was incubated for 30 min at room temperature. Samples for TEM were spotted directly from this solution. Under these conditions it was possible to precipitate silica particles with both the purified R5-MSP-R5 protein as such as well as with the nanodiscs created from it. The MSP protein and MSP nanodiscs did not lead to the formation of particles. The R5-MSP-R5 silica particles are irregularly structured with pores in the range of 100 nm (see figure 4.2.13).

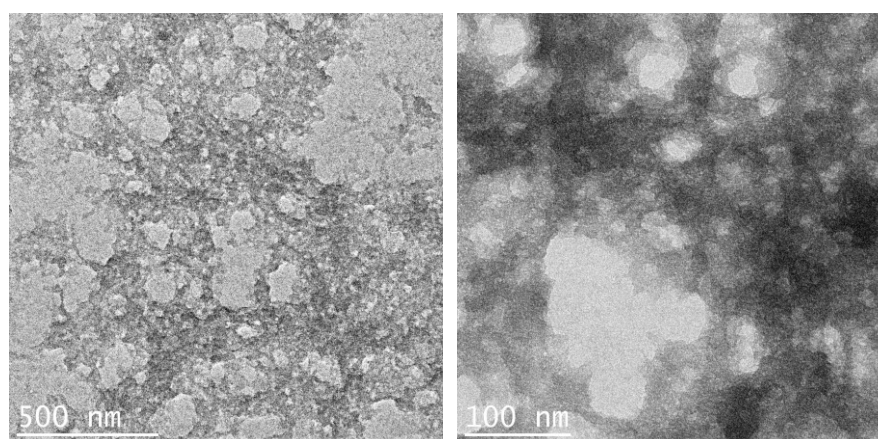


Fig. 4.2.13 | Transmission electron micrographs of silica particles precipitated with the R5-MSP-R5 protein at increasing magnification.

In contrast, the silica-stabilized nanodiscs lead to a fibrillar morphology. TEM analysis of the precipitate reveals a loose structure composed of striated fibers, most likely corresponding to stacks of nanodiscs covered in silica (see fig. 4.2.14a-b). The arrows point to a bundle of fibers in a, and several individual fibers forming a bundle in b. Measurements of 16 individual fibers reveal an average diameter of 23.8 ± 1.1 nm, which is enough for the accommodation of entire nanodiscs. A line plot shows that the striations seen on the fibrils are approximately 6 nm apart (fig. 4.2.14c), further indicating that nanodiscs stacks form the core of the fibre.

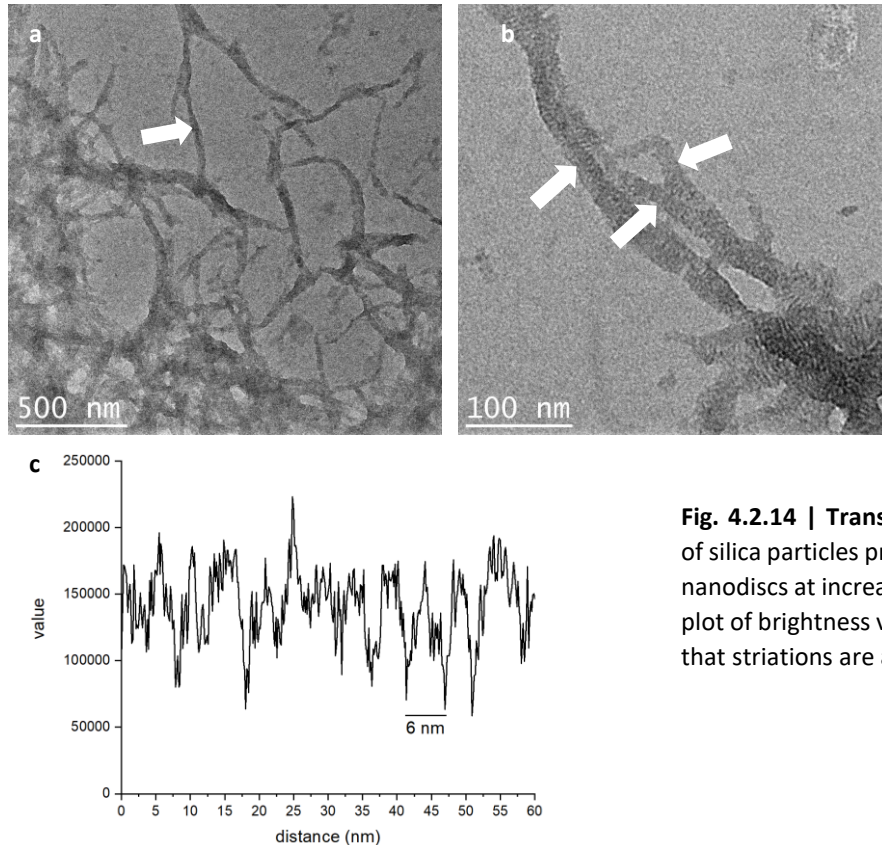


Fig. 4.2.14 | Transmission electron micrographs of silica particles precipitated with the R5-MSP-R5 nanodiscs at increasing magnification (**a**, **b**). A line plot of brightness values (**c**) along one fibril shows that striations are approximately 6 nm apart.

Again, the sample was also imaged using AFM (see fig. 4.2.15). Again, fibrillar structures could be observed, which correspond to those seen using TEM. However, the AFM image is less finely resolved.

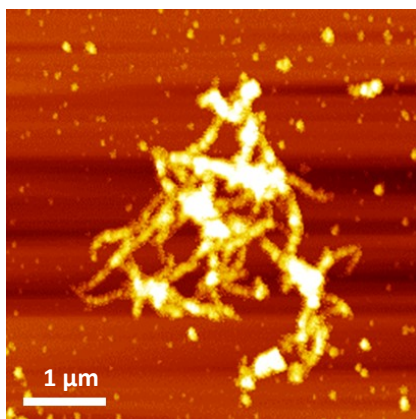


Fig. 4.2.15 | Atomic force microscopy image of silica-covered nanodisc fibrils.

4.2.6 Nanodisc loading

After showing that the nanodiscs could indeed be incorporated into silica particles, it was attempted to embed the integral membrane protein diacylglycerol kinase in these stabilized nanodiscs. Accordingly, the nanodisc formation procedure was repeated with DGK added. For example, the following mixture was prepared:

- 500 μ l R5-MSP-R5 (2.095 mg/ml)
- 80,7 μ l DOPC solution (50 mM DOPC, 100 mM NaCl, 100 mM sodium cholate)
- 310 μ l DGK 3.2 (2.121 mg/ml)

This corresponds to 31 nmol (1 eq.) R5-MSP-R5, 4,0 μ mol (131 eq.) DOPC, and 46 nmol (1.5 eq.) of DGK. The mixture was incubated and dialysed as before. It was then attempted to purify the nanodiscs, which contain DGK, using a Ni-NTA column (1 mL). The sample was loaded onto the column and a gradient from 0 – 100% MSP Elution buffer in MSP Washing buffer 3 was used to elute the nanodiscs. However, a peak was obtained already in the flow-through, showing that the nanodiscs did not bind to the column. Subsequent SDS-PAGE analysis of the flow-through and the eluent did also not show any DGK band (see figure 4.2.16).

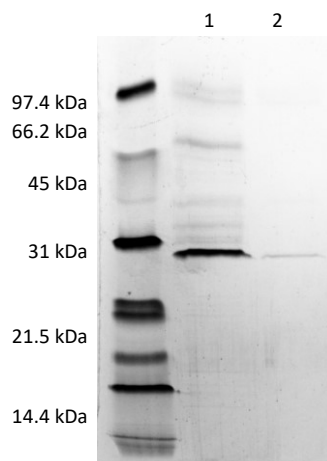


Fig. 4.2.16 | SDS-PAGE of the Nanodiscs with DGK after Ni-NTA column purification. 1 – flow-through, 2 – eluent.

An activity assay performed with the nanodiscs (as described in section 3.4.23) did not show any activity. Thus, it was concluded that the DGK is not embedded in the nanodiscs under these conditions and a different strategy using beta-sheet peptides was used to embed the enzyme.

4.3 Modified amphiphilic BP-1 peptides for the direct encapsulation of membrane proteins in silica

4.3.1 Synthesis and characterization of modified BP-1-peptides

Four new constructs were designed from the BP-1 peptide by introducing one of two different silica-precipitating tags, the full-length R5 peptide from *C. fusiformis* or its five N-terminal amino acids, at either the N- or the C-terminus (see fig. 4.3.1).

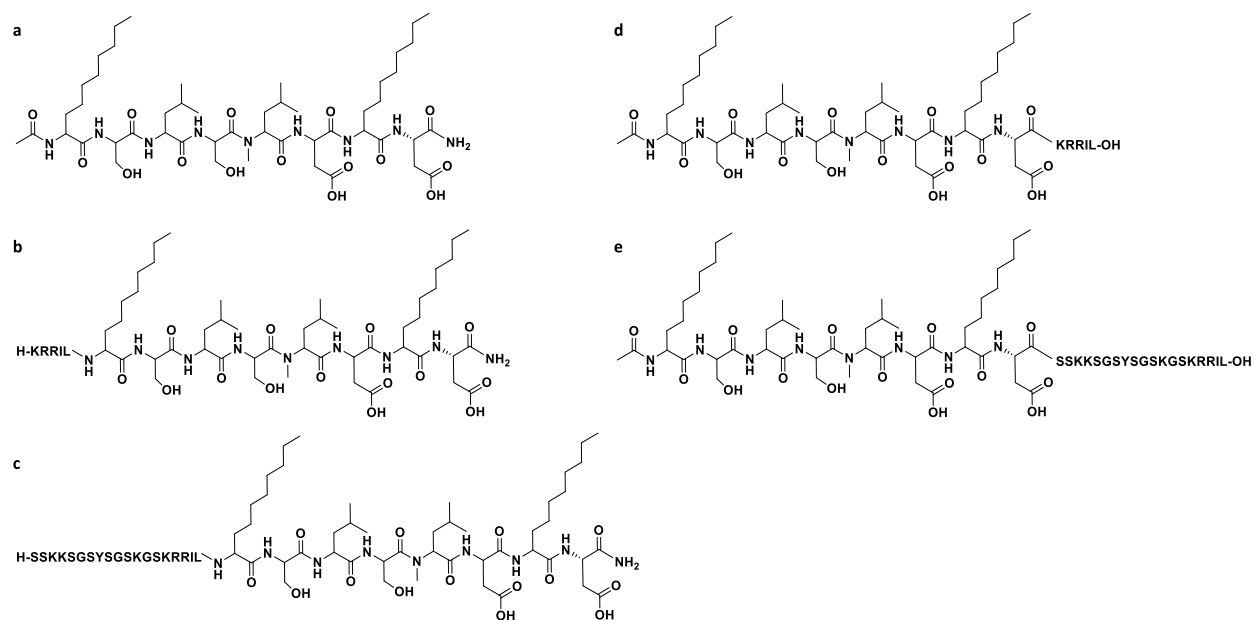


Fig. 4.3.1 | Amino acid sequences of the modified BP-1 peptides. a, BP-1. b, KRRIL-BP-1. c, R5-BP-1. d, BP-1-KRRIL. e, BP-1-R5. Non-canonical amino acids are in italics, the silica-precipitating tags are underlined.

SPPS was performed as described by Tao et al. for the BP-1 peptide²¹⁶ on a Rink Amide AM resin (100-200 mesh) for the BP-1, KRRIL-BP-1, and R5-BP-1 peptides and on a Wang resin (100-200 mesh) pre-loaded with Leucine for the BP-1-KRRIL and BP-1-R5 peptides. Amino acid activation was performed with HATU for N-methyl-L-leucine and HCTU for all other amino acids. Double couplings were performed for the serine following N-methyl-L-leucine. After cleavage from the resin, the new variants could be precipitated in diethyl ether as described in the methods section. The unmodified BP-1 peptide, however, did not precipitate under these conditions due to its low polarity. Accordingly, for this peptide, the cleavage solution was diluted in 100 times its volume of water/ACN (1:1) and lyophilized to obtain the crude product.

The unmodified BP-1 peptide was synthesized successfully according to the protocol by Tao *et al.* and purified by RP-HPLC²¹⁶. It was obtained in 41% - 60% yield; in one example, 31.2 mg (29.9 μ mol) of purified peptide were obtained from a synthesis performed at 50 μ mol scale. No yield is provided in the original publication.

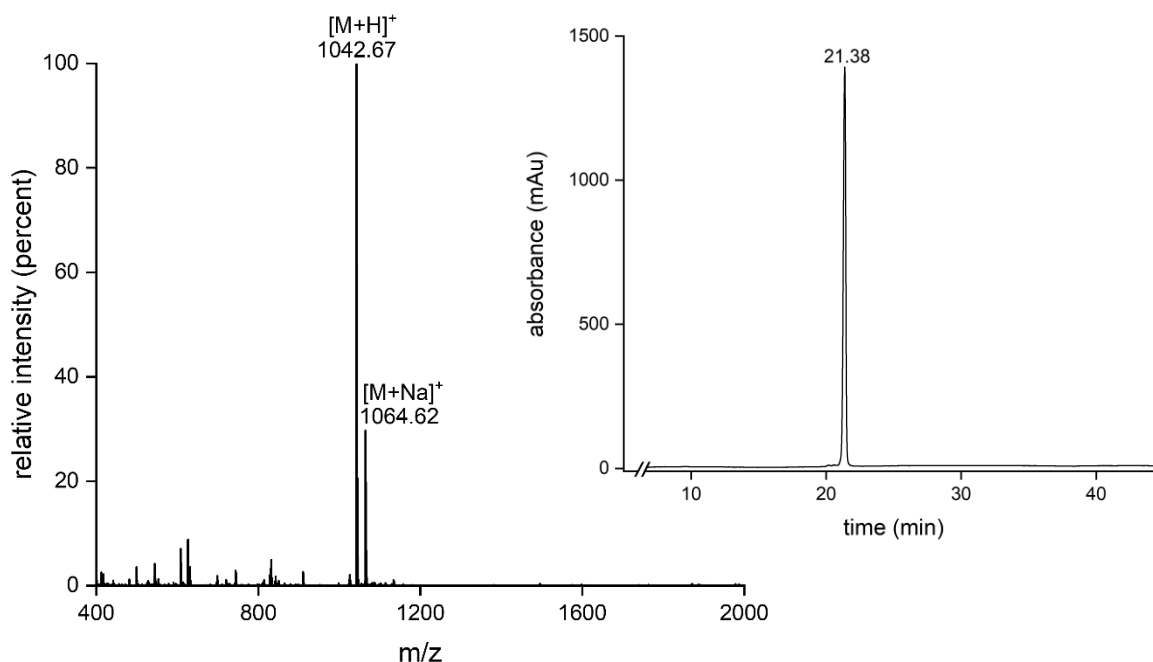


Fig. 4.3.2 | BP-1 final analysis. Mass spectrum (left) and HPLC chromatogram (insert). The injection peak was cut off.

The mass spectrum (see fig. 4.3.2) shows the $[M+H]^+$ -ion of the desired peptide (m/z (calc.): 1042.64). There is also a species at 1064.62, with 30% intensity, corresponding to the sodium adduct $[M+Na]^+$ (m/z (calc.): 1064.62). The HPLC chromatogram shows a single sharp peak, which indicates that the peptide was obtained in excellent purity. However, there are some peaks in the 400 – 800 m/z range of the mass spectrum which could not be assigned.

The KRRIL-BP-1 peptide was also synthesized successfully as described above. It was obtained in 35% - 88% yield; in one example, 73.7 mg (44.2 μmol) of purified peptide were obtained from a synthesis with a 50 μmol scale. The results of the HPLC analysis and the mass spectrum are shown in figure 4.3.3. The mass spectrum shows the two expected peaks for the $[M+2H]^{2+}$ (m/z (calc.): 834.05) and $[M+H]^+$ ions (m/z (calc.): 1667.09). However, there are again some minor peaks in the 400 – 800 m/z range which could not be assigned. The chromatogram shows a single peak, indicating that this product was also obtained in high purity.

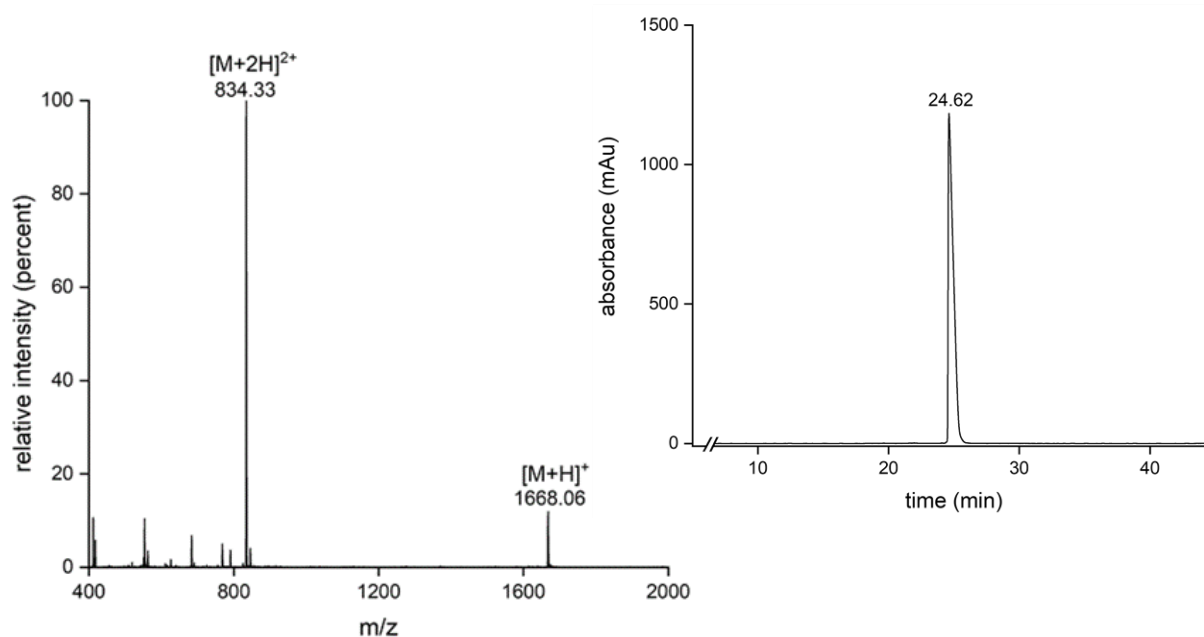


Fig. 4.3.3 KRRIL- BP-1 final analysis. Mass spectrum (left) and HPLC chromatogram (insert). The injection peak was cut off.

The BP-1-KRRIL peptide was obtained in 11% yield; in one example, synthesis on a 50 μmol scale yielded 9.7 mg (5.7 μmol) of purified peptide. The reason for the low yield is likely the low solubility of the compound and its tendency to aggregate which might have caused oligomers which did not elute with the monomer. The analytical data is shown in figure 4.3.4. The mass spectrum shows the three expected peaks for the $[M+3H]^{3+}$ (m/z (calc.): 570.70) $[M+2H]^{2+}$ (m/z (calc.): 855.55) and $[M+H]^+$ ions (m/z (calc.): 1710.09). Also visible is a dimer of the peptide $[2M+3H]^{3+}$ (m/z (calc.): 1141.06). The LC chromatogram shows a single peak, again indicating that the peptide could be obtained in high purity. However, the purified peptide was hardly soluble.

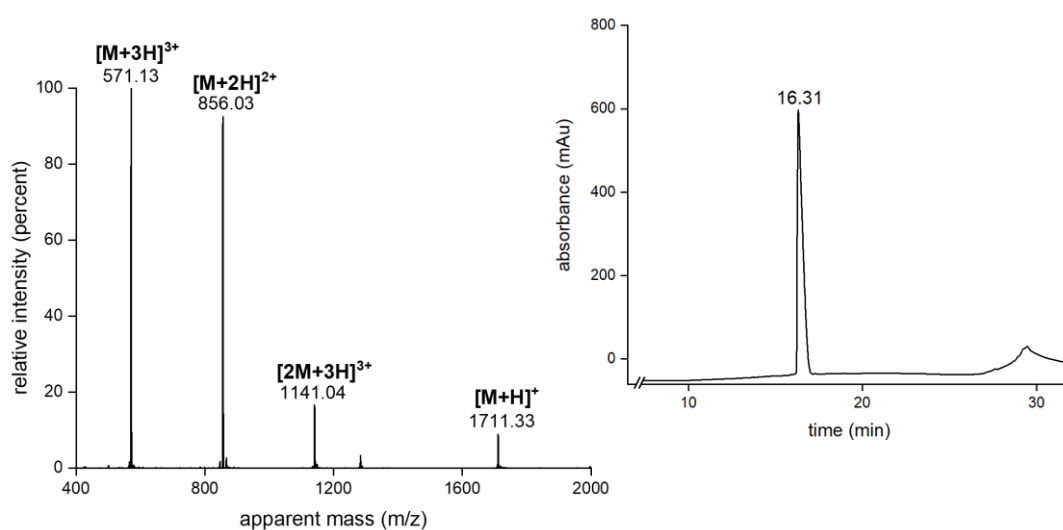


Fig. 4.3.4 BP-1-KRRIL final analysis. Mass spectrum (left) and HPLC chromatogram (insert). The injection peak was cut off.

The R5-BP-1 peptide was also synthesized and purified as described in the methods section. A synthesis at 50 μmol scale resulted in 29.4 mg (9.5 μmol) product, corresponding to a yield of 19%, which is significantly lower than that obtained for the BP-1 and KRRIL-BP-1 peptides. This might simply be because the peptide is longer, and more couplings are necessary. The mass spectrum (see fig. 4.3.5) shows the expected peaks for the $[\text{M}+4\text{H}]^{4+}$ (m/z (calc.): 749.69), $[\text{M}+3\text{H}]^{3+}$ (m/z (calc.): 999.25), and $[\text{M}+2\text{H}]^{2+}$ ions (m/z (calc.): 1498.64). The chromatogram shows a single peak (see fig. 4.3.5), indicating that the peptide could be obtained in good purity.

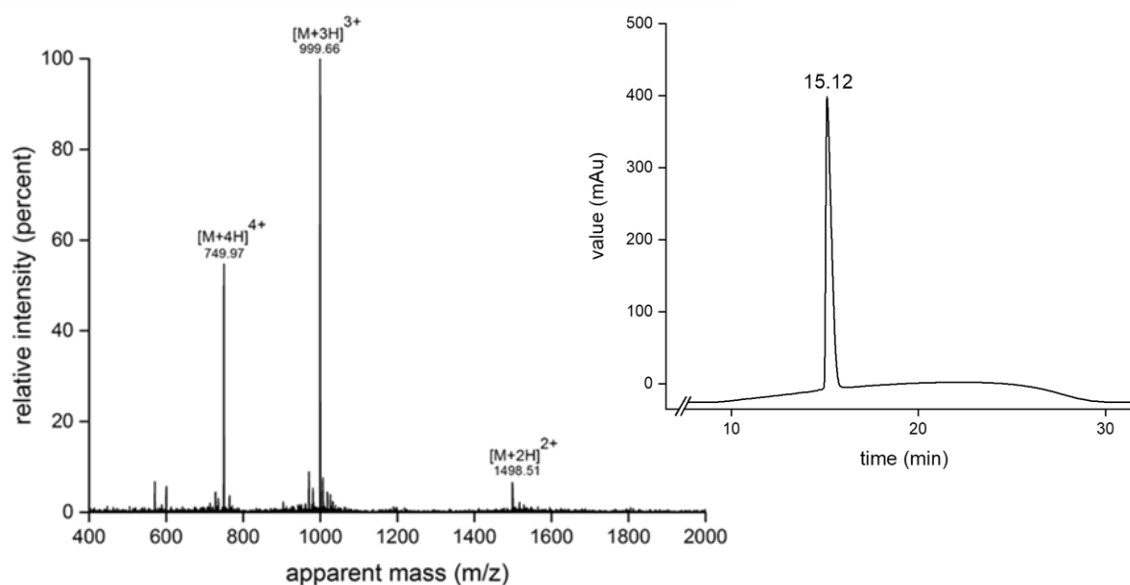


Fig. 4.3.5 | R5-BP-1 BP-1 final analysis. Mass spectrum (left) and HPLC chromatogram (insert). The injection peak was cut off.

The BP-1-R5 peptide was synthesized at 50 μmol scale but only 7.9 mg (2.6 μmol) of purified product (5.2%) were obtained. The low yield was due to a deletion product (M-625), likely missing the 5 N-terminal amino acids, which was separated from the desired product. The HPLC chromatogram shows a single peak and the mass spectrum shows the expected peaks for the $[\text{M}+6\text{H}]^{6+}$ (m/z (calc.): 507.29), $[\text{M}+5\text{H}]^{5+}$ (m/z (calc.): 608.55), $[\text{M}+4\text{H}]^{4+}$ (m/z (calc.): 760.44), $[\text{M}+3\text{H}]^{3+}$ (m/z (calc.): 1013.58), and $[\text{M}+2\text{H}]^{2+}$ ions (m/z (calc.): 1519.87) as shown in figure 4.3.6.

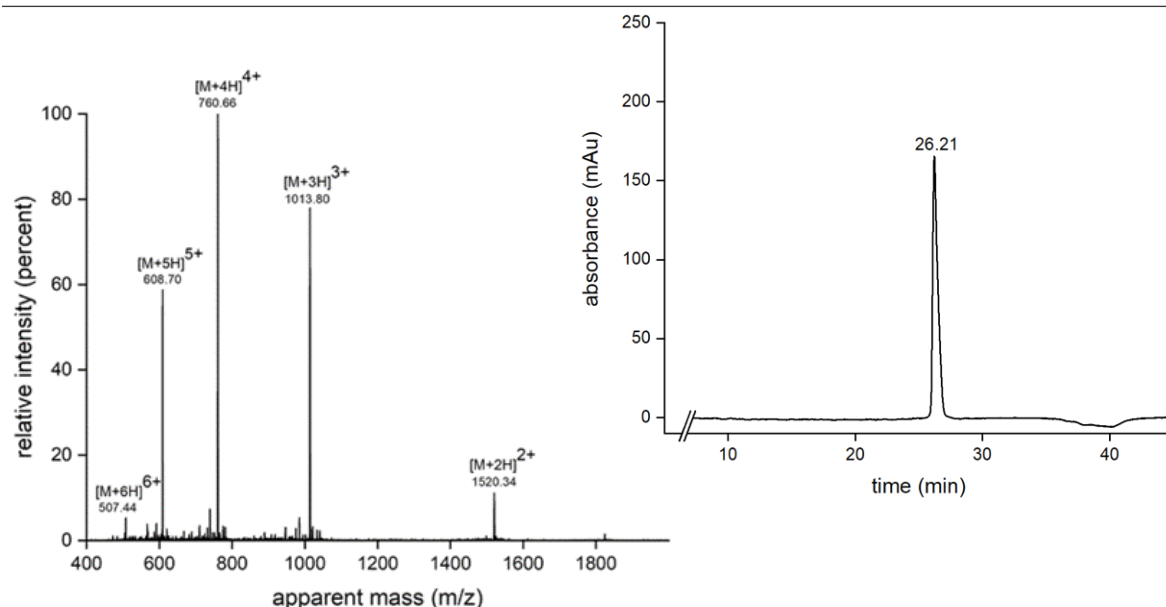


Fig. 4.3.6 | BP-1-R5 final analysis. Mass spectrum (left) and HPLC chromatogram (insert). The injection peak was cut off.

To investigate the folding state of the synthesized peptides, CD spectra were measured as described in the methods section (3.4.21). As expected, the unmodified BP-1 peptide shows a curve shape with a minimum at 220 nm wavelength (see figure 4.3.7a), indicating a β -sheet conformation²⁵⁹, which is in accordance with the literature on BP-1²¹⁶. After replicating the BP-1 CD spectrum as expected, the modified peptides R5-BP-1, BP-1-R5, and KRRIL-BP-1 and BP-1-KRRIL were measured as well. The BP-1-KRRIL peptide was not soluble in the CD buffer and was therefore dissolved by adding 3% ethanol. As can be seen, the curve shape is similar for all variants, which indicates that the modifications do not prevent the peptides from adopting a β -sheet structure. The BP-1-R5 peptide, however, shows an additional drop between 200 – 210 nm, which might be due to self-assembly induced by the C-terminal RRIL-motif. Accordingly, the BP-1-KRRIL peptide shows the same additional drop and the drop at 220 nm is even more shallow, indicating stronger self-assembly, which also explains the low solubility.

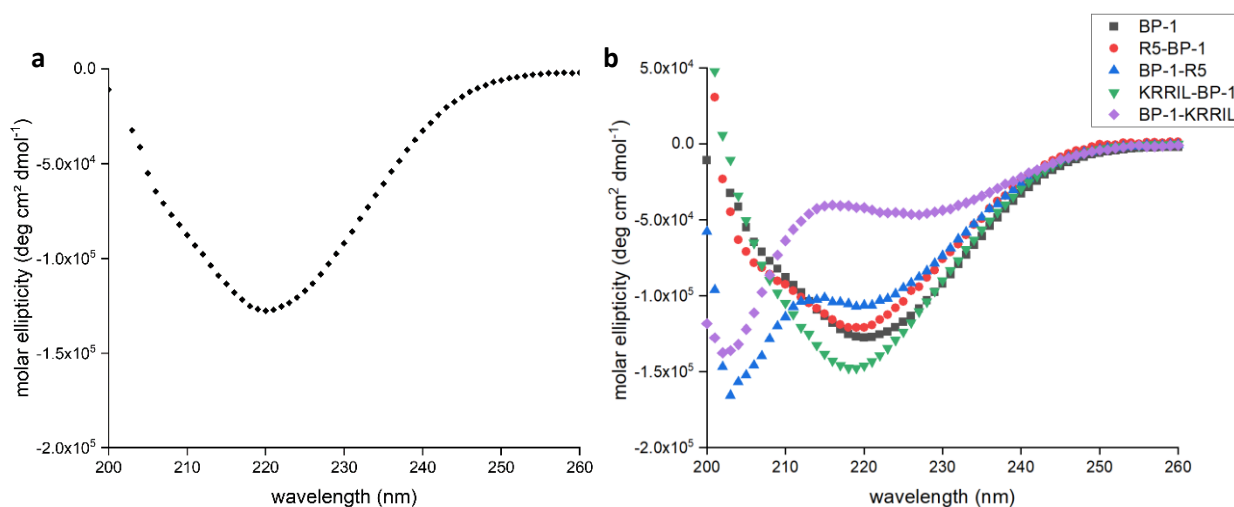


Fig. 4.3.7 | CD spectrum of the BP-1 peptide (a,b) and the modified BP-1 peptides (b) at 0.5 mg/ml.

4.3.2 Silica-precipitation activity of modified BP-1-peptides

The different peptide variants were tested for their induction of silica particle formation as described in the methods section (3.4.8). Under these conditions, no precipitate was observed for unmodified BP-1 peptide. As expected, colourless silica precipitates were observed for the KRRIL-BP-1, R5-BP-1, and BP-1-R5 variants, which were characterized by scanning electron microscopy (SEM) (see figure 4.3.8). The different morphologies of the precipitates are revealed under the microscope: the particles obtained with the KRRIL-BP-1 peptide (see figure 4.3.8a) are fibrillary structures which aggregate to form larger clusters, in contrast, the R5-BP-1 peptide leads to almost spherical particles, some of which aggregate to larger structures (see figure 4.3.8b). The average diameter of the single nanospheres was 316 ± 8 nm as obtained from measurements of 46 individual particles. The BP-1-R5 peptide leads to almost perfectly spherical silica particles (see figure 4.3.8c), which are slightly larger; measurements of 36 individual particles show an average diameter of 408 ± 8 nm. A possible explanation might be that the RRIL motif, which has been shown to play a crucial role in assembly of the R5 peptide²³⁴, is more exposed at the C-terminus of the BP-1-R5 peptide than in the middle of the R5-BP-1 peptide. This would lead to a more symmetrical morphology in the BP-1-R5 peptide assemblies and thus more uniform particle shape. The degree to which the peptides are integrated into the particles was also tested. A sample of the precipitation solution was taken before the addition of silicic acid and compared to a sample of the supernatant after particle precipitation by LC. The results are shown in figure 4.3.8d-e. For the R5-BP-1 and BP-1-R5 samples, the peptide peak from the mixture (grey curves) is completely vanished after precipitation (black curves), indicating full integration of the peptides into the silica particles. For the KRRIL-BP-1 sample, however, no initial peak is observed, indicating that the peptide precipitated over time from the mix even in the absence of silicic acid. Further experiments are needed to verify this conclusion. For example, the precipitated peptide could be resolubilized by the addition of guanidinium before injection.

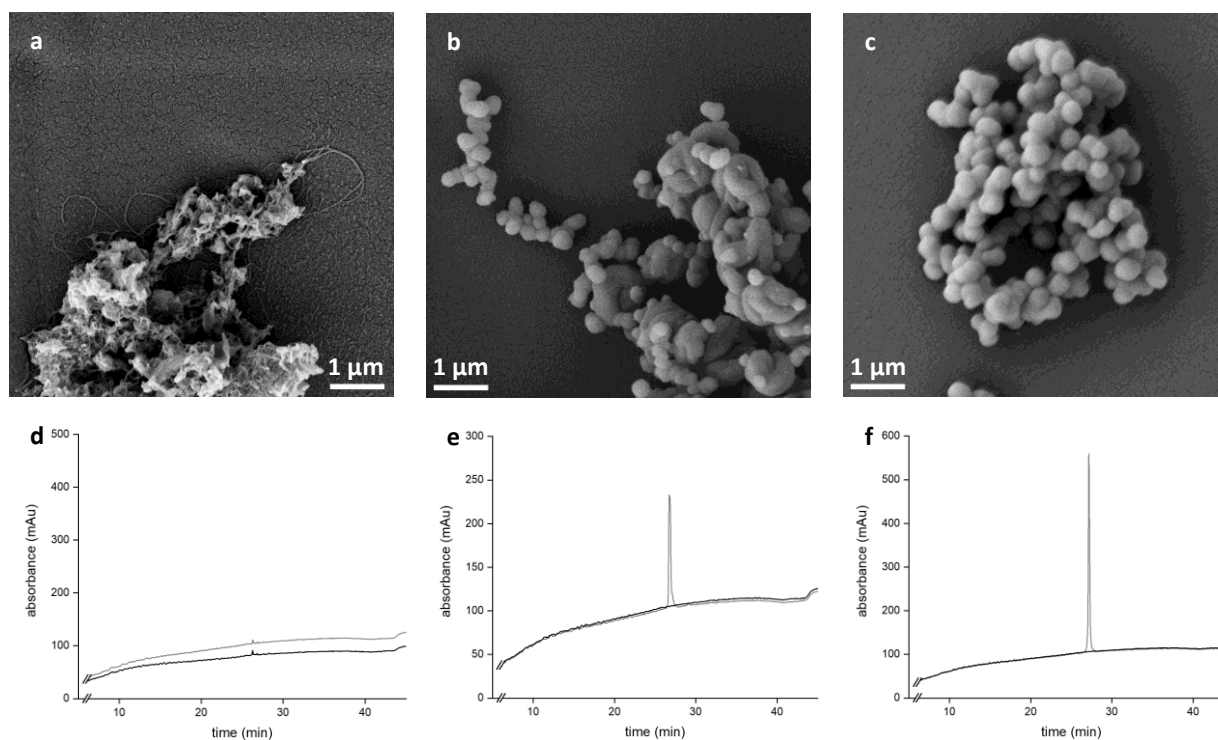


Fig. 4.3.8 | Silica particle formation with modified BP-1 peptides. Scanning electron micrographs (10,000 x magnification) of silica particles precipitated with the peptides KRRIL-BP-1 (a), R5-BP-1 (b), and BP-1-R5 (c). HPLC chromatograms of precipitation mixtures before the addition of silicic acid (grey curve) and of the supernatant after precipitation (black curve) with the peptides KRRIL-BP-1 (d), R5-BP-1 (e), and BP-1-R5 (f).

4.3.3 Expression and purification of diacylglycerol kinase

The available plasmid psD004 was purified from a culture of *E. coli* XL-1 using a miniprep kit and its sequence determined (see fig. 4.3.9a). The membrane protein diacylglycerol kinase (DGK) was then expressed in *E. coli* BL21 (DE3) transformed with the plasmid and purified according to the protocol used by Lau *et al.* as described in the methods section²²¹. The detergent n-octyl- β -D-glucoside (OG) was used to solubilize the protein from the cell walls of the bacteria. The solubilized protein was bound to a Ni-NTA column via its His-tag and eluted using n-dodecyl- β -D-maltoside (DDM), as shown in the SDS-PAGE analysis (see fig. 4.3.9b). The diacylglycerol kinase was obtained in acceptable purity, the correct molecular weight was confirmed by LC-MS (see fig. 4.3.9c).

a

AAAATTAAGAGGTATATATTAATGTATCGATTAAATAAGGAGGAATAAACCATGGGGCATCATCATCATCATGAGCTC
 GCTAACCAACACCACCGGTTTACCCGATCATCAAAGCGGCCGTTACAGCTGGAAAGGCTGCGTGTGCTTGGATCAACG
 AAGCTGCATTCCGTCAGGAAGGTGTTGCTGTTCTGCTGGCTGTTGTATCGTCTGCTGGCTGGACGTCGACGCTATCACCCG
 TGTCTGCTGATCTCGAGCGTTATGCTGGTTATGATCGTTGAAATCCTGAATCCGCTATCGAAGCTGTTGTTGACCGTATC
 GGATCCGAATACCACGAAGTGAAGCATGAGCGGCCGCGCTAAAGACATGGGTTCTGCAGCTGTTCTGATCGCTATCATCGTTGCTGTTA
 TCACCTGGTGCATCCTGCTGTGGTCCCACCTCGGTTAAGCTTGGCTGTTTTGGCGGATGAGAGAAGATTTTCAGCCTGATAC
 AGATTAATCAGAACGCAGAAGCGGTCTGATAAAACAGAATTTGCCTGGCGGCAGTAGCGCGGTGGTCCCACCTGACCCCAT
 GCCGAACCTAGAAGTGAACGCCGTAGCGCCGATGGTAGTGTGGGGTCTCCCATGCGAGAGTAGGGAAGTCCAGGCATCA
 AATAAAACGAAAGGCTCAGTCGAAAGACTGGGCCTTTTCGTTTTATCTGTTGTTTGTGCGTGAACGCTCTCCTGAGTAGGACA
 AATCCGCCGGGAGCGGATTTGAACGTTGCGAAGCAACGGCCCGAAGGGTGGCGGGCAGGGACGCCCGCCATAAACTGCCAG
 GCATCAAATTAAGCAGAAGCCATCCTGACGGATGGCCTTTTTGCGTTTTCTACAAACTCTTTTGTATTCTAAATACA
 TTCAAATATGTATCCGCTCATGAGACAATAA

KLKRYILMYRLNKEE - TMGHHHHHHELANNTGFTRIIKAAGYSWKGLRAAWINEAAFRQEGVAVLLAVVIACWLDVDAITR
 VLLISSVMLVMIVEILNSAIEAVVDRIGSEYHELSSRAKDMGSAAVLIAIIVAVITWCILLWSHFG - **AWLFWRMREDFQPDT**
D - IRTQKRSDKTEFAWRQ - RGGPT - PHAELRSETP - RRW - CGVSPCESRELPGIK - NERLSRKTGPFVLSVCCR - TLS - VGO
IRRERI - TLRNNGPEGWRAGTPAINCQASN - AEGHPDGWPFCVSTNSFVYFSKYIQCIRS - DN
 (130 aa, 14233.83 Da, pI 6.46, $\epsilon_{280\text{nm}} = 30,480 \text{ M}^{-1} \text{ cm}^{-1}$)

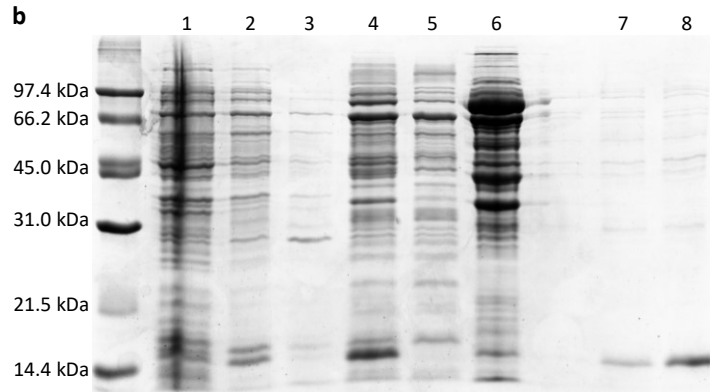
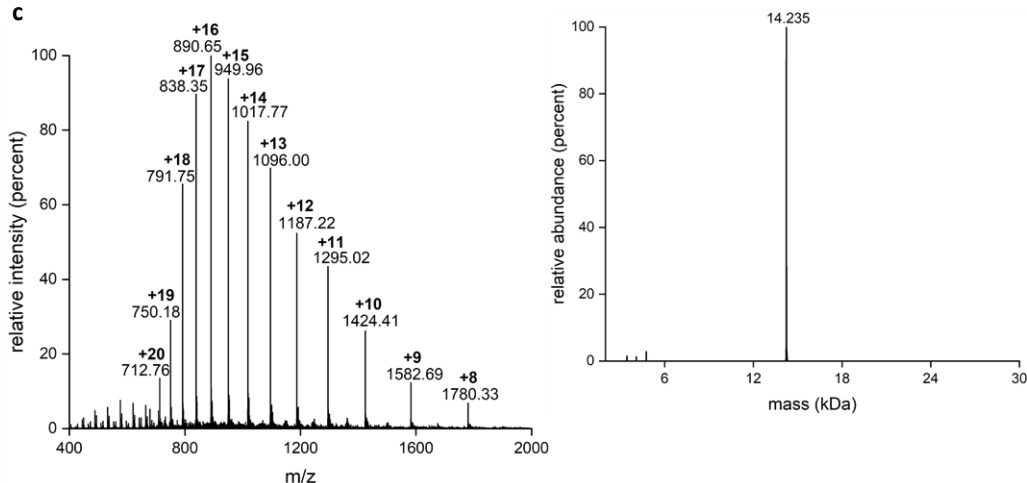
b**c**

Fig. 4.3.9 | Expression and purification of DGK. a, result of nucleotide sequence and translated amino acid sequence. The protein of interest is shown in black and its properties are indicated below. **b**, expression gel. Lanes: before induction (1), overnight expression (2), pellet (3), supernatant (4), flow-through (5), eluted fractions from Ni-NTA (6 - 8). **c**, mass spectrum and deconvoluted mass spectrum (insert) from LC-MS of the purified protein.

4.3.4 DGK Encapsulation in silica

Silica particles were generated from the DGK protein complexed with the modified BP-1 peptides as follows. A solution of DGK was diluted to 1 mg/ml concentration in DGK dialysis buffer at a total volume of 200 μ l. 20 eq. of the respective peptide were added, and the mixture incubated for at least 30 min. The mixture was dialysed against 200 ml of 50 mM potassium phosphate buffer at 4 $^{\circ}$ C and the dialysis buffer changed twice. Particles were prepared by adding 10 μ l of freshly prepared silicic acid (960 μ l 1mM HCl and 40 μ l TMOS, pre-incubated for 4 min) to 90 μ l of the dialysed solution and incubating the mixture at room temperature for 30 min. The particles were obtained by centrifuging the precipitation mixture for 5 min at 14,000 rpm in a table-top centrifuge and removing the supernatant. They were washed with 100 μ l of water before further use. To monitor the encapsulation efficiency, samples of the dialysed solution and the supernatant after precipitation were analysed by SDS-PAGE. As expected, the complex with the unmodified peptide did not lead to the formation of silica particles. Again, scanning electron microscopy revealed that the particles were of different morphologies, depending on the peptide used. Particles containing DGK and KRRIL-BP-1 were irregularly structured, so that the dimensions of single particles could not be determined from the micrographs (see figure 4.3.10a). Those containing DGK and R5-BP-1 were more uniform and on average 345 ± 8 nm in diameter (see figure 4.3.10b). DGK BP-1-R5 particles were spherical and on average 697 ± 6 nm in diameter (see figure 4.3.10c). EDX spectra showed the presence of silicon in the samples (data shown in appendix, fig. A11-A13), confirming that the particles are indeed silica.

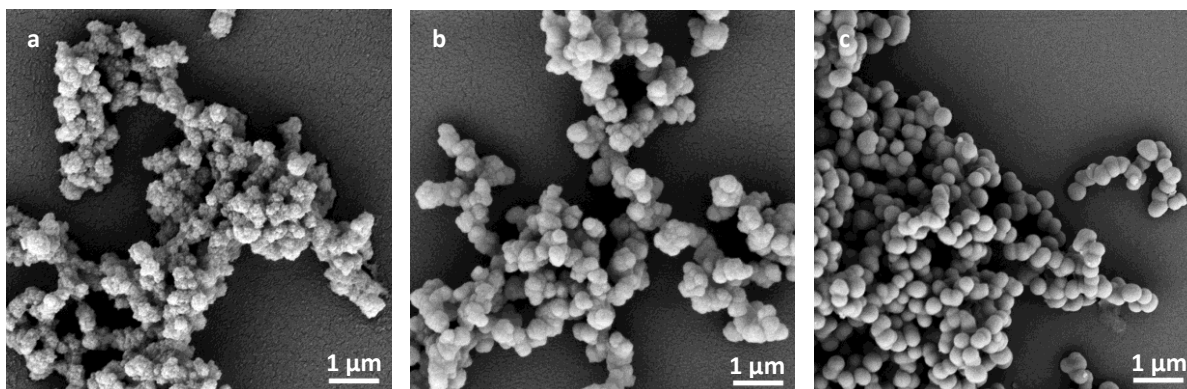


Fig. 4.3.10 | Scanning electron micrographs (10,000 x magnification) of silica particles precipitated with the DGK protein stabilized with KRRIL-BP-1 (a), R5-BP-1 (b), and BP-1-R5 (c).

The encapsulation efficiency using R5-BP-1 and BP-1-R5 was determined by SDS-PAGE. The CR5 and BP-1 peptides were used as controls. The gel in figure 4.3.11 shows the decrease of DGK and peptide concentration in the supernatant after particle precipitation as compared to the mixture before precipitation. The DGK protein forms a band at 14 kDa and the peptides used are visible as diffuse bands at the bottom of the gel. The peptide band could have been resolved better using a gradient gel²⁶⁰, but for quantification of the DGK encapsulation, the method used here was sufficient. The BP-1 peptide is too small and cannot be seen on the gel. Both bands clearly decrease during the precipitation, corresponding to the fraction which is entrapped in the particles. Band intensities from three separate precipitation reactions were analysed and gave the encapsulation efficiencies listed in table 4.3.1. The BP-1-R5 peptide is

clearly the most suitable variant, with the highest DGK encapsulation efficiency and the least variation among the samples (lowest standard deviation) and was therefore used for further assays. With the regular R5 peptide, an encapsulation efficiency higher than 50% could already be achieved, however the BP-1-R5 construct gives superior results which is why work was continued with this construct. The particles resulting from encapsulation of DGK with R5 were also characterized by SEM (4.3.11b). Their morphology is less regular than that of the DGK encapsulated with BP-1-R5. The integration efficiency of the peptides was also measured by integrating the CR5, R5-BP-1 and BP-1-R5 band intensities from the gels (see table 4.3.1). The low integration efficiencies were unexpected, since the peptides by themselves were completely integrated into the silica particles (see fig. 4.3.8d-f) but is explained by the fact that the concentrations used were much higher in this case. The 25 equivalents correspond to 3.0 mg/mL for CR5, 4.2 mg/mL for R5-BP-1, and 4.3 mg/mL for BP-1-R5. This suggests that the amount of peptide equivalents added to DGK could be reduced for further experiments.

Table 4.3.1 | DGK Encapsulation efficiency of R5 peptide and BP-1 variants.

silica-precipitating peptide	CR5	BP-1	R5-BP-1	BP-1-R5
DGK encapsulation efficiency	58% ± 13%	13% ± 5%	21% ± 10%	81% ± 4%
Peptide integration	29% ± 8%	n. a.	34% ± 8%	25% ± 3%

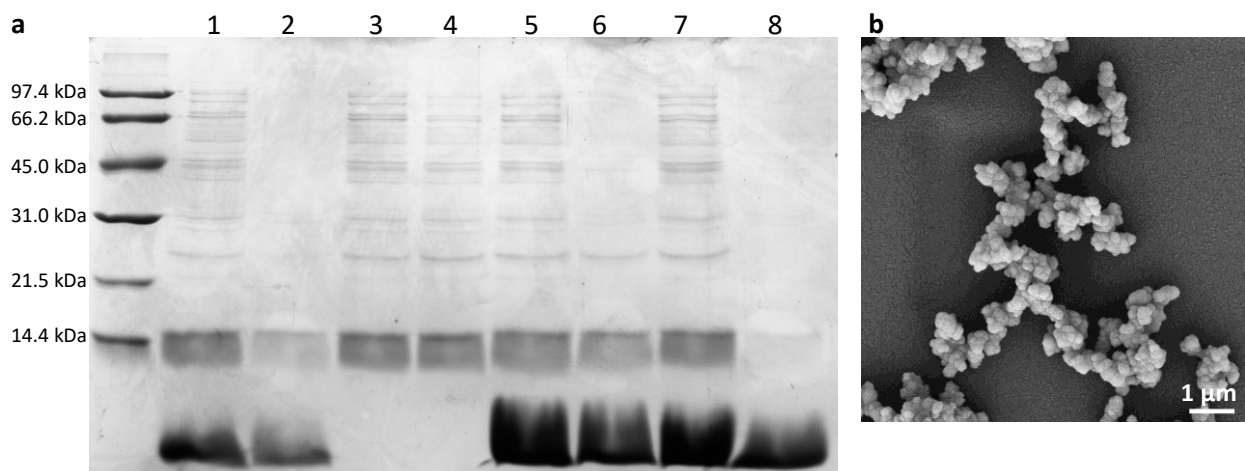


Fig. 4.3.11 | DGK encapsulation efficiency. **a**, SDS-PAGE: the left lane was filled with a sample from the precipitation mixture, the right lane with a sample of the supernatant after precipitation and centrifugation. DGK was precipitated with: R5 peptide (1,2), KRRIL-BP-1 (3,4), R5-BP-1 (5,6), and BP-1-R5 (7,8). **b**, SEM of the particles obtained by co-precipitating a mixture of the R5 peptide and the DGK protein.

4.3.5 Stabilization of DGK using BP-1 peptides

To evaluate whether the stabilization of DGK with the BP-1 peptide prevents protein degradation, the enzyme activity was measured after incubation at 37 °C and 60 °C for up to 72 h with or without addition of 20 eq. BP-1 (see fig. 4.3.12a). As expected, the graph shows a decrease in activity when the enzyme is incubated at 37 °C (dark blue bars). After 72 h, approximately half the initial activity was measured. The addition of BP-1 indeed prevents this degradation (light blue bars); within error, the activity stays the same. The results for the incubation at 60 °C are unexpected, because the activity for the untreated sample increases after 24 h incubation (dark orange bars). After 3 d, however, the activity has decreased to nearly the same value as for the sample which was incubated at 37 °C. The addition of BP-1 does not prevent this degradation, the activity for the sample with BP-1 at 60 °C (light orange bars) is lower than that of the free enzyme. The same experiments were performed for the BP-1-R5 peptide (compare fig. 4.3.12b). For this variant, no protective effect was observed at all, the enzyme activity was consistently lower than that incubated without addition of the peptide. However, when encapsulating the enzyme in silica particles, a different outcome was observed.

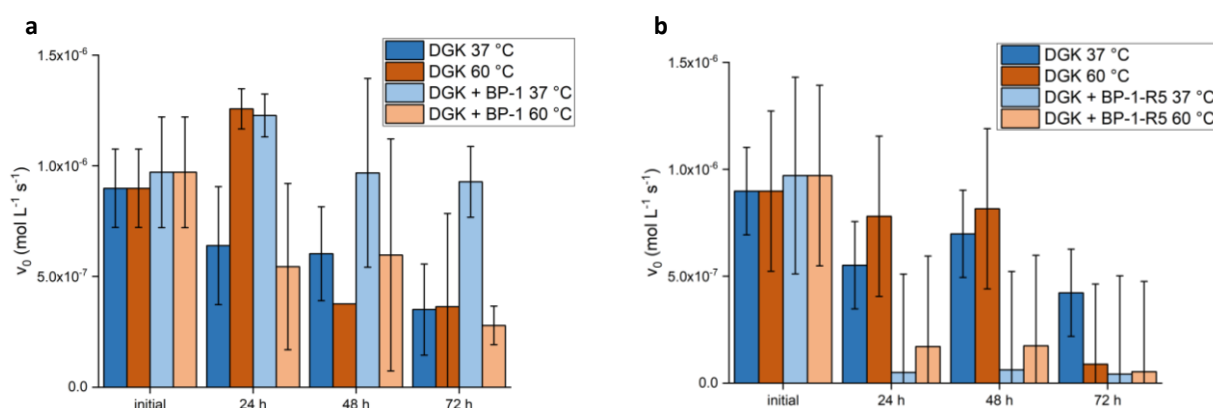


Fig. 4.3.12 | Activity decrease of DGK incubated at 37 °C and 60 °C for 3 d with or without 20 eq. of BP-1 (a) and BP-1-R5 (b). Samples were taken every 24 h and the activity measured.

4.3.6 Stabilization of silica encapsulated DGK

Silica encapsulated DGK was prepared as described in chapter 4.3.4. To evaluate a protective effect of the encapsulation, the enzyme activity decrease was measured when incubating the free or encapsulated enzyme with pronase E, simulated gastric fluid, or simulated intestinal fluid, as described in chapter 3.4.24. The incubation with pronase E abolishes 96% of the activity of the free enzyme (blue bars), whereas the encapsulated enzyme retains 30% of its activity (see figure 4.3.13a). Thus, even though the initial activity of the encapsulated enzyme is lower, it does show a protective effect against protease degradation. Similar results were obtained for simulated gastric fluid (fig. 4.3.13b) and simulated intestinal fluid (fig. 4.3.13c). To find out whether any silica degradation had occurred in the particles during incubation, they were again observed by scanning electron microscopy and compared to a control, which was incubated at room temperature without buffer. As seen in figure 4.3.14, no obvious morphological changes have occurred during the overnight incubation in any of the conditions.

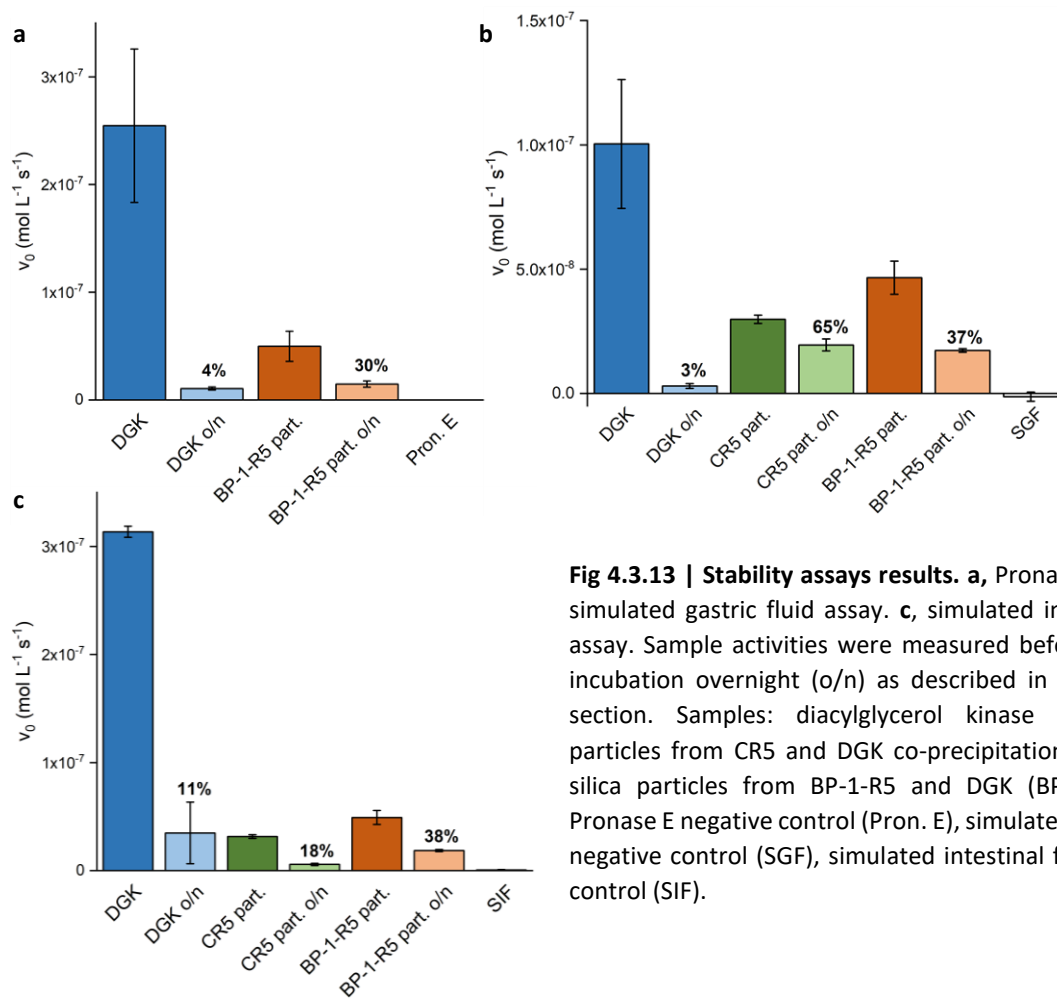


Fig 4.3.13 | Stability assays results. **a**, Pronase E assay. **b**, simulated gastric fluid assay. **c**, simulated intestinal fluid assay. Sample activities were measured before and after incubation overnight (o/n) as described in the methods section. Samples: diacylglycerol kinase (DGK), silica particles from CR5 and DGK co-precipitation (CR5 part.), silica particles from BP-1-R5 and DGK (BP-1-R5 part.), Pronase E negative control (Pron. E), simulated gastric fluid negative control (SGF), simulated intestinal fluid negative control (SIF).

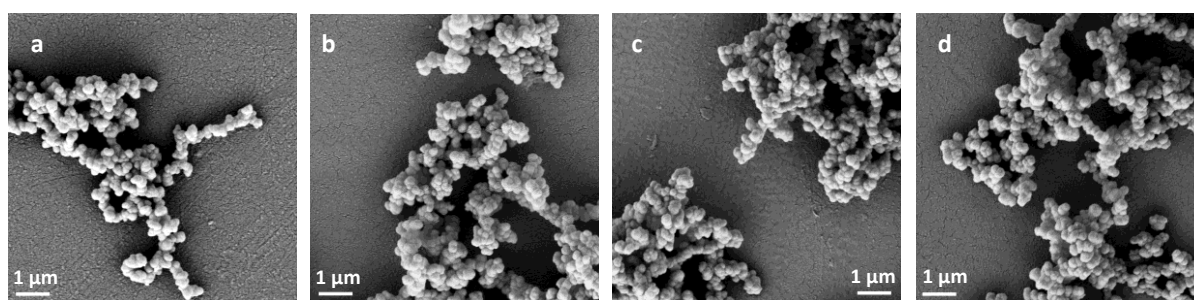


Fig. 4.3.14 | Scanning electron micrographs of DGK BP-1-R5 silica particles. **a**, control. **b**, treated with Pronase E. **c**, treated with SGF. **d**, treated with SIF.

Conclusions and Outlook

5.1 Polyphenol-conjugated R5 silica nanoparticles for targeted delivery

Two polyphenol-R5 conjugates were created. It was shown that both the galangin-R5 conjugate and the quercetin-R5 conjugate form spherical silica particles which are very similar to those formed by the unmodified R5 peptide. This was fully expected, as it was shown before that a cargo molecule can be attached to the R5 peptide, which also does not obstruct the silica particle formation⁵⁵. However, the galangin-R5 construct leads to slightly larger particles under the same conditions. To assess whether this is a trend, more conjugates could be manufactured with more or less polar molecules, featuring larger or smaller aromatic systems to see what the influence of each parameter is.

Silica particles formed with the quercetin-R5 conjugate were taken up into colon epithelial cell nuclei by an active, energy-dependent mechanism. This was shown in the HT-29 human colorectal carcinoma cell line. Further experiments could be performed to gather information on the exact mechanism of cell uptake, for example by using knock-out cell lines lacking certain genes needed for uptake pathways. Further research is also needed to evaluate the uptake not only in the colon but also to monitor the interaction of the particles with other cell lines, such as those of the vascular endothelium, for example HMEC-1²⁶¹. Depending on the result, the particles might provide a universal tool for nuclear delivery, or more specific toward colon cells. In that case, a therapeutic application might be in the treatment of diseases affecting the colon epithelium, such as inflammatory bowel disease (IBD)²⁶² or coeliac disease²⁶³. To deliver a cargo into the nucleus, the thiol group on the N-terminal cysteine of the quercetin-R5 conjugate can be made use of, so that it is bound via a disulfide⁵⁵ or selenosulfide²⁶⁴ bond. Such a platform has potential use for drugs such as gemcitabine²⁶⁵ and ganciclovir²⁶⁶, used to treat cancers and viral infections, respectively, which act in the nucleus to inhibit DNA replication and are highly toxic, which makes targeted delivery even more desirable.

Further research is also needed to elucidate the structural difference in the polyphenol that is responsible for the difference in uptake of the particles. Conjugates could be made with the polyphenol genistein, which is a regioisomer of the galangin molecule, to see if this induces different uptake behaviour (see figure 5.1.1). Perhaps the flavonol motif is also not needed and a simpler polyphenol, such as a galloyl moiety would facilitate particle uptake.

Another project would be to use the established modified quercetin for coupling not to the full-length R5 peptide, but to smaller, rod forming peptides derived from the RRILKRRIL sequence. Since these particles feature a different morphology, their uptake behaviour might be completely different, as has been observed previously²⁶⁷.



Fig. 5.1.1 | Structures of the polyphenols galangin, genistein and the galloyl motif.

5.2 Silica-stabilized nanodiscs

To create the silica-stabilized nanodiscs, new expression plasmids were created with the constructs R5-MSP, MSP-R5, and R5-MSP-R5. Of the constructs that were successfully expressed, the MSP-R5 construct could only be purified along with an impurity likely caused by a degradation product of the protein of interest (POI). If this is indeed the case, a mutant of the construct can be designed in which the cleavage site is changed. This would then prevent the proteolytic degradation and enable protein purification. The R5-MSP-R5 construct was obtained in good purity and nanodiscs were formed.

However, it was not successful to load the nanodiscs with a membrane protein. Future experiments should explore this route further and focus on embedding other proteins in the modified nanodiscs, which could thus be equipped with additional properties. The embedded proteins could then directly be incorporated into silica particles to improve their stability and recyclability.

On the other hand, the silica-covered nanodisc stacks by themselves are a unique nanomaterial, which might prove useful for example for its optical properties. To explore these, their manufacture would need to be upscaled. Also, it would need to be explored, whether some directionality could be introduced into the fibrils, for example in a flow reactor, in which the silica precipitation would be carried out. Perhaps after a calcination step, unique hollow silica nanotubes could also be obtained. Until now, such shapes are unique to carbon nanotubes and find applications in nanodevices such as nanomotors²⁶⁸. As discussed before, silica is a material which is ideally suited to applications in cosmetics and medicine. Thus, a silica-based nanomotor would be useful in these fields.

5.3 Modified amphiphilic BP-1 peptides for the direct encapsulation of membrane proteins in silica

The modified beta-strand peptides were used for the encapsulation of the enzyme diacylglycerol kinase (DGK) in silica particles. It was shown that this indeed increases the stability of DGK towards different proteolytic media. Future research should focus on investigating the universality of this system by testing the encapsulation of other membrane proteins in silica with the BP-1-R5 peptide.

Another direction to explore would be the creation of silica-covered membranes. A mutated version of the R5 peptide with two copies of the KRRIL domain was previously used for the deposition of a layer of silica onto a dipalmitoyl-phosphatidylglycerol (DPPG) monolayer covering an aqueous solution⁶⁰. The KRRIL-BP-1 construct, however, is ideally suited for integration into lipid layers which might enable also the silicification of liposomes and other lipid structures, again enabling the construction of new silica morphologies.

Appendix

NMR-Spectra

2-(3,4-diacetoxyphenyl)-4-oxo-4H-chromene-3,5,7-triyl triacetate

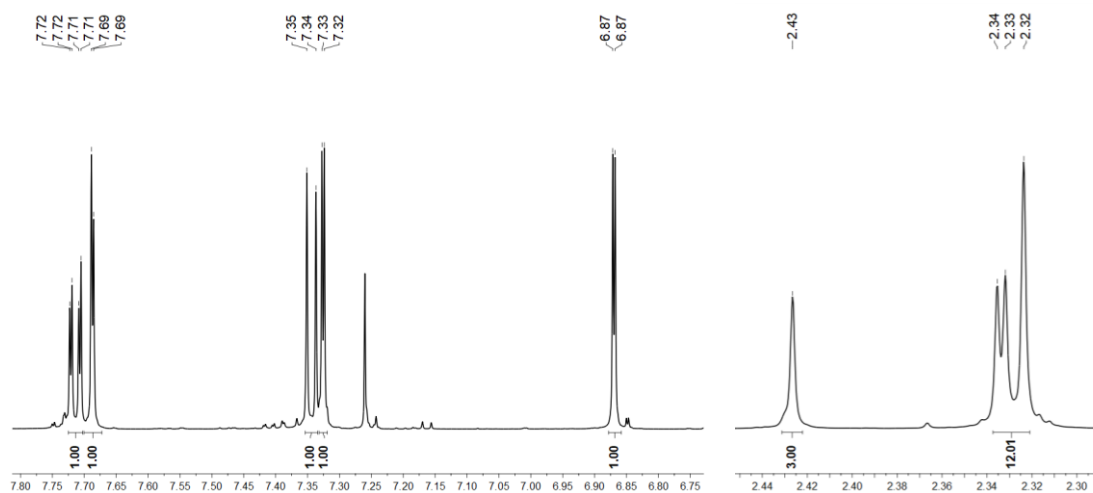
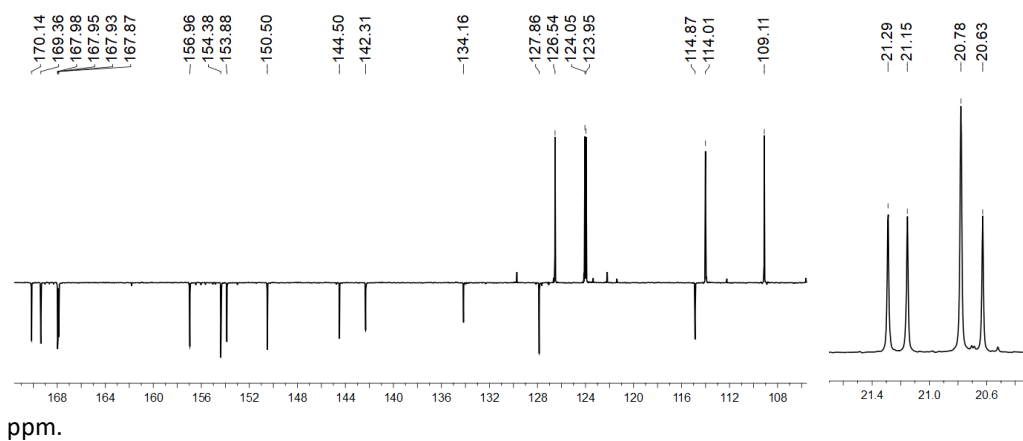
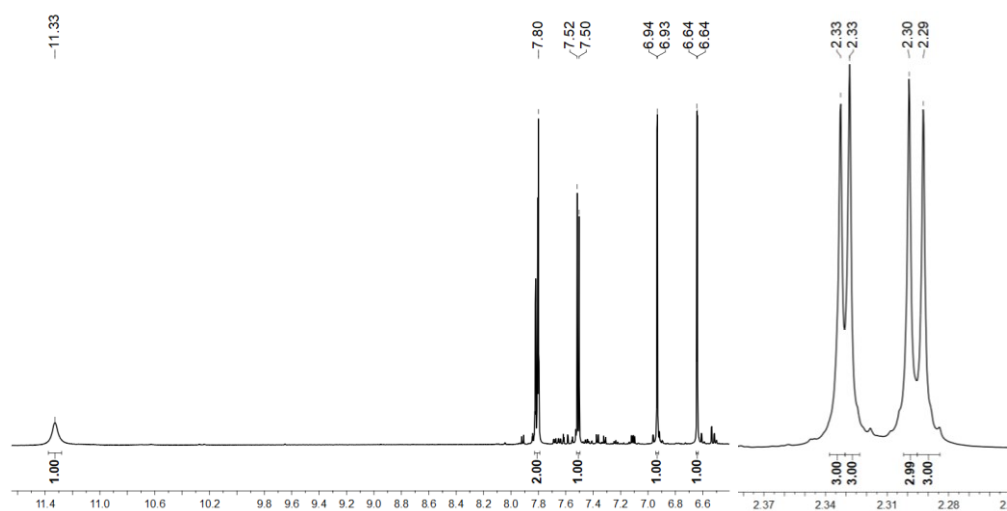
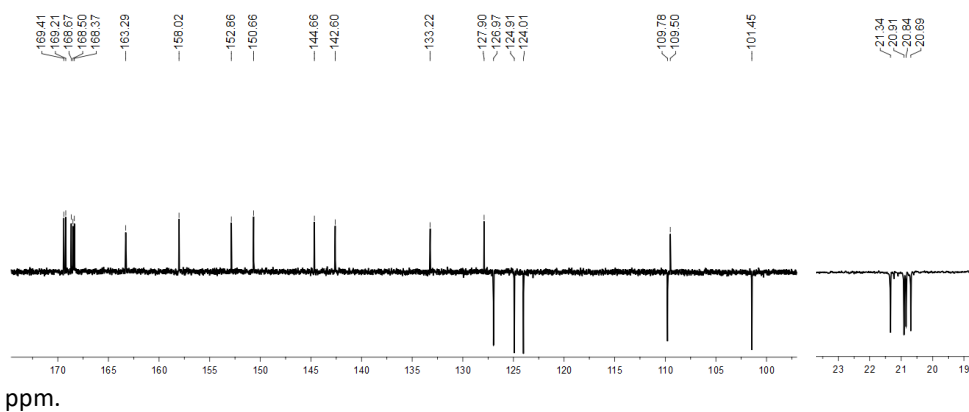


Fig. A1 | $^1\text{H-NMR}$ spectrum (600.25 MHz, CDCl_3) of product 2. Downfield (left) and upfield regions (right) in



ppm.

Fig. A2 | $^{13}\text{C-NMR}$ spectrum (150.95 MHz, CDCl_3) of product 2. Downfield (left) and upfield regions (right) in ppm.

4-(3,5-diacetoxy-7-hydroxy-4-oxo-4H-chromen-2-yl)-1,2-phenylene diacetate**Fig. A3** | $^1\text{H-NMR}$ (400.27 MHz, DMSO) spectrum of product 3. Downfield (left) and upfield regions (right) in

ppm.

Fig. A4 | $^{13}\text{C-NMR}$ (100.65 MHz, DMSO) spectrum of product 3. Downfield (left) and upfield regions (right) in ppm.

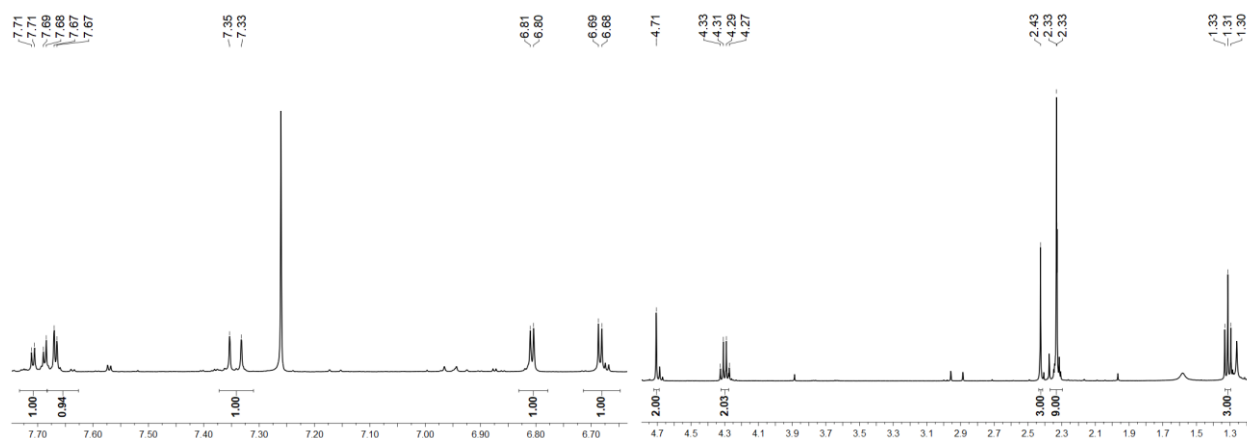
4-(3,5-diacetoxy-7-(2-ethoxy-2-oxoethoxy)-4-oxo-4H-chromen-2-yl)-1,2-phenylene diacetate

Fig. A5 | ¹H-NMR spectrum (400.27 MHz, CDCl₃) of product 4. Downfield (left) and upfield regions (right) in ppm.

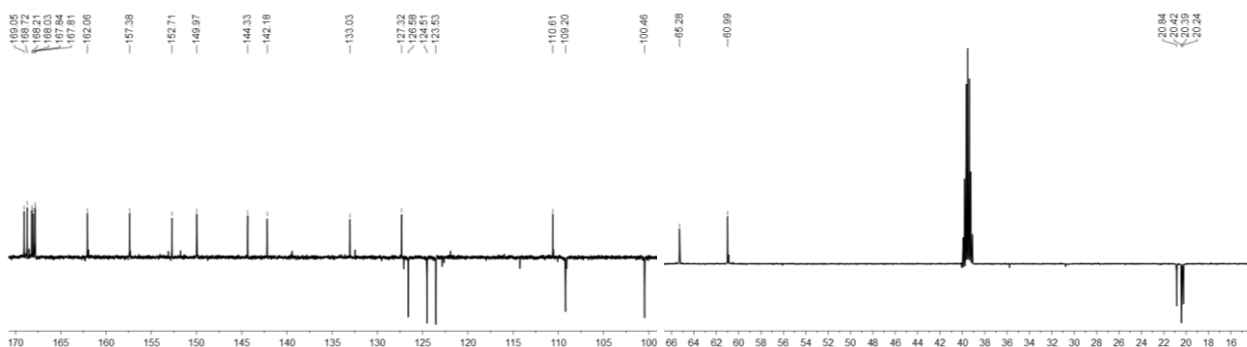


Fig. A6 | ¹³C-NMR spectrum (150.95 MHz, d₆-DMSO) of product 4. Downfield (left) and upfield regions (right) in ppm.

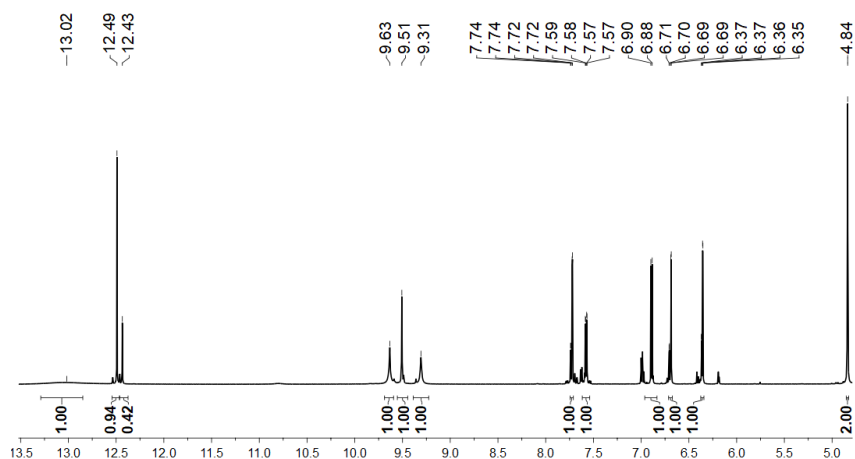
2-((2-(3,4-dihydroxyphenyl)-3,5-dihydroxy-4-oxo-4H-chromen-7-yl)oxy)acetic acid

Fig. A7 | $^1\text{H-NMR}$ spectrum (600.25 MHz, DMSO-d_6) of product 5. Downfield (left) and upfield regions (right) in ppm.

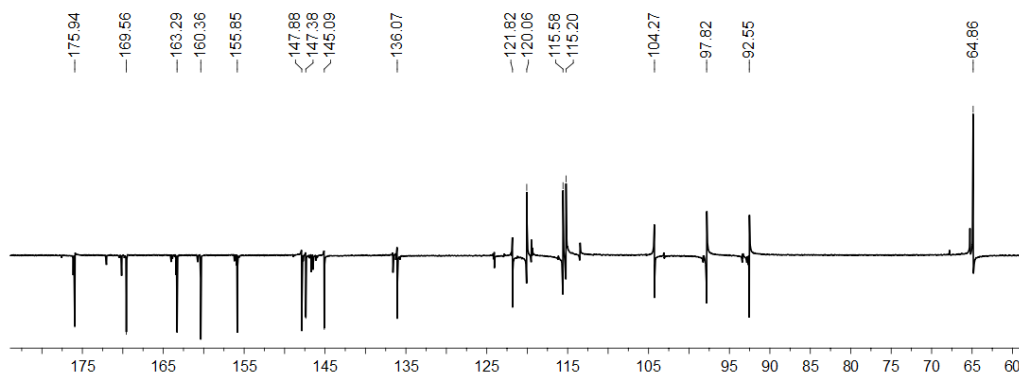
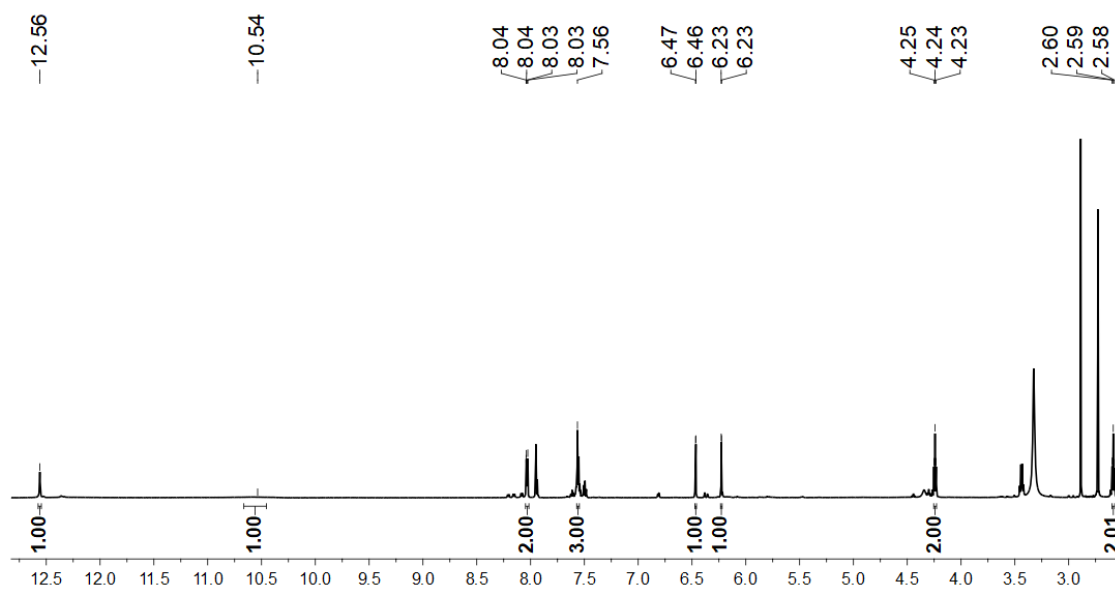
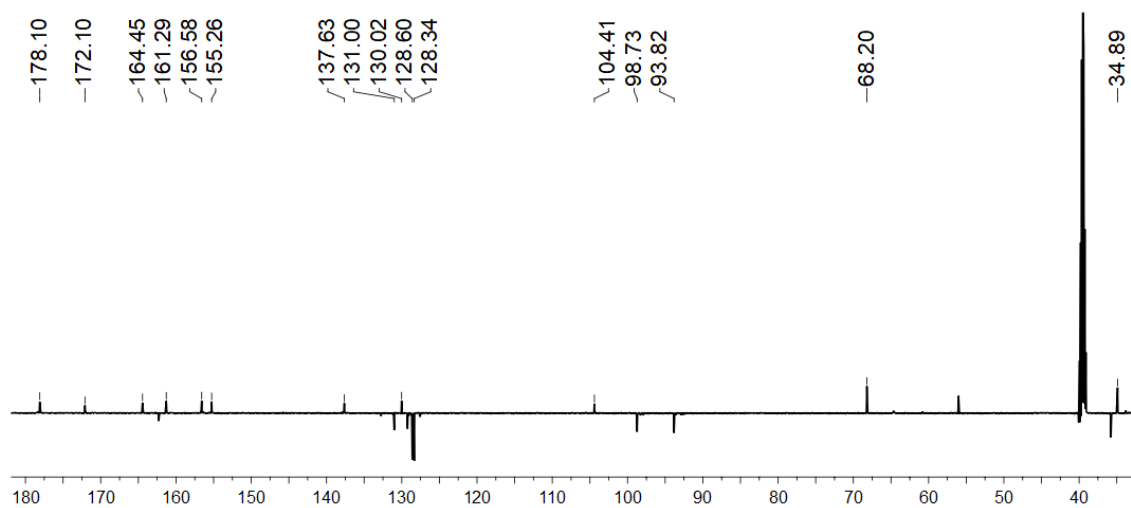


Fig. A8 | $^{13}\text{C-NMR}$ spectrum (150.95 MHz, DMSO-d_6) of product 5.

3-((3,5-dihydroxy-4-oxo-2-phenyl-4H-chromen-7-yl)oxy)propanoic acid**Fig. A9** | $^1\text{H-NMR}$ spectrum (600.25 MHz, DMSO-d_6) of product 7.**Fig. A10** | $^{13}\text{C-NMR}$ spectrum (150.95 MHz, DMSO-d_6) of product 7.

EDX Spectra

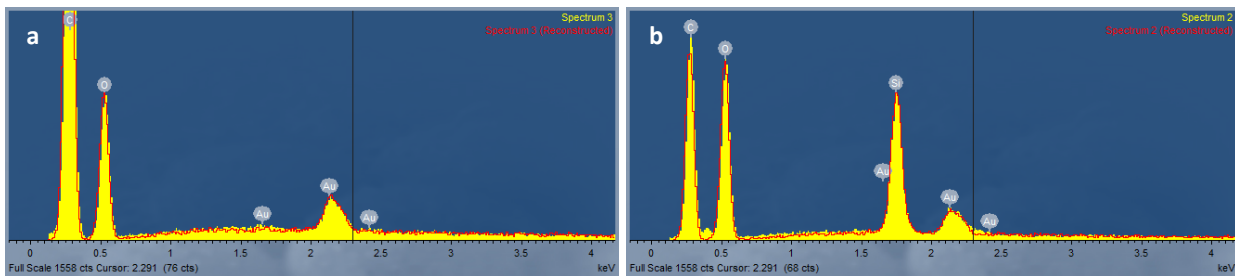


Fig. A11 | EDX spectra of KRRIL-BP-1 encapsulated DGK. Spectrum **a** was taken from the outer part of the cover slide (negative control). Spectrum **b** was taken from the particle sample itself. The additional peak in spectrum **b** is caused by the silicon present in the silica particles. Carbon and oxygen are from the plastic slide the samples were deposited on. The samples were sputtered with a 5 nm coating of gold, resulting in the remaining peak.

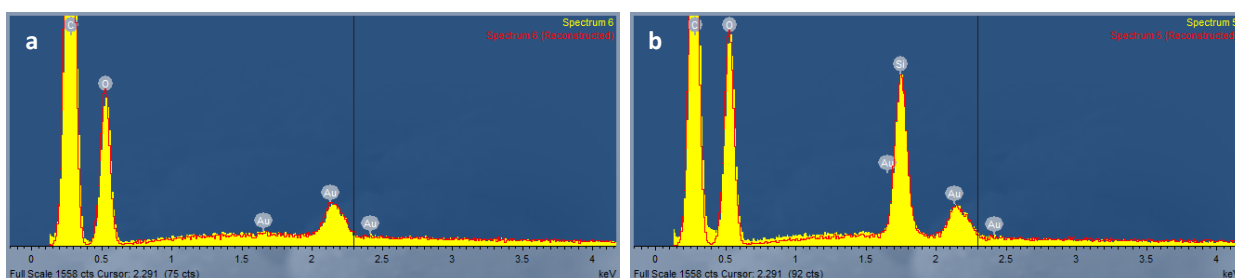


Fig. A12 | EDX spectra of R5-BP-1 encapsulated DGK. Spectrum **a** was taken from the outer part of the cover slide (negative control). Spectrum **b** was taken from the particle sample itself.

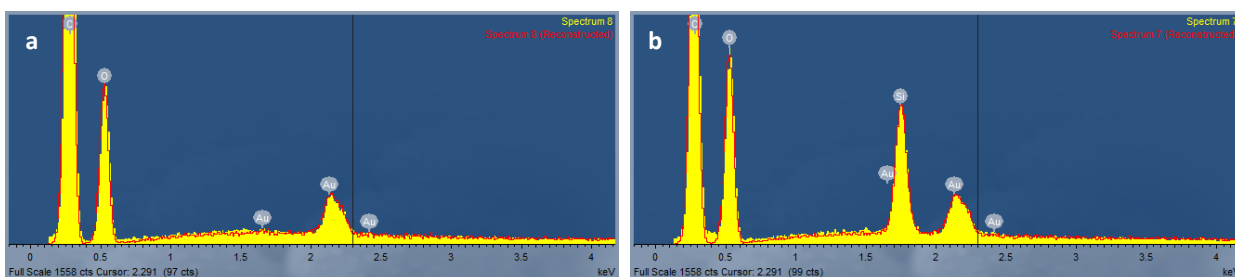


Fig. A13 | EDX spectra of BP-1-R5 encapsulated DGK. Spectrum **a** was taken from the outer part of the cover slide (negative control). Spectrum **b** was taken from the particle sample itself.

Comet assay

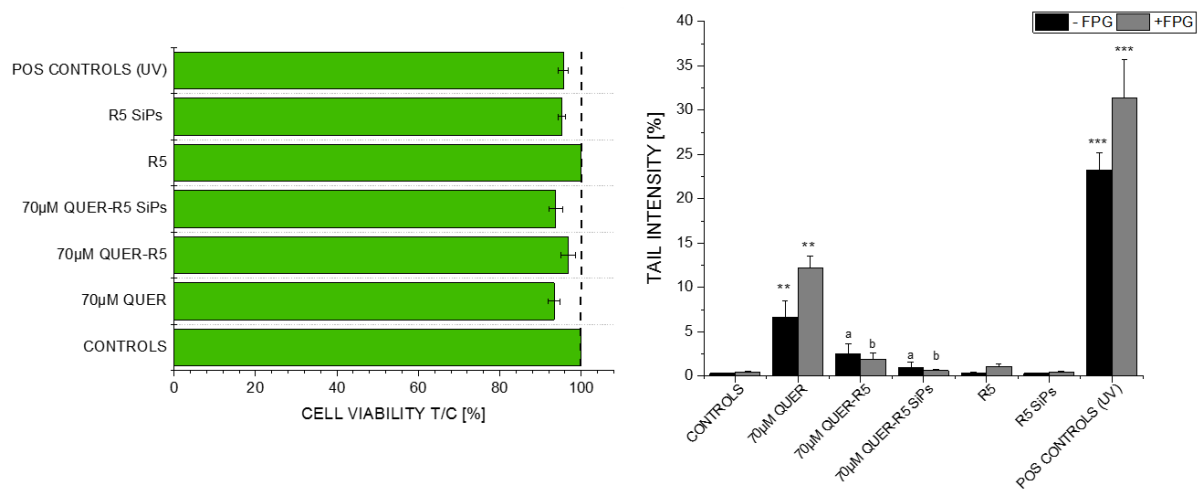


Fig. A14 | Cell damage in HT-29 cells. a, cell viability assay (trypan blue exclusion) with the R5 silica particles, the R5 peptide, the quercetin-R5 silica particles, the quercetin-R5 conjugate, and free quercetin. **b**, comet assay (single cell electrophoresis) with the same samples, indicating the DNA damage induced by the samples. The gray bars show the results obtained when adding formamidopyrimidine DNA-glycosylase for the detection of DNA bases retaining oxidative damage.

List of Abbreviations

AaLS	<i>Aquifex aeolicus</i> lumazine synthase
AChE	acetylcholinesterase
ACN	acetonitrile
AdhD	alcohol dehydrogenase D
ADP	adenosin diphosphate
AldH	aldehyde dehydrogenase
AEPTMS	3-[2-(2-aminoethylamino)ethylamino]propyltrimethoxysilane
AOx	alcohol dehydrogenase
APO	2-aminophenoxazin-3-one
Apo A-I	apolipoprotein A-I
APTES	(3-Aminopropyl)triethoxysilane
ATP	adenosin triphosphate
ATRP	atom-transfer radical polymerization
AqpZ	aquaporin Z
ARGET	activators regenerated under electron transfer
BIS	N,N'-methylenebisacrylamide
BMA	n-butyl methacrylate
bR	bacteriorhodopsin
BSA	bovine serum albumin
BuChE	butyrylcholinesterase
CalB	<i>Candida Antarctica</i> lipase B
CAT	catalase
CCMV	cowpea chlorotic mottle virus
CCP	clathrin-coated pit
CCV	clathrin-coated vesicle
CD	circular dichroism
CelB	β -glucosidase

CHAO	cyclohexylamine oxidase
CLEA	crosslinked enzyme aggregate
CMC	critical micelle concentration
CME	clathrin-mediated endocytosis
CNT	carbon nanotube
CP	coat protein
CTAB	cetrimonium bromide
CVD	chemical vapour deposition
DAO	diamine oxidase
DCC	dicyclohexyl carbodiimide
DCM	dichloromethane
DDAB	dimethyldioctadecylammonium bromide
DDM	n-dodecyl- β -D-maltoside
DEF	N,N-diethylformamide
DETA	diethylenetriamine
DGK	diacylglycerol kinase
DHPC	dihexanoylphosphatidylcholine
DIBMA	poly(diisobutylene- <i>alt</i> -maleic acid)
DILL	detergent-induced loading of liposomes
DI-MS	direct-injection mass spectrometry
DMPC	dimyristoylphosphatidylcholine
DMPE	1,2-dimyristoyl-sn-glycero-3-phosphoethanolamine
DNA	desoxyribonucleic acid
DOSS	dioctyl sulfosuccinate sodium salt
DPPG	dipalmitoyl-phosphatidylglycerol
DTNP	2,2'-Dithiobis(5-nitropyridine)
EDC	1-ethyl-3-(3-dimethylaminopropyl) carbodiimide (EDC)
EGDMA	ethylene glycole dimethacrylate
EGF	epidermal growth factor

ELP	elastin-like polypeptide
EM	electron microscopy
EPR	enhanced permeation and retention
EPT	enzyme prodrug therapy
ETPTA	ethoxylated trimethylolpropane triacrylate
EX	expanded form
FaSSGF	Fasted State Simulated Gastric Fluid
FeSSIF	Fed State Simulated Intestinal Fluid
FITC	fluorescein isothiocyanate
Fmoc	fluorenylmethyloxycarbonyl
FRET	fluorescence resonance energy transfer
Ftn	ferritin
GA	glutaraldehyde
β -gal	β -galactosidase
GALK	galactokinase
GFP	green fluorescent protein
GlpF	glycerol facilitator
GLUK	glucokinase
GMA	glycidyl methacrylate
GOx	glucose oxidase
G6pDH	glucose-6-phosphate dehydrogenase
GuHCl	guanidinium chloride
GUS	β -glucuronidase
HCA	<i>Hahella chejuensis</i> carbonic anhydrase
HDL	high-density lipoprotein
HEBIB	2-hydroxyethyl-2-bromoisobutyrate
HEPES	2-[4-(2-hydroxyethyl)piperazin-1-yl]ethanesulfonic acid
HPLC	high-performance liquid chromatography
HRP	horseradish peroxidase

hyA	hydrogenase 1 subunit A
hyB	hydrogenase 1 subunit B
HyNic	succinimidyl-hydrazino-nicotinamide
IBD	inflammatory bowel disease
IC ₅₀	half maximal inhibitory concentration
IMP	integral membrane protein
IUPAC	International Union of Pure and Applied Chemistry
KatG	catalase-peroxidase
k _{cat}	turnover number
KE	kemp eliminase
βLac	β-lactamase
LB	lysogeny broth
LDH	lactate dehydrogenase
LMV	large multilamellar vesicle
LUV	large unilamellar vesicle
LYS	lysozyme
MALDI	matrix-assisted laser desorption/ionization
MAO	monoamine oxidase
MCM	Mobil crystalline material
MDH	malic dehydrogenase
MMP	matrix metalloprotease
MOF	metal-organic framework
MSN	mesoporous silica nanoparticle
MSP	membrane scaffold protein
MTFB	maleimido trioxa-6-formyl benzamide
MWCO	molecular weight cut-off
NADH	nicotinamide adenine dinucleotide, reduced form
NBD	4-chloro-7-nitrobenzofurazan
NbzA	nitroreductase

NF	National Formulary
NitA	nitrilase A
NMP	1-Methyl-2-pyrrolidinone
NMR	nuclear magnetic resonance
NOX	nicotinamide adenine dinucleotide oxidase
NP	nanoparticles
OG	n-octyl- β -D-glucoside
OmpF	outer membrane protein F
OmpLA	outer membrane phospholipase A
Oxyma	cyanohydroxyiminoacetate
PAL	phenylalanine Ammonia Lyase
PAMAM	polyamido(amine)
PC	phosphatidylcholine
PDB	Protein Data Bank
PEG	polyethylene glycol
PEGA	poly (ethylene glycol) methylether acrylate
PEHA	pentaethylenehexamine
PEI	polyethyleneimine
PEPCase	phosphoenolpyruvate carboxylase
PhoA	alkaline phosphatase
PI	phosphatidylinositol
PMOXA- <i>b</i> -PDMS- <i>b</i> -PMOXA	poly(2-methyloxazoline)-block-poly(dimethylsiloxane)-block-poly(2-methyloxazoline)
PMSF	phenylmethylsulfonyl fluoride
POI	protein of interest
POPC	1-palmitoyl-2-oleoyl-sn-glycero-3-phosphocholine
PTM	post-translational modification
PVA	polyvinyl alcohol
PVP	polyvinyl pyrrolidone

RA	retro-aldolase
RCA	rolling circle amplification
RCT	reverse cholesterol transport
RDH	ribitol dehydrogenase
RNA	ribonucleic acid
ROS	reactive oxygen species
RP-HPLC	reverse-phase high-precision liquid chromatography
rSAP	shrimp alkaline phosphatase
SBA	Santa Barbara
SBP	soybean peroxidase
SDV	silica deposition vesicle
SEC	size-exclusion chromatography
SECN	single enzyme caged nanoparticles
SEM	scanning electron microscopy
SGF	simulated gastric fluid
SIF	simulated intestinal fluid
siRNA	small interfering ribonucleic acid
SMA	poly(styrene- <i>co</i> -maleic acid)
SMALP	styrene maleic acid lipid particles
SP	scaffold protein
SpEH	<i>Sphingomonas</i> epoxide hydrolase
SPPS	solid-phase peptide synthesis
SrtA	sortase A
SSNMR	Solid-state nuclear magnetic resonance
SUV	small unilamellar vesicle
TBOS	tetrabutoxysilane
TCEP	tris(2-carboxyethyl)phosphine
TEM	transmission electron microscopy
TEOS	tetraethoxysilane

TEPA	tetraethylenepentamine
TETA	triethylenetetramine
TEV	tobacco etch virus
Tf	transferrin
TFA	trifluoroacetic acid
THS	thermosome
TIS	triisopropyl silane
TLC	thin layer chromatography
TMOS	tetramethoxysilane
Tris	tris(hydroxymethyl)aminomethane
URE	uricase
USP	United States Pharmacopeia
VEGF	vascular endothelial growth factor
VLP	virus-like particle
WB	wiffle ball
YADH	yeast alcohol dehydrogenase

References

- 1 Boholm, M. & Arvidsson, R. A Definition Framework for the Terms Nanomaterial and Nanoparticle. *Nanoethics* **10**, 25-40, doi:10.1007/s11569-015-0249-7 (2016).
- 2 Lee, K. J., Yoon, J. & Lahann, J. Recent advances with anisotropic particles. *Curr. Opin. Colloid Interface Sci.* **16**, 195-202, doi:10.1016/j.cocis.2010.11.004 (2011).
- 3 Paquet, C. & Kumacheva, E. Nanostructured polymers for photonics. *Mater. Today* **11**, 48-56, doi:10.1016/s1369-7021(08)70056-7 (2008).
- 4 Stepien, M. *et al.* Wear resistance of nanoparticle coatings on paperboard. *Wear* **307**, 112-118, doi:10.1016/j.wear.2013.08.022 (2013).
- 5 Yan, N., Xiao, C. & Kou, Y. Transition metal nanoparticle catalysis in green solvents. *Coord. Chem. Rev.* **254**, 1179-1218, doi:10.1016/j.ccr.2010.02.015 (2010).
- 6 Bobo, D., Robinson, K. J., Islam, J., Thurecht, K. J. & Corrie, S. R. Nanoparticle-Based Medicines: A Review of FDA-Approved Materials and Clinical Trials to Date. *Pharm. Res.* **33**, 2373-2387, doi:10.1007/s11095-016-1958-5 (2016).
- 7 McMahan, B. W., Yu, J., Boatz, J. A. & Anderson, S. L. Rapid Aluminum Nanoparticle Production by Milling in NH₃ and CH₃NH₂ Atmospheres: An Experimental and Theoretical Study. *ACS Appl. Mater. Interfaces* **7**, 16101-16116, doi:10.1021/acsami.5b04806 (2015).
- 8 Gary L. Messing, S.-C. Z., Gopal V. Jayanthi. Ceramic Powder Synthesis by Spray Pyrolysis. *J. Am. Ceram. Society* **76**, 2707-2726 (1993).
- 9 Larry L. Hench, J. K. W. The Sol-Gel Process. *Chem. Rev.* **90**, 33-72, doi:10.1021/cr00099a003, (1990).
- 10 Li, Y., Li, D. & Wang, G. Methane decomposition to CO_x-free hydrogen and nano-carbon material on group 8–10 base metal catalysts: A review. *Catal. Today* **162**, 1-48, doi:10.1016/j.cattod.2010.12.042 (2011).
- 11 Iqbal, P., Preece, J. A. & Mendes, P. M. in *Supramolecular Chemistry* (ed Philip A. Gale) (John Wiley & Sons, 2012).
- 12 C. T. Kresge, M. E. L., W. J. Roth, J. C. Vartuli, J. S. Becht. Ordered mesoporous molecular sieves synthesized by a liquidcrystal template mechanism. *Nature* **359**, 710-712 (1992).
- 13 Akinwande, D. *et al.* A review on mechanics and mechanical properties of 2D materials—Graphene and beyond. *EML* **13**, 42-77, doi:10.1016/j.eml.2017.01.008 (2017).
- 14 H. W. Kroto, J. R. H., S. C. O'Brien, R. F. Curl, R. E. Smalley. C₆₀ : Buckminsterfullerene. *Nature* **318**, 162-163 (1985).
- 15 Mykhailiv, O., Zubyk, H. & Plonska-Brzezinska, M. E. Carbon nano-onions: Unique carbon nanostructures with fascinating properties and their potential applications. *Inorg. Chim. Acta* **468**, 49-66, doi:10.1016/j.ica.2017.07.021 (2017).
- 16 Sinnott, S. B. & Andrews, R. Carbon Nanotubes: Synthesis, Properties, and Applications. *Crit. Rev. Solid State Mater. Sci.* **26**, 145-249, doi:10.1080/20014091104189 (2001).
- 17 De Jong, K. P. & Geus, J. W. Carbon Nanofibers: Catalytic Synthesis and Applications. *Catal. Rev.* **42**, 481-510, doi:10.1081/cr-100101954 (2007).
- 18 Jiang, H., Lee, P. S. & Li, C. 3D carbon based nanostructures for advanced supercapacitors. *Energy Environ. Sci.* **6**, 41-53, doi:10.1039/c2ee23284g (2013).
- 19 Tang, F., Li, L. & Chen, D. Mesoporous silica nanoparticles: synthesis, biocompatibility and drug delivery. *Adv. Mater.* **24**, 1504-1534, doi:10.1002/adma.201104763 (2012).
- 20 Ghosh, P., Han, G., De, M., Kim, C. K. & Rotello, V. M. Gold nanoparticles in delivery applications. *Adv. Drug Deliv. Rev.* **60**, 1307-1315, doi:10.1016/j.addr.2008.03.016 (2008).
- 21 Amoruso, S. *et al.* Generation of silicon nanoparticles via femtosecond laser ablation in vacuum. *Appl. Phys. Lett.* **84**, 4502-4504, doi:10.1063/1.1757014 (2004).
- 22 Niederberger, M. Nonaqueous Sol-Gel Routes to Metal Oxide Nanoparticles. *Acc. Chem. Res.* **40**, 793–800 (2007).

- 23 Ghosh Chaudhuri, R. & Paria, S. Core/shell nanoparticles: classes, properties, synthesis mechanisms, characterization, and applications. *Chem. Rev.* **112**, 2373-2433, doi:10.1021/cr100449n (2012).
- 24 Narayan, R., Nayak, U. Y., Raichur, A. M. & Garg, S. Mesoporous Silica Nanoparticles: A Comprehensive Review on Synthesis and Recent Advances. *Pharmaceutics* **10**, doi:10.3390/pharmaceutics10030118 (2018).
- 25 Croissant, J. G., Fatieiev, Y. & Khashab, N. M. Degradability and Clearance of Silicon, Organosilica, Silsesquioxane, Silica Mixed Oxide, and Mesoporous Silica Nanoparticles. *Adv. Mater.* **29**, 1604634, doi:10.1002/adma.201604634 (2017).
- 26 Juere, E. *et al.* In Vitro Dissolution, Cellular Membrane Permeability, and Anti-Inflammatory Response of Resveratrol-Encapsulated Mesoporous Silica Nanoparticles. *Mol. Pharm.* **14**, 4431-4441, doi:10.1021/acs.molpharmaceut.7b00529 (2017).
- 27 B. G. Trewyn, I. I. S., S. Giri, H.-T. Chen, V. S.-Y. Lin. Synthesis and Functionalization of a Mesoporous Silica Nanoparticle Based on the Sol–Gel Process and Applications in Controlled Release. *Acc. Chem. Res.* **40**, 846–853 (2007).
- 28 W. Stöber, A. F., E. Bohn. Controlled Growth of Monodisperse Silica Spheres in the Micron Size Range. *J. Colloid Interface Sci.* **26**, 62-69 (1968).
- 29 Croissant, J. G., Fatieiev, Y., Almalik, A. & Khashab, N. M. Mesoporous Silica and Organosilica Nanoparticles: Physical Chemistry, Biosafety, Delivery Strategies, and Biomedical Applications. *Adv. Healthc. Mater.* **7**, 1700831, doi:10.1002/adhm.201700831 (2018).
- 30 Rashidi, L., Vasheghani-Farahani, E., Rostami, K., Ganji, F. & Fallahpour, M. Mesoporous silica nanoparticles with different pore sizes for delivery of pH-sensitive gallic acid. *Asia-Pac. J. Chem. Eng.* **9**, 845-853, doi:10.1002/apj.1832 (2014).
- 31 Gu, L. *et al.* One-pot hydrothermal synthesis of mesoporous silica nanoparticles using formaldehyde as growth suppressant. *Microporous and Mesoporous Mater.* **152**, 9-15, doi:10.1016/j.micromeso.2011.11.047 (2012).
- 32 Yu, M. *et al.* A simple approach to prepare monodisperse mesoporous silica nanospheres with adjustable sizes. *J. Colloid Interface Sci.* **376**, 67-75, doi:10.1016/j.jcis.2012.03.014 (2012).
- 33 Yamada, H. *et al.* Preparation of Colloidal Mesoporous Silica Nanoparticles with Different Diameters and Their Unique Degradation Behavior in Static Aqueous Systems. *Chem. Mater.* **24**, 1462-1471, doi:10.1021/cm3001688 (2012).
- 34 N. Lang, A. T. A Fast and Efficient Ion-Exchange Procedure To Remove Surfactant Molecules from MCM-41 Materials. *Chem. Mater.* **16**, 1961-1966 (2004).
- 35 Kecht, J. & Bein, T. Oxidative removal of template molecules and organic functionalities in mesoporous silica nanoparticles by H₂O₂ treatment. *Microporous and Mesoporous Mater.* **116**, 123-130, doi:10.1016/j.micromeso.2008.03.027 (2008).
- 36 Cauda, V., Argyo, C., Piercey, D. G. & Bein, T. "Liquid-phase calcination" of colloidal mesoporous silica nanoparticles in high-boiling solvents. *J. Am. Chem. Soc.* **133**, 6484-6486, doi:10.1021/ja1067492 (2011).
- 37 A. Berggren, A. E. C. P. Particle Size Control of Colloidal Suspensions of Mesostructured Silica. *J. Phys. Chem. C* **112**, 732-737 (2008).
- 38 Wetherbee, R. Biomineralization. The diatom glasshouse. *Science* **298**, 547, doi:10.1126/science.1078222 (2002).
- 39 Addadi, L., Gal, A., Faivre, D., Scheffel, A. & Weiner, S. Control of Biogenic Nanocrystal Formation in Biomineralization. *Isr. J. Chem.* **56**, 227-241, doi:10.1002/ijch.201500038 (2016).
- 40 Lechner, C. C. & Becker, C. F. Silaffins in Silica Biomineralization and Biomimetic Silica Precipitation. *Mar. Drugs* **13**, 5297-5333, doi:10.3390/md13085297 (2015).

- 41 A. Roehrich, G. D. Solid-State NMR Studies of Biomineralization Peptides and Proteins. *Acc. Chem. Res.* **46**, 2136-2144 (2013).
- 42 Bernecker, A. *et al.* Tailored Synthetic Polyamines for Controlled Biomimetic Silica Formation. *J. Am. Chem. Soc.* **132**, 1023–1031 (2009).
- 43 Kröger, N., Deutzmann, R. & Sumper, M. Polycationic Peptides from Diatom Biosilica that direct Silica Nanosphere Formation. *Science* **286**, 1129-1132, doi:10.1126/science.286.5442.1129 (1999).
- 44 Wenzl, S., Hett, R., Richthammer, P. & Sumper, M. Silacidins: highly acidic phosphopeptides from diatom shells assist in silica precipitation in vitro. *Angew. Chem. Int. Ed. Engl.* **47**, 1729-1732, doi:10.1002/anie.200704994 (2008).
- 45 Kröger, N., Deutzmann, R. & Sumper, M. Silica-precipitating peptides from diatoms. The chemical structure of silaffin-A from *Cylindrotheca fusiformis*. *J. Biol. Chem.* **276**, 26066-26070, doi:10.1074/jbc.M102093200 (2001).
- 46 Kröger, N., Lorenz, S., Brunner, E. & Sumper, M. Self-Assembly of Highly Phosphorylated Silaffins and Their Function in Biosilica Morphogenesis. *Science* **298**, 584-586 (2002).
- 47 Knecht, M. R. & Wright, D. W. Functional analysis of the biomimetic silica precipitating activity of the R5 peptide from *Cylindrotheca fusiformis*. *Chem. Commun. (Cambridge, U. K.)*, 3038-3039, doi:10.1039/b309074d (2003).
- 48 Kamalov, M., Hajradini, A., Rentenberger, C. & Becker, C. F. W. N-terminal residues of silaffin peptides impact morphology of biomimetic silica particles. *Mater. Lett.* **212**, 114-117, doi:10.1016/j.matlet.2017.10.050 (2018).
- 49 Senior, L. *et al.* Structure and function of the silicifying peptide R5. *J. Mater. Chem. B* **3**, 2607-2614, doi:10.1039/c4tb01679c (2015).
- 50 Martelli, T. *et al.* Atomic-Level Quality Assessment of Enzymes Encapsulated in Bioinspired Silica. *Chem. - Eur. J.* **22**, 425-432, doi:10.1002/chem.201503613 (2016).
- 51 Lutz, H. *et al.* The Structure of the Diatom Silaffin Peptide R5 within Freestanding Two-Dimensional Biosilica Sheets. *Angew. Chem. Int. Ed.* **56**, 8277-8280 (2017).
- 52 Kamalov, M. *et al.* Silaffin-Inspired Peptide Assemblies Template Silica Particles with Variable Morphologies. *ChemNanoMat* **4**, 1209-1213, doi:10.1002/cnma.201800340 (2018).
- 53 Luckarift, H. R., Spain, J. C., Naik, R. R. & Stone, M. O. Enzyme immobilization in a biomimetic silica support. *Nat. Biotechnol.* **22**, 211-213, doi:10.1038/nbt931 (2004).
- 54 Nam, D. H., Won, K., Kim, Y. H. & Sang, B. I. A novel route for immobilization of proteins to silica particles incorporating silaffin domains. *Biotechnol. Prog.* **25**, 1643-1649, doi:10.1002/btpr.261 (2009).
- 55 Lechner, C. C. & Becker, C. F. W. Modified silaffin R5 peptides enable encapsulation and release of cargo molecules from biomimetic silica particles. *Bioorg. Med. Chem.* **21**, 3533-3541, doi:10.1016/j.bmc.2013.04.006 (2013).
- 56 Sewell, S. L. & Wright, D. W. Biomimetic Synthesis of Titanium Dioxide Utilizing the R5 Peptide Derived from *Cylindrotheca fusiformis*. *Chem. Mater.* **18**, 3108-3113 (2006).
- 57 Cole, K. E., Ortiz, A. N., Schoonen, M. A. & Valentine, A. M. Peptide- and Long-Chain Polyamine- Induced Synthesis of Microand Nanostructured Titanium Phosphate and Protein Encapsulation. *Chem. Mater.* **18**, 4592-4599 (2006).
- 58 Abdelhamid, M. A. A., Yeo, K. B., Ki, M. R. & Pack, S. P. Self-encapsulation and controlled release of recombinant proteins using novel silica-forming peptides as fusion linkers. *Int. J. Biol. Macromol.* **125**, 1175-1183, doi:10.1016/j.ijbiomac.2018.12.160 (2019).
- 59 Zhang, J. *et al.* Protamine-Templated Biomimetic Hybrid Capsules: Efficient and Stable Carrier for Enzyme Encapsulation. *Chem. Mater.* **20**, 1041–1048 (2008).
- 60 Kent, M. S. *et al.* Nanosilica Formation At Lipid Membranes Induced by the Parent Sequence of a Silaffin Peptide. *Langmuir* **25**, 305-310 (2009).

- 61 Pouget, E. *et al.* Hierarchical architectures by synergy between dynamical template self-assembly and biomineralization. *Nat. Mater.* **6**, 434-439, doi:10.1038/nmat1912 (2007).
- 62 Roth, K. M., Zhou, Y., Yang, W. & Morse, D. E. Bifunctional Small Molecules are Biomimetic Catalysts for Silica Synthesis at Neutral pH. *J. Am. Chem. Soc.* **127**, 325-330 (2004).
- 63 Xu, Z. *et al.* Enhanced catalytic stability and reusability of nitrilase encapsulated in ethyleneamine-mediated biosilica for regioselective hydrolysis of 1-cyanocycloalkaneacetonitrile. *Int. J. Biol. Macromol.* **130**, 117-124, doi:10.1016/j.ijbiomac.2019.02.131 (2019).
- 64 Min, K. H., Son, R. G., Ki, M. R., Choi, Y. S. & Pack, S. P. High expression and biosilica encapsulation of alkaline-active carbonic anhydrase for CO₂ sequestration system development. *Chemosphere* **143**, 128-134, doi:10.1016/j.chemosphere.2015.07.020 (2016).
- 65 Brunner, E., Lutz, K. & Sumper, M. Biomimetic synthesis of silica nanospheres depends on the aggregation and phase separation of polyamines in aqueous solution. *Physical Chemistry Chemical Physics* **6**, 854, doi:10.1039/b313261g (2004).
- 66 Neville, F., Broderick, M. J., Gibson, T. & Millner, P. A. Fabrication and activity of silicate nanoparticles and nanosilicate-entrapped enzymes using polyethyleneimine as a biomimetic polymer. *Langmuir* **27**, 279-285, doi:10.1021/la1033492 (2011).
- 67 Miller, S. A., Hong, E. D. & Wright, D. Rapid and efficient enzyme encapsulation in a dendrimer silica nanocomposite. *Macromol. Biosci.* **6**, 839-845, doi:10.1002/mabi.200600140 (2006).
- 68 Simons, K. & Vaz, W. L. Model systems, lipid rafts, and cell membranes. *Annu. Rev. Biophys. Biomol. Struct.* **33**, 269-295, doi:10.1146/annurev.biophys.32.110601.141803 (2004).
- 69 Wilson, D. N. & Doudna Cate, J. H. The structure and function of the eukaryotic ribosome. *Cold Spring Harb. Perspect. Biol.* **4**, a011536, doi:10.1101/cshperspect.a011536 (2012).
- 70 Bandyopadhyay, D., Cyphersmith, A., Zapata, J. A., Kim, Y. J. & Payne, C. K. Lysosome transport as a function of lysosome diameter. *PLoS One* **9**, e86847, doi:10.1371/journal.pone.0086847 (2014).
- 71 Selby, L. I., Cortez-Jugo, C. M., Such, G. K. & Johnston, A. P. R. Nanoescapology: progress toward understanding the endosomal escape of polymeric nanoparticles. *Wiley Interdiscip. Rev. Nanomed. Nanobiotechnol.* **9**, e1452, doi:10.1002/wnan.1452 (2017).
- 72 Zhou, H. *et al.* Biodegradable Inorganic Nanoparticles for Cancer Theranostics: Insights into the Degradation Behavior. *Bioconj. Chem.*, doi:10.1021/acs.bioconjchem.9b00699 (2019).
- 73 Shen, D. *et al.* Biphasic stratification approach to three-dimensional dendritic biodegradable mesoporous silica nanospheres. *Nano Lett.* **14**, 923-932, doi:10.1021/nl404316v (2014).
- 74 Choi, E., Lim, D. K. & Kim, S. Hydrolytic surface erosion of mesoporous silica nanoparticles for efficient intracellular delivery of cytochrome c. *J. Colloid Interface Sci.* **560**, 416-425, doi:10.1016/j.jcis.2019.10.100 (2020).
- 75 Martin, K. R. in *Interrelations between Essential Metal Ions and Human Diseases* Vol. 13 *Met. Ions Life Sci.* 451-473 (Springer, 2013).
- 76 Lin, W., Huang, Y. W., Zhou, X. D. & Ma, Y. In vitro toxicity of silica nanoparticles in human lung cancer cells. *Toxicol. Appl. Pharmacol.* **217**, 252-259, doi:10.1016/j.taap.2006.10.004 (2006).
- 77 Johnston, C. J. *et al.* Pulmonary Chemokine and Mutagenic Responses in Rats after Subchronic Inhalation of Amorphous and Crystalline Silica. *Toxicol. Sci.* **56**, 405-413 (2000).
- 78 He, Q., Zhang, Z., Gao, F., Li, Y. & Shi, J. In vivo biodistribution and urinary excretion of mesoporous silica nanoparticles: effects of particle size and PEGylation. *Small* **7**, 271-280, doi:10.1002/smll.201001459 (2011).
- 79 Nabeshi, H. *et al.* Systemic distribution, nuclear entry and cytotoxicity of amorphous nanosilica following topical application. *Biomaterials* **32**, 2713-2724, doi:10.1016/j.biomaterials.2010.12.042 (2011).

- 80 van Kesteren, P. C. *et al.* Novel insights into the risk assessment of the nanomaterial synthetic amorphous silica, additive E551, in food. *Nanotoxicology* **9**, 442-452, doi:10.3109/17435390.2014.940408 (2015).
- 81 Peters, R. *et al.* Presence of Nano-Sized Silica during In Vitro Digestion of Foods Containing Silica as a Food Additive. *ACS Nano* **6**, 2441–2451 (2012).
- 82 M. van der Zande, R. J. V., M. J. Groot, E. Kramer, Z. E. Herrera Rivera, K. Rasmussen, J. S. Ossenkoppele, P. Tromp, E. R. Gremmer, R. J. B. Peters, P. J. Hendriksen, H. J. P. Marvin, R. L. A. P. Hoogenboom, A. A. C. M. Peijnenburg, H. Bouwmeester. Sub-chronic toxicity study in rats orally exposed to nanostructured silica. *Part. Fibre Toxicol.* **11** (2014).
- 83 Zaitseva, N. V. *et al.* Toxicological assessment of nanostructured silica. The acute oral toxicity. *Voprosy Pitaniia* **83**, 42-49 (2014).
- 84 Gehrke, H. *et al.* In vitro toxicity of amorphous silica nanoparticles in human colon carcinoma cells. *Nanotoxicology* **7**, 274-293, doi:10.3109/17435390.2011.652207 (2013).
- 85 Huang, X., Teng, X., Chen, D., Tang, F. & He, J. The effect of the shape of mesoporous silica nanoparticles on cellular uptake and cell function. *Biomaterials* **31**, 438-448, doi:10.1016/j.biomaterials.2009.09.060 (2010).
- 86 Beddoes, C. M., Case, C. P. & Briscoe, W. H. Understanding nanoparticle cellular entry: A physicochemical perspective. *Adv. Colloid Interface Sci.* **218**, 48-68, doi:10.1016/j.cis.2015.01.007 (2015).
- 87 Canton, I. & Battaglia, G. Endocytosis at the nanoscale. *Chem. Soc. Rev.* **41**, 2718–2739 (2012).
- 88 Doherty, G. J. & McMahon, H. T. Mechanisms of endocytosis. *Annu. Rev. Biochem.* **78**, 857-902, doi:10.1146/annurev.biochem.78.081307.110540 (2009).
- 89 McMahon, H. T. & Boucrot, E. Molecular mechanism and physiological functions of clathrin-mediated endocytosis. *Nat. Rev. Mol. Cell Biol.* **12**, 517-533, doi:10.1038/nrm3151 (2011).
- 90 Tang, R. *et al.* Direct Delivery of Functional Proteins and Enzymes to the Cytosol Using Nanoparticle-Stabilized Nanocapsules. *ACS Nano* **7**, 6667-6673 (2013).
- 91 Vermeulen, L. M. P., De Smedt, S. C., Remaut, K. & Braeckmans, K. The proton sponge hypothesis: Fable or fact? *Eur. J. Pharm. Biopharm.* **129**, 184-190, doi:10.1016/j.ejpb.2018.05.034 (2018).
- 92 Beilhartz, G. L., Sugiman-Marangos, S. N. & Melnyk, R. A. Repurposing bacterial toxins for intracellular delivery of therapeutic proteins. *Biochem. Pharmacol.* **142**, 13-20, doi:10.1016/j.bcp.2017.04.009 (2017).
- 93 M. Vallet-Regi, A. R., R. P. del Real, J. Pérez-Pariente. A New Property of MCM-41: Drug Delivery System. *Chem. Mater.* **13**, 308 - 311 (2001).
- 94 Niu, Y. *et al.* Recent advances in the rational design of silica-based nanoparticles for gene therapy. *Ther. Delivery* **3**, 1217–1237 (2012).
- 95 Müller, R. H., Mäder, K. & Gohla, S. Solid lipid nanoparticles (SLN) for controlled drug delivery - a review of the state of the art. *Eur. J. Pharm. Biopharm.* **50**, 161-177 (2000).
- 96 Castillo, R. R. *et al.* Advances in mesoporous silica nanoparticles for targeted stimuli-responsive drug delivery: an update. *Expert Opin. Drug Deliv.* **16**, 415-439, doi:10.1080/17425247.2019.1598375 (2019).
- 97 Matsumura, Y. & Maeda, H. A New Concept for Macromolecular Therapeutics in Cancer Chemotherapy: Mechanism of Tumor-tropic Accumulation of Proteins and the Antitumor Agent Smancs. *Cancer Res.* **46**, 6387 - 6392 (1986).
- 98 Iyer, A. K., Khaled, G., Fang, J. & Maeda, H. Exploiting the enhanced permeability and retention effect for tumor targeting. *Drug Discov. Today* **11**, 812-818, doi:10.1016/j.drudis.2006.07.005 (2006).

- 99 Prabhakar, U. *et al.* Challenges and key considerations of the enhanced permeability and retention effect for nanomedicine drug delivery in oncology. *Cancer Res.* **73**, 2412-2417, doi:10.1158/0008-5472.CAN-12-4561 (2013).
- 100 Kaplon, H., Muralidharan, M., Schneider, Z. & Reichert, J. M. Antibodies to watch in 2020. *MAbs* **12**, 1703531, doi:10.1080/19420862.2019.1703531 (2020).
- 101 Castillo, R. R., Baeza, A. & Vallet-Regi, M. Recent applications of the combination of mesoporous silica nanoparticles with nucleic acids: development of bioresponsive devices, carriers and sensors. *Biomater. Sci.* **5**, 353-377, doi:10.1039/c6bm00872k (2017).
- 102 Glasgow, J. E., Asensio, M. A., Jakobson, C. M., Francis, M. B. & Tullman-Ercek, D. Influence of Electrostatics on Small Molecule Flux through a Protein Nanoreactor. *ACS Synth. Biol.* **4**, 1011-1019, doi:10.1021/acssynbio.5b00037 (2015).
- 103 Ellis, R. J. Macromolecular crowding: an important but neglected aspect of the intracellular environment. *Curr. Opin. Struct. Biol.* **11**, 114-119 (2001).
- 104 Betancor, L. & Luckarift, H. R. Bioinspired enzyme encapsulation for biocatalysis. *Trends Biotechnol* **26**, 566-572, doi:10.1016/j.tibtech.2008.06.009 (2008).
- 105 Sheldon, R. A. & van Pelt, S. Enzyme immobilisation in biocatalysis: why, what and how. *Chem. Soc. Rev.* **42**, 6223-6235, doi:10.1039/c3cs60075k (2013).
- 106 Sheldon, R. A. & Woodley, J. M. Role of Biocatalysis in Sustainable Chemistry. *Chem. Rev.* **118**, 801-838, doi:10.1021/acs.chemrev.7b00203 (2018).
- 107 Anastas, P. T. & Warner, J. C. *Green Chemistry: Theory and Practice.* (Oxford University Press, 1998).
- 108 Zhang, X. *et al.* Active surfaces engineered by immobilizing protein-polymer nanoreactors for selectively detecting sugar alcohols. *Biomaterials* **89**, 79-88, doi:10.1016/j.biomaterials.2016.02.042 (2016).
- 109 Zhang, L., Du, Y., Song, J. & Qi, H. Biocompatible magnetic nanoparticles grafted by poly(carboxybetaine acrylamide) for enzyme immobilization. *Int. J. Biol. Macromol.* **118**, 1004-1012, doi:10.1016/j.ijbiomac.2018.06.181 (2018).
- 110 Huang, R., Wu, M., Goldman, M. J. & Li, Z. Encapsulation of enzyme via one-step template-free formation of stable organic-inorganic capsules: A simple and efficient method for immobilizing enzyme with high activity and recyclability. *Biotechnol. Bioeng.* **112**, 1092-1101, doi:10.1002/bit.25536 (2015).
- 111 Renggli, K. *et al.* Biocatalytic atom transfer radical polymerization in a protein cage nanoreactor. *Polym. Chem.* **8**, 2133-2136, doi:10.1039/c6py02155g (2017).
- 112 Deng, Y., Misselwitz, B., Dai, N. & Fox, M. Lactose Intolerance in Adults: Biological Mechanism and Dietary Management. *Nutrients* **7**, 8020-8035, doi:10.3390/nu7095380 (2015).
- 113 Nishimura, T. & Akiyoshi, K. Biotransporting Biocatalytic Reactors toward Therapeutic Nanofactories. *Adv. Sci. (Weinh.)* **5**, 1800801, doi:10.1002/adv.201800801 (2018).
- 114 Liu, Y., Li, J. & Lu, Y. Enzyme therapeutics for systemic detoxification. *Adv. Drug Deliv. Rev.* **90**, 24-39, doi:10.1016/j.addr.2015.05.005 (2015).
- 115 Bertoni, S., Albertini, B., Dolci, L. S. & Passerini, N. Spray congealed lipid microparticles for the local delivery of beta-galactosidase to the small intestine. *Eur. J. Pharm. Biopharm.* **132**, 1-10, doi:10.1016/j.ejpb.2018.08.014 (2018).
- 116 Liu, W.-L. *et al.* Novel trypsin-FITC@MOF bioreactor efficiently catalyzes protein digestion. *J. Mater. Chem. B* **1**, 928-932, doi:10.1039/c3tb00257h (2013).
- 117 Zdarta, J., Meyer, A., Jesionowski, T. & Pinelo, M. A General Overview of Support Materials for Enzyme Immobilization: Characteristics, Properties, Practical Utility. *Catalysts* **8**, 92, doi:10.3390/catal8020092 (2018).
- 118 Zhang, Z., Zhang, R. & McClements, D. J. Lactase (β -galactosidase) encapsulation in hydrogel beads with controlled internal pH microenvironments: Impact of bead characteristics on enzyme activity. *Food Hydrocolloids* **67**, 85-93, doi:10.1016/j.foodhyd.2017.01.005 (2017).

- 119 Sheldon, R. A. Cross-linked enzyme aggregates (CLEAs): stable and recyclable biocatalysts. *Biochem. Soc. Trans.* **35**, 1583-1587 (2007).
- 120 T. Douglas, M. Y. Viruses: Making Friends with Old Foes. *Science* **312**, 873-875 (2006).
- 121 van Duin, J. & Tsareva, N. *Single-stranded RNA phages*. Second Edition edn, (Oxford University Press, 2006).
- 122 Glasgow, J. E., Capehart, S. L., Francis, M. B. & Tullman-Ercek, D. Osmolyte-Mediated Encapsulation of Proteins inside MS2 Viral Capsids. *ACS Nano* **6**, 8658–8664 (2012).
- 123 Timmermans, S. B. P. E. & van Hest, J. C. M. Self-assembled nanoreactors based on peptides and proteins. *Curr. Opin. Colloid Interface Sci.* **35**, 26-35, doi:10.1016/j.cocis.2018.01.005 (2018).
- 124 Comellas-Aragones, M. *et al.* A virus-based single-enzyme nanoreactor. *Nat. Nanotechnol.* **2**, 635-639, doi:10.1038/nnano.2007.299 (2007).
- 125 Schoonen, L., Nolte, R. J. & van Hest, J. C. Highly efficient enzyme encapsulation in a protein nanocage: towards enzyme catalysis in a cellular nanocompartment mimic. *Nanoscale* **8**, 14467-14472, doi:10.1039/c6nr04181g (2016).
- 126 D. Botstein, G. H. W., J. King. Mechanism of Head Assembly and DNA Encapsulation in Salmonella Phage P22. *J. Mol. Biol.* **80**, 669-695 (1973).
- 127 Patterson, D. P. *et al.* Virus-like particle nanoreactors: programmed encapsulation of the thermostable CelB glycosidase inside the P22 capsid. *Soft Matter* **8**, 10158, doi:10.1039/c2sm26485d (2012).
- 128 Patterson, D. P., Prevelige, P. E. & Douglas, T. Nanoreactors by Programmed Enzyme Encapsulation Inside the Capsid of the Bacteriophage P22. *ACS Nano* **6**, 5000-5009 (2012).
- 129 Patterson, D. P., Schwarz, B., Waters, R. S., Gedeon, T. & Douglas, T. Encapsulation of an Enzyme Cascade within the Bacteriophage P22 Virus-Like Particle. *ACS Chem. Biol.* **9**, 359-365, doi:10.1021/cb4006529 (2013).
- 130 Jordan, P. C. *et al.* Self-assembling biomolecular catalysts for hydrogen production. *Nat. Chem.* **8**, 179-185, doi:10.1038/nchem.2416 (2015).
- 131 Tetter, S. & Hilvert, D. Enzyme Encapsulation by a Ferritin Cage. *Angew. Chem. Int. Ed. Engl.* **56**, 14933-14936, doi:10.1002/anie.201708530 (2017).
- 132 Wörsdörfer, B., Woycechowsky, K. J. & Hilvert, D. Directed Evolution of a Protein Container. *Science* **331**, 589-592 (2011).
- 133 Azuma, Y., Zschoche, R., Tinzl, M. & Hilvert, D. Quantitative Packaging of Active Enzymes into a Protein Cage. *Angew. Chem. Int. Ed. Engl.* **55**, 1531-1534, doi:10.1002/anie.201508414 (2016).
- 134 Seeman, N. C. & Sleiman, H. F. DNA nanotechnology. *Nat. Rev. Mater.* **3**, 17068, doi:10.1038/natrevmats.2017.68 (2017).
- 135 Kim, S. H. *et al.* Reversible Regulation of Enzyme Activity by pH-Responsive Encapsulation in DNA Nanocages. *ACS Nano* **11**, 9352-9359, doi:10.1021/acsnano.7b04766 (2017).
- 136 Zhao, Z. *et al.* Nanocaged enzymes with enhanced catalytic activity and increased stability against protease digestion. *Nat. Commun.* **7**, 10619, doi:10.1038/ncomms10619 (2016).
- 137 Wan, L. *et al.* Programmable Self-Assembly of DNA-Protein Hybrid Hydrogel for Enzyme Encapsulation with Enhanced Biological Stability. *Biomacromolecules* **17**, 1543-1550, doi:10.1021/acs.biomac.6b00233 (2016).
- 138 Yan, Y. *et al.* DNA flower-encapsulated horseradish peroxidase with enhanced biocatalytic activity synthesized by an isothermal one-pot method based on rolling circle amplification. *Nanoscale* **10**, 22456-22465, doi:10.1039/c8nr07294a (2018).
- 139 Ching, S. H., Bansal, N. & Bhandari, B. Alginate gel particles-A review of production techniques and physical properties. *Crit. Rev. Food Sci. Nutr.* **57**, 1133-1152, doi:10.1080/10408398.2014.965773 (2017).

- 140 Kumar, R. S. S., Vishwanath, K. S., Singh, S. A. & Rao, A. G. A. Entrapment of α -amylase in alginate beads: Single step protocol for purification and thermal stabilization. *Process Biochemistry* **41**, 2282-2288, doi:10.1016/j.procbio.2006.05.028 (2006).
- 141 Nguyen, L. T., Lau, Y. S. & Yang, K. L. Entrapment of cross-linked cellulase colloids in alginate beads for hydrolysis of cellulose. *Colloids Surf. B Biointerfaces* **145**, 862-869, doi:10.1016/j.colsurfb.2016.06.008 (2016).
- 142 Freitas, F. F. *et al.* Optimization of the immobilization process of β -galactosidase by combined entrapment-cross-linking and the kinetics of lactose hydrolysis. *Braz. J. Chem. Eng.* **29**, 15-24 (2012).
- 143 Traffano-Schiffo, M. V., Aguirre Calvo, T. R., Castro-Giraldez, M., Fito, P. J. & Santagapita, P. R. Alginate Beads Containing Lactase: Stability and Microstructure. *Biomacromolecules* **18**, 1785-1792, doi:10.1021/acs.biomac.7b00202 (2017).
- 144 Ozaltin, K., Postnikov, P. S., Trusova, M. E., Sedlarik, V. & Di Martino, A. Polysaccharides based microspheres for multiple encapsulations and simultaneous release of proteases. *Int. J. Biol. Macromol.* **132**, 24-31, doi:10.1016/j.ijbiomac.2019.03.189 (2019).
- 145 Leonida, M. *et al.* Enzyme nanovehicles: Histaminase and catalase delivered in nanoparticulate chitosan. *Int. J. Pharm.* **557**, 145-153, doi:10.1016/j.ijpharm.2018.12.050 (2019).
- 146 Qin, C. *et al.* Water-solubility of chitosan and its antimicrobial activity. *Carbohydr. Polym.* **63**, 367-374, doi:10.1016/j.carbpol.2005.09.023 (2006).
- 147 Bilal, M., Iqbal, H. M. N., Hu, H., Wang, W. & Zhang, X. Enhanced bio-catalytic performance and dye degradation potential of chitosan-encapsulated horseradish peroxidase in a packed bed reactor system. *Sci. Total Environ.* **575**, 1352-1360, doi:10.1016/j.scitotenv.2016.09.215 (2017).
- 148 Zhang, Z., Zhang, R., Chen, L. & McClements, D. J. Encapsulation of lactase (beta-galactosidase) into kappa-carrageenan-based hydrogel beads: Impact of environmental conditions on enzyme activity. *Food Chem.* **200**, 69-75, doi:10.1016/j.foodchem.2016.01.014 (2016).
- 149 Campo, V. L., Kawano, D. F., da Silva, D. B. & Carvalho, I. Carrageenans: Biological properties, chemical modifications and structural analysis – A review. *Carbohydr. Polym.* **77**, 167-180, doi:10.1016/j.carbpol.2009.01.020 (2009).
- 150 Vergara, D. & Shene, C. Encapsulation of lactoferrin into rapeseed phospholipids based liposomes: Optimization and physicochemical characterization. *J. Food Eng.* **262**, 29-38, doi:10.1016/j.jfoodeng.2019.05.012 (2019).
- 151 Akbarzadeh, A. *et al.* Liposome: classification, preparation, and applications. *Nanoscale Res. Lett.* **8**, 102 (2013).
- 152 Onishi, H. Lactoferrin delivery systems: approaches for its more effective use. *Expert Opin. Drug Deliv.* **8**, 1469-1479 (2011).
- 153 Soboleva, S. E., Sedykh, S. E., Alinovskaya, L. I., Buneva, V. N. & Nevinsky, G. A. Cow Milk Lactoferrin Possesses Several Catalytic Activities. *Biomolecules* **9**, doi:10.3390/biom9060208 (2019).
- 154 Li, Y. *et al.* Novel lipidic and bienzymatic nanosomes for efficient delivery and enhanced bioactivity of catalase. *Int. J. Pharm.* **532**, 157-165, doi:10.1016/j.ijpharm.2017.09.006 (2017).
- 155 Borghi, C. *et al.* Serum uric acid and the risk of cardiovascular and renal disease. *J. Hypertens.* **33**, 1729-1741, doi:10.1097/HJH.0000000000000701 (2015).
- 156 Kaszuba, M. & Jones, M. N. Hydrogen peroxide production from reactive liposomes encapsulating enzymes. *Biochim. Biophys. Acta* **1419**, 221-228 (1999).
- 157 Oberholzer, T., Meyer, E., Amato, I., Lustig, A. & Pierre-Alain Monnard, P.-A. Enzymatic reactions in liposomes using the detergent-induced liposome loading method. *Biochim. Biophys. Acta* **1416**, 57-68 (1999).

- 158 S. W. Cowanit, R. M. G., J. N. Jansonius, J. A. Jenkins, R. Karlsson, N. König, E. F. Pai, R. A. Pauptit, P. J. Rizkallah, J. P. Rosenbusch, G. Rummel, T Schirmer. The structure of OmpF porin in a tetragonal crystal form. *Structure* **3**, 1041-1050 (1995).
- 159 Graff, A., Winterhalter, M. & Meier, W. Nanoreactors from Polymer-Stabilized Liposomes. *Langmuir* **17**, 919-923 (2001).
- 160 Yoshimoto, M. *et al.* Novel immobilized liposomal glucose oxidase system using the channel protein OmpF and catalase. *Biotechnol. Bioeng.* **90**, 231-238, doi:10.1002/bit.20422 (2005).
- 161 Abdelmohsen, L. K. *et al.* Dynamic Loading and Unloading of Proteins in Polymeric Stomatocytes: Formation of an Enzyme-Loaded Supramolecular Nanomotor. *ACS Nano* **10**, 2652-2660, doi:10.1021/acsnano.5b07689 (2016).
- 162 Piacentini, E., Yan, M. & Giorno, L. Development of enzyme-loaded PVA microspheres by membrane emulsification. *J. Membr. Sci.* **524**, 79-86, doi:10.1016/j.memsci.2016.11.008 (2017).
- 163 Gau, E., Flecken, F., Ksiazkiewicz, A. N. & Pich, A. Enzymatic synthesis of temperature-responsive poly(N-vinylcaprolactam) microgels with glucose oxidase. *Green Chem.* **20**, 431-439, doi:10.1039/c7gc03111d (2018).
- 164 Gracia, R. *et al.* Enzyme structure and function protection from gastrointestinal degradation using enteric coatings. *Int. J. Biol. Macromol.* **119**, 413-422, doi:10.1016/j.ijbiomac.2018.07.143 (2018).
- 165 Ishizuka, F. *et al.* Polymeric Nanocapsules for Enzyme Stabilization in Organic Solvents. *Macromolecules* **51**, 438-446, doi:10.1021/acs.macromol.7b02377 (2018).
- 166 Berne, C., Betancor, L., Luckarift, H. R. & Spain, J. C. Application of a Microfluidic Reactor for Screening Cancer Prodrug Activation Using Silica-Immobilized Nitrobenzene Nitroreductase. *Biomacromolecules* **7**, 2631-2636 (2006).
- 167 Betancor, L., Berne, C., Luckarift, H. R. & Spain, J. C. Coimmobilization of a redox enzyme and a cofactor regeneration system. *Chem. Commun. (Cambridge, U. K.)*, 3640-3642, doi:10.1039/b604689d (2006).
- 168 Cui, J. *et al.* Encapsulation of Spherical Cross-Linked Phenylalanine Ammonia Lyase Aggregates in Mesoporous Biosilica. *J. Agric. Food Chem.* **65**, 618-625, doi:10.1021/acs.jafc.6b05003 (2017).
- 169 Hong, S.-G. *et al.* Single enzyme nanoparticles armored by a thin silicate network: Single enzyme caged nanoparticles. *Chemical Engineering Journal* **322**, 510-515, doi:10.1016/j.cej.2017.04.022 (2017).
- 170 Zhang, C. *et al.* Encapsulation of enzymes in silica nanocapsules formed by an amphiphilic precursor polymer in water. *J. Mater. Chem. B* **3**, 1261-1267, doi:10.1039/c4tb01701c (2015).
- 171 Naik, R. R., Tomczak, M. M., Luckarift, H. R., Spain, J. C. & Stone, M. O. Entrapment of enzymes and nanoparticles using biomimetically synthesized silica. *Chem. Commun. (Cambridge, U. K.)*, 1684-1685, doi:10.1039/b404586f (2004).
- 172 Luckarift, H. R., Ku, B. S., Dordick, J. S. & Spain, J. C. Silica-immobilized enzymes for multi-step synthesis in microfluidic devices. *Biotechnol. Bioeng.* **98**, 701-705, doi:10.1002/bit.21447 (2007).
- 173 Luckarift, H. R., Dickerson, M. B., Sandhage, K. H. & Spain, J. C. Rapid, room-temperature synthesis of antibacterial bionanocomposites of lysozyme with amorphous silica or titania. *Small* **2**, 640-643, doi:10.1002/sml.200500376 (2006).
- 174 Ortac, I. *et al.* Dual-porosity hollow nanoparticles for the immunoprotection and delivery of nonhuman enzymes. *Nano Lett.* **14**, 3023-3032, doi:10.1021/nl404360k (2014).
- 175 Tu, J. *et al.* Mesoporous Silica Nanoparticles with Large Pores for the Encapsulation and Release of Proteins. *ACS Appl. Mater. Interfaces* **8**, 32211-32219, doi:10.1021/acsnano.6b11324 (2016).

- 176 Gustafsson, H., Thorn, C. & Holmberg, K. A comparison of lipase and trypsin encapsulated in mesoporous materials with varying pore sizes and pH conditions. *Colloids Surf. B* **87**, 464-471, doi:10.1016/j.colsurfb.2011.06.012 (2011).
- 177 Wu, F. *et al.* Monodisperse hybrid microcapsules with an ultrathin shell of submicron thickness for rapid enzyme reactions. *J. Mater. Chem. B* **3**, 796-803, doi:10.1039/c4tb01803f (2015).
- 178 Gulay, S. & Sanli-Mohamed, G. Immobilization of thermoalkalophilic recombinant esterase enzyme by entrapment in silicate coated Ca-alginate beads and its hydrolytic properties. *Int. J. Biol. Macromol.* **50**, 545-551, doi:10.1016/j.ijbiomac.2012.01.017 (2012).
- 179 Chung, J., Hwang, E. T., Kim, J. H., Kim, B. C. & Gu, M. B. Modular multi-enzyme cascade process using highly stabilized enzyme microbeads. *Green Chem.* **16**, 1163-1167, doi:10.1039/c3gc41737a (2014).
- 180 Hwang, E. T., Seo, B.-K., Gu, M. B. & Zeng, A.-P. Successful bi-enzyme stabilization for the biomimetic cascade transformation of carbon dioxide. *Catal. Sci. Technol.* **6**, 7267-7272, doi:10.1039/c6cy00783j (2016).
- 181 Cui, J., Sun, B., Lin, T., Feng, Y. & Jia, S. Enzyme shielding by mesoporous organosilica shell on Fe₃O₄@silica yolk-shell nanospheres. *Int. J. Biol. Macromol.* **117**, 673-682, doi:10.1016/j.ijbiomac.2018.05.227 (2018).
- 182 Han, P. *et al.* Enhancing Catalytic Activity and Stability of Yeast Alcohol Dehydrogenase by Encapsulation in Chitosan-Calcium Phosphate Hybrid Beads. *Ind. Eng. Chem. Res.* **54**, 597-604, doi:10.1021/ie503294a (2015).
- 183 Uhlen, M. *et al.* Proteomics. Tissue-based map of the human proteome. *Science* **347**, 1260419, doi:10.1126/science.1260419 (2015).
- 184 Santos, R. *et al.* A comprehensive map of molecular drug targets. *Nat. Rev. Drug Discov.* **16**, 19-34, doi:10.1038/nrd.2016.230 (2017).
- 185 Arinaminpathy, Y., Khurana, E., Engelman, D. M. & Gerstein, M. B. Computational analysis of membrane proteins: the largest class of drug targets. *Drug Discov Today* **14**, 1130-1135, doi:10.1016/j.drudis.2009.08.006 (2009).
- 186 Postis, V. *et al.* The use of SMALPs as a novel membrane protein scaffold for structure study by negative stain electron microscopy. *Biochim. Biophys. Acta* **1848**, 496-501, doi:10.1016/j.bbamem.2014.10.018 (2015).
- 187 Mizrahi, D. *et al.* Making water-soluble integral membrane proteins in vivo using an amphipathic protein fusion strategy. *Nat. Commun.* **6**, 6826, doi:10.1038/ncomms7826 (2015).
- 188 Popot, J. L. Amphipols, nanodiscs, and fluorinated surfactants: three nonconventional approaches to studying membrane proteins in aqueous solutions. *Annu. Rev. Biochem.* **79**, 737-775, doi:10.1146/annurev.biochem.052208.114057 (2010).
- 189 Ajees, A. A., Anantharamaiah, G. M., Mishra, V. K., Hussain, M. M. & Murthy, H. M. K. Crystal structure of human apolipoprotein A-I: Insights into its protective effect against cardiovascular diseases. *Proc. Natl. Acad. Sci. U. S. A.* **103**, 2126-2131, doi:10.1073/pnas.1003210107 (2006).
- 190 Annema, W. & von Eckardstein, A. High-Density Lipoproteins. *Circ. J.* **77**, 2432-2448, doi:10.1253/circj.CJ-13-1025 (2013).
- 191 Melchior, J. T. *et al.* A consensus model of human apolipoprotein A-I in its monomeric and lipid-free state. *Nat. Struct. Mol. Biol.* **24**, 1093-1099, doi:10.1038/nsmb.3501 (2017).
- 192 Bayburt, T. H., Grinkova, Y. V. & Sligar, S. G. Self-Assembly of Discoidal Phospholipid Bilayer Nanoparticles with Membrane Scaffold Proteins. *NanoLetters* **2**, 853-856 (2002).
- 193 Schuler, M. A., Denisov, I. G. & Sligar, S. G. Nanodiscs as a new tool to examine lipid-protein interactions. *Methods Mol. Biol.* **974**, 415-433, doi:10.1007/978-1-62703-275-9_18 (2013).

- 194 Denisov, I. G., Grinkova, Y. V., Lazarides, A. A. & Sligar, S. G. Directed Self-Assembly of Monodisperse Phospholipid Bilayer Nanodiscs with Controlled Size. *J. Am. Chem. Soc.* **126**, 3477-3487 (2004).
- 195 Ujwal, R. & Bowie, J. U. Crystallizing membrane proteins using lipidic bicelles. *Methods* **55**, 337-341, doi:10.1016/j.ymeth.2011.09.020 (2011).
- 196 Roy, J., Pondenis, H., Fan, T. M. & Das, A. Direct Capture of Functional Proteins from Mammalian Plasma Membranes into Nanodiscs. *Biochemistry* **54**, 6299-6302, doi:10.1021/acs.biochem.5b00954 (2015).
- 197 Bayburt, T. H. & Sligar, S. G. Self-assembly of single integral membrane proteins into soluble nanoscale phospholipid bilayers. *Protein Sci.* **12**, 2476-2481, doi:10.1110/ps.03267503 (2003).
- 198 Civjan, N. R., Bayburt, T. H., Schuler, M. A. & Sligar, S. G. Direct solubilization of heterologously expressed membrane proteins by incorporation into nanoscale lipid bilayers. *BioTechniques* **35**, 556-563 (2003).
- 199 Tekobo, S. & Pinkhassik, E. Directed covalent assembly of rigid organic nanodisks using self-assembled temporary scaffolds. *Chem. Commun. (Cambridge, U. K.)*, 1112-1114, doi:10.1039/b817598e (2009).
- 200 Knowles, T. J. *et al.* Membrane Proteins Solubilized Intact in Lipid Containing Nanoparticles Bounded by Styrene Maleic Acid Copolymer. *J. Am. Chem. Soc.* **131**, 7484-7485 (2009).
- 201 Oluwole, A. O. *et al.* Solubilization of Membrane Proteins into Functional Lipid-Bilayer Nanodiscs Using a Diisobutylene/Maleic Acid Copolymer. *Angew. Chem. Int. Ed.* **56**, 1919 - 1924 (2017).
- 202 Yasuhara, K. *et al.* Spontaneous Lipid Nanodisc Formation by Amphiphilic Polymethacrylate Copolymers. *J. Am. Chem. Soc.*, doi:10.1021/jacs.7b10591 (2017).
- 203 Loughlin, W. A., Tyndall, J. D. A., Glenn, M. P. & Fairlie, D. P. Beta-Strand Mimetics. *Chem. Rev.* **104**, 6085-6117 (2004).
- 204 Loughlin, W. A., Tyndall, J. D., Glenn, M. P. & Fairlie, D. P. Update 1 of: Beta-strand mimetics. *Chem. Rev.* **110**, PR32-PR69, doi:10.1021/cr040648k (2010).
- 205 Tamm, L. K., Arora, A. & Kleinschmidt, J. H. Structure and Assembly of β -Barrel Membrane Proteins. *J. Biol. Chem.* **276**, 32399-32402 (2001).
- 206 Fülöp, V. & Jones, D. T. β Propellers: structural rigidity and functional diversity. *Curr. Opin. Struct. Biol.* **9**, 715-721 (1999).
- 207 Halaby, D. M., Poupon, A. & Mornon, J.-P. The immunoglobulin fold family: sequence analysis and 3D structure comparisons. *Protein Eng.* **12**, 563-571 (1999).
- 208 Tycko, R. Insights into the Amyloid Folding Problem from Solid-State NMR. *Biochemistry* **42**, 3151-3159 (2003).
- 209 Chiti, F. & Dobson, C. M. Protein Misfolding, Functional Amyloid, and Human Disease. *Annu. Rev. Biochem.* **75**, 333-366, doi:10.1146/ (2006).
- 210 Marcos, E. *et al.* De novo design of a non-local beta-sheet protein with high stability and accuracy. *Nat. Struct. Mol. Biol.* **25**, 1028-1034, doi:10.1038/s41594-018-0141-6 (2018).
- 211 Dawson, W. M., Rhys, G. G. & Woolfson, D. N. Towards functional de novo designed proteins. *Curr. Opin. Chem. Biol.* **52**, 102-111, doi:10.1016/j.cbpa.2019.06.011 (2019).
- 212 Wang, J. *et al.* Antimicrobial peptides: Promising alternatives in the post feeding antibiotic era. *Med. Res. Rev.* **39**, 831-859, doi:10.1002/med.21542 (2019).
- 213 Chellat, M. F., Raguz, L. & Riedl, R. Targeting Antibiotic Resistance. *Angew. Chem. Int. Ed. Engl.* **55**, 6600-6626, doi:10.1002/anie.201506818 (2016).
- 214 Li, J., Xing, R., Bai, S. & Yan, X. Recent advances of self-assembling peptide-based hydrogels for biomedical applications. *Soft Matter* **15**, 1704-1715, doi:10.1039/c8sm02573h (2019).

- 215 Bechinger, B. & Lohner, K. Detergent-like actions of linear amphipathic cationic antimicrobial peptides. *Biochim. Biophys. Acta* **1758**, 1529-1539, doi:10.1016/j.bbamem.2006.07.001 (2006).
- 216 Tao, H. *et al.* Engineered nanostructured beta-sheet peptides protect membrane proteins. *Nat. Methods* **10**, 759-761, doi:10.1038/nmeth.2533 (2013).
- 217 Doig, A. J. A three stranded β -sheet peptide in aqueous solution containing N-methyl amino acids to prevent aggregation. *Chem. Commun. (Cambridge, U. K.)*, 2153-2154 (1997).
- 218 Gordon, D. J., Sciarretta, K. L. & Meredith, S. C. Inhibition of β -Amyloid(40) Fibrillogenesis and Disassembly of β -Amyloid(40) Fibrils by Short β -Amyloid Congeners Containing N-Methyl Amino Acids at Alternate Residues. *Biochemistry* **40**, 8237-8245 (2001).
- 219 Hoi, H. *et al.* Immobilization of membrane proteins on solid supports using functionalized beta-sheet peptides and click chemistry. *Chem. Commun. (Cambridge, U. K.)* **54**, 1889-1892, doi:10.1039/c7cc08652k (2018).
- 220 Lahiri, S., Brehs, M., Olschewski, D. & Becker, C. F. Total chemical synthesis of an integral membrane enzyme: diacylglycerol kinase from *Escherichia coli*. *Angew. Chem. Int. Ed. Engl.* **50**, 3988-3992, doi:10.1002/anie.201006686 (2011).
- 221 Lau, F. W. & Bowie, J. U. A Method for Assessing the Stability of a Membrane Protein. *Biochemistry* **36**, 5884-5892 (1997).
- 222 Li, D. *et al.* Crystal structure of the integral membrane diacylglycerol kinase. *Nature* **497**, 521-524, doi:10.1038/nature12179 (2013).
- 223 Van Horn, W. D. *et al.* Solution Nuclear Magnetic Resonance Structure of Membrane-Integral Diacylglycerol Kinase. *Science* **324**, 1726-1729 (2009).
- 224 Sanders, C. R. *et al.* *Escherichia coli* Diacylglycerol Kinase Is an α -Helical Polytopic Membrane Protein and Can Spontaneously Insert into Preformed Lipid Vesicles. *Biochemistry* **35**, 8610-8618 (1996).
- 225 Sanders, C. R. & Landis, G. C. Reconstitution of Membrane Proteins into Lipid-Rich Bilayered Mixed Micelles for NMR Studies. *Biochemistry* **34**, 4030-4040 (1995).
- 226 Durazzo, A. *et al.* Polyphenols: A concise overview on the chemistry, occurrence, and human health. *Phytother Res* **33**, 2221-2243, doi:10.1002/ptr.6419 (2019).
- 227 Castro-Acosta, M. L., Lenihan-Geels, G. N., Corpe, C. P. & Hall, W. L. Berries and anthocyanins: promising functional food ingredients with postprandial glycaemia-lowering effects. *Proc Nutr Soc* **75**, 342-355, doi:10.1017/S0029665116000240 (2016).
- 228 Hilger, D., Masureel, M. & Kobilka, B. K. Structure and dynamics of GPCR signaling complexes. *Nat. Struct. Mol. Biol.* **25**, 4-12, doi:10.1038/s41594-017-0011-7 (2018).
- 229 Brace, M. H., Cravatt, B. F. & Stevens, R. C. Structural commonalities among integral membrane enzymes. *FEBS Lett* **567**, 159-165, doi:10.1016/j.febslet.2004.04.084 (2004).
- 230 Lechner, C. C. & Becker, C. F. Immobilising proteins on silica with site-specifically attached modified silaffin peptides. *Biomater. Sci.* **3**, 288-297, doi:10.1039/c4bm00310a (2015).
- 231 Denisov, I. G. & Sligar, S. G. Nanodiscs for structural and functional studies of membrane proteins. *Nat. Struct. Mol. Biol.* **23**, 481-486, doi:10.1038/nsmb.3195 (2016).
- 232 Wang, S.-S. p-Alkoxybenzyl Alcohol Resin and p-Alkoxybenzyloxycarbonylhydrazide Resin for Solid Phase Synthesis of Protected Peptide Fragments. *J. Am. Chem. Soc.* **95**, 1328-1333 (1972).
- 233 Kaiser, E., Colecott, R. L., Bossinger, C. D. & Cook, P. I. Color test for detection of free terminal amino groups in the solid-phase synthesis of peptides. *Anal. Biochem.* **34**, 595-598 (1970).
- 234 Carolin C. Lechner, C. F. W. B. A sequence-function analysis of the silica precipitating silaffin R5 peptide. *Journal of Peptide Science* **20**, 152-158 (2013).
- 235 Hafner, M. *Biomimicry nano- and microparticles: applications for peptide/protein delivery and encapsulation* PhD thesis, University of Vienna, (2016).

- 236 Ragazzon, P. A., Bradshaw, T., Matthews, C., Iley, J. & Missailidis, S. The Characterisation of Flavone-DNA Isoform Interactions as a Basis for Anticancer Drug Development. *Anticancer Res.* **29**, 2273-2284 (2009).
- 237 Ciccione, J. *et al.* Unambiguous and Controlled One-Pot Synthesis of Multifunctional Silica Nanoparticles. *Chem. Mater.* **28**, 885-889, doi:10.1021/acs.chemmater.5b04398 (2016).
- 238 Luthra, A., Gregory, M., Grinkova, Y. V., Denisov, I. G. & Sligar, S. G. Nanodiscs in the studies of membrane-bound cytochrome P450 enzymes. *Methods Mol. Biol.* **987**, 115-127, doi:10.1007/978-1-62703-321-3_10 (2013).
- 239 in *United States Pharmacopeia and National Formulary (USP35-NF30)* (Rockville, MD, 2012).
- 240 Jeong, H., Kim, H. J. & Lee, S. J. Complete Genome Sequence of Escherichia coli Strain BL21. *Genome Announc* **3**, doi:10.1128/genomeA.00134-15 (2015).
- 241 Pan, S.-H. & Malcolm, B. A. Reduced Background Expression and Improved Plasmid Stability with pET Vectors in BL21 (DE3). *BioTechniques* **29**, 1234-1238.
- 242 Merck Millipore. The Complete Molecular Biology Toolkit. *Expert workflow solutions from DNA cloning to protein expression* (2011).
- 243 Del Favero, G. *et al.* Silica particles with a quercetin-R5 peptide conjugate are taken up into HT-29 cells and translocate into the nucleus. *Chem. Commun. (Camb.)* **55**, 9649-9652, doi:10.1039/c9cc02215e (2019).
- 244 Li, B. W. *et al.* Design and discovery of flavonoid-based HIV-1 integrase inhibitors targeting both the active site and the interaction with LEDGF/p75. *Bioorg Med Chem* **22**, 3146-3158, doi:10.1016/j.bmc.2014.04.016 (2014).
- 245 Kim, M. K., Choo, H. & Chong, Y. Water-soluble and cleavable quercetin-amino acid conjugates as safe modulators for P-glycoprotein-based multidrug resistance. *J. Med. Chem.* **57**, 7216-7233, doi:10.1021/jm500290c (2014).
- 246 Wang, R. E., Hunt, C. R., Chen, J. & Taylor, J. S. Biotinylated quercetin as an intrinsic photoaffinity proteomics probe for the identification of quercetin target proteins. *Bioorg. Med. Chem.* **19**, 4710-4720, doi:10.1016/j.bmc.2011.07.005 (2011).
- 247 Mattarei, A. *et al.* Regioselective O-derivatization of quercetin via ester intermediates. An improved synthesis of rhamnetin and development of a new mitochondriotropic derivative. *Molecules* **15**, 4722-4736, doi:10.3390/molecules15074722 (2010).
- 248 Verghese, J. *et al.* Flavone-based analogues inspired by the natural product simocyclinone D8 as DNA gyrase inhibitors. *Bioorg. Med. Chem. Lett.* **23**, 5874-5877, doi:10.1016/j.bmcl.2013.08.094 (2013).
- 249 Nifli, A.-P. *et al.* Quercetin Exhibits a Specific Fluorescence in Cellular Milieu: A Valuable Tool for the Study of Its Intracellular Distribution. *J. Agric. Food Chem.* **55**, 2873 - 2878 (2007).
- 250 Baran, I. *et al.* Fluorescence Properties of Quercetin in Human Leukemia Jurkat T-cells. *Rom. Journ. Phys.* **56**, 388-398 (2011).
- 251 Grimme, S. Do special noncovalent pi-pi stacking interactions really exist? *Angew. Chem. Int. Ed. Engl.* **47**, 3430-3434, doi:10.1002/anie.200705157 (2008).
- 252 Sulpizi, M., Gageot, M. P. & Sprik, M. The Silica-Water Interface: How the Silanols Determine the Surface Acidity and Modulate the Water Properties. *J. Chem. Theory Comput.* **8**, 1037-1047, doi:10.1021/ct2007154 (2012).
- 253 Forgue-Lafitte, M.-E., Coudray, A.-M., Bréant, B. & Mešter, J. Proliferation of the Human Colon Carcinoma Cell Line HT29: Autocrine Growth and Deregulated Expression of the c-myc Oncogene. *Cancer Res.* **49**, 6566-6571 (1989).
- 254 Herd, H. *et al.* Nanoparticle Geometry and Surface Orientation Influence Mode of Cellular Uptake. *ACS Nano* **7**, 1961-1973 (2013).

- 255 Zhang, X. *et al.* Membrane cholesterol modulates the fluid shear stress response of polymorphonuclear leukocytes via its effects on membrane fluidity. *Am. J. Physiol. Cell. Physiol.* **301**, C451-460, doi:10.1152/ajpcell.00458.2010 (2011).
- 256 Royle, S. J. The cellular functions of clathrin. *Cell. Mol. Life Sci.* **63**, 1823-1832, doi:10.1007/s00018-005-5587-0 (2006).
- 257 Zhang, Q. *et al.* Alumina at 50 and 13 nm nanoparticle sizes have potential genotoxicity. *J. Appl. Toxicol.* **37**, 1053-1064, doi:10.1002/jat.3456 (2017).
- 258 Galande, A. K., Weissleder, R. & Tung, C.-H. An Effective Method of On-Resin Disulfide Bond Formation in Peptides. *J. Comb. Chem.* **7**, 174-177 (2005).
- 259 Kelly, S. M. & Price, N. C. The Use of Circular Dichroism in the Investigation of Protein Structure and Function. *Curr. Protein Pept. Sci.* **1**, 349-384 (2000).
- 260 Casas-Terradellas, E. *et al.* Simultaneous electrophoretic analysis of proteins of very high and low molecular weights using low-percentage acrylamide gel and a gradient SDS-PAGE gel. *Electrophoresis* **27**, 3935-3938, doi:10.1002/elps.200600141 (2006).
- 261 Bouïs, D., Hospers, G. A. P., Meijer, C., Molema, G. & Mulder, N. H. Endothelium in vitro: A review of human vascular endothelial cell lines for blood vessel-related research. *Angiogenesis* **4**, 91-102 (2001).
- 262 Ramos, G. P. & Papadakis, K. A. Mechanisms of Disease: Inflammatory Bowel Diseases. *Mayo Clin. Proc.* **94**, 155-165, doi:10.1016/j.mayocp.2018.09.013 (2019).
- 263 Lebwohl, B., Sanders, D. S. & Green, P. H. R. Coeliac disease. *The Lancet* **391**, 70-81, doi:10.1016/s0140-6736(17)31796-8 (2018).
- 264 Abdo, M., Sun, Z. & Knapp, S. Biohybrid -Se-S- coupling reactions of an amino acid derived seleninate. *Molecules* **18**, 1963-1972, doi:10.3390/molecules18021963 (2013).
- 265 de Sousa Cavalcante, L. & Monteiro, G. Gemcitabine: metabolism and molecular mechanisms of action, sensitivity and chemoresistance in pancreatic cancer. *Eur. J. Pharmacol.* **741**, 8-16, doi:10.1016/j.ejphar.2014.07.041 (2014).
- 266 Hakki, M. Moving Past Ganciclovir and Foscarnet: Advances in CMV Therapy. *Curr. Hematol. Malign. Rep.*, doi:10.1007/s11899-020-00557-6 (2020).
- 267 Kinnear, C., Moore, T. L., Rodriguez-Lorenzo, L., Rothen-Rutishauser, B. & Petri-Fink, A. Form Follows Function: Nanoparticle Shape and Its Implications for Nanomedicine. *Chem. Rev.* **117**, 11476-11521, doi:10.1021/acs.chemrev.7b00194 (2017).
- 268 Laocharoensuk, R., Burdick, J. & Wang, J. Carbon-Nanotube-Induced Acceleration of Catalytic Nanomotors. *ACS Nano* **2**, 1069-1075 (2008).